UNIVERSITY OF LONDON
University College London
Department of Electrical and
Electronic Engineering

MEASUREMENT TECHNIQUES, NUMERICAL METHODS AND PHOTODIODE RISETIME TRANSFER STANDARDS FOR PICOSECOND OPTOELECTRONIC DEVICE METROLOGY AT 1 - 1.6 μm

David Anderson Humphreys

A Thesis, submitted for the degree of
Doctor of Philosophy
from the University of London

April 1990

ABSTRACT

Techniques to measure high speed photodiode performance have been reviewed. A number of heterodyne systems have been compared and their limitations discussed. A measurement system, using a novel detection scheme, has been developed. The operating frequency range is >40 GHz and the dynamic range is >20 dB.

A Heterodyne system which returns both the phase and the magnitude of the photodiode response has been presented. The results have been compared with time-domain measurements.

A new measurement system based on Integrated Optic Modulators has been described. The system produces a continuously levelled, modulated optical signal of >4 μW at frequencies of up to 22.6 GHz and at selected frequencies up to 25.6 GHz.

Results measured with an electrical autocorrelation system have been presented. This system has an estimated bandwidth of 40 GHz.

A procedure to correct for errors due to electrical reflection between the device under test and the measurement system has been described.

Three photodiodes have been measured by GTE (USA) using the FM sideband technique and at NPL using Heterodyne and Integrated Optic Modulator systems. Good agreement has been obtained with errors typically <1 dB.

Deconvolution techniques for extracting the device response from the measured waveform have been reviewed. An optimal method has been developed which is suitable for non-specialist users.

The effects of noise on a sampling system have been discussed. An algorithm to remove or reduce the effects of jitter has been presented. Techniques to measure jittered signals using both analogue and digital sampling oscilloscopes have been described and results presented.

The concept, philosophy and requirements for a photodiode risetime transfer standard have been discussed. A simple numerical model has been used to determine the optimum diode and package design. Three iterations of the design cycle have been reported. A 40 μm diameter optimised device has a 3 dB frequency of 17 GHz.

To Sharon, my wife

CONTENTS

LIST OF FIGURES

PART 1: TECHNIQUES FOR THE ACCURATE MEASUREMENT OF PHOTODIODES WITH FREQUENCY RESPONSES TO MILLIMETRE WAVELENGTHS

2. COMB HARMONIC METHOD

3. BEAT FREQUENCY METHOD

PART 3: DEVELOPMENT OF A GaInAs PHOTODIODE SUITABLE FOR USE AS A TRANSFER STANDARD AT 1.3 - 1.5 μm

LIST OF TABLES

PART 1: TECHNIQUES FOR THE ACCURATE MEASUREMENT OF PHOTODIODES WITH FREQUENCY RESPONSES TO MILLIMETRE WAVELENGTHS

PART 2: NUMERICAL TECHNIQUES TO IMPROVE THE ACCURACY OF PICOSECOND ELECTRICAL MEASUREMENTS

PART 3: DEVELOPMENT OF A GaInAs PHOTODIODE SUITABLE FOR USE AS A TRANSFER STANDARD AT 1.3 - 1.5 μm

GENERAL INTRODUCTION

1. BACKGROUND

Metrology, the science of measurement, is fundamental to the technological society in which we live. Good and accurate measurements are the basis for trade and are required to maintain efficient and competative industries. As technologies change and advance, the need for new measurements and new measurement standards will arise. Much of the work of the *National Physical Laboratory* (NPL) is involved with the development and provision of new and improved measurement standards. In the UK, NPL is the focus of the national measurement system. Standards used by industry can be referred back to the primary standards held at NPL by this means.

NPL has an extensive programme of research to develop standards for fibre optics. The fibre optics work carried out in the *Division of Electrical Science* has a common theme, the high frequency modulation properties of the fibre and optoelectronic components. At the time this work was started, DES had existing programmes in the areas of *Laser Measurements* and *Picosecond Optoelectronics*. It was therefore a natural progression for the high frequency modulation properties of the sources and detectors to be covered by this division.

2. AIMS OF THE WORK COVERED

This thesis is based on a programme of work to develop suitable measurement techniques to characterise the optoelectronic components used at either end of an optical fibre. The wavelength range of interest was 1 - 1.6 μm, covering the main fibre optic communications wavelengths of 1.3 μm and 1.55 μm. The aims of this programme were threefold: to provide improved measurement techniques; to provide numerical methods to decrease the uncertainties in the measured result and improve comparisons between different systems; and finally, to provide calibration artifacts which can be used to disseminate standards of temporal and frequency response measurement.

Photodiodes were identified as suitable devices for use as the transfer standard devices. The fabrication of these devices could not be carried out at NPL because we have no semiconductor facilities and so this work has been carried out in collaboration with *Plessey Research (Caswell)*.

3. LAYOUT AND CONTENT OF THE THESIS

The thesis is divided into three parts, covering the major areas of work. The order in which the contents have been presented has been chosen to form a coherent and structured pattern, allowing the reader to build on information presented in previous chapters. There are a few instances where reference has been made to work presented in later chapters but these have been minimised. There may also appear to be some inconsistancies in the measurement practices adopted during the course of the work. These arise because the order of presentation has little bearing on the sequence in which the work was performed.

In the first part of the thesis, different measurement techniques are described and new measurement methods are presented. Procedures to increase the accuracy of frequency response measurements are described. Comparisons between the different methods are presented.

The second part of the thesis describes numerical methods to improve the accuracy and interpretablity of the measured results. The measured results will be a convolution of the source, measurement system and unknown device responses. At high speeds (<100 ps timescale), these components will be comparable and it will therefore be difficult to separate out, by inspection, the response of the unknown device. The deconvolution method presented is designed for use with a photodiode risetime transfer standard, to determine the response of an unknown device.

An analysis of the effect of *Jitter*, the uncertainty in time between the trigger and the measurement signals, is also presented in this part of the thesis. Techniques to measure signals containing jitter and an algorithm to remove the effects of the jitter are described.

The third part of the thesis describes work performed as part of a joint research programme, in collaboration with *Plessey Research (Caswell)*, to develop high speed photodiodes for use as transfer standards for temporal risetime and frequency response. The requirements for these devices is discussed and the possible photodiode structures are compared. A numerical model of the photodiode has been used to determine the optimum design. The aim is to simultaneously maximise the diode active area and the bandwidth whilst retaining a good electrical return loss. Results obtained during three cycles of the design procedure will be presented.

PART 1

TECHNIQUES FOR THE ACCURATE MEASUREMENT OF PHOTODIODES WITH FREQUENCY RESPONSES TO MILLIMETRE WAVELENGTHS

1. INTRODUCTION TO MEASUREMENT TECHNIQUES

1.1. BACKGROUND AND CONTENT OF PART 1

This chapter provides an introduction to the first part of this thesis. The rationale for the work is outlined and the basic terms are defined.

Measurement is becoming increasingly important for the development of current and future communication systems. Standards for optoelectronic device metrology are being developed at NPL as part of the picosecond optoelectronics and fibre optics programmes. Fibre optics is the main driving force behind the development of the high speed optoelectronic devices. Optical communications systems with >2 Gb/s data rate are planned for installation within the next two years[1]. The development of future systems, operating at higher bit rates, will require advances in the optoelectronic device metrology to underpin such work.

In this part of the thesis a number of different measurement techniques will be evaluated and compared. The comparison of the different techniques is an important part of the evaluation process. New measurement systems, which overcome systematic errors inherent in conventional techniques, will be described. Procedures to improve the accuracy of frequency response measurements will be presented.

1.2. MEASUREMENT DOMAINS

Measurements are normally performed in either the time or the frequency domain. These two domains are related by the *Fourier transform*:

$$F(f) = \int_{-\infty}^{\infty} f(t)\, \exp(-2\pi j f t)\, dt \qquad \text{(eq. 1)}$$

and

$$f(t) = \int_{-\infty}^{\infty} F(f)\, \exp(2\pi j f t)\, df \qquad \text{(eq. 2)}$$

where f(t) is the time domain and F(f) is the frequency domain representation of the signal.

Under certain conditions[2], a waveform in one domain can be transformed to the other and vice-versa. The *Discrete Fourier Transform* (DFT) and *Fast Fourier Transform* (FFT) are more generally used to process measured results.

The major application of fast photodiodes is for digital

telecommunications, time is therefore the natural measurement domain. However, limitations of the measurement systems may make it impractical or even impossible to perform measurements in the time domain. A temporal measurement of a device response is exactly equivalent to a measurement of the frequency and phase responses of the device. In the case of an electrical device it is possible to define standards which determine the reference plane for the phase measurements. It would be difficult to define suitable reference planes for an optoelectronic device.

1.3. LIMITED MEASUREMENTS

As has already been stated, at high frequencies it may not be possible to determine both the phase and the frequency responses of a photodiode. A partial characterisation of the device can be obtained by measuring the magnitude of the frequency response. If a suitable system is chosen so that the degree of modulation of the optical signal is known, then the device response can be determined by measuring the r.f. power as a function of frequency. The temporal response of the device cannot be determined as no phase information is available.

1.4. PARAMETRIC MEASURES

Figures of merit such as the *Full Width at Half Maximum* (FWHM) of the impulse response, the risetime of to a step excitation T_r and the frequency at which the power in the modulation response drops to half (*3 dB frequency*) are commonly used to describe the performance of a device. These simple parametric measures are very helpful but should be treated with some caution as the result may be strongly dependent on the choice of the reference. For example, at low frequencies (<1 GHz) the resoponse of a fast photodiode may rise by 1 dB or so because of signals from light absorbed in undepleted material. The 3 dB frequency would therefore be strongly affected by the choice of the zero dB reference. The risetime of an impulse response is sometimes quoted. This is not a particularly useful parameter and should be ignored.

1.5. REFERENCES

1. *S O Johannsson*: 'Optical communication and new services in Sweden - present and future', ECOC'89 conference, Vol. 2, pp. 1 - 6, September 1989.

2. *R N Bracewell*: 'The fourier transform and its applications', McGraw-Hill, ISBN 0-07-Y66196-0, 1978.

2. COMB HARMONIC METHOD

2.1. INTRODUCTION

A train of impulses in the time domain has the important property of being equivalent to a comb of harmonics in the frequency domain. The spacing of the harmonics in the frequency domain Δf will be uniform and will be related to the separation of the impulses in the time domain such that $\Delta f = 1/\Delta t$. Using the Fourier transform relation between time and frequency, it can be shown that a convolution in the time domain corresponds to a multiplication in the frequency domain and vice-versa[1].

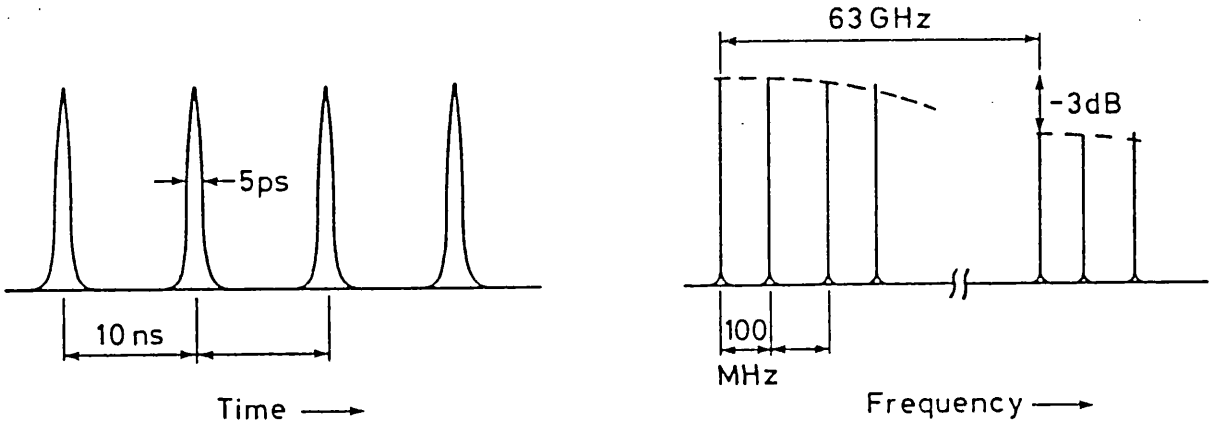

Figure 2.1. Relation between a comb of pulses in the time and frequency domains

An impulse is a mathematical concept and therefore an optical impulse is not physically realisable. Modelocked laser sources can produce pulses of picosecond or sub-picosecond duration. These pulses are often considerably shorter than the photodiode response and will therefore behave as optical impulses. The non-zero width of the optical pulses in the time domain will correspond to an envelope in the frequency domain. This relationship is illustrated in figure 2.1. The width of the pulse is normally determined by autocorrelation, performed using second harmonic generation (SHG) in an optically nonlinear material such as lithium iodate. The strength of the second harmonic signal is proportional to the optical intensity squared. Autocorrelation using SHG in nonlinear optical materials requires relatively high peak powers, of the order of several watts, to produce a real time response

and this tends to limit its application to the measurement of higher power lasers. However, the method has been sucessfully applied to semiconductor laser diodes[2] with peak powers in the milliwatt range. The pulse shape cannot be deduced from the autocorrelation trace however, a theoretical approximation such as a Gaussian or $sech^2$ pulse shape can be fitted to the autocorrelation trace. The envelope of the pulses in the frequency domain can be determined directly from the autocorrelation trace or by using the fitted curve.

The frequency response of a photodiode can be determined using a comb of ultra-short pulses to excite the detector. The power in the harmonic can then be measured using a spectrum analyser. The measurement could be performed in one of two ways: either as an absolute measurement or relative to a second detector whose response is known.

To perform an absolute measurement the response of the spectrum analyser must be calibrated and the pulse width of the source must also be known. Measurements of this type have been performed by *Burrus* using a 100 MHz colour centre laser[3] and by *Parker* using a colliding pulse modelocked dye laser[4]

If a relative measurement is required then the accuracy is determined by the stability of the spectrum analyser and laser over the period of the measurement and the accuracy of the reference detector calibration.

2.2. EFFECTS OF NOISE ON THE OPTICAL COMB SPECTRUM

Consider the effect of an amplitude variation that causes no change to the pulse shape. The amplitude modulation of a sinusoidal carrier at a frequency ω_c by a sinusoidal modulation frequency ω_m gives rise to sidebands at $\omega_c \pm \omega_m$ (equation 1). Since the pulse shape of the comb is unchanged, each of the comb harmonics will experience an equivalent modulation. Amplitude modulation, therefore, gives rise to sidebands for each of the comb harmonics, with a fixed ratiometric relation between the comb and sideband amplitudes as illustrated in figure 2.2 a and b.

$$\cos(\omega_c t)\ (1 + A\cos(\omega_m t)) = A\cos((\omega_c - \omega_m)t) + \cos(\omega_c t) + A\cos((\omega_c + \omega_m)t) \qquad \text{(eq. 1)}$$

where ω_c is the carrier frequency; ω_m is the modulation frequency and A is the modulation amplitude parameter which will be between zero and unity.

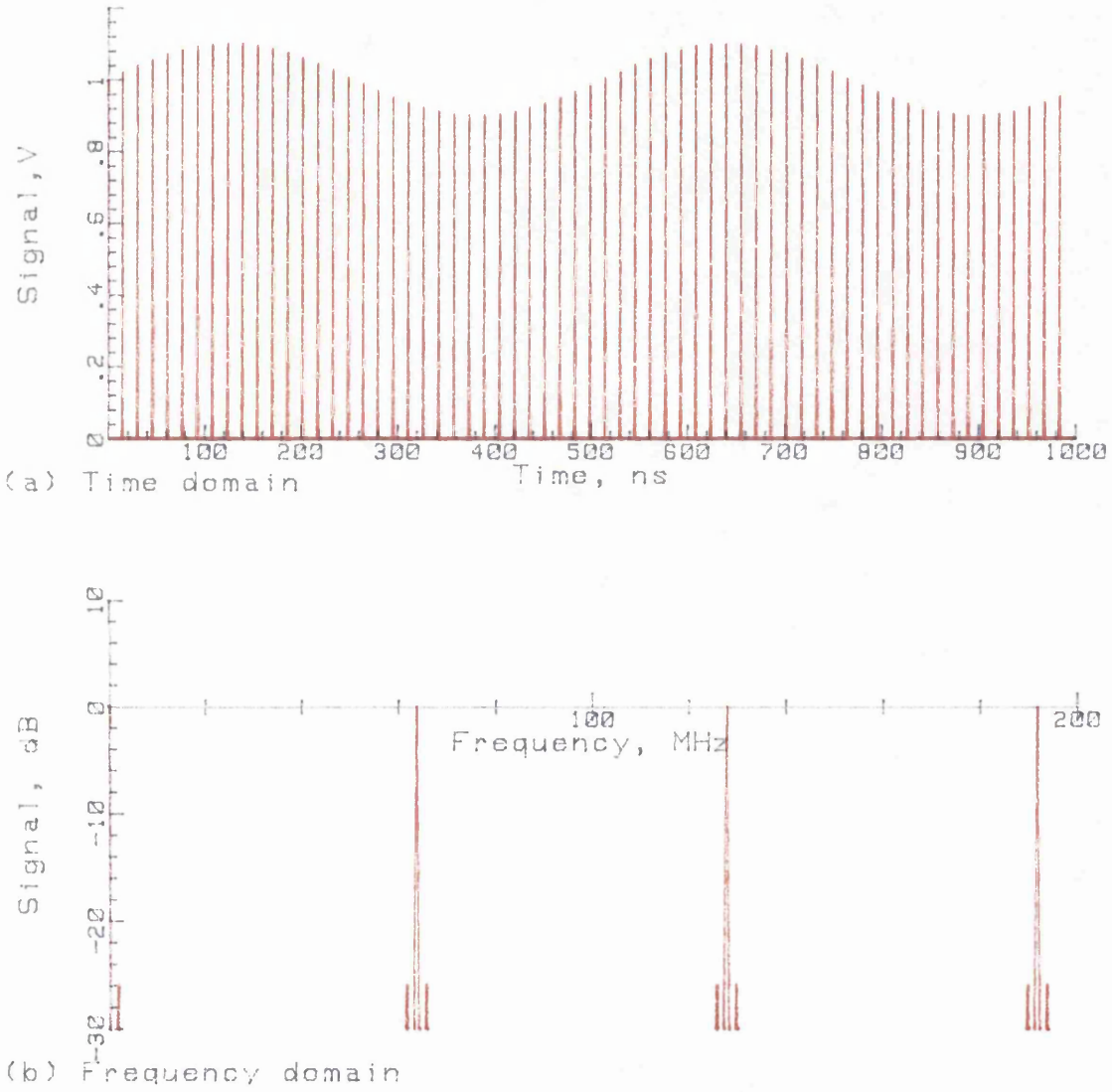

Figure 2.2. Effect of amplitude modulation on a comb of harmonics

Now consider the effect of frequency variations on the fundamental comb frequency. If the comb fundamental frequency ω_c is sinusoidally modulated at a frequency ω_m with a peak deviation β then the sidebands generated will be described by equation 2:

$$\cos((\omega_c + \beta\sin(\omega_m t))t) = J_0(\beta)\cos(\omega_c t) + \sum_{k=1}^{\infty} J_k(\beta)\,(\cos((\omega_c - k\omega_m)t) + (-1)^k \cos((\omega_c + k\omega_m)t)\,) \qquad \text{(eq. 2)}$$

where β is the modulation index and $J_n(\beta)$ is a n^{th} order Bessel function of the first kind.

Extending this analysis from a single frequency to a comb of harmonics, the modulation index of the i^{th} harmonic (β_i) will be $i\beta_1$ so that the pulse shape remains unchanged. The higher harmonics of the frequency modulated comb will therefore have more power in the sidebands, unlike the case of the amplitude modulated comb.

The example chosen here shows the harmonics and sidebands generated by modulating a 100 MHz comb at 50 kHz with a modulation index for the fundamental signal (β_1) of 0.01. The predicted response of a spectrum analyser with a 100 kHz resolution bandwidth has also been determined. The results are shown on a 2 MHz span, figure 2.3 (a) shows the response at the fundamental frequency. Figures 2.3(b) and (c) show the response at 10 GHz (i=100) and 25 GHz (i=250).

In the example the effect of a single modulation frequency has been considered. If the frequency variation were caused by noise or a complex signal then broad sidebands would result. The highest useable harmonics would be limited because the sidebands from the n^{th} harmonic would run into those from the next harmonic (n+1).

2.3. DISADVANTAGE OF THE OPTICAL COMB METHOD - SATURATION

The optical pulses from the comb source can give rise to high levels of injected signal and saturation. A typical mean photocurrent of 10 μA at 76 MHz corresponds to a charge of 130 pC/pulse. If a device diameter of 30 μm is assumed then the light will be confined to an area of < 30 μm^2 and the absorption depth will be of the order of 1 μm. These sizes are typical for a high speed photodiode. The initial injected carrier density will be of the order of $10^{15} cm^{-3}$ which is comparable to the background doping levels. As the optically generated carriers move apart, the electric field created by their presence will locally reduce the externally applied field due to the bias voltage[5]. If too large a photocurrent is injected then the reduction of the electric field will be sufficient that the carriers can no longer be considered to be

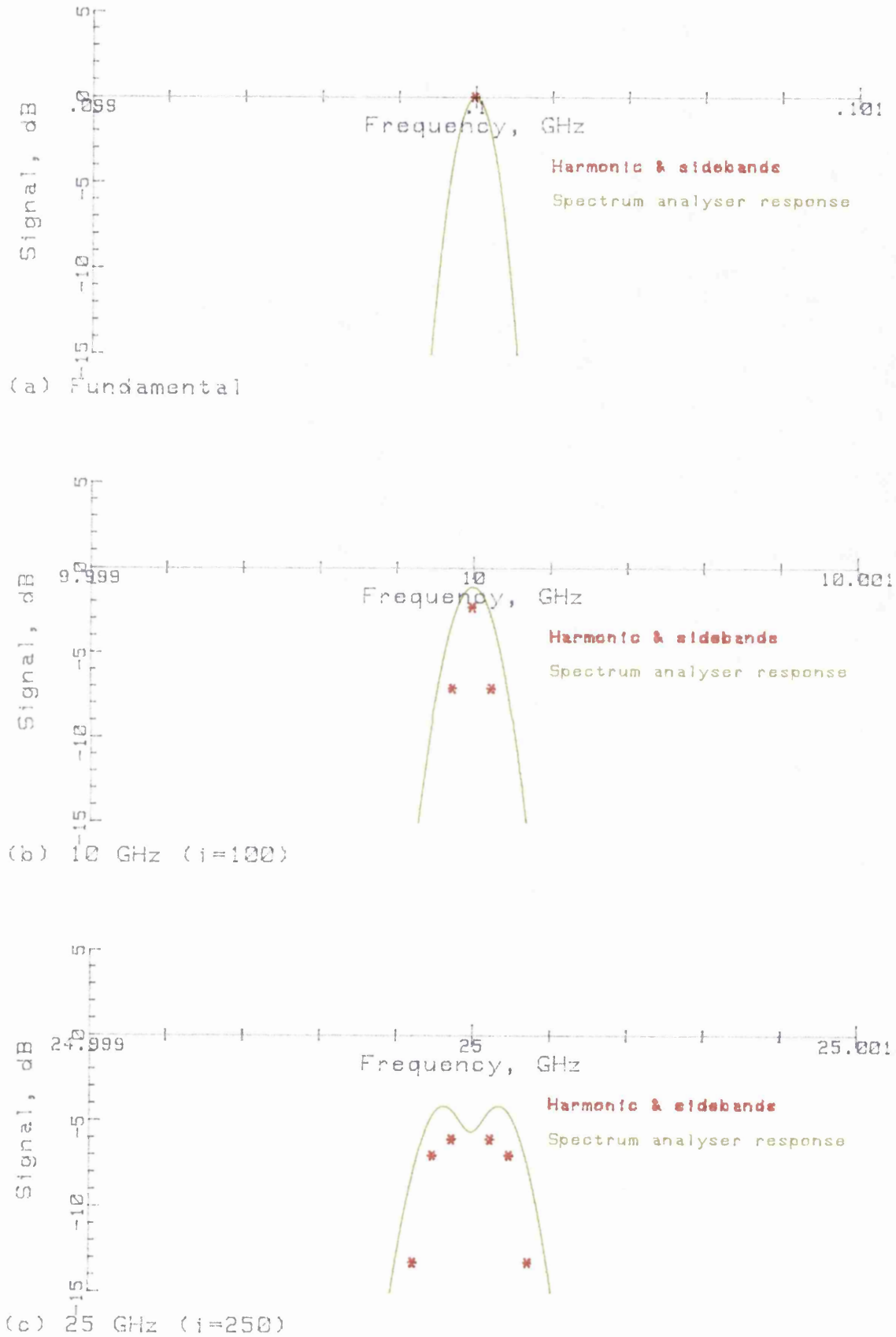

Figure 2.3. Effect of frequency modulation on a comb of harmonics

travelling at their saturated drift velocities. This will give rise to changes in the pulse shape and therefore the measured response will be incorrect.

2.4. MEASUREMENT OF A DIODE RESPONSE USING A STABLE OPTICAL COMB

To demonstrate the measurement technique the response of a fast GaAs photodiode has been measured at up to 40 GHz using a stable comb from a dye laser. A Rhodamine 6G dye laser at 590 nm, pumped by Argon Ion laser at 514nm, was used as the pulse source. The laser gives pulses with a width of 2 ps, determined by autocorrelation, and has low jitter and amplitude variations.

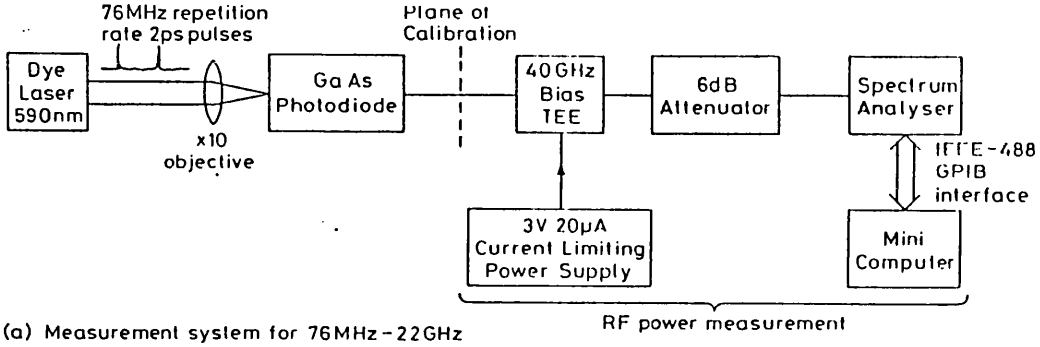

(a) Measurement system for 76MHz-22GHz

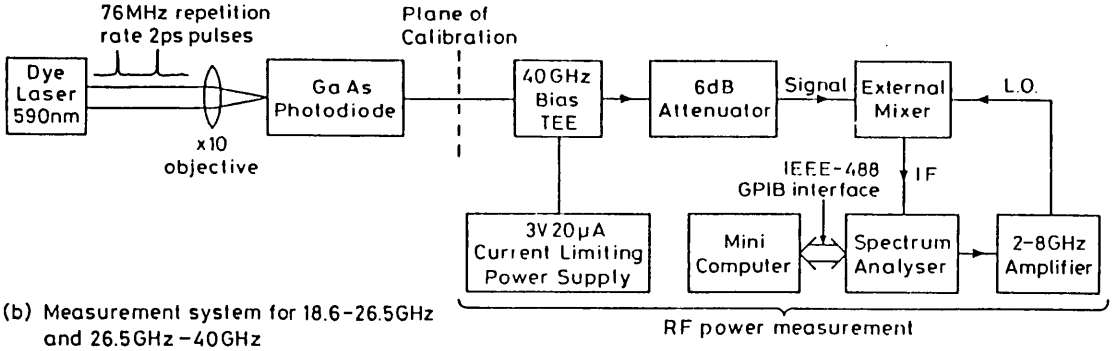

(b) Measurement system for 18.6-26.5GHz and 26.5GHz-40GHz

Figure 2.4. Comb measurement system using dye laser at 590 nm

The detector under test was a commercially available GEC GaAs device (#AOPH017.AB.11.1) with a circular active area of 20 μm in diameter (*1). The diode was biased at 3 V through a Wiltron K250 40 GHz bias tee. The measurement systems are shown in figures 2.4 a and b. The measurements were performed at frequencies below 20 GHz using a

---

(*1) *Private communication*: S Jones, GEC Hirst Research Plc, 1988.

spectrum analyser and preamplifier. At higher frequencies external mixers were used to cover the frequency ranges 18.6-26.5 GHz and 25-40 GHz. The external mixers do not contain a preselector and therefore a large number of spurious components will be present in the trace. It is essential that the fundamental frequency is well known so that the correct signal can be identified. The system was calibrated against a Wiltron 70KC50 10 MHz - 40 GHz r.f. detector to compensate for the response of the spectrum analyser and mixers. The calibrations were performed at a power level of -30 dBm to avoid nonlinearities in the r.f. detector response. A Wiltron 26.5 GHz sweeper was used as the power source. At frequencies above 26.5 GHz a doubler was used to extend the frequency range. The calibration systems are shown in figures 2.5a and b.

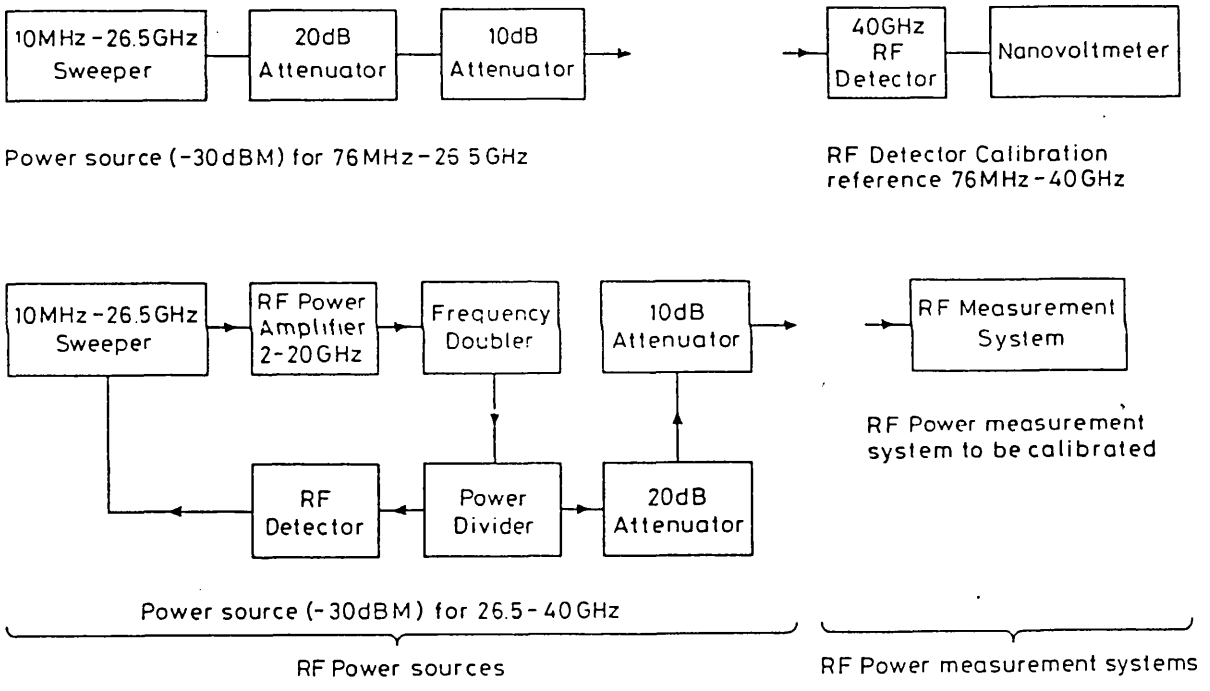

Figure 2.5. System to calibrate the sensitivity of the spectrum analyser and mixers

The results are shown in figure 2.6. The scatter in the measurements over the 26.5 - 40.0 GHz band was mainly caused by the large variations in the mixer sensitivity. The measured 3 dB frequency for this photodiode was 19.6 GHz with an uncertainty of ±2.8 GHz. The ripples in the result are due to electrical reflections between the photodiode under test and the measurement system.

This example demonstrates that measurements of a photodiode response can be made over a wide frequency range using a stable comb of

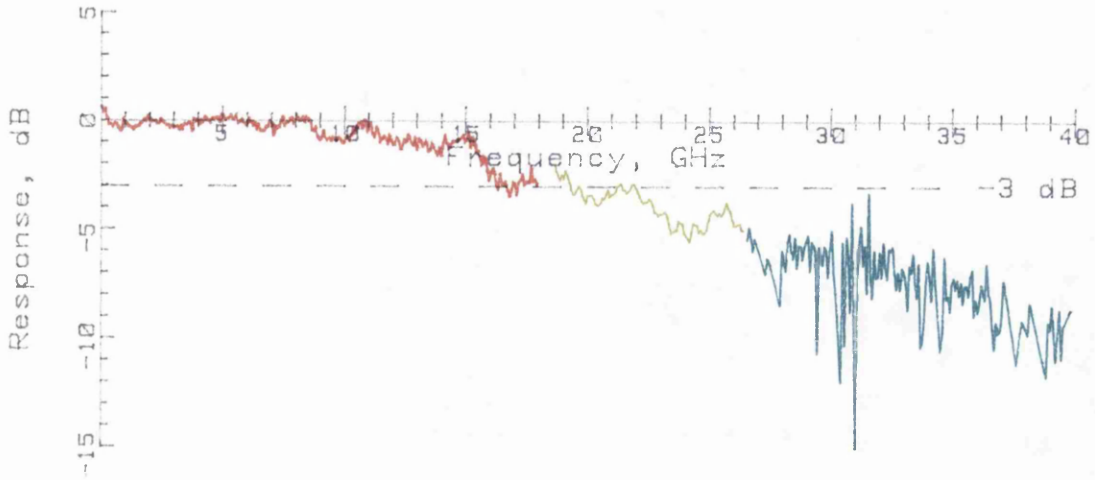

Figure 2.6. Response of GEC GaAs photodiode at 590 nm over 0 - 40 GHz

frequencies and a calibrated spectrum analyser.

2.5. MEASUREMENTS USING A TRANSFER STANDARD DIODE

The method described in the previous section assumes that the optical pulses are short compared to the detector response and that corrections for the optical pulse width can be made through the use of simple models. If these assumptions are false then an alternative approach must be chosen to correct for the optical comb spectrum.

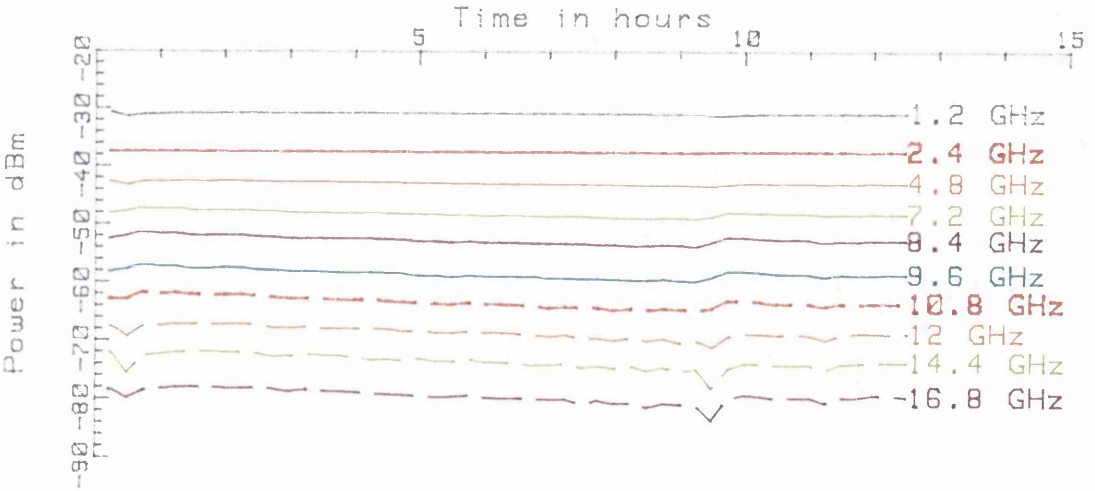

Figure 2.7. Stability of the comb power measured over
a twelve hour period.

If measurements of the comb harmonic spectrum are made with the device under test and with a photodiode which has a known frequency response

then corrections can be made for the response of the laser and for variations in the sensitivity of the measurement system. Two factors are necessary for the corrections to be accurate: firstly the laser comb must be stable for a period greater than the measurement period and secondly the spectrum analyser response must be linear. The overall accuracy of this type of measurement will be lower than that of a single direct measurement because two sets of measurements must be taken.

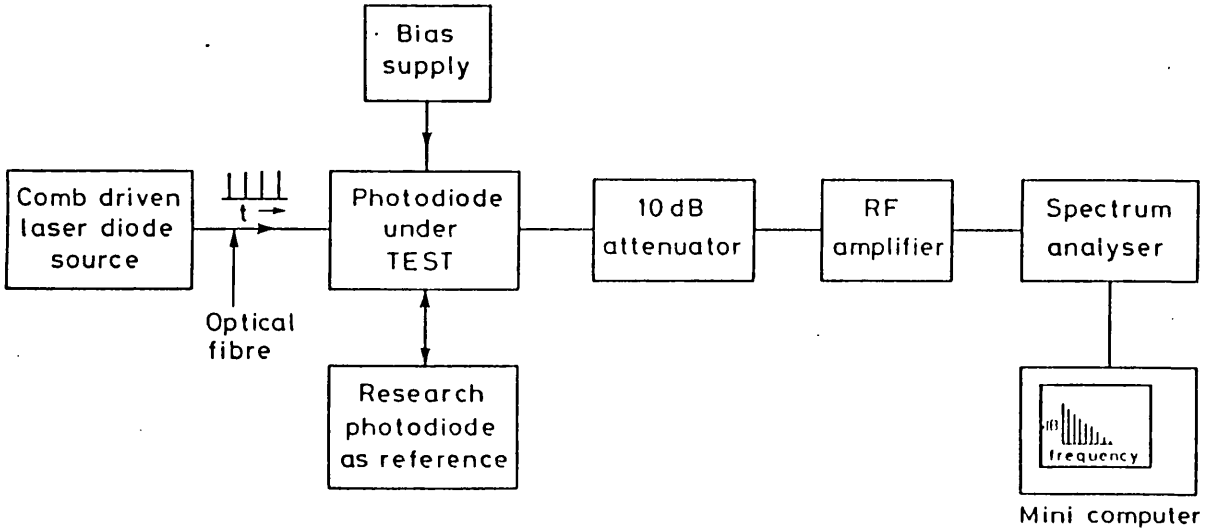

Figure 2.8. Layout of the comb harmonic measurement system using the AT&T diode as a transfer standard

The technique has been demonstrated using an Optoelectronics PPL50M laser as the source of the optical pulses. The FWHM of the pulses measured using a sampling oscilloscope is 60 - 70 ps, corresponding to a 3 dB frequency of about 3 GHz. The variation of the power in a number of the comb harmonics, measured over a twelve hour period, is shown in figure 2.7. The results indicate that the optical comb from the laser system is very stable although as one might expect the stability is reduced at the higher harmonics. The power in the harmonics has dropped by over 40 dB at 18 GHz when compared with the power in the fundamental. The dynamic range of this system is therefore considerably reduced at high frequencies.

A sequence of measurements were performed with both the Plessey and AT&T devices. The layout of the measurement system is shown in figure 2.8. Figure 2.9 shows the mean response and the error bars indicate the 95% confidence limits of the measurements due to statistical errors. No corrections have been made for the systematic

Figure 2.9. Measured response of the Plessey #20 diode using the AT&T diode as a transfer standard

errors introduced by the the AT&T diode response. The results indicate that provided the optical comb is stable and the response of the transfer standard diode is known, the use of a reference device can considerably extend the capabilities of the measurement system.

2.6. CHAPTER SUMMARY

A train of pulses in the time domain corresponds to a comb of harmonics in the frequency domain. In this chapter the method for determining the response of a photodiode by measuring the power in the harmonics has been described.

The effects of amplitude and frequency modulation of the pulse train has been considered. Amplitude modulation of the pulse train gives rise to equal sidebands on all of the harmonic frequencies. Frequency modulation of the pulse train causes a degradation of the comb at high frequencies and therefore the phase noise in the fundamental frequency source will ultimately limit the highest harmonic that can be used. The limitations of the comb method, due to saturation of the optical detector have also been considered.

The measurement of a GaAs photodiode at 590 nm, using a modelocked dye laser source, has been described. The 3 dB frequency of the photodiode has been measured as 19.6 GHz.

A measurement method using a fast photodiode with a known response as a transfer standard has been described. The photodiode was used with a

stable comb from a laser at 1300 nm to determine the response of a GaInAs photodiode. This photodiode had a measured 3 dB frequency of 14 GHz. Over the range of measurement (18 GHz), the power in the harmonics dropped by over 40 dB. Despite the considerable drop in the comb power at higher frequencies a dynamic range of greater than 15 dB was achieved at all frequencies.

The comb harmonic method can be used either with a calibrated spectrum analyser or with a calibrated transfer standard photodiode to measure the response of an unknown photodiode. The limitations and merits of the method have been discussed.

3. BEAT FREQUENCY METHOD

3.1. INTRODUCTION

The absorption of light within a semiconductor material gives rise to electron-hole pairs in proportion to the intensity of the incident light. The photocurrent produced by two plane polarised optical signals with different optical frequencies incident on a photodiode will be given by:

$$I_d = \eta \, (P_1 + P_2 + 2\sqrt{P_1 P_2} \cos((\omega_1 - \omega_2)t) \cos(\emptyset)) \qquad \text{(eq. 1)}$$

where I_d is the photocurrent; η is the sensitivity in A/W; P_1 and P_2 are the optical intensities in watts; ω_1 and ω_2 are the laser frequencies in radians/sec and $\emptyset$ is the angle in radians between the polarisation vectors of the two signals.

The heterodyne principle is shown in figure 3.1. This measurement technique has been used by a number of authors to measure photodiode responses at a variety of wavelengths[6-14].

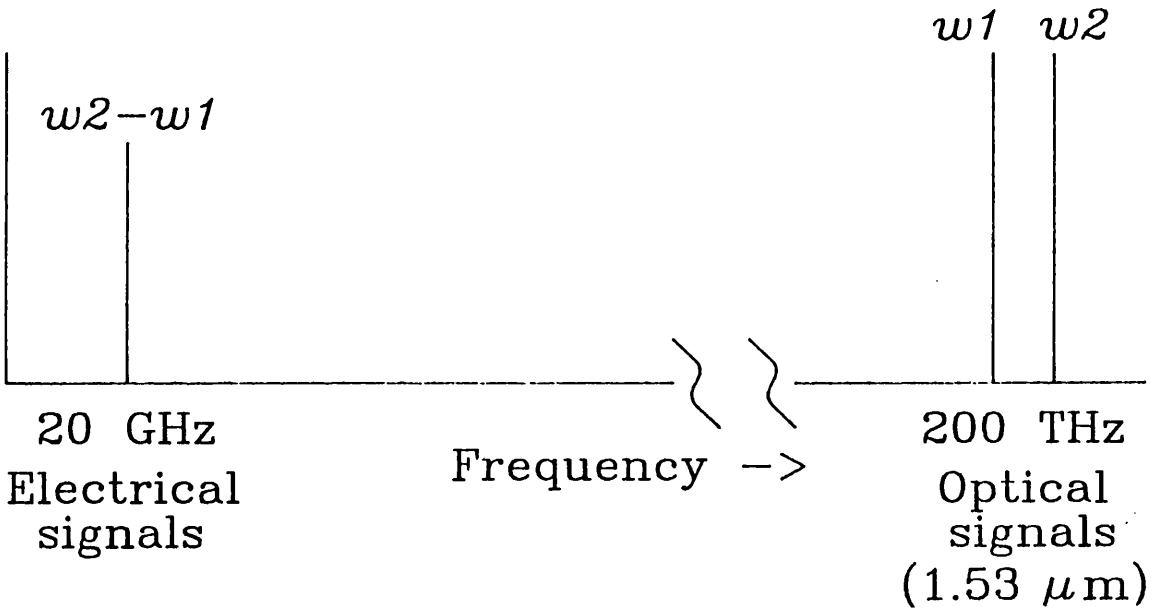

Figure 3.1. Heterodyne principle

If the optical frequencies of the two sources can be accurately controlled the magnitude response of the detector can be determined by measuring the r.f. power in the beat and the photocurrent due to the two optical signals. If the beat frequency resolution required is

±20 MHz then this would correspond to a source stability of $\pm 10^{-7}$ for the two lasers at a nominal wavelengths of 1.5 μm.

Tunable optical sources are required in the 1 - 1.6 μm region of interest for fibre optic communications applications. Gas lasers such as Helium-Neon at 1.522 nm will give linewidths of the order of 1 MHz, limited by Doppler broadening, but the tunable range will be limited. The power available from these sources is of the order of a few milliwatts.

Nd-YAG ring lasers at 1319 nm can be thermally tuned to give difference frequencies of up to 20 GHz with linewidths of a few tens of kilohertz[15,16]. By careful device selection the difference frequency range can be extended to roughly 40 GHz (*1). This type of laser will give powers of a few milliwatts. Neodymium lasers using a $NaNdP_4O_{12}$ host can be tuned from 1.312 μm to 1.334 μm giving a potential range of 3.8 THz[17].

Colour centre lasers can be tuned over the range of interest and have linewidths comparable to those of the gas laser sources[18]. The optical power available from such sources is higher - several tens of milliwatts. However, this type of laser has a number of drawbacks: it is optically pumped, requiring several watts of optical power and the crystal must be kept at cryogenic temperatures.

The power requirements to measure photodiodes are modest and therefore semiconductor lasers offer the potential of providing a compact and portable source with low power requirements. A typical Fabry-Perot semiconductor communications laser will emit a spectrum of modes. Such a laser would be unsuitable for use in a beat frequency system. Two approaches are available to ensure that the laser produces a single optical frequency: either a frequency selecting element can be incorporated into the diode structure, or the laser can be anti-reflection coated and incorporated into an external cavity.

3.2. DISTRIBUTED FEEDBACK AND DISTRIBUTED BRAGG REFLECTOR LASERS

The Distributed Feedback laser (DFB) and Distributed Bragg Reflector (DBR) lasers incorporate a grating within the laser cavity to reduce

---

(*1) *Private communication*: D Wake, BTRL, Ipswich, Suffolk

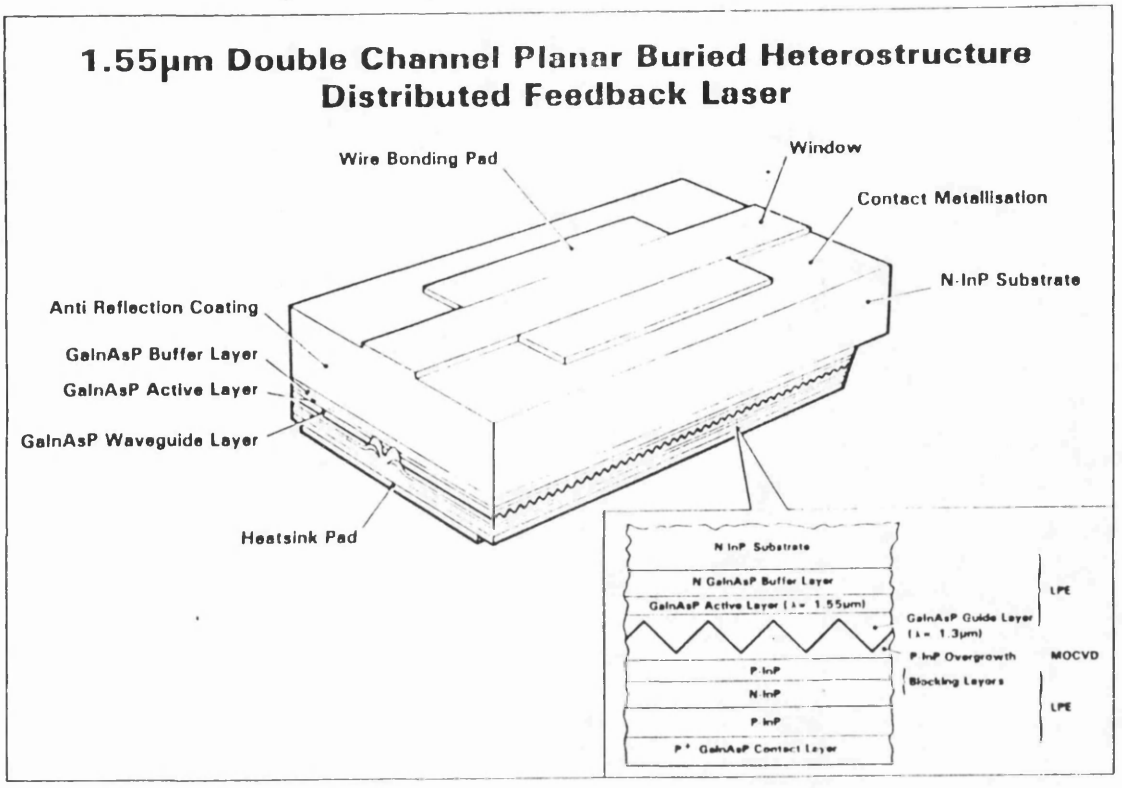

Figure 3.2. Distributed Feedback laser structure (Plessey Caswell)

the linewidth. These lasers have been developed to overcome the effects of dispersion in optical fibres at high bit rates and for coherent optical communications. The structures of these two types of lasers are shown in figures 3.2 and 3.3.

Early devices were fabricated using photolithographic techniques to define the grating. More recently the use of electron beam lithography has allowed the inclusion of a $\lambda/4$ phase shift in the pattern to improve the yield of single mode devices[19] and the tailoring of the grating pitch to the layer thickness within the wafer to improve the wavelength tolerence[20].

The periodic gratings act as reflectors for the forward and reverse travelling waves. In a conventional DFB structure the grating is uniform and this gives rise to two resonance peaks. If a "phase jump" of $\lambda/4$ is included the structure will have only a single resonance. The power output from the two facets can be controlled by the position of the phase jump. The measured linewidth (Δf) varies linearly with inverse power[21]. The lasing linewidth can be reduced by extending the cavity length and by detuning the lasing wavelength from the gain peak by 5 - 50 nanometers[22,23,24]. Linewidths of 3 MHz have been obtained

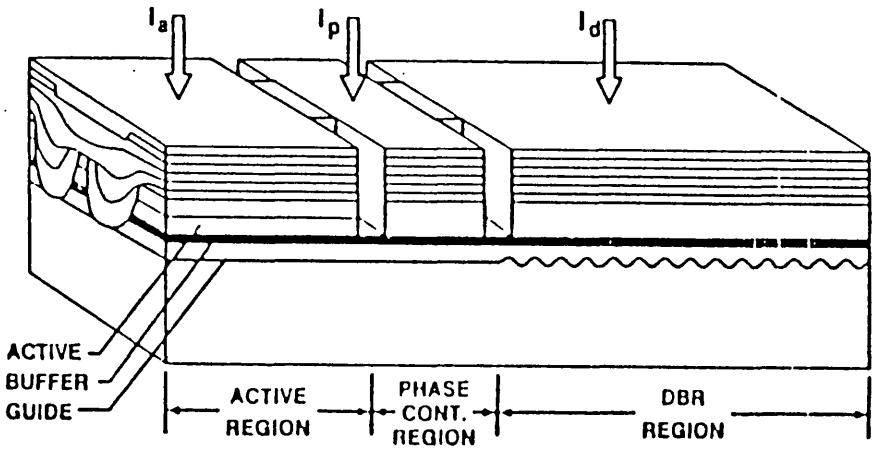

Figure 3.3. Multi-electrode DBR structure (after *Lee*)

for a buried heterostructure (BH) DFB laser grown by atmospheric metal organic vapour phase epitaxy (MOVPE) with 25 nm of detuning at a power of 4 mW[25,26].

Under modulation the lasing frequency shows a tendency to chirp[27] causing inter-symbol interference in communication systems. This property can be used to provide the basis for a measurement system and will be discussed later.

The distributed Bragg reflector (DBR) lasers offer the potential of tuning ranges in excess of 1 THz[28]. The multi-electrode structure allows separate adjustment of the gain, phase matching and grating regions[29,30]. The control of the currents to each of the elements can be performed under computer control, allowing the direct selection of the desired optical frequency[31].

3.3. EXTERNAL CAVITY LASERS

The inclusion of a semiconductor laser into an external cavity can greatly reduce the linewidth. *R Wyatt* at British Telecom Research Laboratories has developed an external cavity laser diode system with a linewidth of 10 kHz[32]. These lasers have been more recently re-engineered[33] to give a rugged and compact source. Other authors have also been developing extended cavity laser sources for spectroscopy[34,35] and to improve the stability of caesium clocks by optical pumping[36].

Integrated optic devices have also been used in external cavities to

provide linewidth reduction and modulation capabilities[37]. External cavities have been used with DFB lasers[38,39] and DBR lasers for coherent optical communications[40].

3.4. LOSS PENALTY CAUSED BY BEATWIDTH

The linewidth of the external cavity lasers is only a few tens of kilohertz and therefore the width of the beat signal was considerably smaller than the resolution bandwidth of the spectrum analyser. If the width of the beat signal is comparable to, or greater than, the resolution bandwidth of the spectrum analyser then a lower power will be measured than would be predicted from equation 1. The reduction in measured power is because the spectrum analyser measures the spectral density of the beat signal as expessed in equation 2.

$$P(f_a) = \int_{-\infty}^{+\infty} S(f_a - f')\, B(f_b - f')\, df' \qquad \text{(eq. 2)}$$

where P is the observed power at a frequency f_a; S is the spectrum analyser power spectrum response function; and B is the beat frequency power spectral density centered at frequency f_b.

A lower limit to the sensitivity will be imposed by the noise performance of the spectrum analyser. This will give a reduced dynamic range for the measurement system. These effects are illustrated in figure 3.4.

The signal to noise ratio of the beat signal cannot be enhanced by reducing the resolution bandwidth of the spectrum analyser because if the beat width is large compared to the resolution bandwidth of the instrument then the ratio of the beat power and the noise power will be nearly constant.

The lineshape of a DFB laser is normally assumed to be *Lorentzian* and so the beat signal will also have a Lorentzian lineshape:

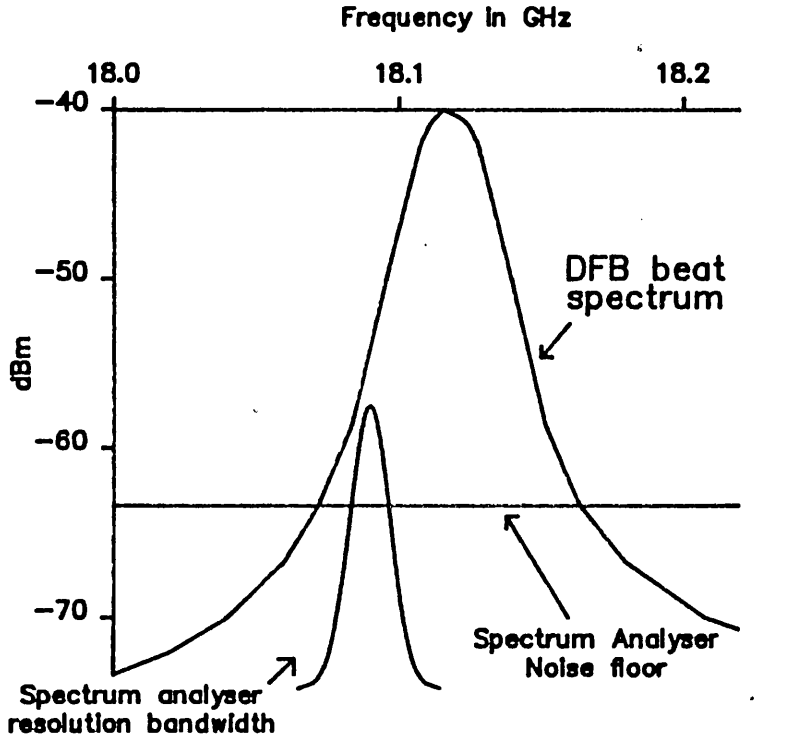

(a) Components of measured response

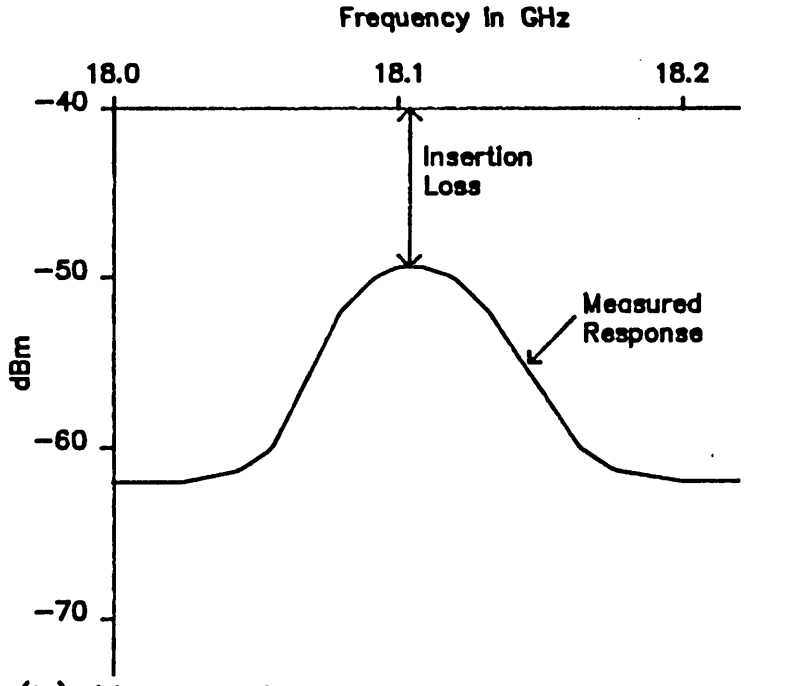

(b) Measured response

Figure 3.4. Effect of spectrum analyser bandwidth and noise limits on the measured beat signal

$$I_B(f) = \frac{\delta f_B}{2\pi\left((f-f_B)^2 + (\frac{\delta f_B}{2})^2\right)} \qquad \text{(eq. 3)}$$

and the FWHM of the beat signal will be the sum of the FWHMs of the two lasers:

$$\delta f_B = \delta f_1 + \delta f_2 \qquad \text{(eq. 4)}$$

where $I_B(f)$ is the spectral density of the photocurrent at a frequency f; f_B is the laser frequency and δf_B, δf_1 and δf_2 are the full width at half maximum (FWHM) of the beat signal and the two lasers respectively.

The filter response of a typical spectrum analyser (HP 8566B) will be approximately *Gaussian*[41] and therefore the expected insertion loss and the error in the measured width can be readily calculated. Figure 3.5 shows the variation of the insertion loss with the width of the beat and figure 3.6 shows the error between the width of the measured and the true widths as a function of the true width. The calculations have assumed Lorentzian and Gaussian lineshapes for the spectrum analyser and heterodyne signals. A filter width of 3 MHz has been chosen for the spectrum analyser. Neither the laser nor the spectrum analyser will have the ideal characteristic assumed though the error in the result is expected to be small.

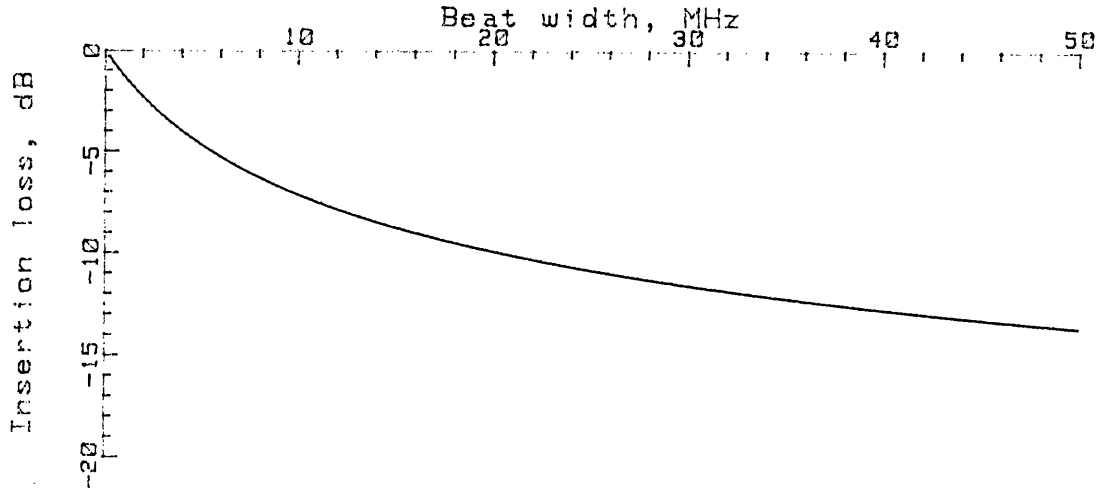

Figure 3.5. Variation of the insertion loss with beatwidth

This analysis assumes that there is no correlation between the

amplitude and frequency noise. The amplitude of the beat signal remains constant for small changes in the lasing frequency. The lineshape therefore represents a probability density distribution with frequency. This infers that the spectral distributions of the optical signal, the photocurrent and the r.f. power will be identical. If there were a correlation between the amplitude and frequency noise then the spectral distributions would differ.

3.5. OPTICAL FEEDBACK

Feedback from reflections within the measurement system may cause the laser linewidth to vary. Both DFB and DBR lasers are very sensitive to optical feedback causing instability in the lasing wavelength and linewidth[42,43]. This has been studied and five distinct regimes of optical feedback have been identified[44].

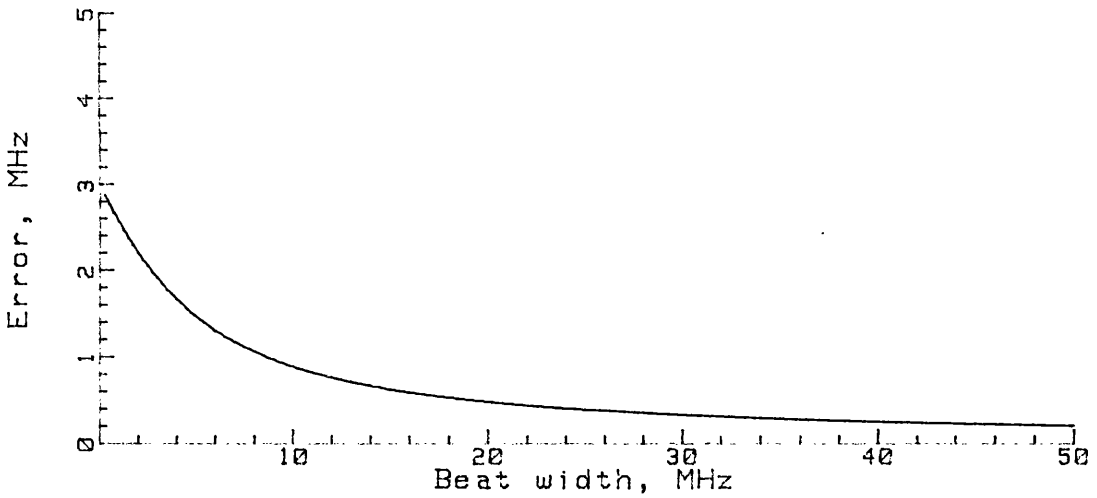

Figure 3.6. Effect of the spectrum analyser response on the measured heterodyne width

The effects of optical feedback can be reduced by the inclusion of optical isolators. The phase of the reflected signal will be dependent on the distance to the reflection, and on the laser frequency. Therefore as the laser is tuned the reflections within the system may give rise to a systematic variation of the beatwidth. The optical isolator can be positioned close to the laser and although some reflection may be present the systematic variation of the beat width will occur over a much larger frequency range. Figure 3.7 shows the

effect of optical feedback in a heterodyne system. In the upper trace, the optical coupling from the laser to the optical fibre was maximised, giving a launch efficiency of 25 - 30%. The laser was optically isolated (30 dB) and the optical feedback level is expected to be less than -40 dB. The observed signal shows ripples of roughly 5 dB which are believed to be caused by the variation of the laser linewidth which affects the insertion loss. If the lens launching the light into the fibre is defocussed, giving a 10 dB loss of signal and reducing the optical feedback by roughly 20 dB, then the ripples in the response are considerably reduced.

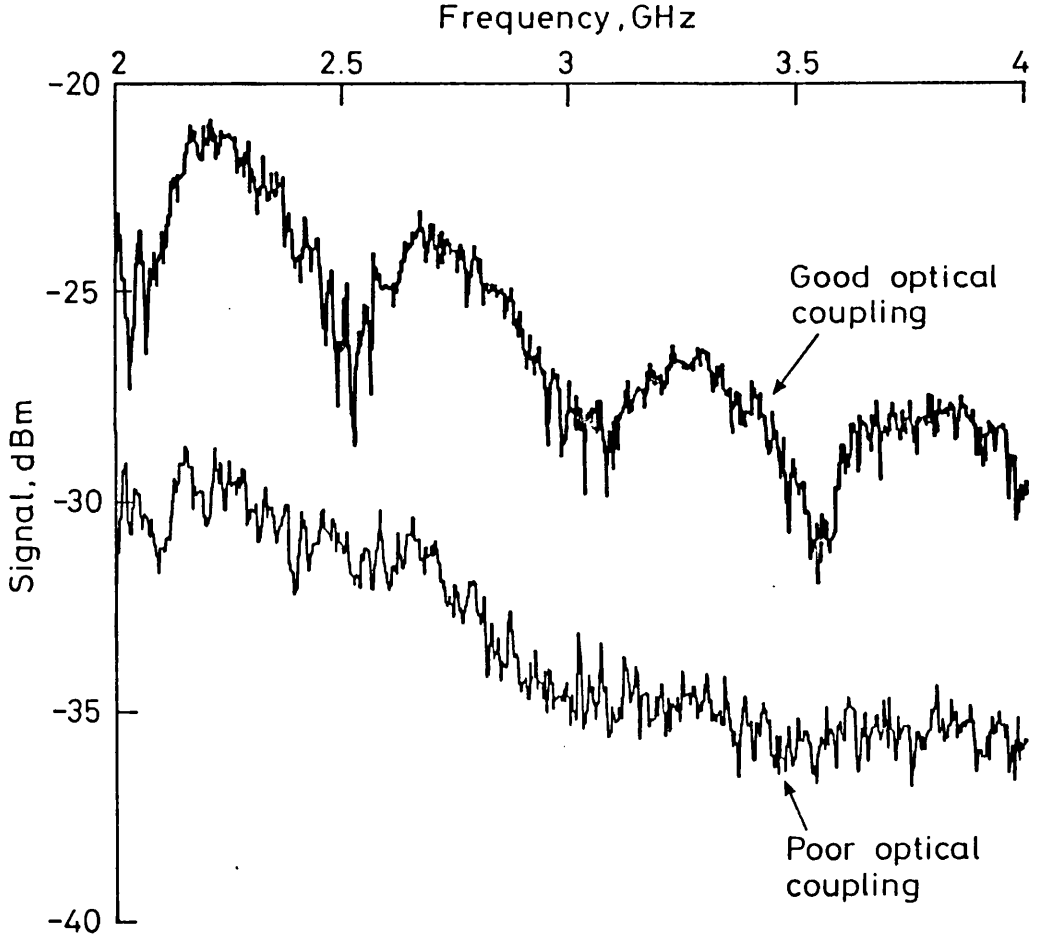

Figure 3.7. Effect of optical feedback on the beat signal

3.6. MEASUREMENTS USING AN EXTERNAL CAVITY DIODE LASER BEAT FREQUENCY SYSTEM

A beat frequency measurement system consisting of two external cavity laser diodes at 1.52 μm was used to measure the performance of a 45 device. The experimental arrangement is shown in figure 3.8.

Optical isolators were included in the system otherwise feedback from reflections would give rise to frequency instability in the lasers.

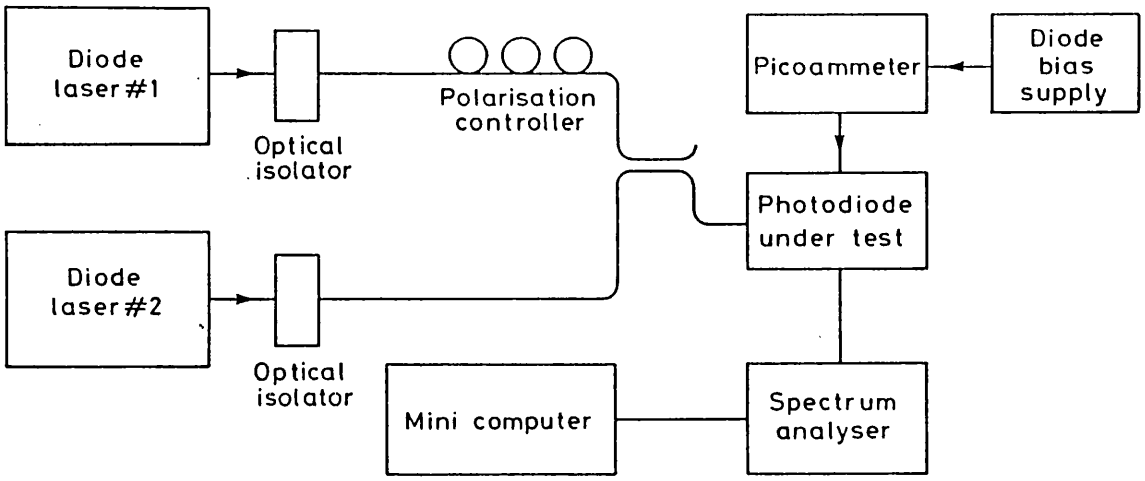

Figure 3.8. Experimental layout for beat frequency measurements with extended cavity lasers

The lasers are the external cavity devices developed at BTRL[32]. The length of the cavity is about 7.5 cm giving rise to a longitudinal mode spacing of roughly 2 GHz. The lasers are tuned by adjusting the grating angle and etalon spacing using piezoelectric positioners. The tuning range between mode jumps is one or two hundred megahertz. The laser linewidth is a few tens of kilohertz which is very much less than the resolution bandwidth of the spectrum analyser. The high mechanical stability requirements for the external cavity laser makes this system very sensitive to vibration and temperature change. For this reason the Spectrum analyser had to be operated with a span of 100 MHz to avoid losing the signal.

The optical powers of the lasers vary during tuning and therefore the photocurrent was monitored to allow the results to be corrected for the variation of the beat power. The mean photocurrent measured with the Plessey photodiode was roughly 33 μA at a beat frequency of 2.2GHz. The mean measured r.f. power was -52 dBm. which is in good agreement with the theoretically calculated figure.

The measured signals were corrected for noise, variation of the beat signal during tuning, and the response of the spectrum analyser. The

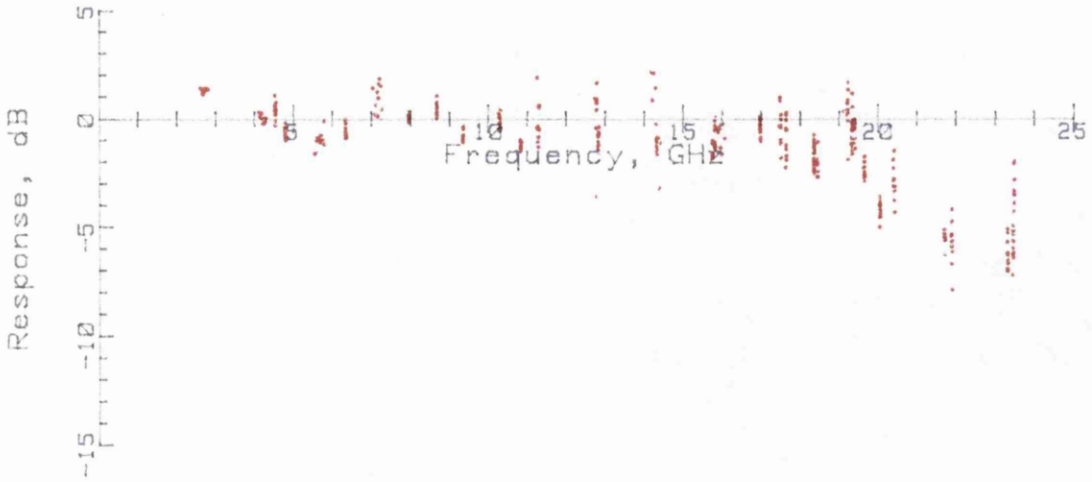

Figure 3.9. Response of AT&T diode measured with extended cavity laser heterodyne system

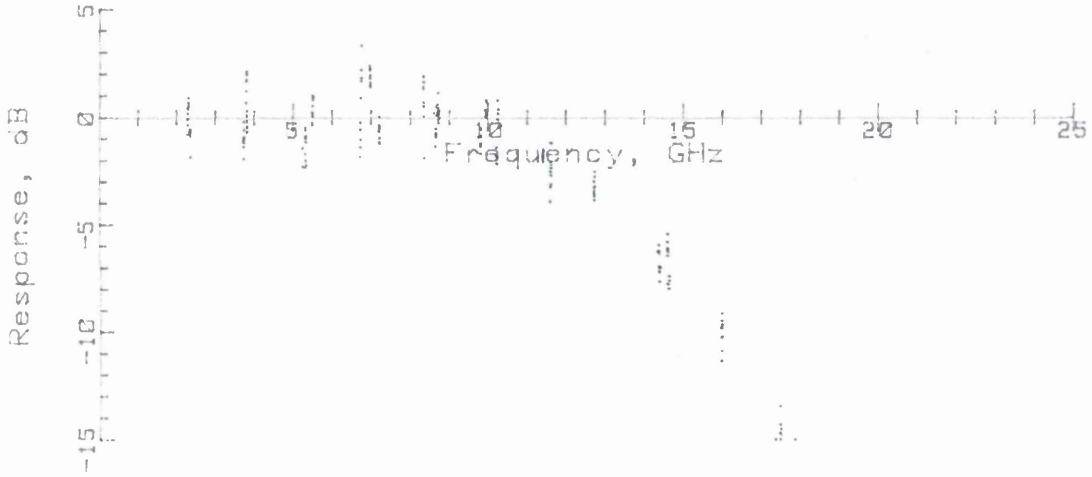

Figure 3.10. Response of Plessey #20 diode measured with extended cavity laser heterodyne system

Wiltron 6659B sweeper was used as the reference. The results obtained for the AT&T photodiode are shown in figure 3.9 and indicate that the response is flat to greater than 20 GHz. The response of the Plessey device is shown in figure 3.10. Both results show a considerable ammount of scatter and the overall dynamic range was approximately 20 dB.

3.7. MEASUREMENT OF THE AT&T AND PLESSEY #20 DIODES USING A DFB BEAT FREQUENCY SYSTEM

A swept frequency measurement was made of the AT&T diode response at

1532 nm using a DFB beat fequency laser system. The layout of the measurement system is shown in figure 3.11. Two optically isolated *Double Channel Planar Buried Heterostructure* (DCPBH) structure DFB lasers with 550 μm cavity length were used to produce the beat signal. The laser structure is shown in figure 3.2.

One of the two lasers contained a GRIN lens external cavity to reduce the linewidth. The laser linewidths were 24 MHz and 800 kHz respectively for the standard and external cavity devices. The isolator performance was better than 30 dB. The lasers gave photocurrents of 15.8 μA and 14.4 - 33 μA on the AT&T device.

A 50/50 optical fibre coupler was used to combine the signals as this gives good overlap of the optical fields from the two lasers. Early experiments, performed using a beam splitter cube in place of the fibre coupler, showed that the maximum photocurrent did not necessarily coincide with the optimum beat signal, suggesting that the wavefronts from the two lasers did not overlap well.

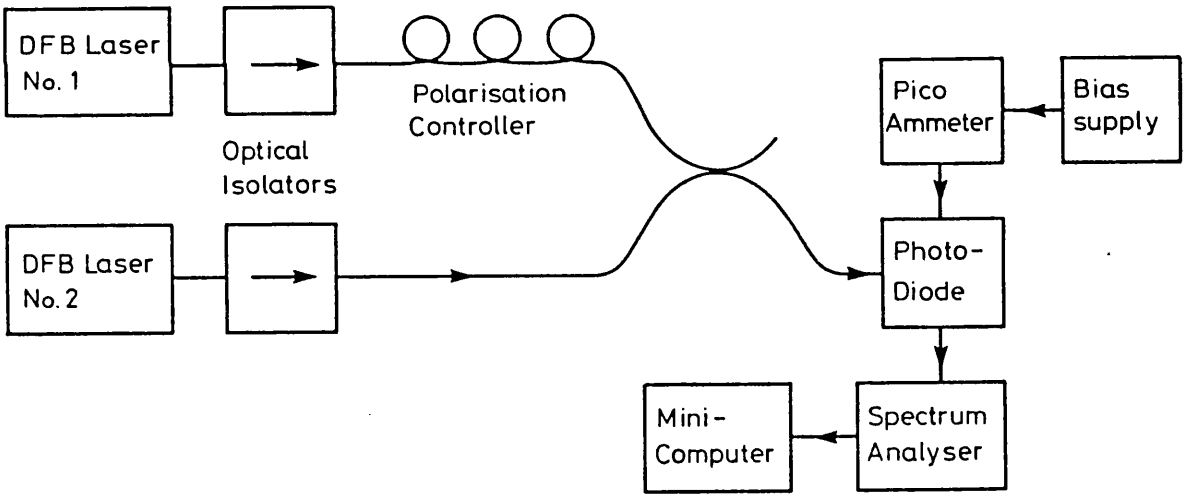

Figure 3.11. Layout of DFB beat frequency system

The external cavity laser was kept at a fixed frequency and the standard DFB was tuned by varying the current. This will give rise to a small systematic error as the laser linewidth is a function of the drive current. The photocurrent is approximately linear with laser drive and therefore the corrections for power variation were made using the measured values at 2 and 18 GHz. The signal was amplified using an

ERA 0.05 - 20 GHz amplifier and measured using an HP8566B spectrum analyser. The system was calibrated using a Wiltron 6659B sweeper as the source assuming that the internal levelling is flat with frequency. The measurement was made with the spectrum analyser set to peak hold and the lasers were tuned under computer control.

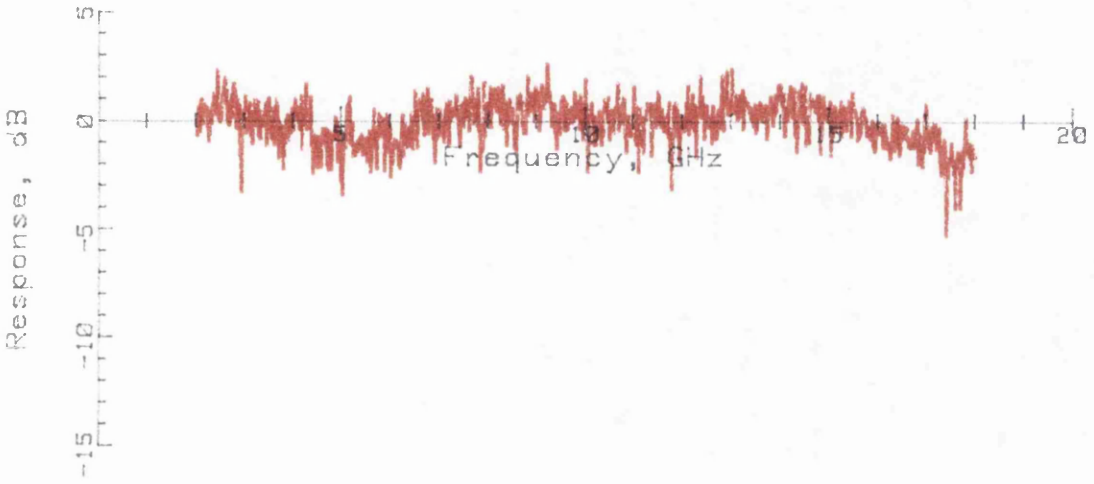

Figure 3.12. Response of AT&T diode measured using a DFB beat system

The results are shown in figures 3.12 and 3.13 for the AT&T and Plessey 45 μm diodes respectively. The AT&T results show a slow ripple with about a 6 GHz period and approximately 2 dB peak to peak amplitude. This is also present in the Plessey diode results. The origin of the effect is not known, but it is assumed to be either a systematic calibration error or a feedback effect.

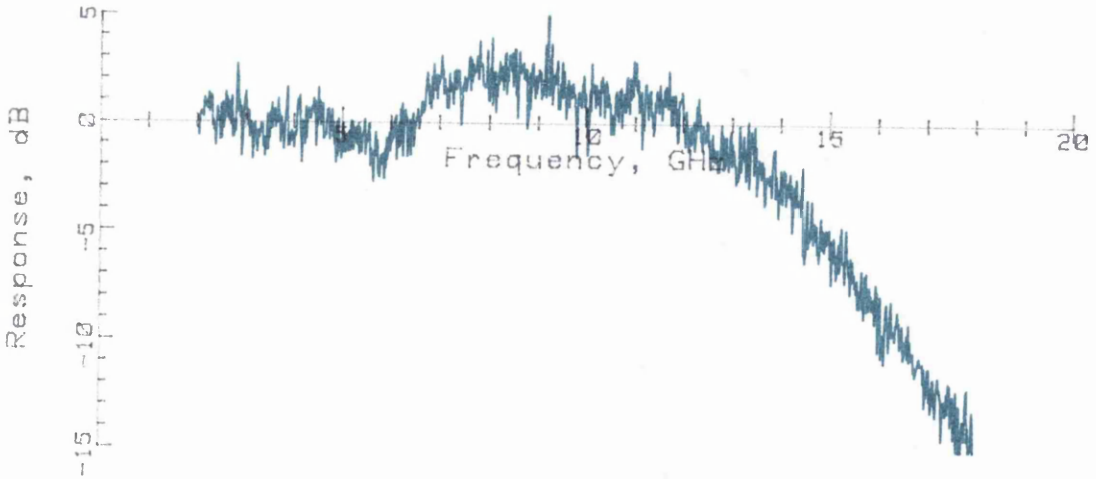

Figure 3.13. Response of Plessey #20 photodiode measured using a DFB beat system

The DFB beat frequency method has the advantage over the external

cavity laser in that the former technique is continuously tunable. However the wide beatwidth introduces sensitivity penalties due to insertion loss, if a spectrum analyser is used as the detection system.

3.8. ALTERNATIVE DETECTION STRATEGY FOR DFB HETERODYNE SYSTEMS

The insertion loss due to the laser beatwidth imposes severe limitations on the use of a spectrum analyser as a detection system. If the width of the beat signal were to vary as a function of frequency this would give rise to serious systematic errors in the measurement. An alternative detection strategy would be to use r.f. detector diodes directly to measure the signal. These devices have a reasonably flat response and can extend to greater than 50 GHz in coaxial geometries. The variations of the beat width would not alter the measured signal. The drawbacks are as follows: firstly at high signal levels the response will be sublinear, and secondly some decoupling must be provided to overcome problems caused by the dc photocurrent. The sensitivity of a typical device is 0.5 mV/μW at 1μW r.f. power. The minimum power that can be detected is of the order of -60 dBm, limited by the measurement of the small dc voltages involved (0.5 μV).

To obtain a beat power of -30 dBm, assuming equal laser powers, a mean photocurrent of 200 μA is required. For a 5V bias voltage and a sensitivity of 0.85 A/W this would give a total device power dissipation of 1.24 mW. This may present power dissipation problems for small area devices of 30 μm diameter or less. If the temperature of the active area were to increase significantly this might affect the drift velocities of the carriers and hence the speed of response.

The use of r.f. detector diodes allows the design of a scalar beat frequency system that is relatively insensitive to the linewidth of the lasers. However, the overall system dynamic range is restricted by the problem of measuring very small dc voltages and by the linearity of the r.f. detector at higher powers.

During the setting up procedure for a heterodyne system the polarisation of the two lasers is aligned to maximise the beat signal by the use of a controlling element such as a half wave plate or a fibre polarisation rotator. If the controlling element were caused to rotate continuously then the beat signal would vary sinusoidally at twice the rotation rate (equation 1). This is shown in figure 3.14.

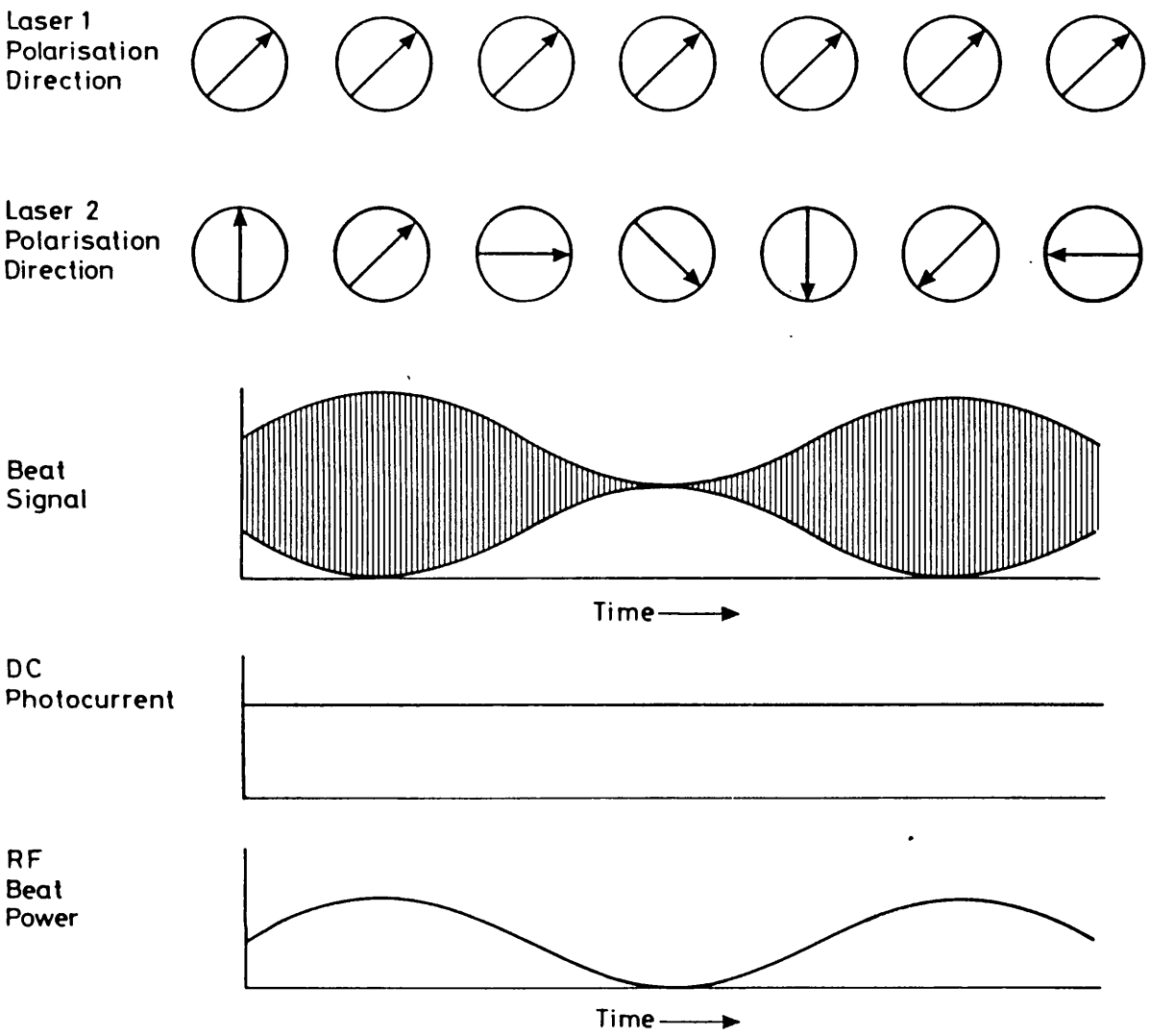

Figure 3.14. Modulation of the r.f. heterodyne signal by rotating the laser polarisation vector

The layout of the beat frequency system using a rotating half-wave plate to control the polarisation vector is shown in figure 3.15. A photograph of this system is shown in figure 3.16. The lasers used in this system were described in section 3.7.

The envelope of the r.f. beat signal measured by the detector diode will vary sinusoidally and the detected signal will be measured by the lock-in amplifier. The r.f. detector must contain a dc blocking capacitor otherwise the mean photocurrent would change the detector bias conditions and thus alter its sensitivity. Elements such as the beam splitter may have some sensitivity to polarisation giving rise to amplitude variations in the mean photocurrent. A Wiltron K250 bias tee with a 3 dB lower frequency limit of 10 MHz was used to give a very high degree of isolation (approximately 70 dB) between the r.f. beat

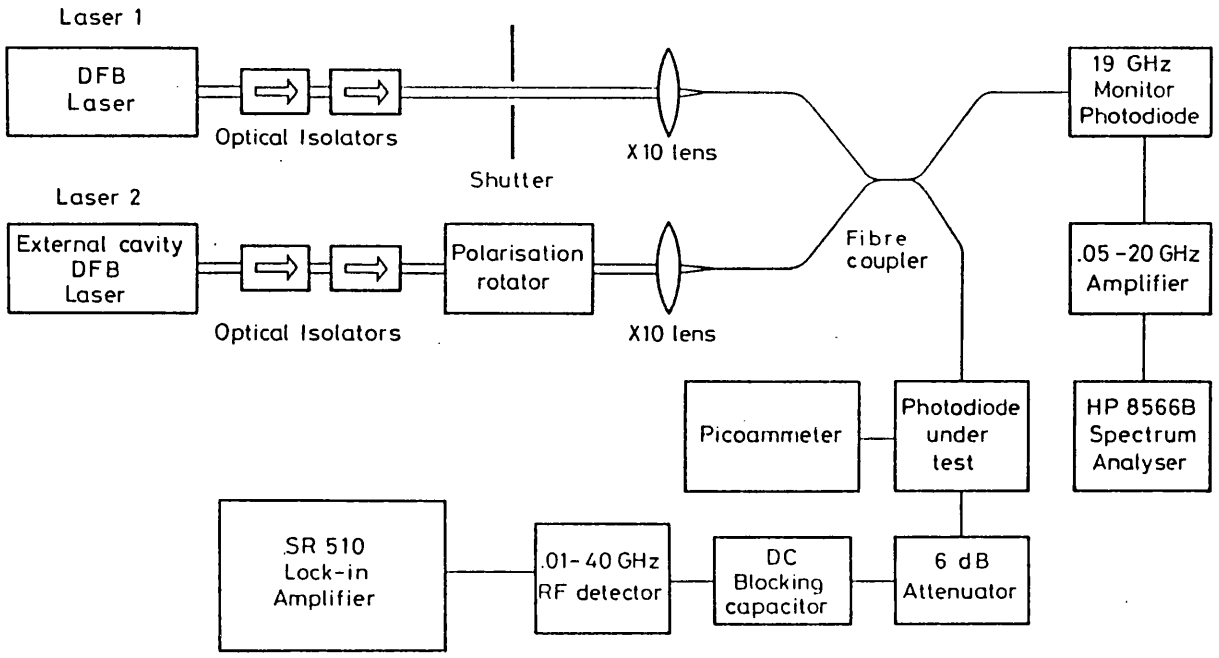

Figure 3.15. Heterodyne system using a half-wave plate to modulate the detected signal by rotating the laser polarisation vector

signal and the variations in the photocurrent. A fixed r.f. attenuator of 6 - 10 dB may be included between the photodiode and the bias tee or between the bias tee and the detector diode to improve the accuracy of the measurement system by reducing the errors caused by reflected r.f. signal power from the detector. The mean photocurrent was in the range of 20 - 30 μA, giving rise to signals of about 0.5 μV rms on the lock-in amplifier. Despite the low signal levels a dynamic range of approximately 20 dB could be achieved.

The beat frequency is controlled by varying the laser drive current. The beat frequency can only be monitored over the range 2 - 19 GHz because of limitations of the spectrum analyser. The tuning characteristics have been measured over the range 48 to 96 mA in a piecewise manner. The lasing frequency of the external cavity DFB is tuned between each set of measurements so that the beat signal will be returned to within the 2 - 19 GHz frequency range. The beat frequency is chosen such that there will be some overlap between successive measurement sets. The overall tuning response of the laser can then be obtained. The results are shown in figure 3.17. The curve is nearly linear for currents of up to 80 mA. The deviation from the linear relationship is less than ± 500 MHz as shown in figure 3.18.

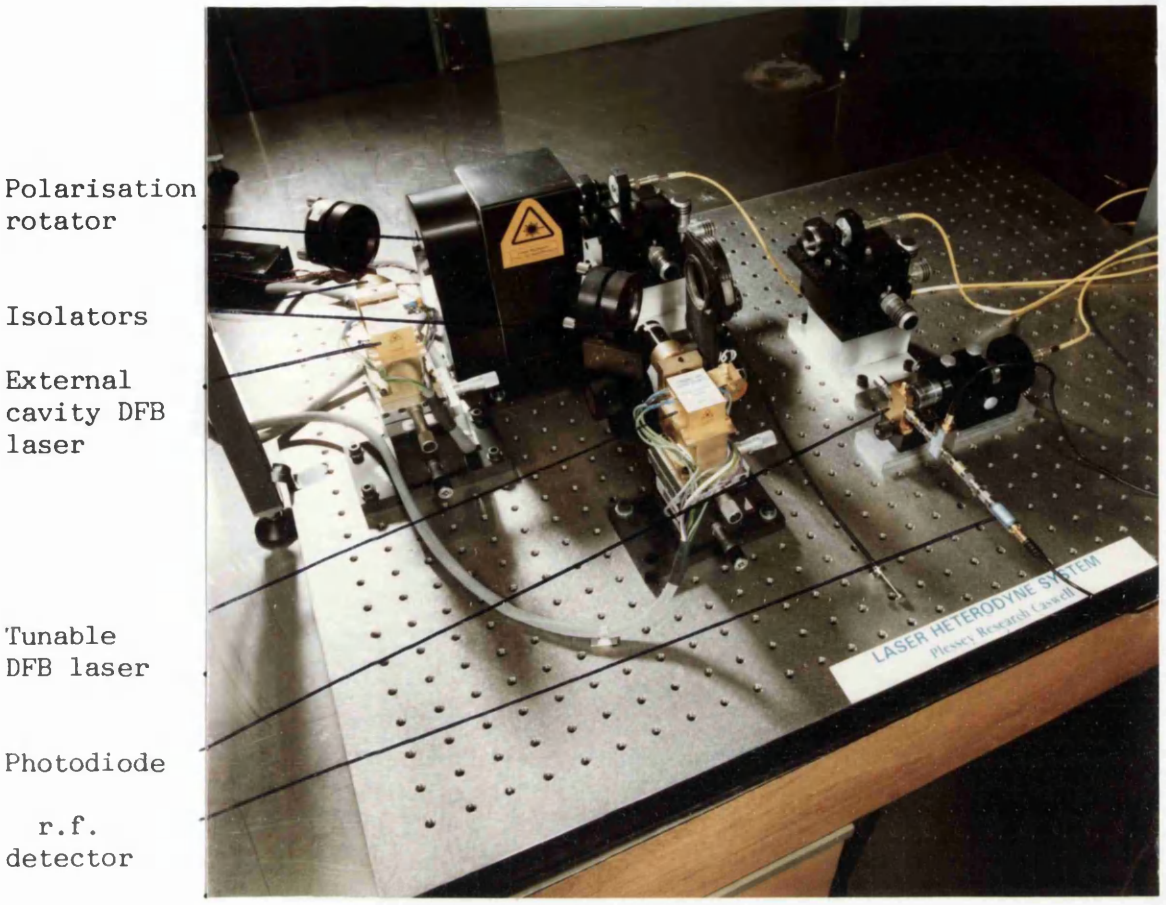

Figure 3.16. Photograph of the rotating polarisation heterodyne system

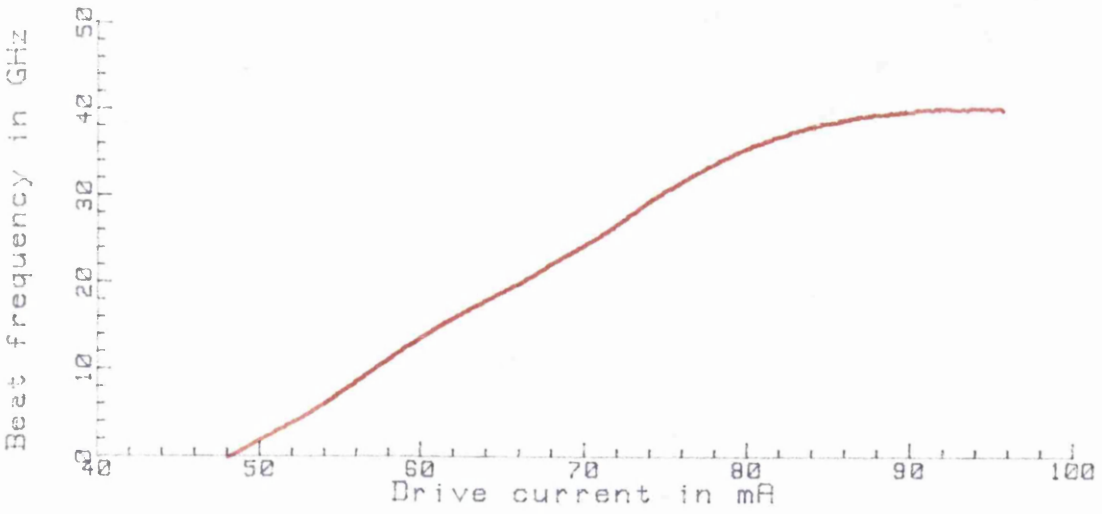

Figure 3.17. Tuning characteristics of the DFB laser.

The response of the AT&T diode was measured at up to 25 GHz using a linear approximation for the laser current/frequency characteristic. The results are plotted in figure 3.19 and show a 3 dB frequency of roughly 19 GHz. However at higher frequencies the response shows ripple

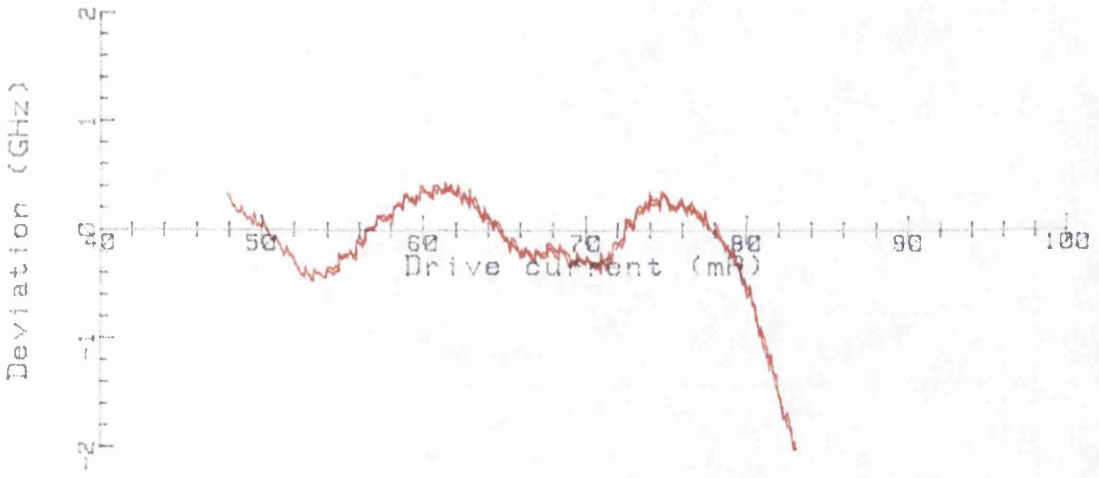

Figure 3.18. Deviation of beat frequency from linear fit

which may be attributed to electrical reflections. This effect will be discussed in chapter 6.

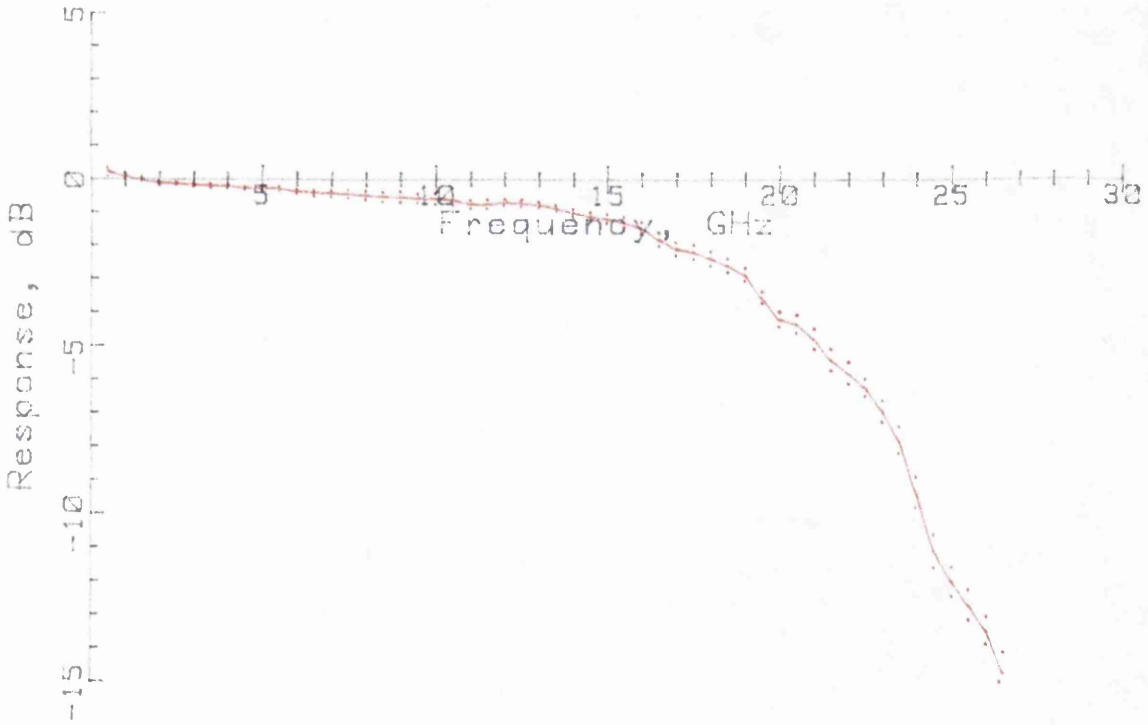

Figure 3.19. AT&T diode response measured by rotating polarisation heterodyne system

3.9. EXTERNAL FREQUENCY REFERENCE

The beat frequency is subject to drift over a period of a few hours and so although the beat frequency/drive current nonlinearity can be compensated in the short term by the use of software, some errors will still occur. Also the measurement system still requires the spectrum analyser to provide the frequency calibration.

If the lasers were locked to some form of reference then drift due to current and internal temperature variations of the laser would be compensated.

Figure 3.20 shows the layout of an all fibre interferometer network to control the beat frequency and the signals expected at each output. The path imbalance between the two Mach-Zehnder arms is 1 metre giving a free spectral range of roughly 200 MHz. It was hoped that the interferometer system would allow measurements to be made at multiples of the free spectral range frequency by locking the laser to a fringe. The spectrum analyser would only be required to provide an initial calibration of the Mach-Zehnder free spectral range.

Two major problems were encountered in preliminary experiments: the first is due to the temperature sensitivity of the interferometer (2 GHz/°C), and the second is due to birefringence of the optical fibre.

The thermal drift does not present too serious a problem because both the interferometers drift together in frequency. If the lasers were each locked to an interferometer fringe then the change in the difference frequency would be small. A serious problem could arise if the frequency drift were sufficient to cause the external cavity laser to mode-hop. If this were to occur the knowledge of the beat frequency would be lost. The interferometer is mounted in a thermally insulated enclosure to reduce these effects.

The drift of the beat signal has been measured over a three hour period, together with the output from the two interferometers. The results are shown in figure 3.21. The top trace shows the beat signal, measured by the spectrum analyser. The overall drift is approximately 500 MHz. The periodic cycling of the beat frequency was due to the air-conditioning which alters the room temperature by up to 4°C. The lower traces show the interferometer outputs for the DFB (middle) and

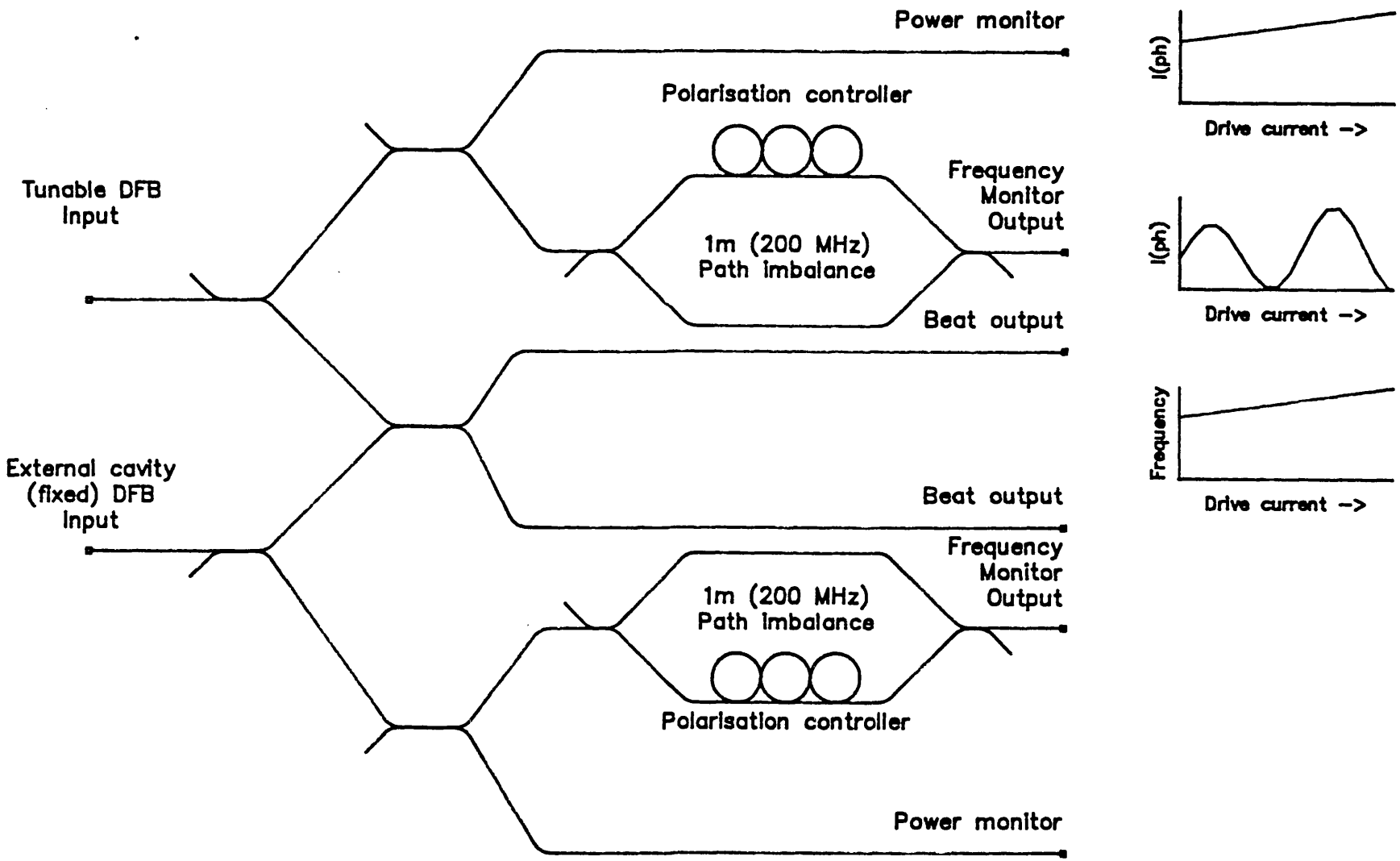

Figure 3.20. Fibre frequency discriminator and power monitor network

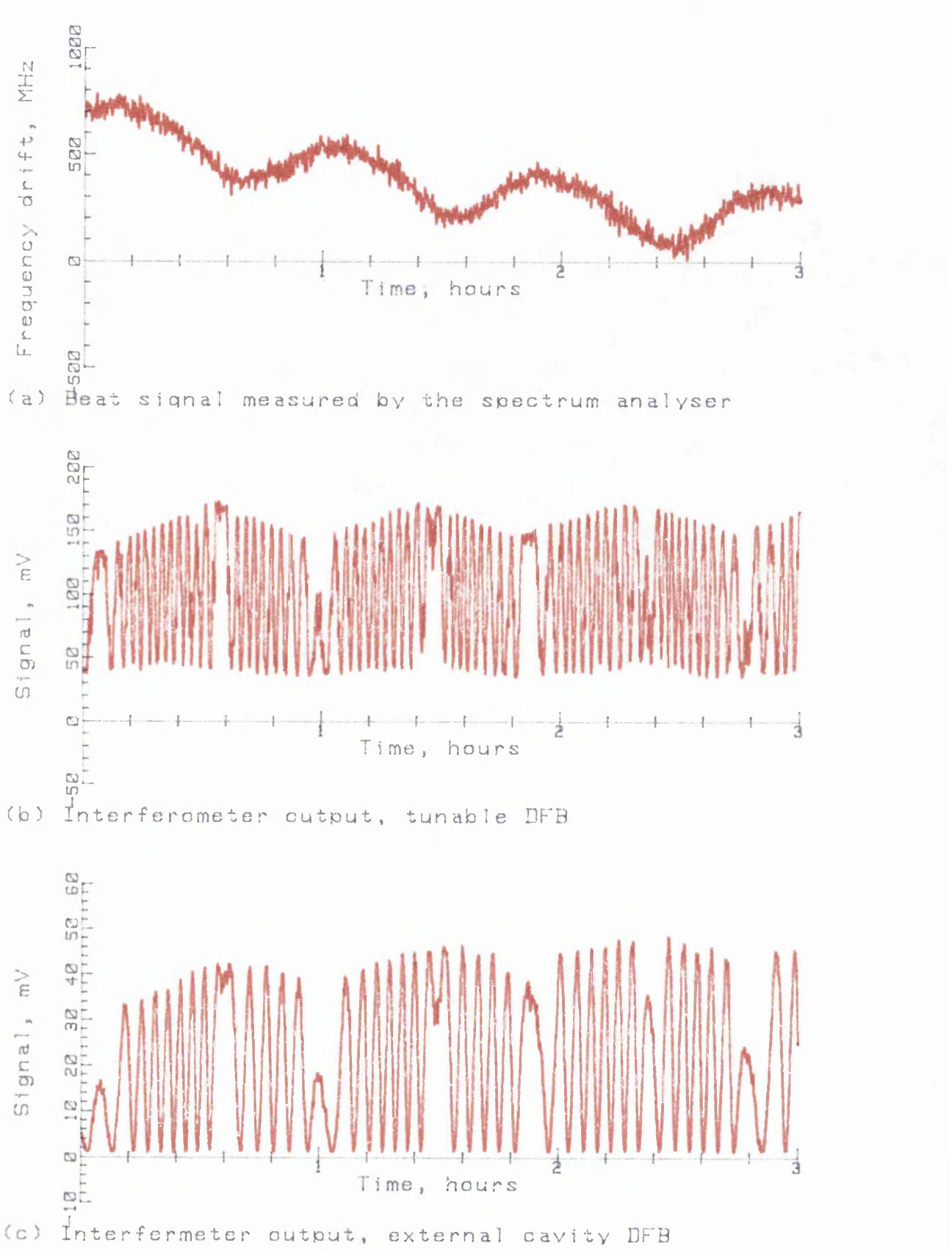

Figure 3.21. Variation of the beat signal and the output from the two interferometers over a three hour period

the external cavity DFB (bottom). Although the interferometer cycles through a number of fringes, the pattern for the two lasers is almost identical. The beat frequency drifts slowly over the period and cycles by approximately ±100 MHz with the change in the room temperature. The large number of cycles of the interferometer and the relative stability of the beat signal over the same period suggest that the interferometer cycles by ±0.5°C. During the same period the room cycles by ±2°C. Further work will be required to improve the thermal stability of the enclosure.

The fibre birefringence, believed to be caused by coiling the fibre in the thermal enclosure, presents a more serious problem. The interferometer will have two different free spectral ranges, depending on the polarisation vector of the light. The birefringence required to obtain a half wave shift in a 1 meter interferometer at 1.5 μm is small (5×10^{-7}). To overcome this problem the birefringence will have to be *exactly* compensated.

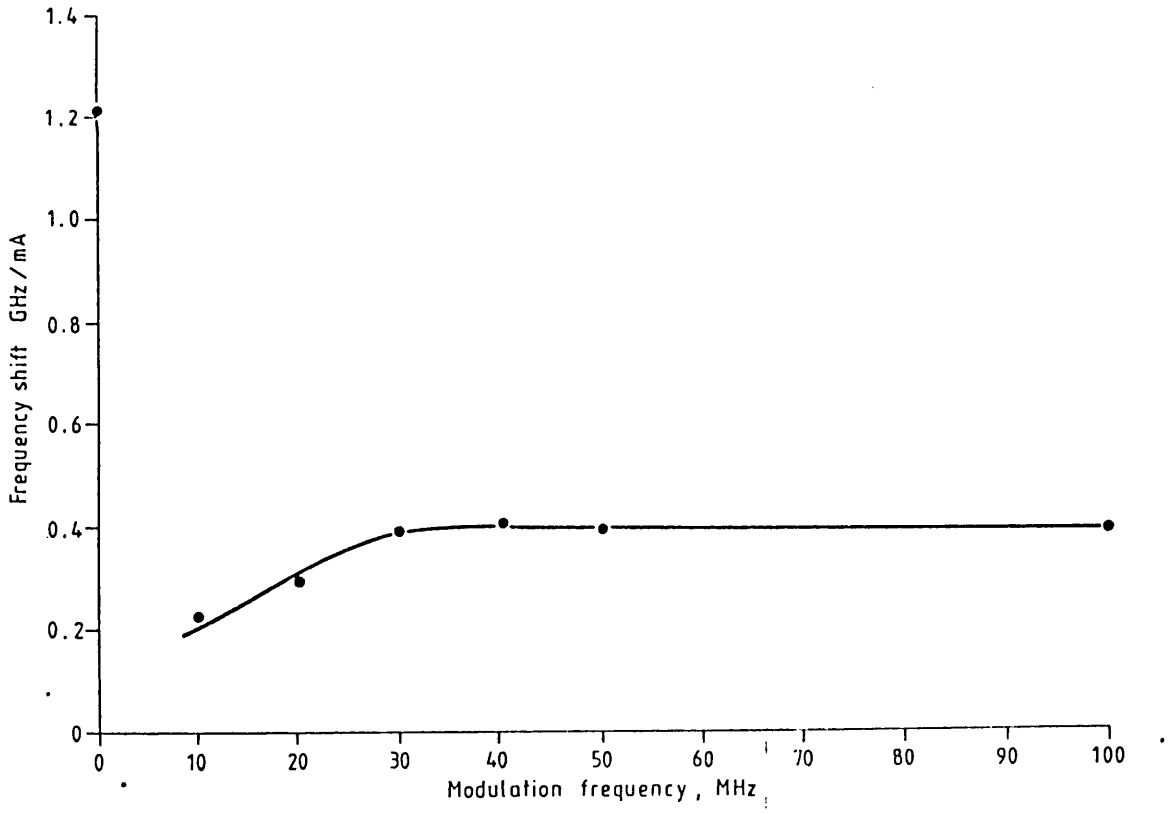

Figure 3.22. FM response of the tunable laser diode (Plessey Caswell)

3.10. HETERODYNE SYSTEMS USING A SINGLE LASER

Heterodyne systems with two lasers require close tolerence selection of devices. Temperature tuning can be used to match lasers with wavelengths differing by roughly 1 nm at 1.5 μm. Alternatively, a single laser can be used to provide a delayed self-heterodyne signal. A delayed self-heterodyne approach has been used to measure the FM performance of a laser diode[45].

The measured frequency modulation (FM) response of the 1532 nm DCPBH laser available at NPL is shown in figure 3.22. The thermal tuning and current tuning effects have the opposite sense. The frequency crossover point between the two effects occurs at roughly 200 kHz (*1). At high frequencies the FM response is roughly 400 MHz/mA. Below 30 MHz the FM response drops off because a high pass filter was included in the biasing arrangements.

Square wave modulation

If the laser were modulated with a square wave then the lasing frequency would be switched between two values. By dividing the optical signal in two and using an appropriate delay the signals could be recombined to give a single beat frequency as shown in figure 3.23. This method has been used by *R S Tucker* to make a beat frequency system with a DBR laser (*2).

The DFB laser available at NPL should be able to give a maximum beat frequency range of roughly 20 GHz, based on the FM modulation index and the current difference between threshold and the onset of tuning nonlinearity. The measurement layout was identical to figure 3.11. The laser was driven by a square wave with <160 ps rise and fall times. The beat frequency responses for no modulation, 4 GHz and 10 GHz frequency shift are shown in figures 3.24 a, b and c respectively. The figures show clear peaks suggesting that an acceptable beat frequency could be generated. At higher difference frequencies the imbalance between the powers would have to be compensated, otherwise a systematic error would be introduced in the result. The drive signals measured with a sampling

---

(*1) *Private communication:* C A Park, Plessey Research (Caswell)

(*2) *Private communication*: R S Tucker, AT&T Laboratories, Crawfords Corner, NJ, USA

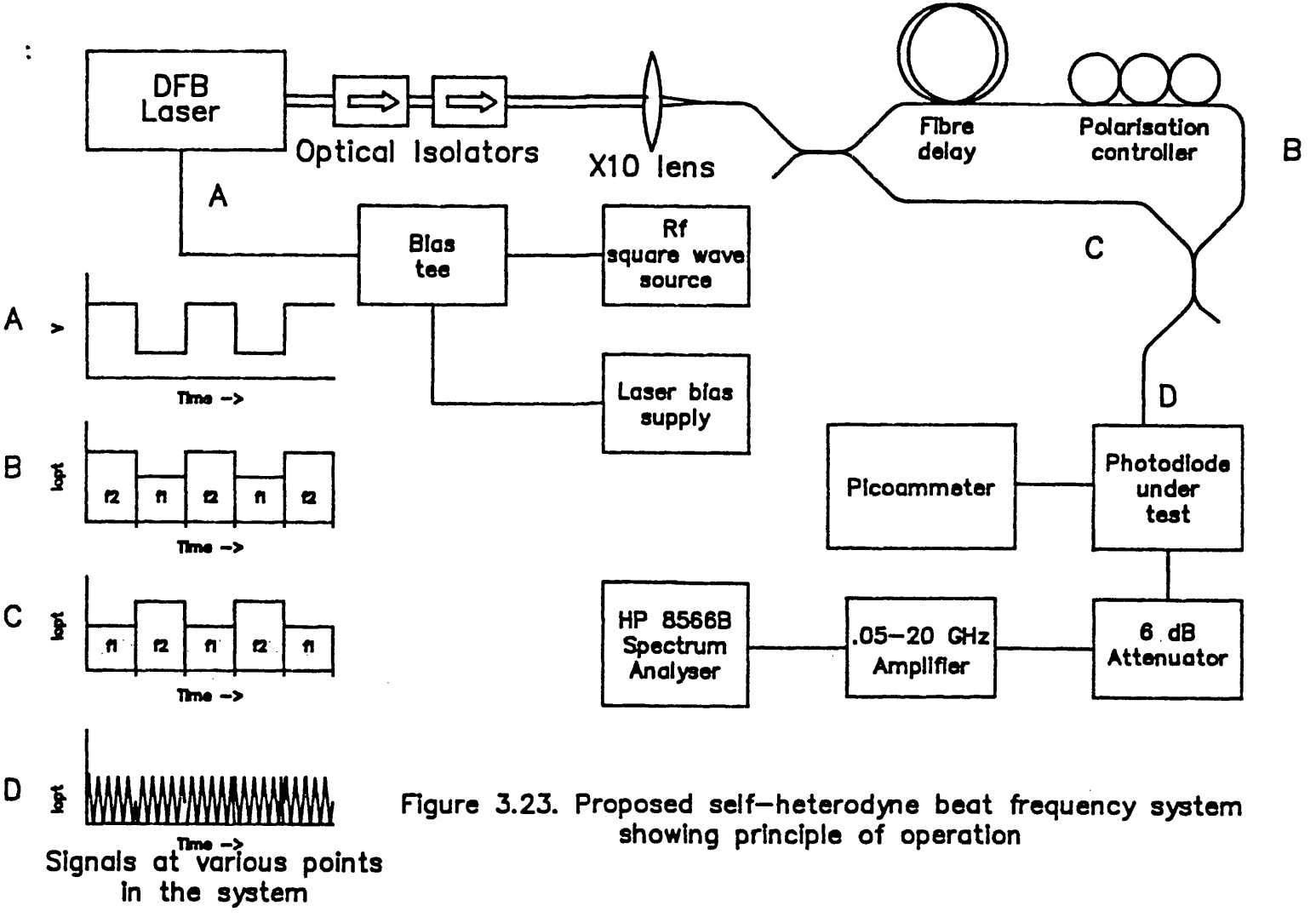

Figure 3.23. Proposed self–heterodyne beat frequency system showing principle of operation

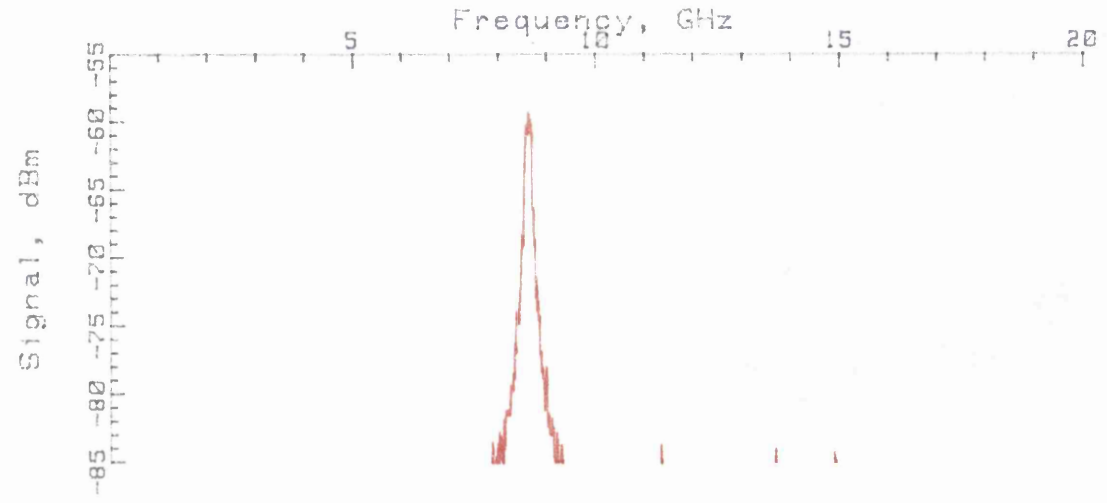

(a) No modulation

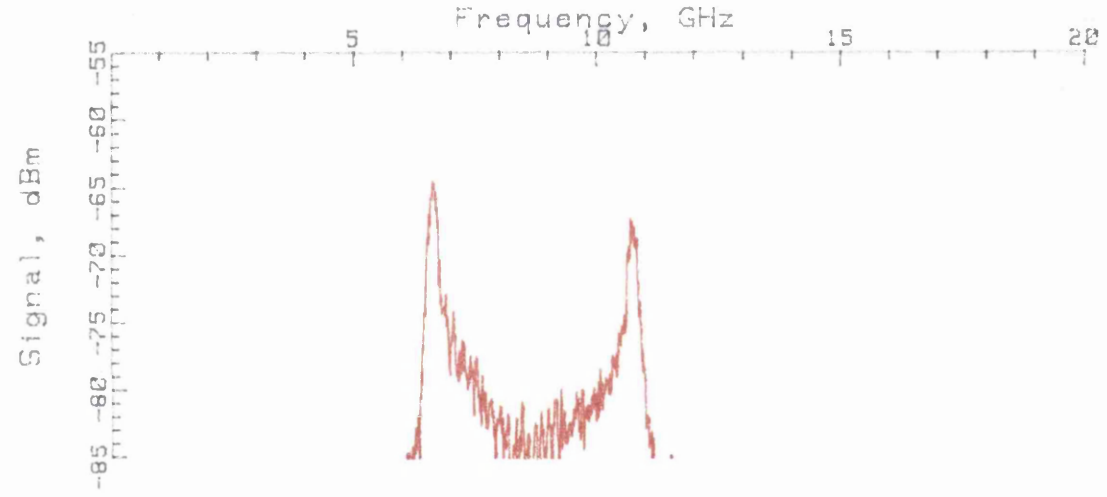

(b) 4 GHz difference

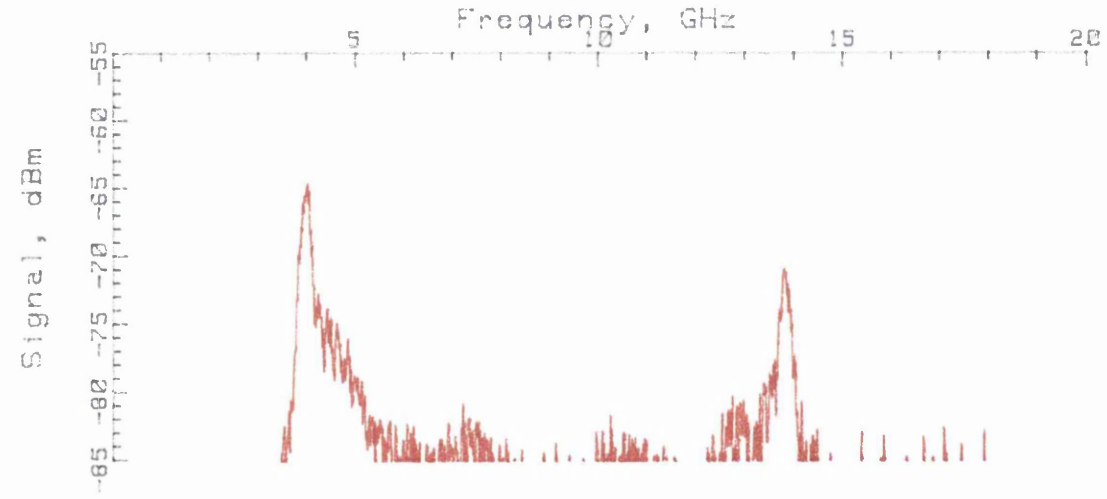

(c) 10 GHz difference

Figure 3.24. Frequency shift induced by square wave modulation of the laser drive

oscilloscope are shown in figures 3.25 a and b.

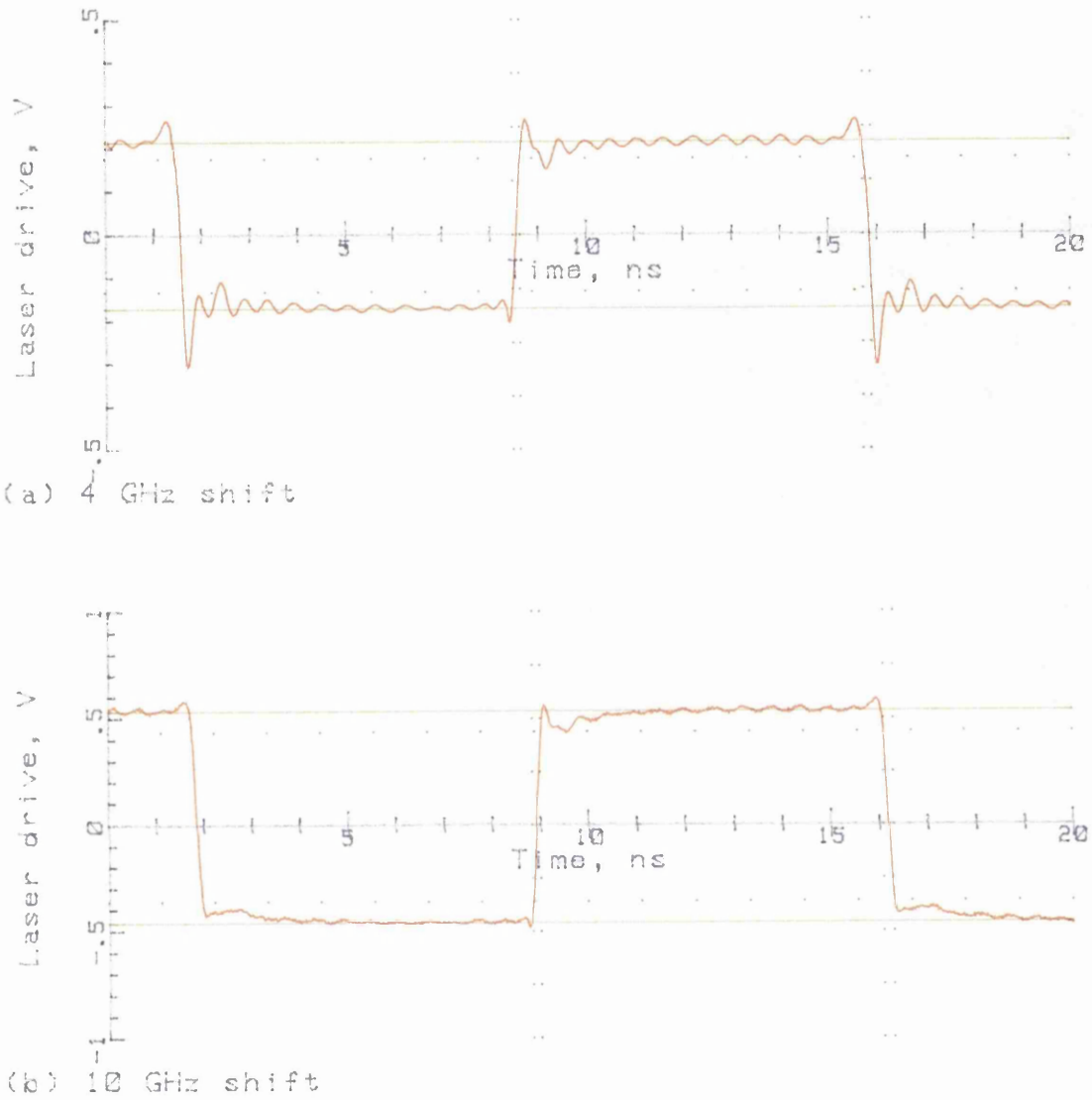

Figure 3.25. Laser drive signals for 4 GHz and 10 GHz frequency shift

Sinusoidal modulation

An alternative approach is to modulate the laser with a sinusoidal signal and pass the light through an interferometer[46,47], as shown in figure 3.26.

The modulation of the drive signal gives rise to both amplitude and frequency modulation of the optical amplitude. If the light is passed through an interferometer with a path length corresponding to half a cycle of the modulation frequency, then the amplitude modulation effects are greatly reduced.

Eichen and *Silletti* used an interferometer based on corner cubes and

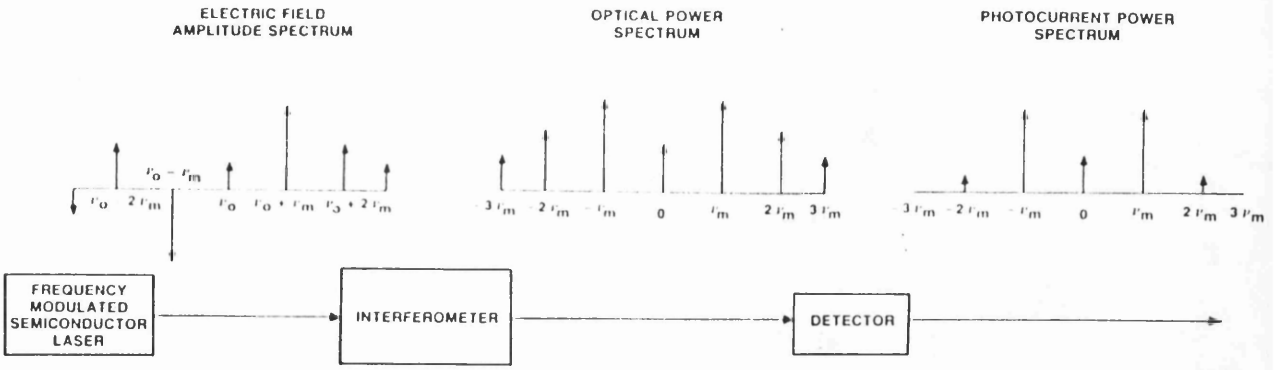

Figure 3.26. Conceptual picture of the FM sideband technique. The sidebands in the optical spectrum of a frequency modulated semiconductor laser are converted to a baseband AM intensity spectrum by an interferometer. The sidebands are spaced at a frequency ν_m. (after *Eichen and Sillettí*).

suggested that a compact all fibre device could be easily made. An all fibre device could be easily tuned by adjusting the laser or fibre temperature to give bright or grey fringes, thus selecting the even or odd sidebands.

The measurement method can be used as an absolute technique because the power in each of the sidebands is related. However, this assumes that the amplitude modulation is small. If the modulation signal is large the amplitude modulation terms cannot be neglected. Each of the sidebands will contain components due to a mixture of AM and FM terms. The method is better suited to use as a relative method, using a detector of known performance to measure the power in the sidebands. Results obtained using this method are presented in chapter 7. This method will not be considered further here.

3.11. VECTOR BEAT FREQUENCY MEASUREMENT SYSTEMS

The beat frequency techniques considered so far have all been scalar measurements, returning the magnitude of the detector response with no phase information. To obtain both phase and magnitude information the delay within the device must also be measured. Commercial electrical vector network analysers require a stable r.f. signal source with low phase noise, locked to a phase reference. A DFB beat frequency system is continuously tunable and could therefore provide a suitable source

for an opto-electronic vector network analyser system. The width of the beat signal would be of the order of tens of megahertz even using an external cavity source for one of the lasers. This may make it impossible to achieve phase locking using the system. Electrical feedback has been used to give a linewidth reduction of over an order of magnitude and it may be possible to produce a phase locked beat signal by this means[48,49].

An alternative approach is to use a technique that does not require high phase stability. A DFB with a linewidth of a few tens of megahertz will have a coherence length of several metres. Therefore the electrical signals from the unknown device and the internal reference can be compared interferometrically, provided that the differential delay is less than the coherence time. Two approaches have been considered here: a homodyne and a heterodyne technique. In both methods a fast photodiode has been used to provide the internal reference signal. In an electrical vector network analyser system both the signal source and the detector are electrical. The through calibration can be effected by connecting the input and output ports together and measuring the magnitude and phase of the transmitted power. The results can then be used as a reference for future measurements. In an opto-electronic system the source is optical and the detector is electrical. the system calibration must therefore be carried out using a transfer standard photodiode with a well characterised response. The magnitude of the photodiode response can be measured absolutely using one of the techniques described in this section, however the phase response of the photodiode may not be known. If the device has been modelled an estimate of the phase response can be made. This can then be used as a correction to the reference device response.

Homodyne vector measurement system

The fibre coupler used to combine the signals from the two lasers has two output ports. One of these is used to drive the unknown device and the other is used to drive a second photodiode which is used as an internal phase reference. A variable attenuator and an adjustable delay are introduced into the reference channel so that the magnitude and the phase of the reference signal can be controlled. The layout of the system is shown in figure 3.27.
The magnitudes of the signals in the two channels is balanced, and a measurement of the combined signal is made for different path delays.

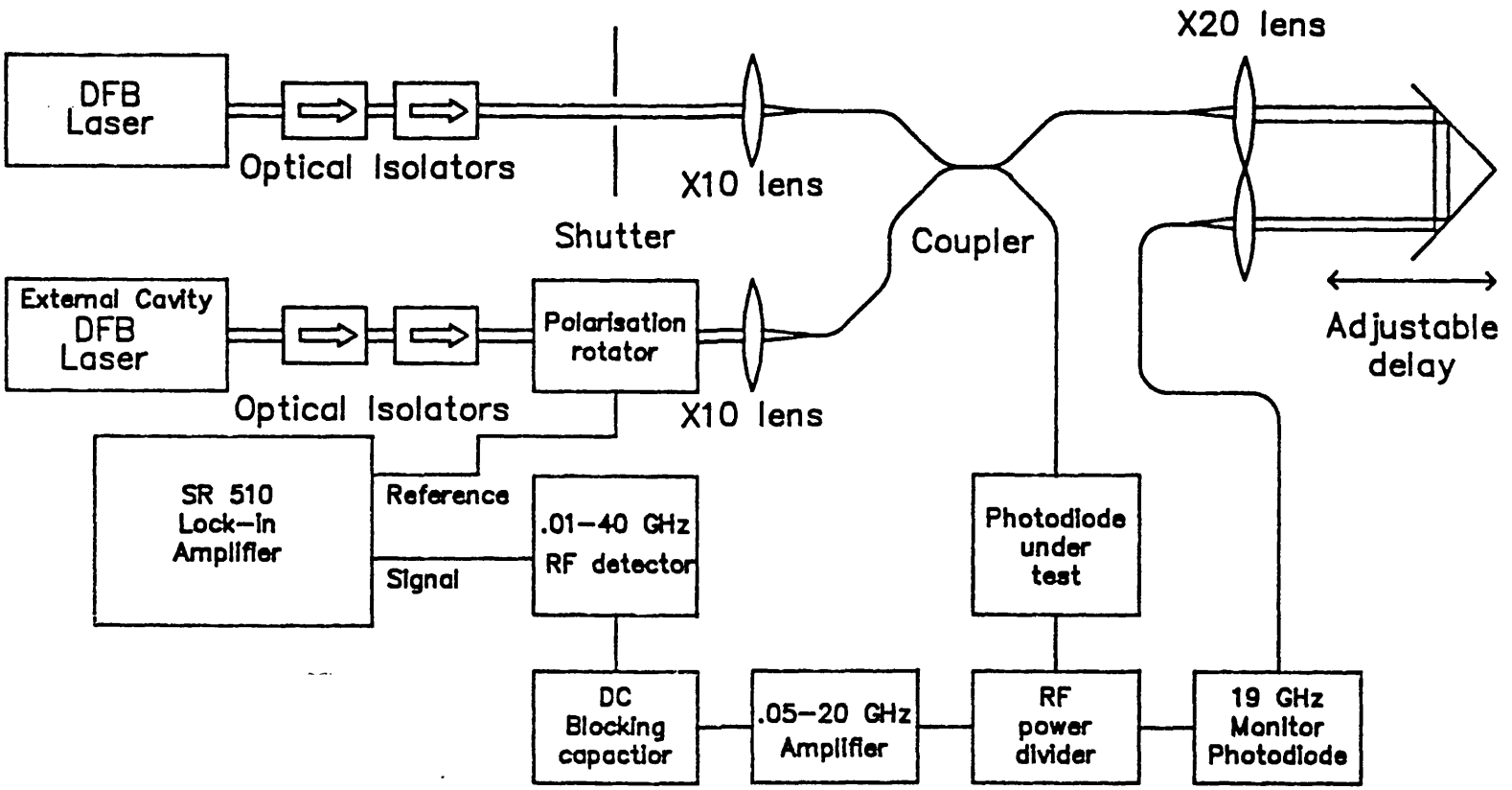

Figure 3.27. Layout of homodyne vector beat frequency system

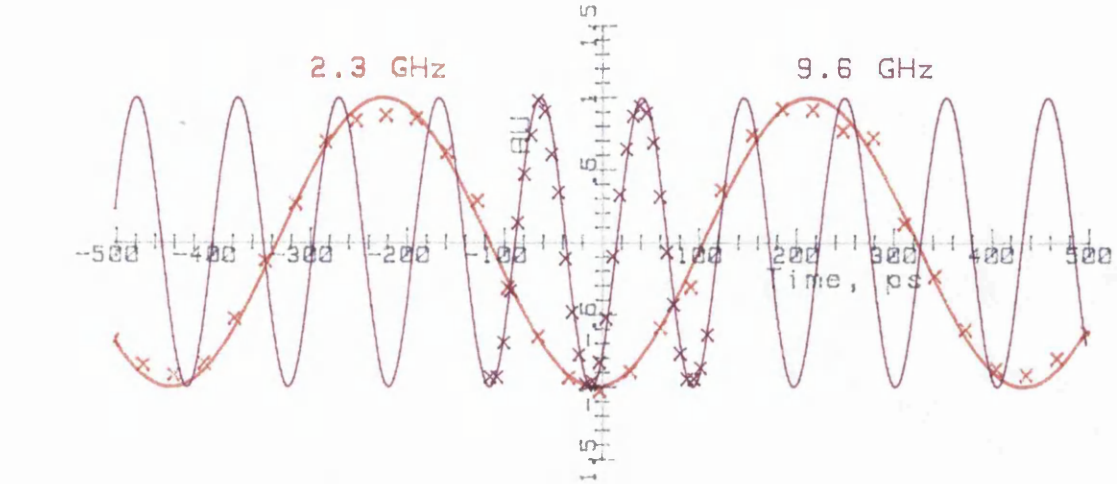

(a) AT&T diode positioned at -20 ps

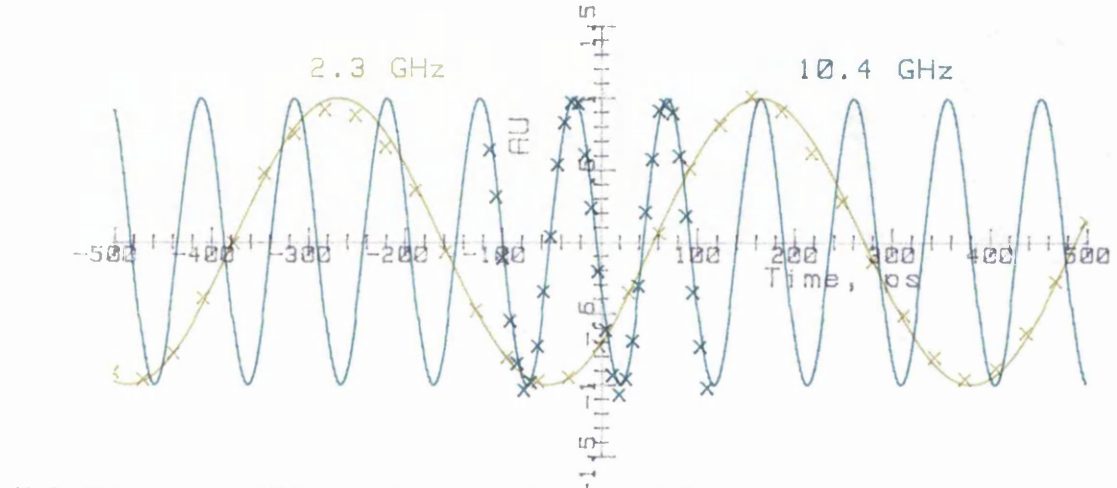

(b) Plessey #20 positioned at +160 ps

Figure 3.28. Normalised interference patterns to determine the phase response of the Plessey #20 photodiode and the AT&T reference

The measured beat power varies sinusoidally with delay and so the frequency and phase can then be calculated by curve fitting. A number of measurements must be made at each and so it is essential that the beat frequency does not drift during the measurement.

The lasers are believed to be sufficiently stable over the period of a measurement and so no offset frequency locking of the beat signal was performed. The beat frequency was determined from the spacing of the fringe pattern. The accuracy of this method will be limited by the calibration of the optical translation stage.

A measurement was made of the Plessey #20 photodiode, using the AT&T photodiode as a reference and using a Plessey research device as the

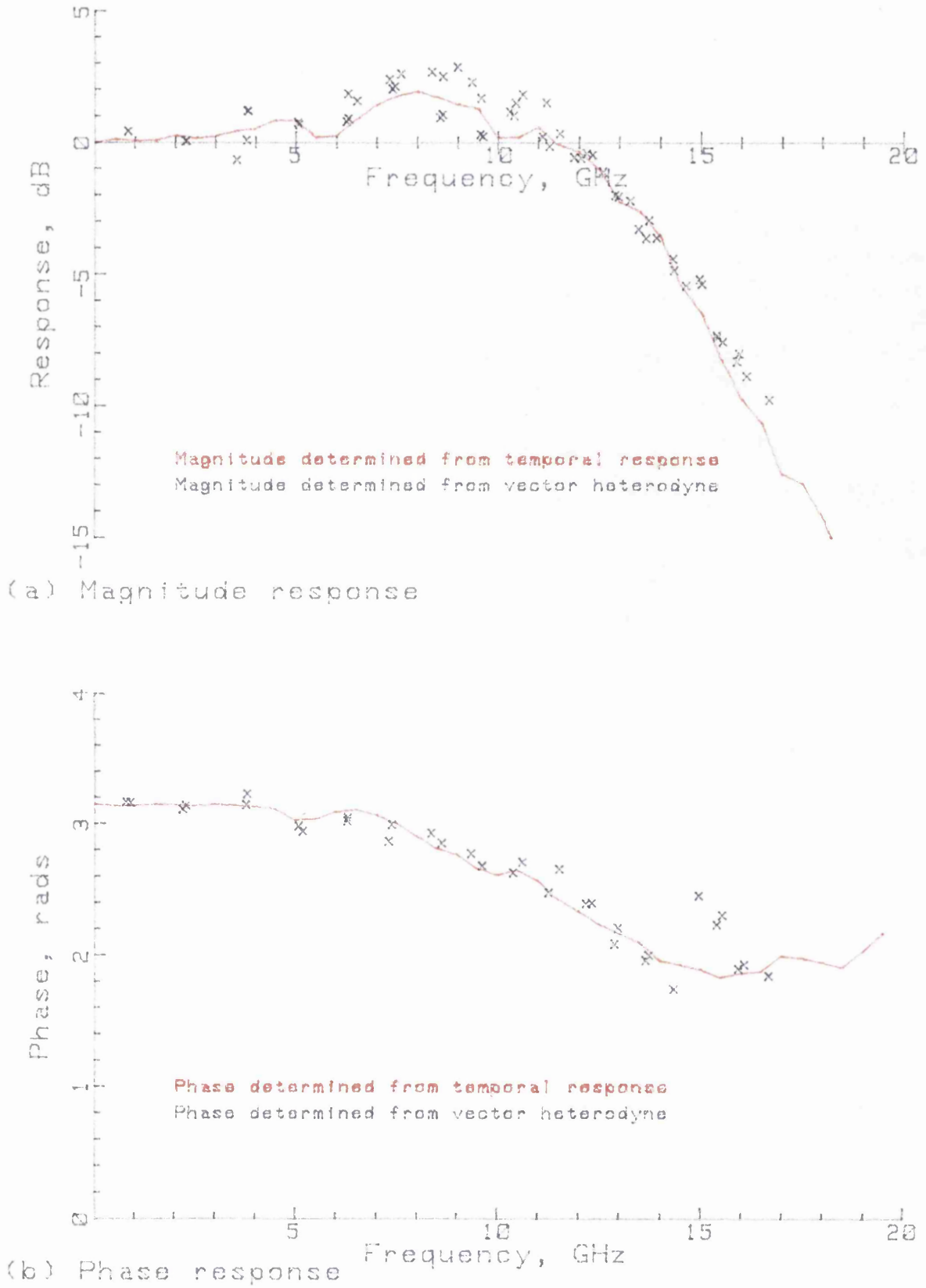

Figure 3.29. Magnitude and phase response of the Plessey #20 photodiode, determined by the *Vector Homodyne* method and by *Fourier transform deconvolution* of temporal measurements

internal reference. Two sets of measurements were made for each device. The normalised interferometric patterns obtained using the Plessey and AT&T diodes are shown in figures 3.28a and b. $T\omega_B$ frequencies are shown for each device, together with the measured data points.

The magnitude and phase responses of the Plessey diode have been determined and are shown in figure 3.29. Results obtained by a *Fourier transform deconvolution* technique from measurements made in the time domain have also been presented. The deconvolution method is described in part 2 of this thesis. The results show reasonable agreement except at high frequencies where the signal is low.

The method has been demonstrated and works successfully. In principle measurements could be made at higher frequencies provided that a suitable transfer standard photodiode were available. However, at present the system is slow to operate because of the number of points required.

Heterodyne vector beat frequency system

An acoustooptic deflector or *Bragg cell* has the useful property that the diffracted beam is frequency shifted by the modulation frequency. If the light from one of the lasers in the beat frequency system is passed through the Bragg cell then two beat signals can be produced at ω_B and $\omega_B + \omega_{mod}$. These two signals will be phase locked provided that the delay between the signal and reference paths is less than the coherence length of the laser.

The total r.f. power will fluctuate at the modulation frequency ω_{mod} as shown in equations 5 and 6. A phase delay at the beat frequency ω_B between the signal and reference channels gives rise to an equivalent phase difference between the Bragg cell modulation signal and the detected beat signal.

$$P_B(t) = \frac{(V_1 \cos((\omega_B + \omega_{mod})t) + V_2 \cos(\omega_B t + \phi))^2}{R} \qquad \text{(eq. 5)}$$

If only the low frequency terms are considered then the beat signal becomes:

$$P_B(t) = \frac{(V_1)^2 + (V_2)^2 + 2V_1V_2 \cos(\omega_{mod} t - \phi)}{2R} \qquad \text{(eq. 6)}$$

where P_B is the power in the beat signal; ω_B and ω_{mod} are the beat and modulation signals; ϕ is the phase delay between the two signals and R is the load impedance.

Figure 3.30 shows a block diagram of a proposed vector network analyser system. The phase response is measured directly using a vector voltmeter. The variable optical attenuator has been included so that the magnitude of the beat signal can be kept approximately constant. This is because in other work we have found amplitude dependent phase effects (*1).

The choice of modulation frequency will be restricted by the availability of suitable Bragg cells and the detection electronics. A higher modulation frequency will increase the accuracy of the phase measurement for a given system resolution and a lower modulation frequency will simplify the detection circuitry. Commercial Bragg cells are available at 70 MHz and 110 MHz as standard products. Higher frequency devices operating at up to several GHz are also available though those tend to be more expensive. Operation at 70 MHz is ideal because of the availability of suitable devices and for the simplicity of the electronics.

Dynamic range of vector systems

The scalar measurement system discussed earlier relied on the flatness of the frequency response of a detector diode to give accurate results. Both the vector measurement systems proposed use a photodiode as an internal reference and are calibrated by measuring the response of a photodiode transfer standard with known characteristics. The flatness of the response is therefore less important, allowing the use of broadband amplifiers to boost the response. Distributed amplifiers with millimetre wave performance are available commercially.

(*1) *Private communications*: B Walker and R L Palmer, NPL

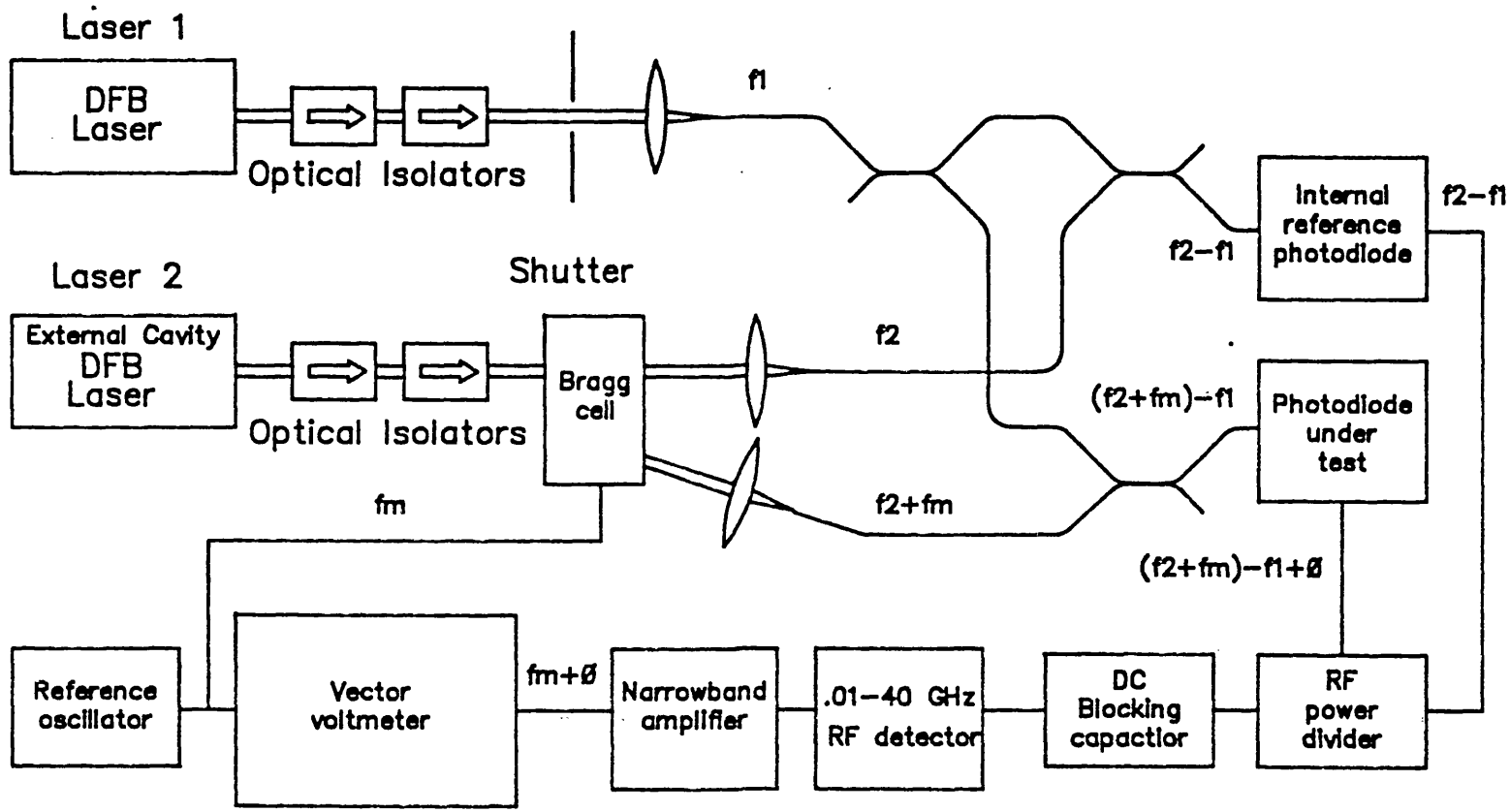

Figure 3.30. Proposed heterodyne vector beat frequency system

At higher frequencies the sensitivity of both the transfer standard diode and the internal reference photodiode will be reduced. This will reduce the overall dynamic range of the system.

3.12. DISCUSSION AND CHAPTER CONCLUSIONS

In this chapter the heterodyne concept and its application to fast photodiode measurement has been discussed. The merits and disadvantages of conventional heterodyne systems based on external-cavity and DFB lasers with spectrum analyser detection have been discussed. The external cavity lasers can only be operated at selected frequencies. In the example chosen these were spaced by 2 GHz. The system based on DFB lasers was continuously tunable but suffered from optical feedback and a wide beatwidth. These effects, when combined, could give rise to serious systematic measurement errors.

A novel DFB based heterodyne system has been developed. This new system overcomes many of the problems associated with the conventional approach. A r.f. detector diode is used to measure the heterodyne power. The polarisation direction of one of the lasers is continuously rotated using a half-wave plate, causing the r.f. heterodyne signal to be amplitude modulated at twice the rotation rate. The detected signal can be measured using a lock-in amplifier. This system currently can be operated to beat frequencies in excess of 40 GHz (3.5 mm) or 50 GHz (2.4 mm) and the system has a dynamic range of more than 20 dB.

Heterodyne systems normally give the scalar frequency response of the device being tested. The potential for using this type of system to measure both the frequency and the phase of a device has been explored. Two measurement systems were proposed: the first - a homodyne approach - used a variable delay to determine the phase response of the device being tested; the second system used a Bragg cell to offset the frequency of one of the lasers. Two beat signals would be produced, one of which would be offset by the modulation frequency of the Bragg cell. When the two r.f signals from the two photodiodes are combined onto an r.f. detector, the modulation frequency would be recovered. This would contain both the magnitude and phase performances of the unknown device.

Measurements have been made of the Plessey #20 photodiode using the homodyne vector beat frequency system and the principle of operation

has been successfully proven. At present the frequency response of this system is currently limited to about 20 GHz by a lack of suitable high bandwidth photodiodes.

Further work will be required to provide improved diagnostic systems to control the beat frequency of the Rotating Polarisation Heterodyne system. Also the heterodyne vector measurement system has not yet been proven.

4. INTEGRATED OPTIC MODULATORS

4.1. INTRODUCTION

In recent years optical modulators based on electro-optic and electro-absorptive principles have been extensively studied. The main areas of application for these devices have been the fields of optical communication, phased array radar and more recently short range communications between integrated circuits. In this chapter techniques using integrated optic modulators to measure photodiode responses have been considered. Only modulators based on the lithium niobate integrated optic technology have been used. These are the 'first generation' of devices and are currently being studied for their potential in high bit-rate and coherent optical communication systems. The design of the modulators is not important to the thesis and will not be covered here. The papers 2 and 6 referenced in appendix 2 describe the work carried in collaboration with University College London to develop wideband integrated optic modulators.

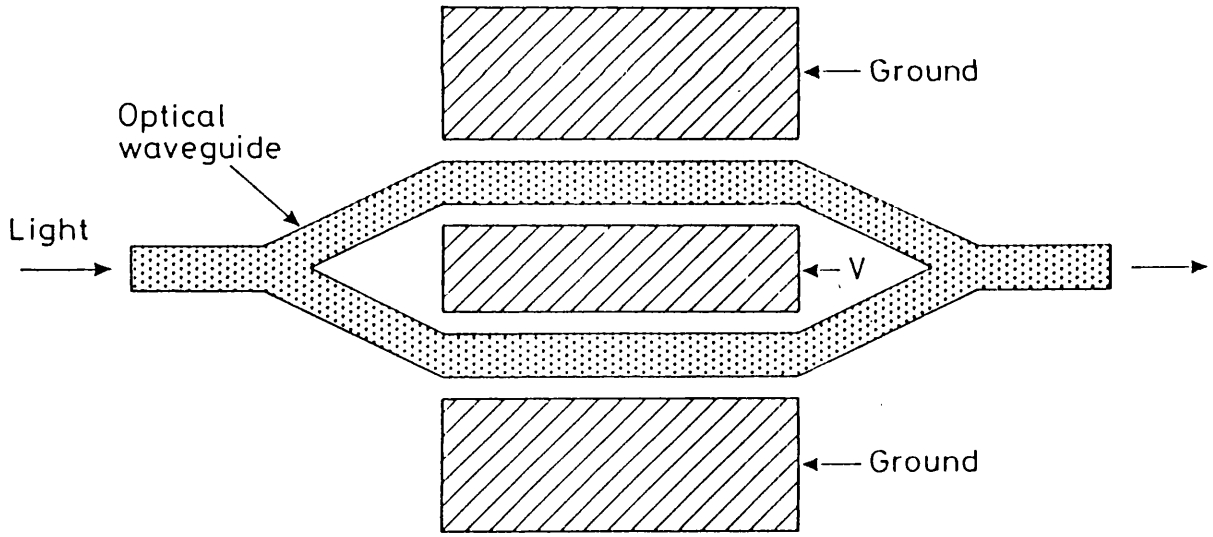

Figure 4.1. Simple Mach-Zehnder modulator

Mach-Zehnder modulator

The simplest form of integrated optic intensity modulator consists of a Mach-Zehnder waveguide arrangement as shown in figure 4.1. A potential difference between the two electrodes causes a change in the refractive index of the lithium niobate material by the electro-optic effect. This gives rise to a phase shift between the optical signals in the two arms of the interferometer and hence a variation in the optical

intensity at the output. The device will exhibit a sinusoidal transfer characteristic and must be correctly biased to ensure linear operation. This type of modulator is limited by the capacitance of the electrodes to frequencies of a few gigahertz. The capacitance can be reduced at the expense of sensitivity by reducing the length of the electrode structure.

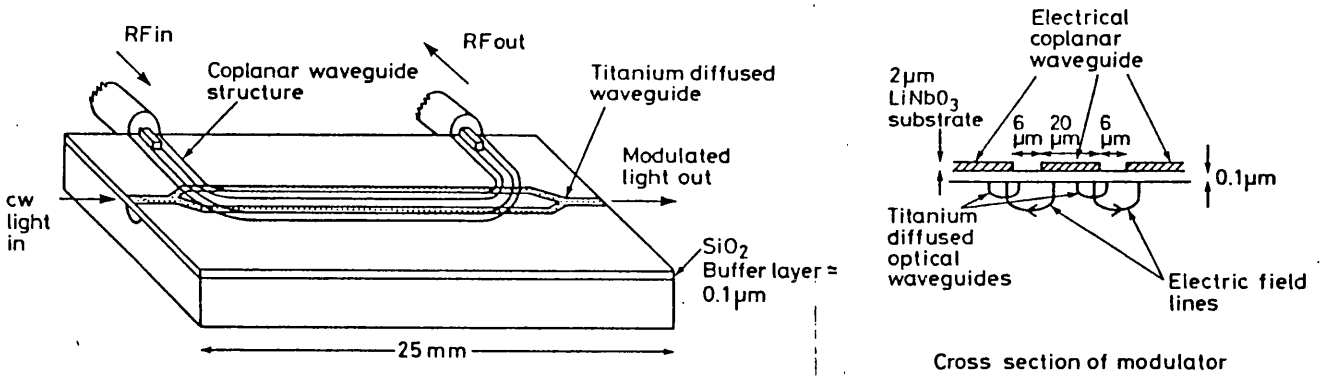

Figure 4.2. Travelling wave Mach-Zehnder modulator

If the electrode structure is modified to form part of a transmission line, as shown in figure 4.2, then the capacitive effect of the modulator no longer represents a limitation for the speed of response. This will now be limited by the difference in the propagation velocities of the optical and electrical signals in the modulator. The electro-optic effect is caused by asymmetry in the electronic polarisation of the material and is hence a fast effect.

4.2. SCALAR MEASUREMENT OF PHOTODIODE RESPONSES

Principle of operation

A Mach-Zehnder integrated optic modulator has a raised cosine bias characteristic. Normally the device would be operated in the linear regime. If the bias is adjusted to give a minimum (or maximum) optical transmission then the light will be modulated only at even harmonics of the drive signal, as illustrated in figure 4.3. The mean optical power will also be a function of the r.f. drive level. This technique has previously been used to measure the modulator response[50]. The r.f. drive power can be adjusted at different frequencies to compensate for

the modulator response and keep the mean optical power constant, thus levelling the optical modulated signal. The following relations govern the optical intensities of the mean and second harmonic signals:

$$I(dc) = \tfrac{1}{2} I_o (1 - \cos(Z_b)\ J_0(\beta_1)) \qquad \text{(eq. 1)}$$

and

$$I(2\omega_1) = I_o \cos(Z_b)\ J_2(\beta_1) \qquad \text{(eq. 2)}$$

where I_o is the maximum optical intensity; Z_b is a normalised bias parameter; and β_1 is the modulation index of the r.f. drive at ω_1. J_0 and J_2 are zero and second order Bessel functions.

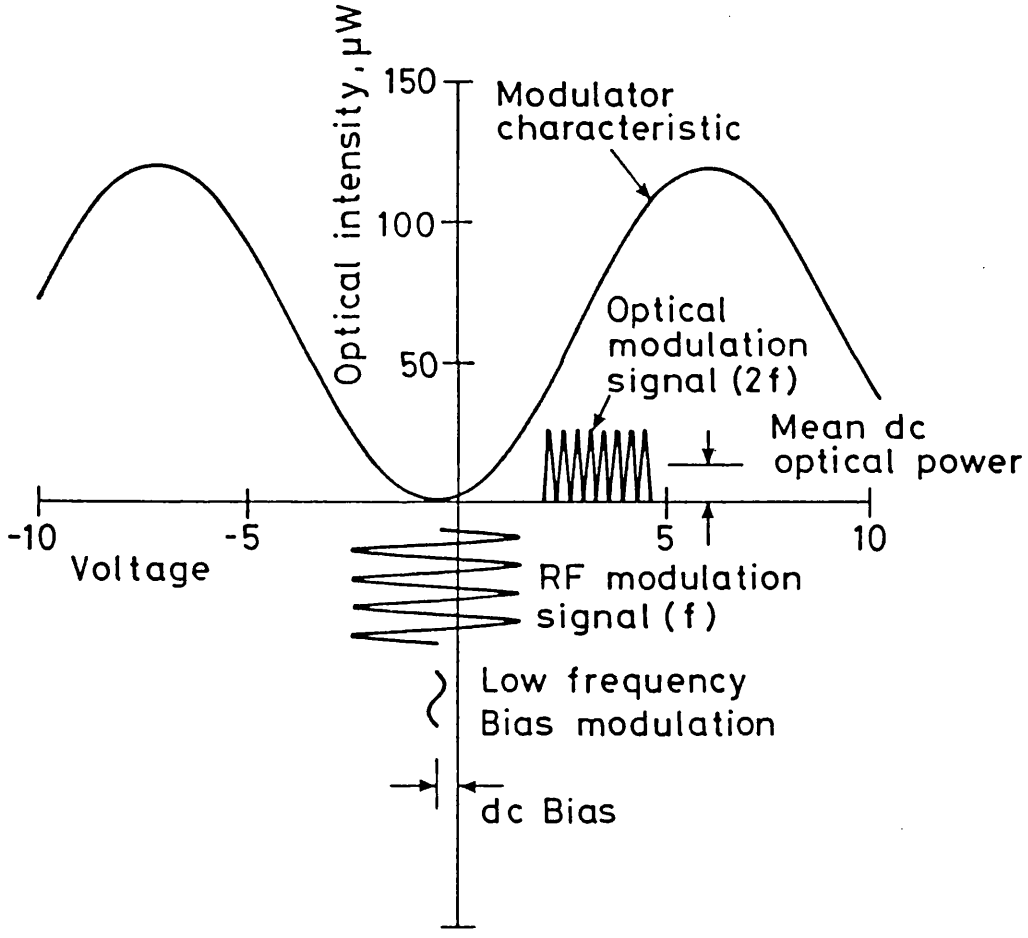

Figure 4.3. Principle of operation of the scalar integrated optic measurement system

In principle this technique could be used to generate optical signals at higher harmonics, however distortion inherent in the amplifier could give rise to competing signals of arbitrary phase. The power in these harmonics would therefore be uncertain.

To ensure that the modulated signal can be accurately levelled it is important that the bias point does not drift from the minimum optical transmission, otherwise the mean optical power will be incorrect. If a low level ($\beta_2 << \beta_1$) low frequency modulation ω_2 is added to the r.f. signal then the optical output will contain a component at the modulating frequency:

$$I(\omega_2) = I_o \sin(Z_b)\ \beta_2\ J_0(\beta_1) \qquad \text{(eq. 3)}$$

where β_2 is the modulation index at the frequency ω_2.

A feedback loop can then be used to correct for variations in the bias point with temperature and r.f. power. To ensure stability of the control loop the r.f. drive signal must not exceed a modulation index of about 2.2.

Measurement system

The system arrangement is shown in figure 4.4. The optical source is a STC 1.3 μm telecommunications laser, giving 1.3 mW in single mode fibre.

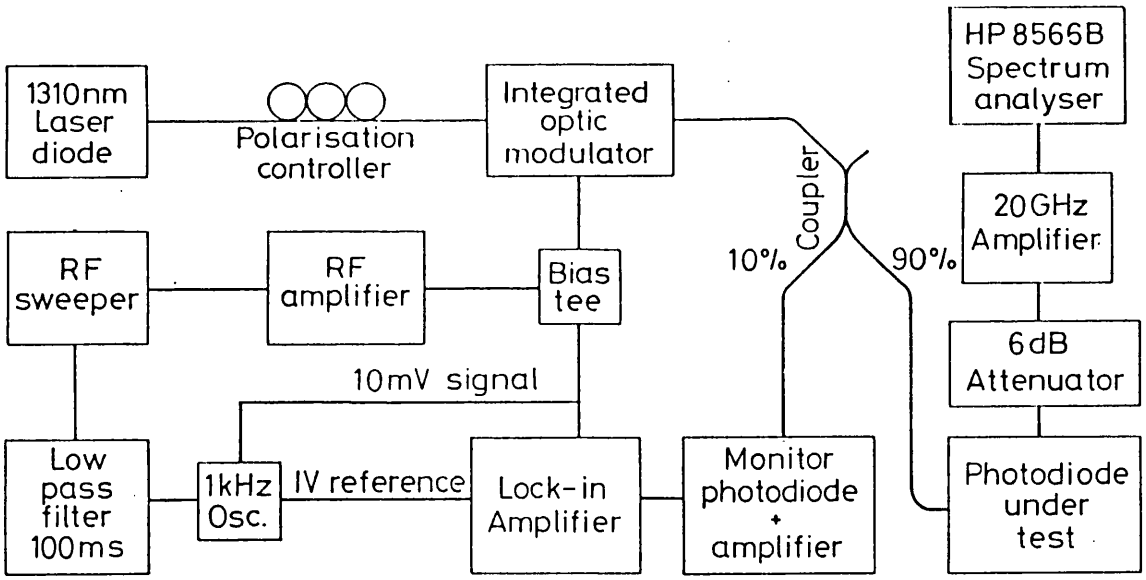

Figure 4.4. Measurement system layout

The integrated optic modulator is an 8 GHz Mach-Zehnder device with a V_π of 6.6 V and an extinction ratio of 30 dB (GEC Y-35-5600-01). The modulator was selected to have optical extinction at a bias of approximately -0.5 V. This device has been modified to include a

decoupling capacitor so that a static bias voltage can be applied.

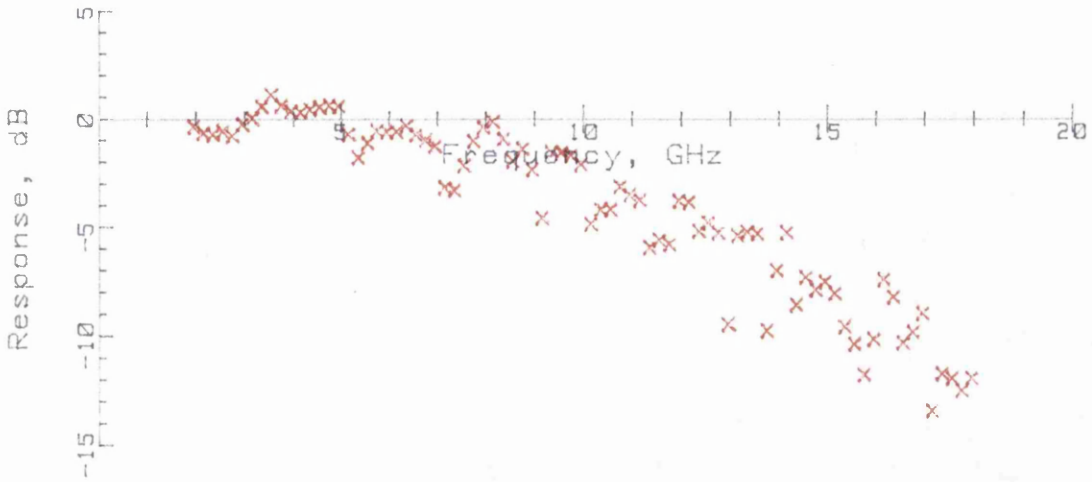

Figure 4.5. Modulator frequency response

The frequency response of the modulator is shown in figure 4.5. The modulator exhibits a number of relatively high Q resonant features at frequencies above 8 GHz. These are due to r.f. power in the lithium niobate substrate[51]. The resonances will limit the maximum continuously tuneable levelled modulated optical power that can be obtained from the system.

Ten per cent of the light from the modulator has been used to monitor the optical power and provide the feedback signal for the control loops. A maximum of 120 μW could be coupled through the system giving an overall optical loss of 10.5 dB. The low pass filter was required to separate the operation of the control loops stabilising the bias point and r.f. drive. Some transient effects were observed when the frequency, and hence r.f. drive power, was changed. These effects were overcome by reducing the gain of the lock-in amplifier prior to changing the frequency.

The output from the sweeper was amplified to give a drive signal in the range 16 - 22 dBm. In early experiments two amplifiers were used to cover the frequency range. Later a single high power amplifier, capable of covering the whole frequency range and giving powers of 24 dBm or greater was used.

A levelled optical signal of 4 μW could be achieved continuously at up to 22.6 GHz and at selected frequencies at up to 25.6 GHz using the wideband amplifier. The variation of the levelled signal as a function of frequency is shown in figure 4.6. At the lowest drive power a continuously levelled signal can be achieved to greater than 20 GHz. At

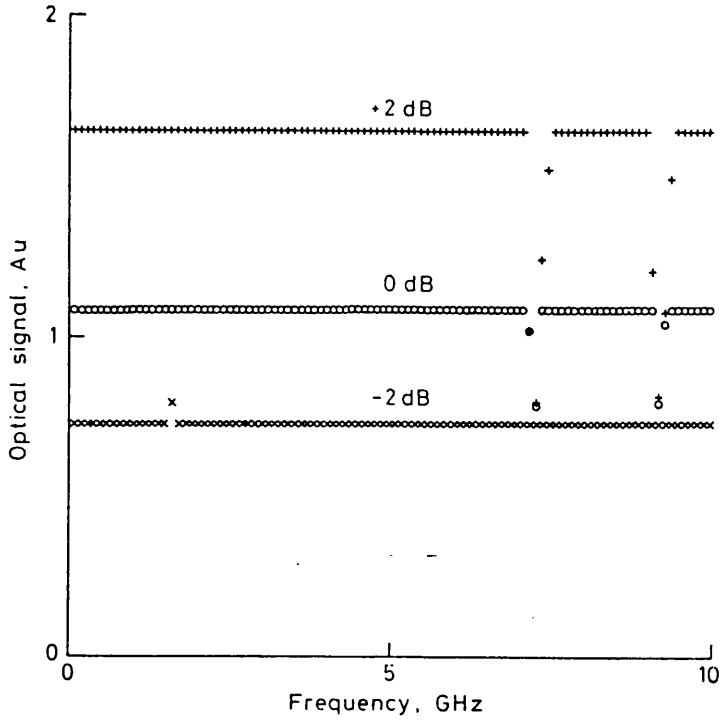

Figure 4.6. variation of the levelled signal with frequency

higher powers the amplifier cannot supply sufficient power to overcome the resonances in the modulator response at 7.2 and 9 GHz and maintain a levelled output. A 100% modulated optical signal with a mean power of 4 μW corresponds to an r.f. power of -66 dBm, assuming a 50 Ω load and a photodiode responsivity of 0.8 A/W.

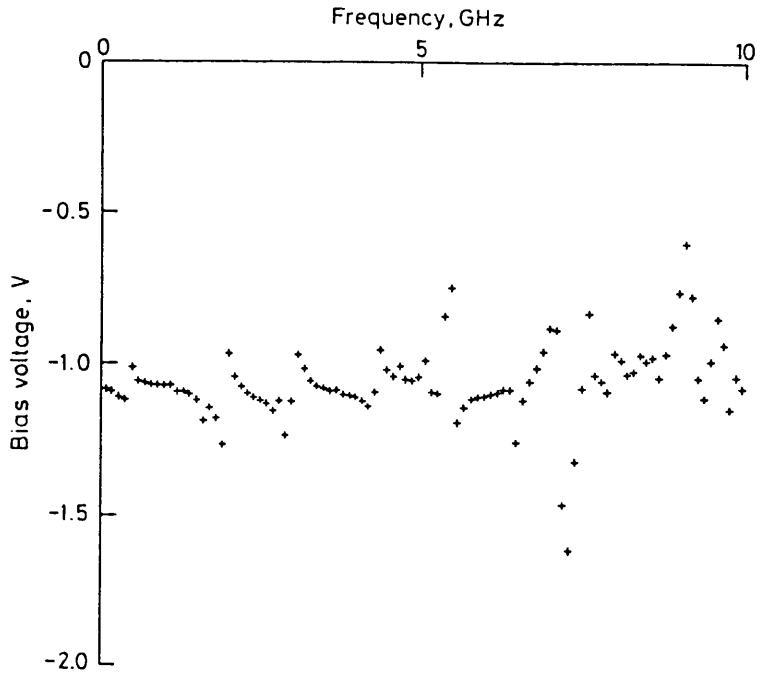

Figure 4.7. Variation of the bias voltage with frequency

The r.f. signal was measured using a spectrum analyser (HP 8566B)

pre-amplified by a distributed amplifier (ERA 0.05 - 20 GHz) to overcome the harmonic mixing noise. The 6 dB attenuator was included to improve the electrical reflection coefficient. The system sensitivity was calibrated at a power level of -46 dBm using a r.f. power meter (HP 437B) with a broadband power sensor (HP 8485D).

The r.f. power could be considerably increased by raising the optical power level. The modulator is rated at 10 mW optical input though higher powers have been launched in a similar design[52]. However, lasers with several longditudinal modes spaced by a few gigahertz would be unsuitable because of intermodulation products.

The bias voltage, required to keep the modulator at the minimum of the transfer characteristic, varies as a function of r.f. power and frequency. The variation of the bias voltage with frequency is shown in figure 4.7. The sharp changes in the required bias voltage at certain frequencies are believed to be due to the electrical resonances within the modulator. It is believed that the pattern of dissipation of the r.f. power above and below the resonance is different, locally changing the refractive index and giving rise to a shift in the static bias voltage.

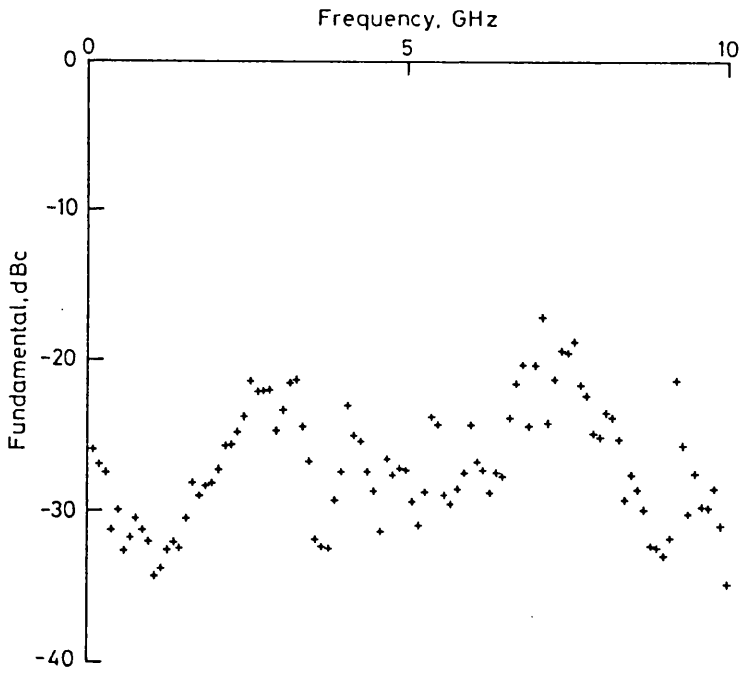

Figure 4.8. Residual signal at the fundamental frequency

The residual fundamental component of the optical signal is primarily due to power at higher harmonics of the modulation frequency. The low level low frequency modulation used to stabilise the bias voltage will

also give a contribution but this is negligable. The residual fundamental signal will be given by:

$$I(\omega_1) = I_o \cos(Z_b)\ \beta_3\ 2J_1(\beta_1) \qquad \text{(eq. 4)}$$

where β_3 is the modulation index of the r.f. distortion at $2\omega_1$.

The variation of the residual r.f. signal at the fundamental frequency is shown in figure 4.8. The results, typically better than -20 dBc, indicate that the amplifier has low harmonic distortion.

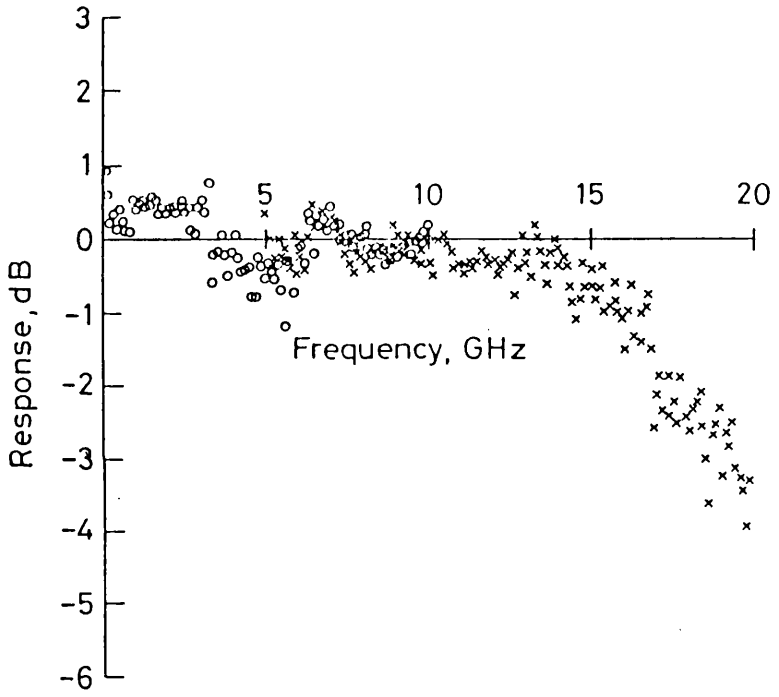

Figure 4.9. Frequency response of the 25 μm diameter AT&T research photodiode

Measured results

Measurements of the AT&T research photodiode[4] were made over the range 100 MHz to 10 GHz and 5 to 20 GHz at 100 MHz intervals. The results, corrected for the sensitivity of the photodiode (11.7 dB offset), are shown in figure 4.9. The low measured point at 5 GHz was caused by an instrumentation effect. The electrical reflection coefficient of the photodiode (S_{11}) has been measured to be better than -18 dB over the frequency range of interest. No correction has been made for electrical mismatches between the photodiode and the measurement system or residual non-linearities in the spectrum analyser. The ripples in the

results have been attributed to these effects.

The mean statistical uncertainties in the measurement are less than ±0.2 dB and the systematic uncertainties have been estimated to be ±0.4 dB. All the uncertainties are at the 95% confidence level. The results indicate that this photodiode has a 3 dB frequency of 19.2 ±0.8 GHz.

Future work with this system

At present the r.f. power measurement is performed using a spectrum analyser. The r.f. signal level is relatively low (-60 to -70 dBm) and substantially different from the calibration level (-50 dBm). This discrepancy presents a possible source of error as the linearity of the spectrum analyser is not known. Also, the maximum frequency that can be conveniently used is limited to 20 GHz by the preamplifier bandwidth.

In the near future a high power semiconductor laser, giving in excess of 10 mW (OKI 354L), will be incorporated into the system. This should allow a levelled signal in excess of 50 μW to be achieved continuously at frequencies of up to 22 GHz. The higher optical power may also allow the r.f. signal to be directly measured using a r.f. power meter. This will give a twofold improvement in the system: firstly, the r.f. calibration chain will be shorter, with a source of systematic uncertainty removed and secondly, the return losses of the measurement system will be lower.

4.3. VECTOR MEASUREMENT OF PHOTODIODE RESPONSES

Integrated optic modulators can readily be used in conjunction with a vector network analyser and a photodiode frequency response transfer standard to measure the response of an unknown photodiode. The layout of such a system is shown in figure 4.10. Such a measurement system could offer considerable advantages over the scalar techniques because the device under test is fully characterised in terms of its optical response and its electrical return loss. Both parameters are available in terms of their magnitude and phase. The disadvantage is that a transfer standard photodiode is required so that a calibration of the system can be performed. This is because, unlike the previous system discussed, the modulator output will not be levelled. It is therefore not possible to use the system to calibrate a transfer standard device

against optical and r.f. power standards.

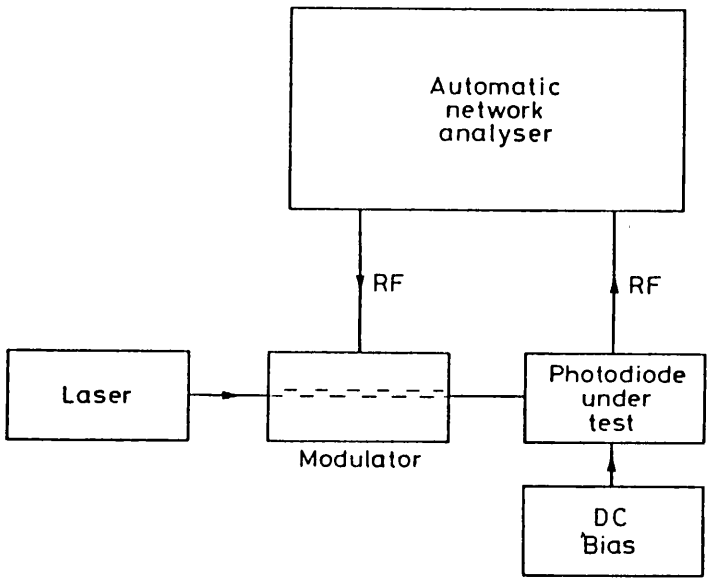

Figure 4.10. Layout of integrated optic modulator based vector measurement system

A GaAs/AlGaAs modulators with a frequency response extending to greater than 25 GHz has been reported[53]. Lithium niobate devices with bandwidths in excess of 18 GHz are available commercially[54] and a Lithium niobate modulator[55] with a frequency response extending to 40 GHz and a drive voltage (V_π) of 7.5 V has also been reported. It would therefore be quite feasible to construct a system, operating at up to mm-wave frequencies, using such components. An instrument operating at up to 20 GHz is available commercially[56]. Vector network analysis systems based on integrated optic modulators will not be discussed further here.

4.4. DISCUSSION AND CONCLUSIONS

In this chapter a scalar measurement system, based on integrated optic modulators, has been described in detail. The use of integrated optic modulators to measure the magnitude and phase responses of an unknown device has also been discussed. The vector measurement technique has the advantage that it offers a complete characterisation of the device under test. However, the systematic uncertainty in the measurement will depend on the accuracy of the characterisation of the transfer standard device. This type of measurement system is unlikely to be able to characterise a transfer standard device against suitable r.f. and

optical power standards.

The scalar measurement system was based on a commercially available 8 GHz modulator. The modulating frequency was doubled by using the intrinsic nonlinearity of the device. A levelled, modulated optical signal of 4 μW could be achieved at frequencies of up to 22.6 GHz. In the near future a high power semiconductor laser will be installed into the system. This will allow the levelled optical output power to be increased by almost an order of magnitude.

The maximum operating frequency of the system described was limited by the modulator frequency response. Modulators with frequency responses of greater than 18 GHz are commercially available[54]. Suitable r.f. power amplifiers to drive such modulators are also available. It would therefore be possible to construct a system with a maximum levelled frequency output in excess of 40 GHz, using the technique.

5. SAMPLING AND CORRELATION METHODS

5.1. INTRODUCTION

A fast oscilloscope can aquire a complete photodiode response using a single trigger event. Commercially available instruments have risetimes of a few hundred picoseconds[57]. Ultra-high speed photodiodes have risetimes of a few tens of picoseconds (tens of gigahertz) and are therefore very much faster than conventional oscilloscopes. An alternative approach must be chosen to measure these photodiodes.

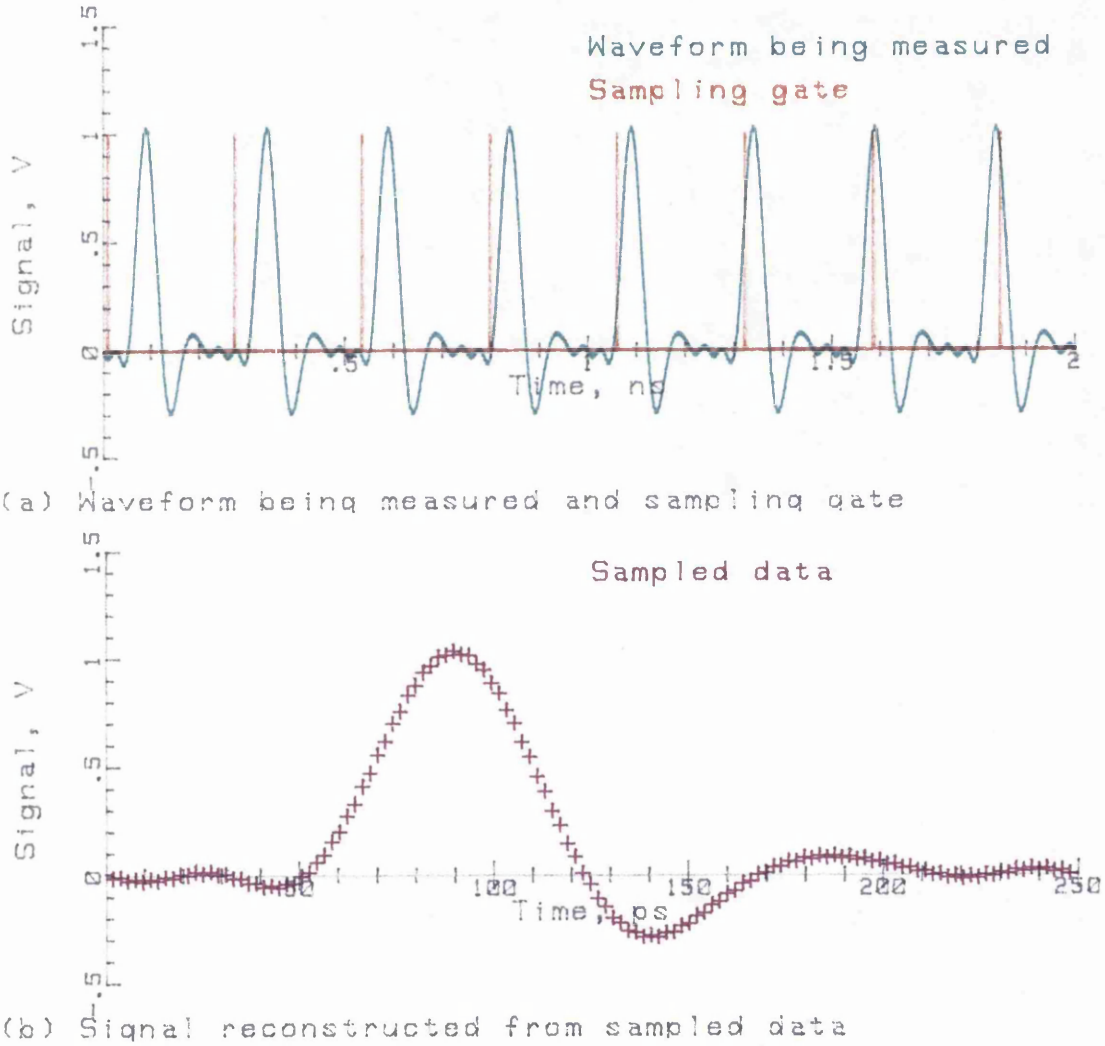

Figure 5.1. Principle of the sampling method. One sample is taken per pulse. The waveform shape is then determined from the average voltage at each delay position.

Sampling and correlation methods offer the potential for measuring the response of a photodiode with a resolution of a few picoseconds provided that a suitable source of repetitive optical pulses is

available. The principle of the sampling method is shown in figure 5.1. The sampling system acts as a temporal vernier, a different part of the signal is measured for each trigger event. The sampling 'gate' will have a finite temporal response and therefore the measured signal will be the cross correlation of the sampling gate and the unknown signal responses as shown by:

$$m(t) = \int_{-\infty}^{\infty} g(\tau)x(t+\tau)d\tau \qquad \text{(eq. 1)}$$

where m(t) is the measured signal, g(t) is the temporal response of the gate and x(t) is the unknown signal.

The result will contain noise and jitter due to variations in the amplitude of the unknown and trigger signals. These effects will be considered in part 2 of this thesis.

In this chapter the sampling oscilloscope and electrical correlation methods will be described and their limitations discussed. Other techniques such as *Photoconductive sampling* and *Electro-optic sampling* are important as they will provide the next generation of instruments for waveform metrology. These techniques are treated in depth elsewhere[58] and will not be covered here. The emphasis of this chapter will be on systems that are readily available or can be assembled from commercial equipment, rather than one-off research devices.

5.2. SAMPLING OSCILLOSCOPE

Introduction

The sampling oscilloscope uses an electrical sampling gate, consisting of a number of high speed switching diodes, to capture the instantaneous voltage a repetitive waveform at one temporal position within the signal. These instruments were developed by *Tektronix* and *Hewlett Packard* in the late 1960s. The first generation of analogue sampling oscilloscopes have risetimes in the region of 20 - 25 ps, corresponding to a frequency response of 14 - 18 GHz. This type of sampling oscilloscope has more recently been superceded by new designs but the first generation instruments are still widely used in many research and production environments.

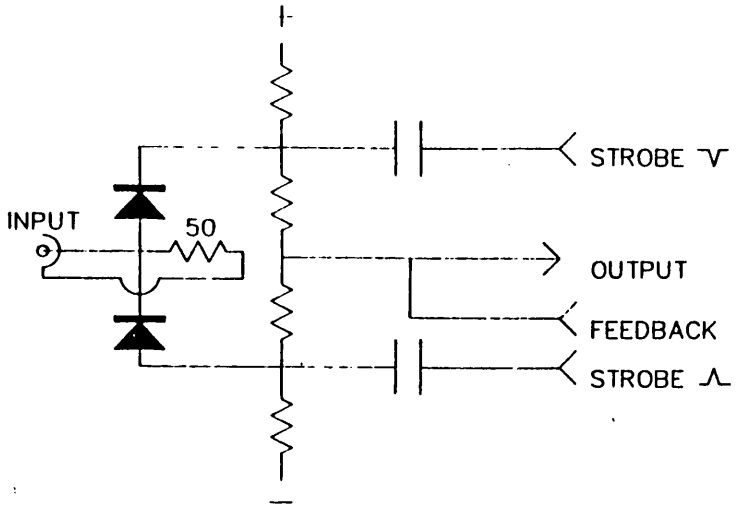

Figure 5.2. Balanced sampling gate

Design of the sampling gate

Two designs of sampling gate are commonly used: the *balanced sampling bridge* and the *travelling wave sampling bridge*. The circuit for the former is shown in figure 5.2. The two reverse biased sampling diodes are forced into conduction for a short time by a pair of complementary strobe pulses applied to each of the diodes through a capacitor. The potential at the input, during the sampling interval, causes a small difference between the charges passed by each of the diodes to its respective capacitor. This in turn gives rise to a small potential at the output of the sampling bridge. The dynamic range of the system can be improved by applying feedback which returns the output voltage to a common reference. The measured signal can be obtained by integrating the feedback current[59]. Risetimes of 20 ps have been achieved with this system by careful design of the microwave network used to shape the strobe pulse and by improved sampling diodes[60]. The overall speed of response is strongly dependent on the length of the strobe pulse.

The travelling wave sampling gate structure is shown in figure 5.3. As before, a complementary pair of strobe pulses is applied to the diodes causing them to conduct. The falling edge of the strobe pulse turns off the diode pairs in sequence: first A3 and B3; then A2 and B2 and finally A1 and B1. Charge is trapped between the diodes. The difference in the charges trapped between the two diode pairs, A2+A3 and B2+B3, causes a potential difference across the capacitor C. A similar feedback arrangement is employed as before to increase the dynamic range of the sampler and to recover the signal.

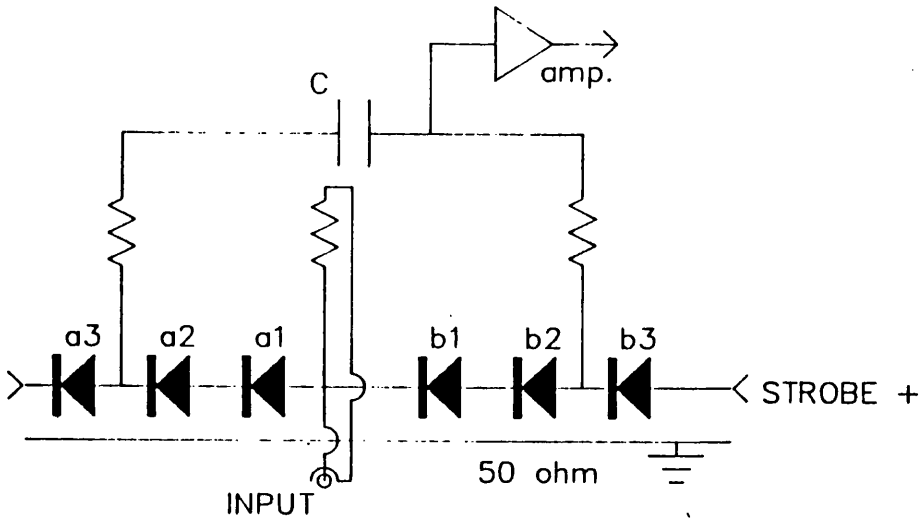

Figure 5.3. Travelling wave sampling gate

The speed of response if this scheme is not dependent on the duration of the strobe pulses but is limited by the turn-off times of the diodes and their mechanical spacing[61].

The waveforms recorded by these instruments will contain distortions due to the coupling of the signal into the charge amplifier when the sampling diodes are turned off, and coupling of the strobe pulses into the charge amplifier. Various circuits have been designed to reduce the effect of these unwanted signals[62].

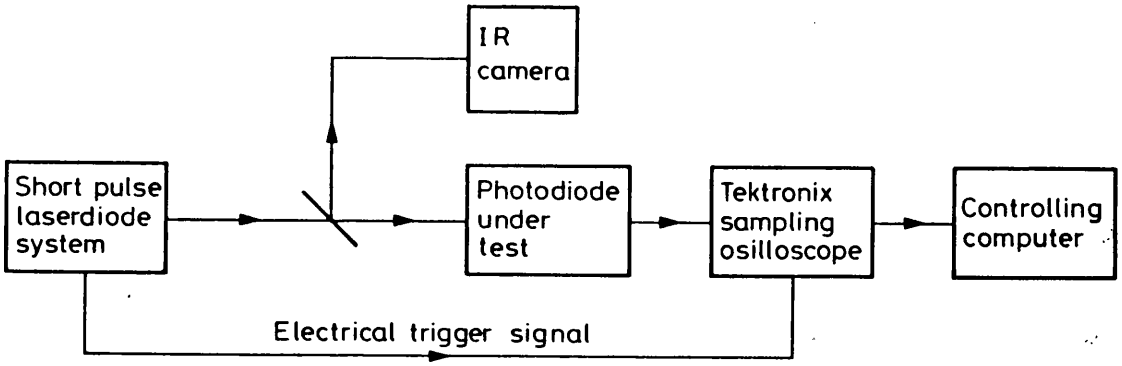

Figure 5.4. Layout of the measurement system

Measurements made with a sampling oscilloscope

The recorded waveform from a sampling oscilloscope will be the convolution of the exciting pulse, the device under test and the oscilloscope. A measurement has been made of a 25 μm diameter research photodiode from AT&T using an Optoelectronics PLS10 pulsed laser diode

source. The layout of the measurement system is shown in figure 5.4. The photodiode has a frequency response which extends to greater than 19 GHz. This has been measured by the Heterodyne (chapter 3) and the Integrated Optic Modulator (chapter 4) systems. The laser is driven by a high current electrical pulse. Under ideal conditions this would give rise to a single optical pulse with a duration of a few tens of picoseconds[63,64]. Unfortunately, the drive pulse is not ideal and the laser exhibits multiple pulses. The duration and spacing of the pulses depends on the bias voltage. The measured results for this laser and photodiode are shown in figure 5.5.

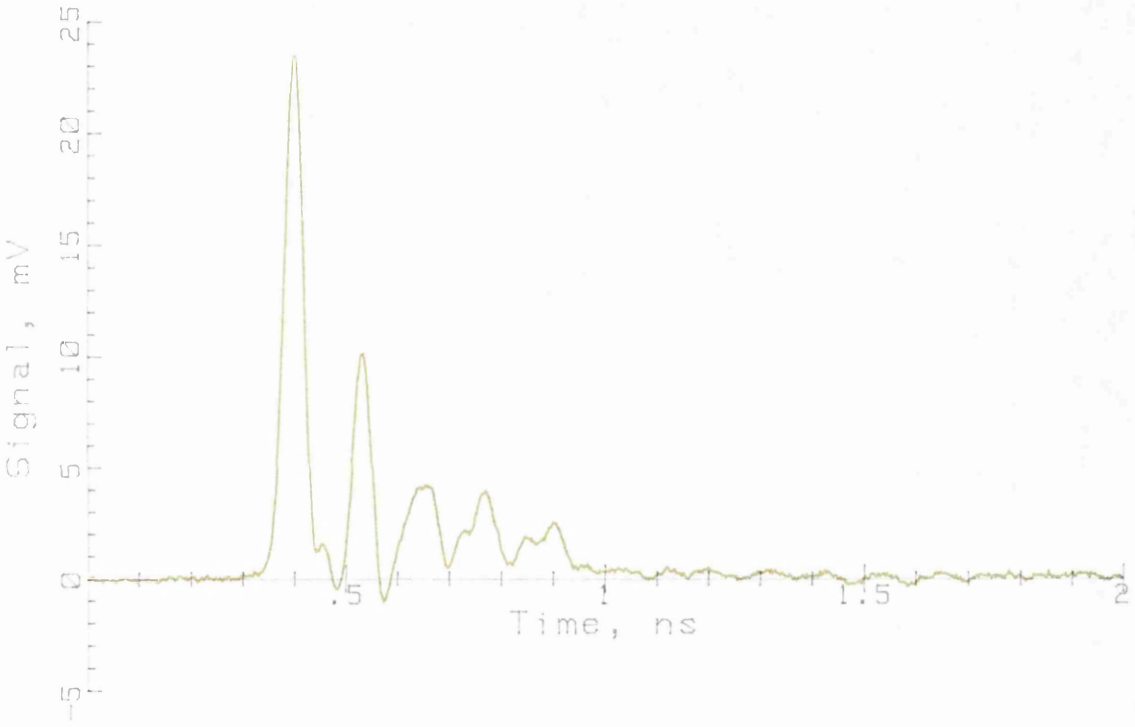

Figure 5.5. AT&T photodiode and Optoelectronics PLS 10 @1324 nm, measured with a Tektronix 7S-12 sampling oscilloscope with S-4 sampling head and S-53 trigger recogniser

The results show clearly that at these high speeds it is difficult, if not impossible, to separate, by inspection, the responses of the laser, the photodiode and the sampling oscilloscope by inspection. For this reason, numerical deconvolution techniques must often be employed to 'clean up' the results. These will be discussed in part 2 of this thesis.

Timebase calibration

The measured results will contain systematic errors due to the accuracy of the timebase calibration. The Tektronix 7S12 sampling oscilloscope

has an analogue timebase with a specified accuracy of ± 3%. This figure can be improved by calibrating the system with a known high frequency signal. The S-53 trigger recogniser can only use signals of up to 1 GHz. Internally the response drops off above 50 MHz making the unit insensitive at higher frequencies[65]. This problem can be overcome by calibrating the system with a high frequency sinewave, derived by harmonic generation.

A step recovery diode comb generator will produce power at the harmonics of the drive frequency. The output from the comb generator can then be attenuated and filtered to remove the unwanted harmonics. The system developed at NPL to generate a high purity 10 GHz signal, suitable for the timebase calibration, uses a 250 MHz comb generator, 14 dB of attenuation, two 100 MHz bandpass comb line filters, and a narrow-band amplifier. The layout of this system is shown in figure 5.6.

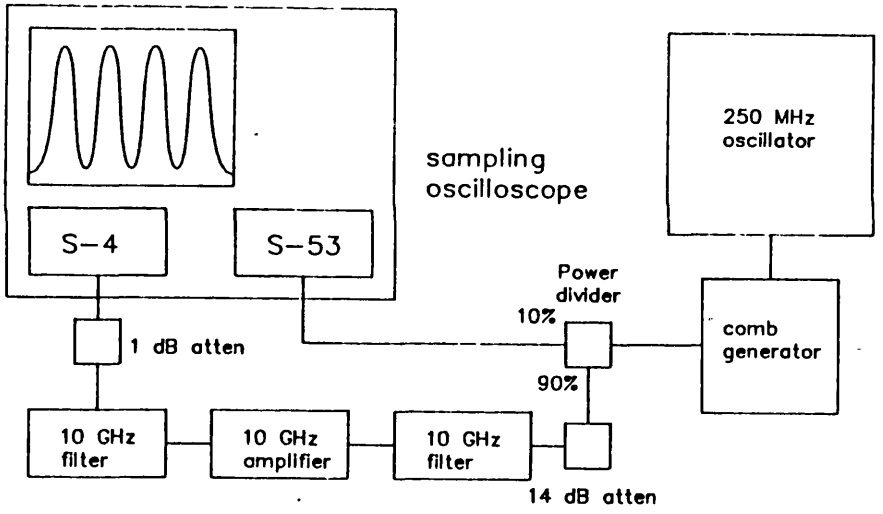

Figure 5.6. Layout of the system used to calibrate sampling oscilloscope timebases at NPL

The attenuator is required to remove the unwanted harmonic power reflected from the filters. This power, if not correctly terminated, causes instability in the comb generator. Additional frequencies are generated within the bandpass of the filters, leading to ambiguous results. The power in the comb harmonics drops off with frequency, and so the filters have been designed to complement the response of the comb generator and give >100 dB supression of all unwanted harmonics. A similar system has been designed for operation at 1 GHz to calibrate longer timebase settings. That system does not require a narrow-band amplifier as the comb power is greater.

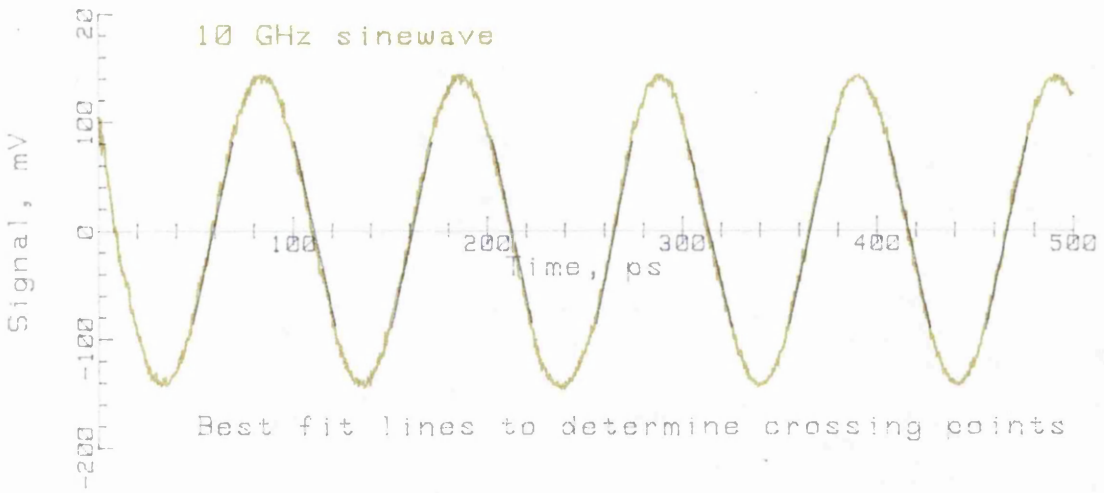

Figure 5.7. 10 GHz sinewave calibration of a 50ps/div timebase. Curves are fitted to determine the zero crossing points.

The harmonic generation technique has also been used by *Andrews* and *Gans*[66] for this purpose. In their system the filtering was performed by a 3-port cavity wavemeter. That system offers the flexibility of choosing the calibration frequency which best suits the timebase. The system developed here is rather easier to use but is less flexible.

The measured results obtained using this system to calibrate a 50 ps/div timebase are shown in figure 5.7. The zero crossing points were determined by curve fitting. In this case, the calibration factor was calculated to be 0.986±0.016 with 95% confidence. The accuracy of the technique is limited by the determination of the crossing points, rather than the frequency accuracy of the sinewave.

Assessment of the sampling oscilloscope performance

A full assessment of the performance of a sampling oscilloscope can only be made if a faster measurement system, such as the electro-optic sampling technique, is available. Measurements have been made by *Henderson*[58] of the response of a Tektronix 7S12 sampling plug-in with S-4 sampling head and S-53 trigger-recogniser using a high speed GaAs photodiode and a dye laser source producing ~2 ps optical pulses. The measured results for both the sampling oscilloscope and the electro-optic sampler are shown in figure 5.8.

These results have been processed using the Fourier transform deconvolution technique developed by *Nahman*[67] to remove the response of the photodiode from the result. The electro-optic sampler has been assumed to have a Gaussian response of 8 ps FWHM. The deconvolved

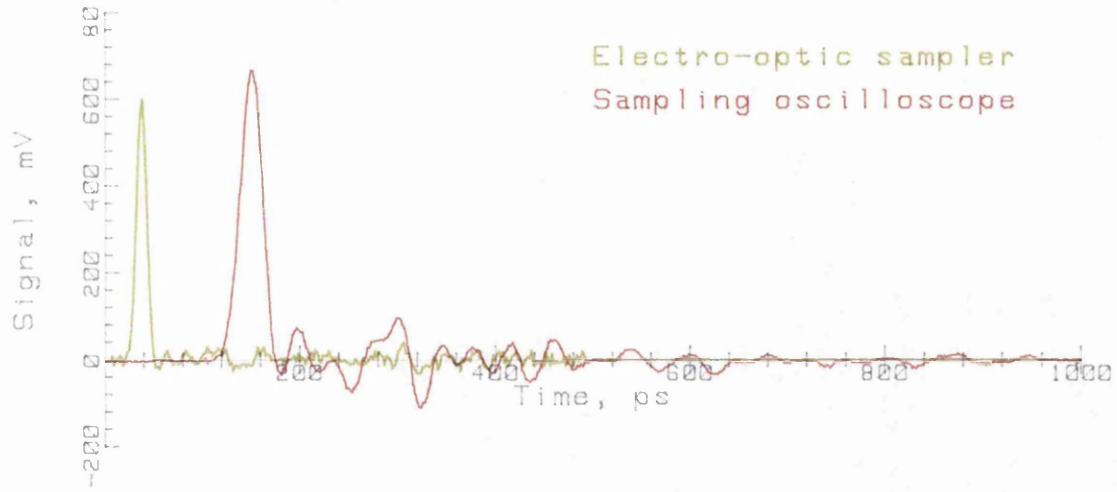

Figure 5.8. Measured responses of a 50 GHz GaAs photodiode using the Tektronix sampling oscilloscope and the electro-optic sampler

result is shown in figure 5.9.

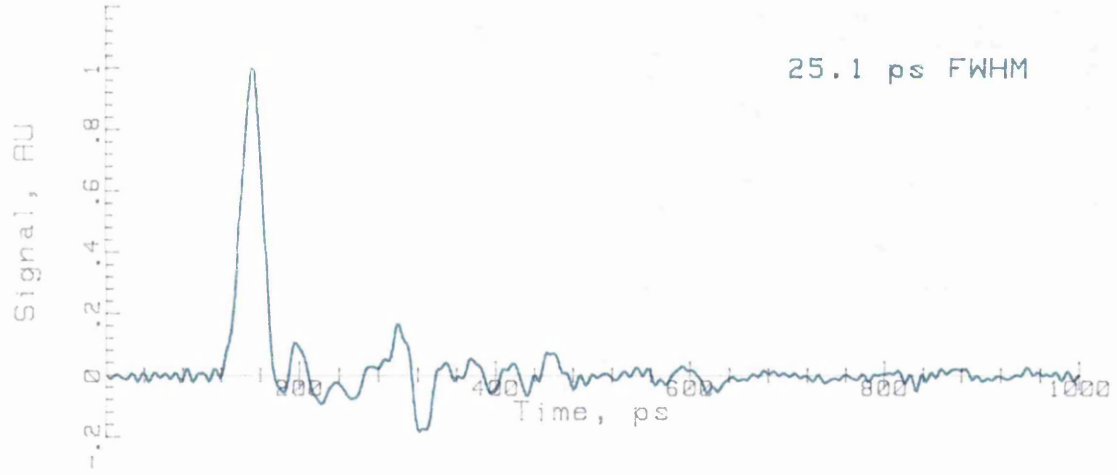

Figure 5.9. Deconvolved response of the Tektronix sampling oscilloscope

The sampler response is not smooth with components in excess of 15% of the height of the main pulse occurring approximately 150 ps later. These additional components may be the cause of dips in the response at certain frequencies. The r.f. power spectrum response of the sampler, shown in figure 5.10, can be obtained as a by-product of the deconvolution process. The response shows dips at 11, 16 and 24 gigahertz.

These results have been confirmed using a frequency domain technique which allows a partial assessment of the response to be made. The temporal response of pulse train was measured by the sampling

oscilloscope and the results transformed to the frequency domain. The power in the harmonics of the train of pulses was measured with a spectrum analyser (chapter 2). The two sets of results were then compared. The dip in the frequency response at 10-11 GHz was also observed by this method.

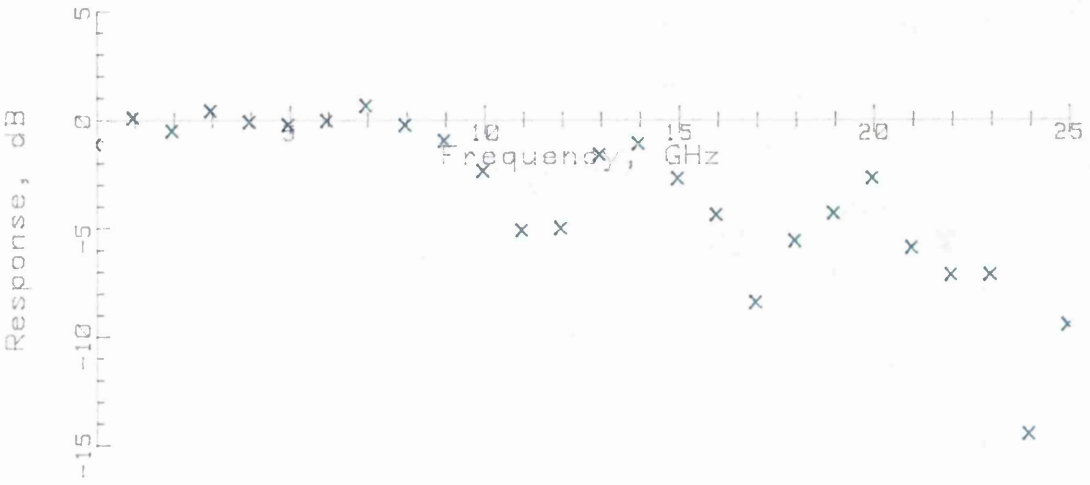

Figure 5.10. Power spectrum response of the Tektronix S-4 sampler showing dips in the response at 10, 16 and 24 GHz

Discussion

Measurement of a photodiode response may be limited by the speed of the sampling oscilloscope and the source. A trigger signal must be provided and there is an instrument dependent delay between the trigger and the measurement signals. In certain applications this can give rise to jitter where there is some uncertainty between the timing of the trigger and measurement events. The sampling oscilloscope is the most convenient method of making measurements in the 20+ ps regime.

5.3. ELECTRICAL CORRELATION

Introduction

An ideal r.f. power meter is a true square law detector, giving a reading which is proportional to the square of the rms voltage of the microwave signal. The power meter can therefore be used to determine the autocorrelation function of a high speed photodiode temporal response, provided that a suitable source of picosecond optical pulses is available. The output from the r.f. power meter will be the autocorrelation of the electrical pulse as shown by:

$$P(\tau) = \frac{K}{R}(\langle V_1(t)^2\rangle + 2\langle V_1(t)V_2(t+\tau)\rangle + \langle V_2(t+\tau))^2\rangle) \qquad \text{(eq. 2)}$$

where K is the sensitivity of the power meter; R is the load impedance; V_1 and V_2 are the voltages in the two pulse trains and τ is the delay.

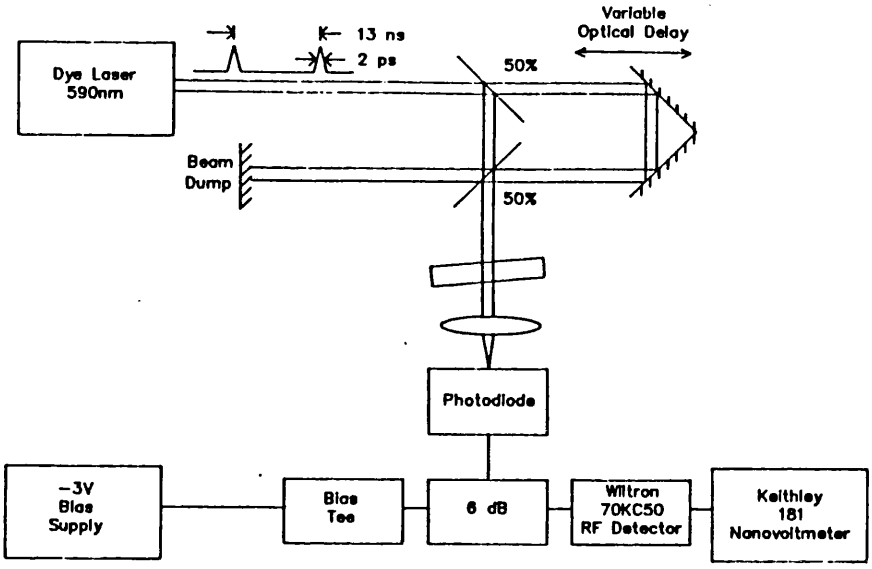

Figure 5.11. Layout of an electrical correlation system

The correlation technique has been used by *Paulus* and *Jäger* to measure picosecond electrical pulses[68]. The autocorrelation function can be transformed to the frequency domain where it is equivalent to the magnitude of the frequency response.

The layout of an autocorrelation system for photodiode measurements is shown in figure 5.11. The optical delay alters the relative temporal positions of the two pulse trains. Figure 5.12 parts (a) to (d) show the simulated optical and electrical pulse trains, together with the power meter output for four delay positions. Part (e) shows the autocorrelation response as a function of path delay.

Limitations of the correlation method

There are three limitations of this method: the dynamic range, drift and the maximum signal. The dynamic range is limited because the signal will only vary over about an octave range. The resolution of the power meter will therefore limit the accuracy of the results because the signal will be low except close to the correlation peak. The power meter reading may drift due to environmental changes such as temperature fluctuations.

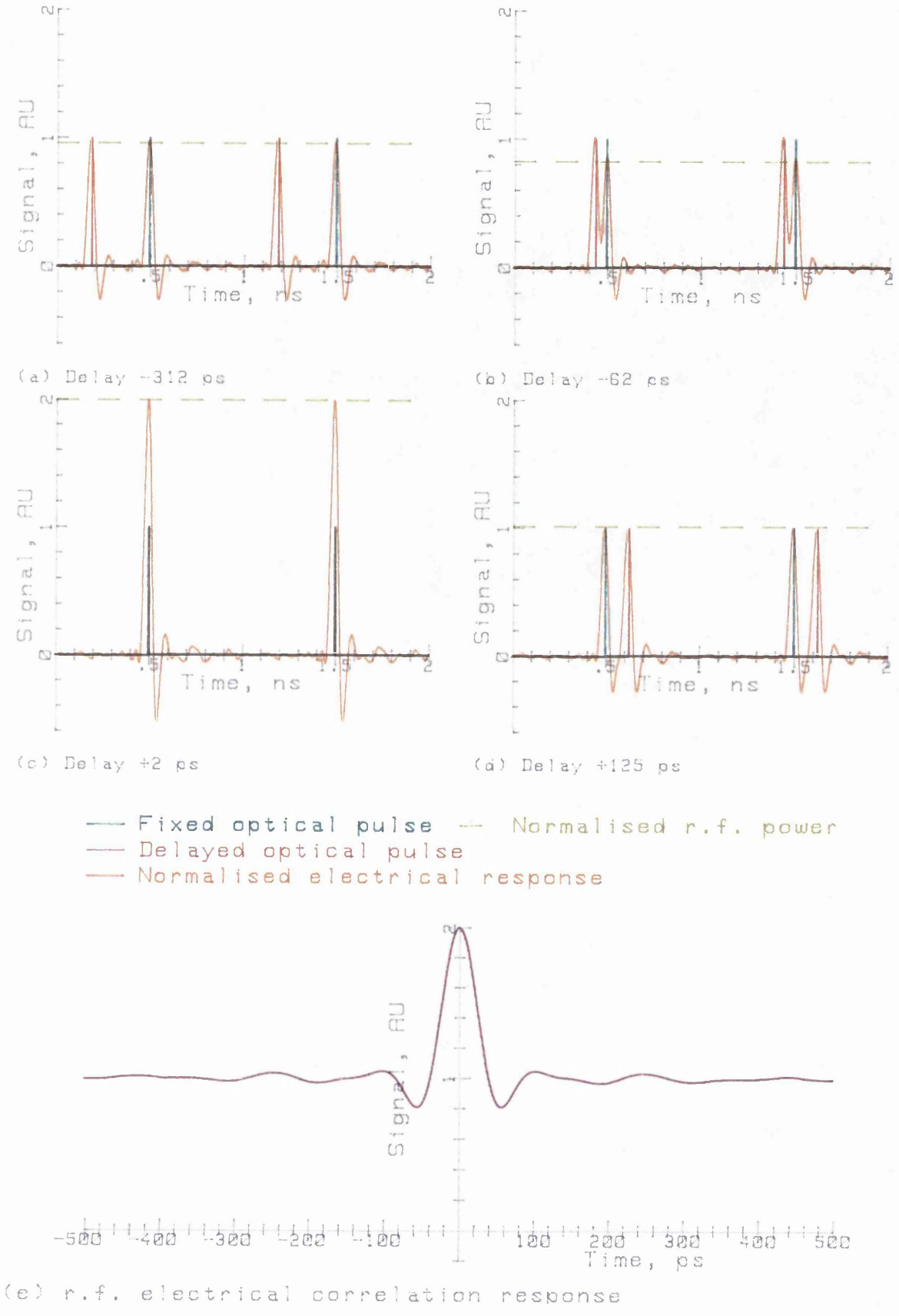

Figure 5.12. Simulated optical and electrical output from a correlator system, showing the r.f. power level

The maximum signal which can be obtained from the device under test will be limited by one of two mechanisms: the first is power dissipation and the second is saturation of the photocurrent, causing a change in the temporal response shape. Both these effects were discussed in chapter 2.

r.f. power detectors

Two distinct types of r.f. power sensors are available: the first uses a high speed semiconductor diode and the second is a thermal device. The semiconductor diode uses the nonlinear diode characteristic:

$$i = I_s\left(\exp\left(\frac{qV}{nkT}\right) - 1\right) \qquad \text{(eq. 3)}$$

where i is the diode current; V is the voltage across the diode; I_s is the saturation current, which is constant at a given temperature; k is the Boltzmann constant; T is the absolute temperature and n is a correction constant to fit the experimental data. The value of n is about 1.1 for the diodes used for r.f. power sensing[69].

The second and even order terms of equation 3 provide the rectification and give an output voltage proportional to the r.f. power. These devices are sensitive to very low power levels (-70 dBm) but at higher powers (-20 dBm and above) the response becomes sublinear due to the higher order terms in the series expansion of the exponential. The diode characteristic may give rise to problems when this type of device is used to measure the power in a train of short electrical pulses because the mean power may be low but the peak power will be high.

The second type of power meter is based on a thermal sensor. This may either be a thermistor or a thermocouple. Power sensors of this type are considerably less sensitive than diode detectors to r.f. power. The typical sensitivity range is -30 dBm to +20 dBm for a thermocouple based sensor (HP8485A). These detectors are also more sensitive to environmental changes such as temperature[69]. The response of a thermal detector, unlike the diode detector, is not affected by the shape of the r.f. waveform.

The approximate expected r.f. power can be calculated from a simple expression:

$$P_{dBm} = 10\ (\log_{10}(\frac{V^2}{R}W\ F)+3) \qquad \text{(eq. 4)}$$

where P_{dBm} is the power in dBm; V is the peak voltage; R is the load impedance; W is the pulse width and F is the pulse repetition rate.

The predicted r.f. power is about -30 dBm for electrical pulses of 180 mV with a width of 20 ps and a repetition rate of 76 MHz. It should therefore be possible to use thermal detectors to detect the autocorrelation signal.

Experimental measurements

A measurement has been made of a GaAs/ITO photodiode to assess the electrical correlation technique. A 590 nm modelocked dye laser was used as the source. The laser produces optical pulses of 2 ps FWHM, determined by optical autocorrelation, at a repitition rate of 76 MHz. A semiconductor r.f. detector diode (Wiltron 70KC50) was used as the detecting element. The photodiode was biased at -3 V through a decoupling network. A 6 dB attenuator was positioned between the diode and the r.f. detector to reduce the effect of electrical reflections. The electrical pulses from the photodiode are negative with a peak value of approximately 700 mV.

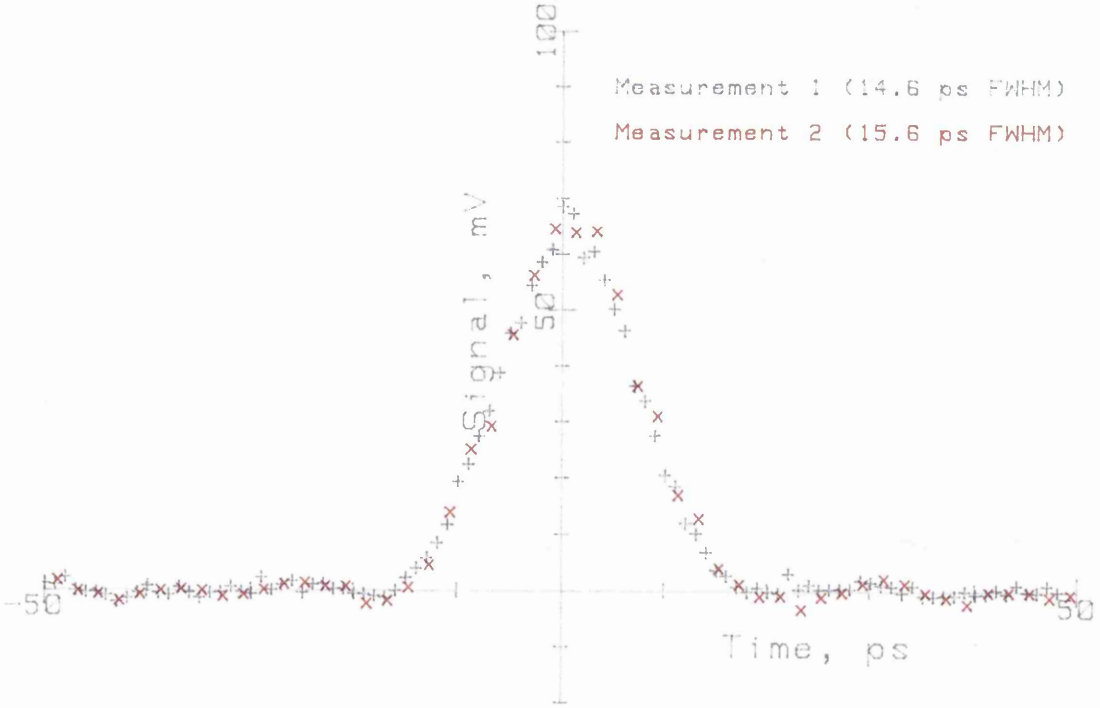

Figure 5.13. Measured electrical autocorrelation results for the GEC 50 GHz GaAs/ITO photodiode

Two autocorrelation measurements were made and the results are shown in figure 5.13. The measured FWHMs of the two measurements are 14.6 ps and 15.6 ps respectively.

These time domain results have been transformed to the frequency domain by a Fourier transform. The combined results from the photodiode and r.f. detector have a 3 dB frequency of 30 GHz, as shown in figure 5.14. An estimate of the photodiode response, made by electro-optic sampling[58], has been used to correct the results for the diode response. The overall response of the system is 40 GHz 3 dB frequency, suggesting that this method could be used as a simple technique to measure high speed photodiodes.

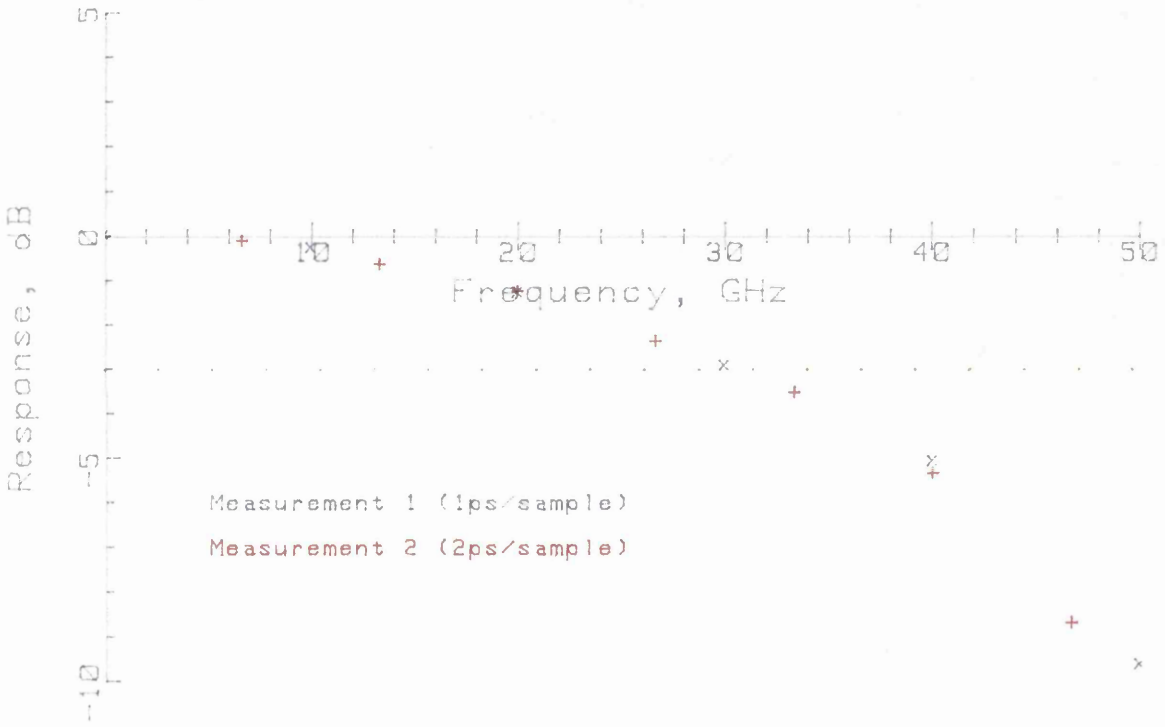

Figure 5.14. Measured combined frequency response of the correlation system and GaAs/ITO photodiode

A second experiment was performed using a similar photodiode which produced a *positive* electrical pulse. In this experiment no correlation peak could be found. This is believed to be due to the semiconductor response, which differs from the true square law detector at high signal levels.

The two experiments demonstrate that the electrical correlation technique can be used to measure high speed photodiodes but considerable care must be exercised in the choice of the r.f. power

sensor. r.f. detector diodes are not well suited for this application if the peak electrical signal is high.

Temporal measurements using a correlation system

Temporal measurements can be made using an electrical correlation system, provided that a suitable transfer standard photodiode is available. The result will be the response of the unknown device relative to the transfer standard reference.

Two sets of measurements must be made: the first is a cross-correlation of the two device responses and the second is the autocorrelation response of the reference device. These results can be deconvolved either by a fourier transform or a matrix technique. transformed to the frequency domain and deconvolved. Deconvolution is the inverse of the convolution operation. It is an unstable process, requiring some filtering to obtain a stable result. Both of these deconvolution techniques will be described in the following part of this thesis.

Discussion

The correlation technique offers the potential for measuring high speed photodiodes provided that a suitable source of picosecond optical pulses is available. The technique is limited by the range of the detected signal, which varies by about an octave, and the saturation/power dissipation limits of the device being tested. The method should be very cheap to implement as the detecting element is inexpensive.

5.4. CHAPTER CONCLUSION

Two correlation techniques have been described: the sampling oscilloscope and an electrical correlation method. The principle of operation and the limitations of each technique have been discussed.

The sampling oscilloscope is a convenient commercially available instrument. It is the easiest method for making temporal measurements in the 20+ ps regime.

The r.f. electrical correlation technique can be performed using an optical delay and a r.f. power meter. This method has the potential for measuring high speed photodiodes and is inexpensive to implement. The

temporal response of an unknown device can be obtained if a suitable risetime transfer standard photodiode is available.

6. HIGH ACCURACY MEASUREMENTS

6.1. INTRODUCTION

If high accuracy measurements, with uncertainties of less than ±0.5 dB, are to be made then the sources of the systematic uncertainty must be identified and corrections made. Many of the frequency reponse results shown in previous chapters have exhibited a ripple in the measured response. This effect is caused by the reflection of the microwave signals between the device being tested and the measurement system. The second major source of uncertainty is the calibration of the r.f. measurement system. This chapter will concentrate on the former problem as a discussion of accurate r.f. power measurement standards is beyond the scope of this thesis.

6.2. ELECTRICAL REFLECTIONS - THEORY

At high frequencies neither the measurement system nor the device being tested will be a perfect match to the impedance of the connecting line. The reflection coefficient ρ is defined as follows:

$$\rho(\omega) = \frac{V^-(\omega)}{V^+(\omega)} \qquad \text{(eq. 1)}$$

where V^+ is the amplitude of the travelling voltage wave incident on the device; V^- is the amplitude of the travelling voltage wave reflected from the device and ω is the frequency of the travelling wave.

The electrical reflection coefficient or *return loss* is normally measured using a vector network analyser such as a Hewlett Packard HP8510 or a Wiltron 360. These instruments normally provide the results in terms of *scattering parameters*. A good introduction to scattering parameters can be found in a number of texts[70,71]. The reflection coefficient of the photodiode (ρ_1) is equivalent to its output scattering parameter S_{22} and the reflection coefficient of the measurement system (ρ_2) is equivalent to its input scattering parameter S_{11}.

Consider the simple measurement arrangement shown in figure 6.1. The device under test has an electrical reflection coefficient ρ_1 at the

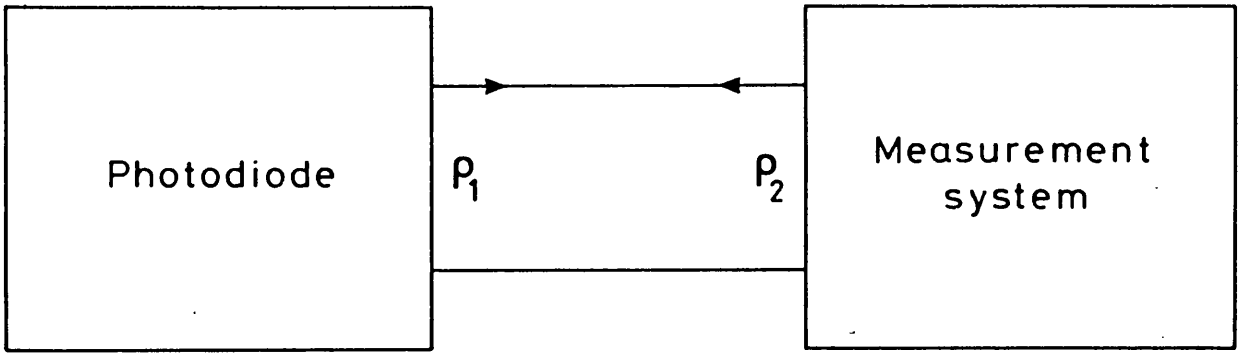

$$V_m = \frac{V_d}{(1 - \rho_1 \rho_2)}$$

Figure 6.1. Reflection of electrical signals between the measurement system and the device under test

measurement frequency ω, and the measurement system will have a reflection coefficient ρ_2 at this frequency. The parameters (ρ_1 and ρ_2) are both complex containing the magnitude and the phase of the reflected signal. The magnitude of the reflected signal will be less than unity ($|\rho|<1$).

The measured voltage V_m will be the sum of the true signal V_d and all the multiple reflections:

$$V_m = V_d \ (1 + \rho_1\rho_2 + (\rho_1\rho_2)^2 + (\rho_1\rho_2)^3 + \ldots) \qquad \text{(eq. 2)}$$

This expression can be rewritten in a more compact form:

$$V_m = \frac{V_d}{(1 - \rho_1\rho_2)} \qquad \text{(eq. 3)}$$

High speed photodiodes typically have a very poor electrical reflection coefficient. This is because in most designs, no attempt has been made to match the device to the line impedance. The measurement system will have a lower return loss (typically -10 dB or better[72]). The maximum uncertainty limits due to electrical reflection can be calculated from the following expressions:

$$E_{max} = -20 \log_{10}(1 - |S_{11}S_{22}|) \quad \text{(eq. 4)}$$

$$E_{min} = -20 \log_{10}(1 + |S_{11}S_{22}|) \quad \text{(eq. 5)}$$

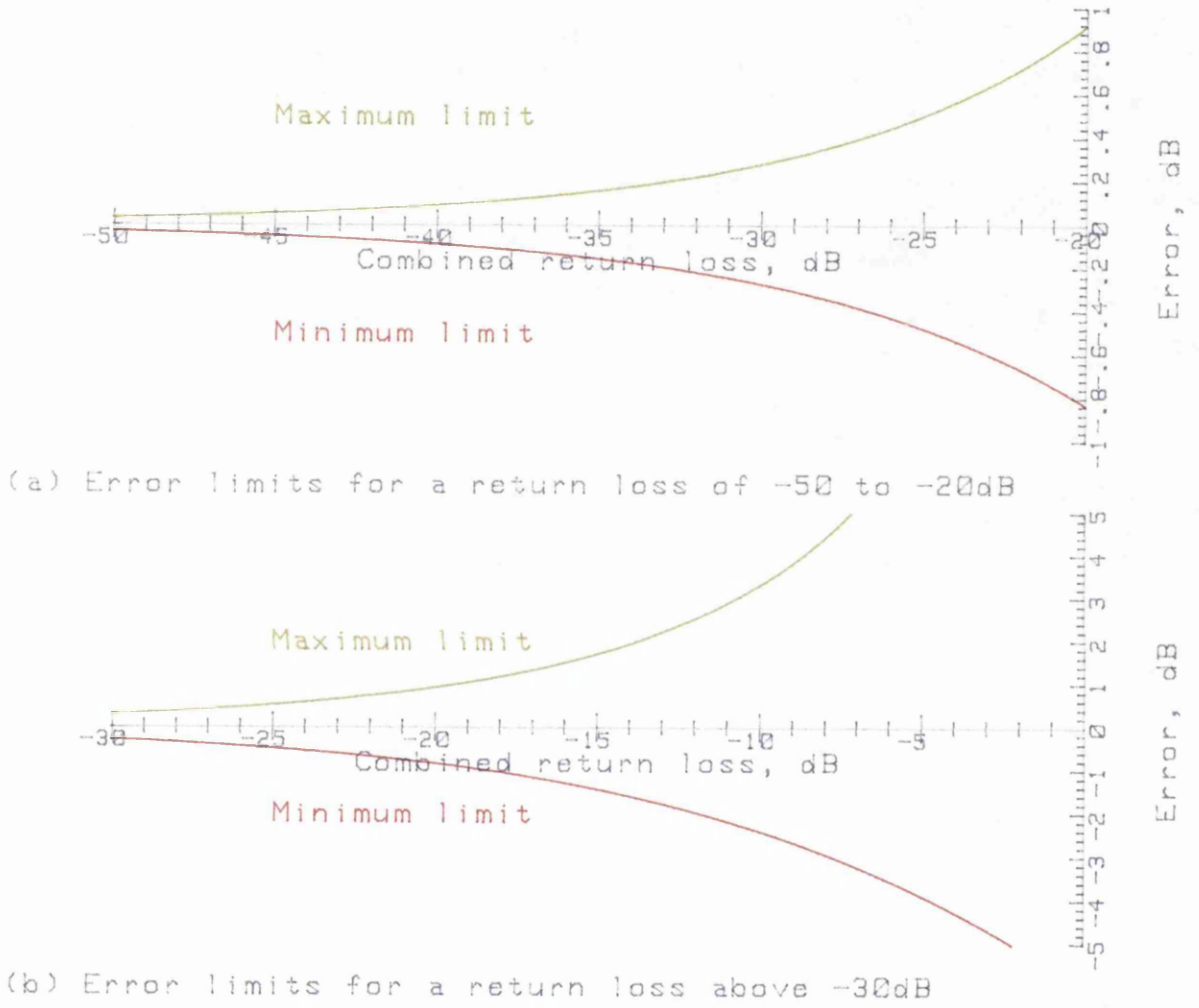

Figure 6.2. Uncertainties due to electrical reflections

Figure 6.2. shows the variation of the minimum and maximum uncertainties as a function of the combined return loss $|S_{11}S_{22}|$ in dB. The results are plotted for a combined return loss in the range -50 dB to -20 dB and for a combined return loss of greater than -30 dB. The uncertainty in the result for a return loss of -20 dB is greater than ±0.8 dB. To improve the accuracy of the measurements a correction must be made to reduce these uncertainties. Measurements must be made of the electrical reflections from both the measurement system and the device

under test. These results can then be used, together with equation 3, to calculate the correction factor.

6.3. PHOTODIODE MEASUREMENTS CORRECTED FOR ELECTRICAL REFLECTIONS

To illustrate the method outlined in the previous section two high speed GaInAs photodiodes - supplied on loan by *J Schlafer* of GTE Laboratories, USA - were measured using the rotating polarisation heterodyne system described in chapter 3. These diodes have a circular active region approximately 20 μm in diameter. The measured responses of the photodiodes are shown in figure 6.3a and b for the D230k10 and D230k12 devices respectively. These results are not corrected for electrical reflections and the ripple in the result becomes increasingly more apparent at frequencies above 18 GHz.

A Hewlett Packard HP437B r.f. power meter with a HP8485D power sensor was used to calibrate the sensitivity of the measurement system. This instrument is calibrated at frequencies of up to 26.5 GHz. Above this frequency an estimate of the performance was made, based on typical figures provided by the manufacturers (26.5 - 34 GHz).

Measurements of the return loss were made for both the photodiodes and for the r.f. detector, and bias tee and a correction factor was calculated from these results. A bicubic spline[73] was fitted to these corrected, measured optical results to smooth any remaining ripples. The rms error of the fit to the spline curve was 0.26 dB for the D230k10 device and 0.24 dB for the D230k12 device.

The optically measured results (S_{21}), corrected for the electrical reflections and the system sensitivity are plotted in figures 6.4a and 6.5a, together with the curve fitted to the results. The photodiode return loss (S_{22}) and the return loss of the measurement system (S_{11}) have also been plotted in this figure. The correction factors are plotted in figures 6.4b and 6.5b on a larger scale. At frequencies below about 18 GHz the correction is typically below ±0.5 dB. The correction factor shown in these curves would be typical of the errors that would be encountered in an uncorrected measurement system with equivalent return loss performance.

The two photodiodes had 3 dB frequencies of 30.8 ±0.5 GHz for the D230k10 device and 26.9 ±0.5 GHz for the D230k12 device. The

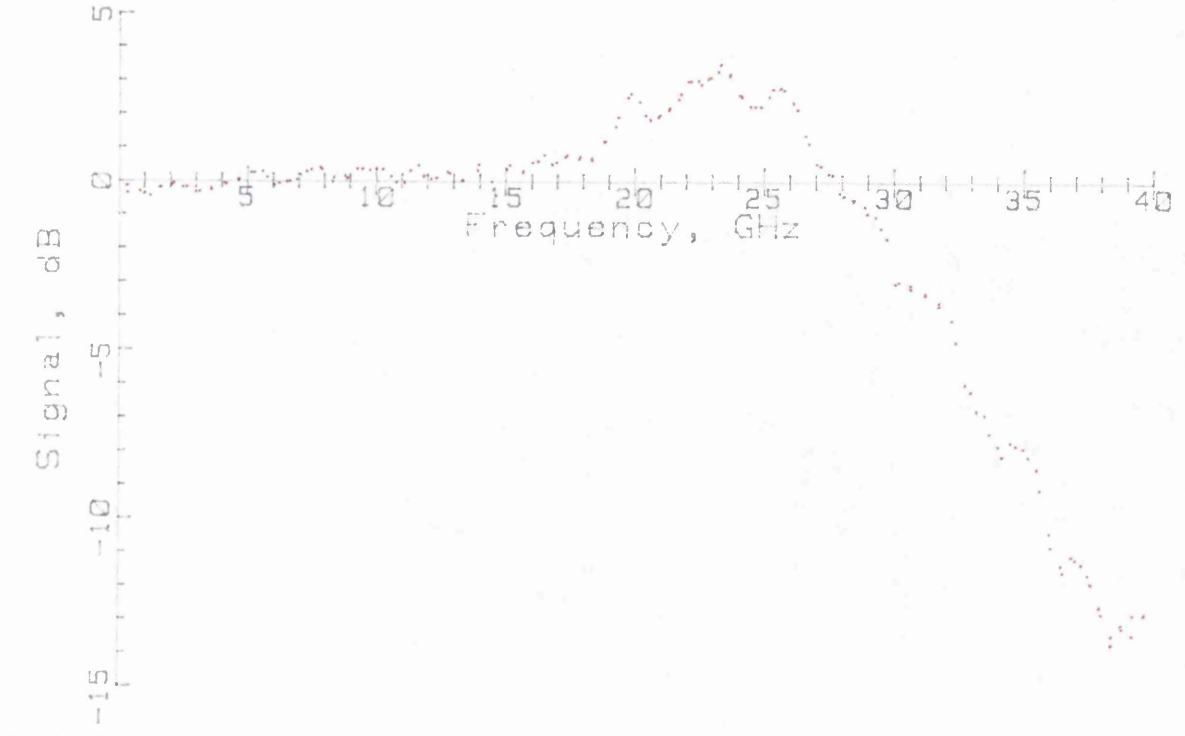

(a) Measured response of GTE D230k10 photodiode

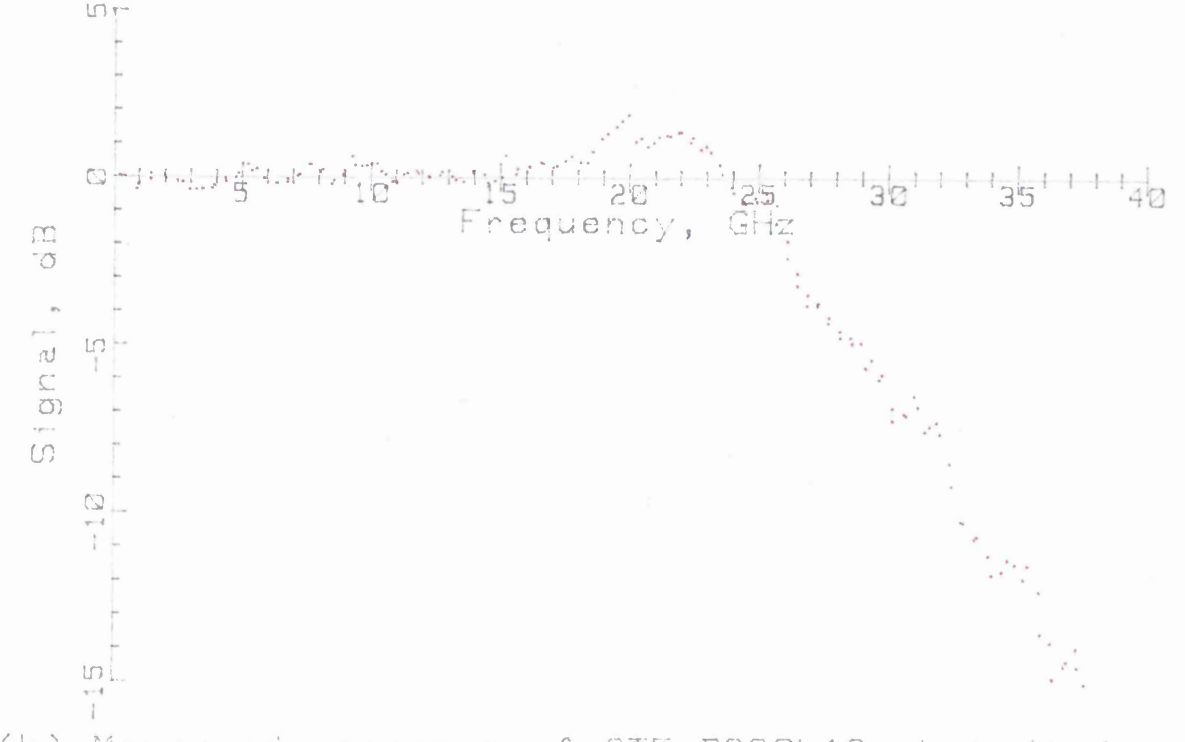

(b) Measured response of GTE D230k12 photodiode

Figure 6.3. Measured responses of the GTE D230k10 and D230k12 photodiodes at 1532 nm, not corrected for electrical reflections.

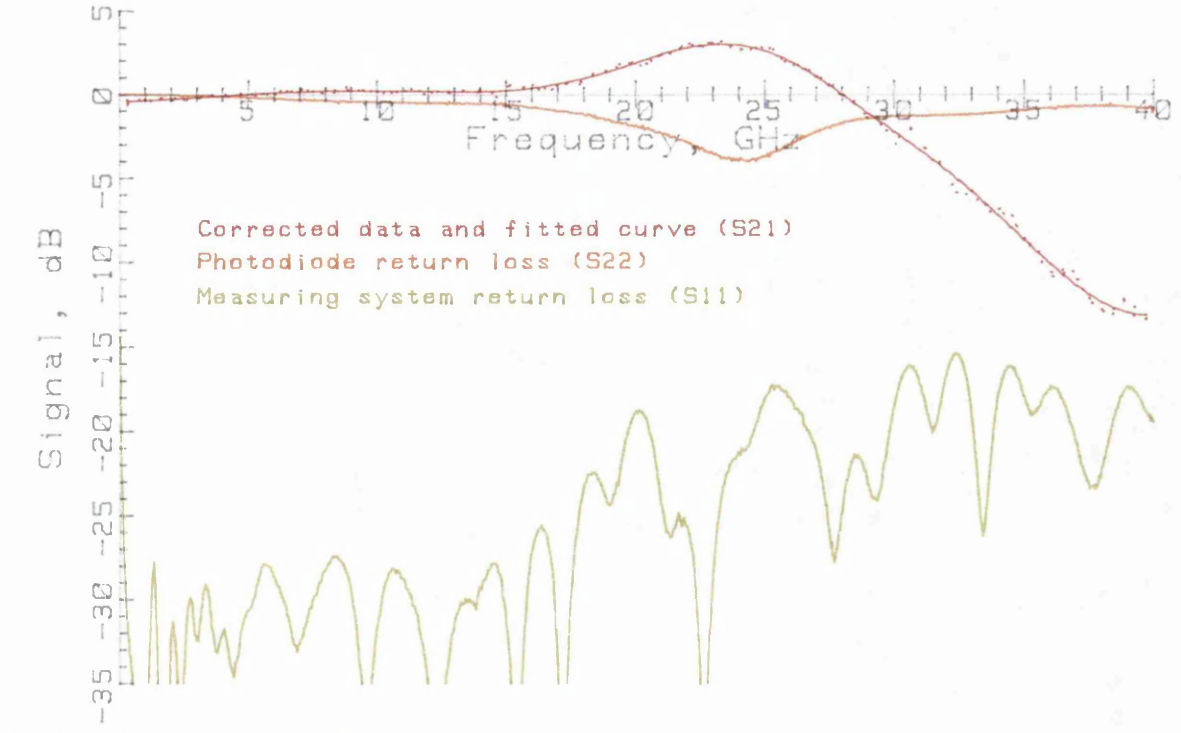

(a) Measured and corrected responses

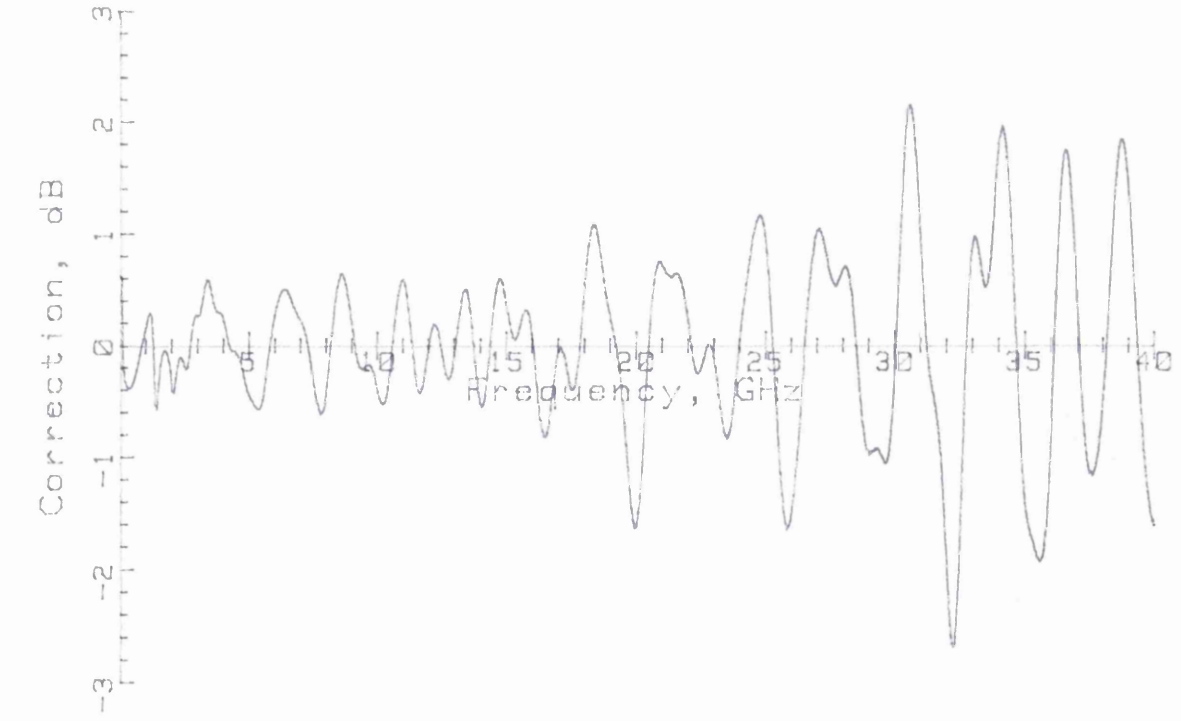

(b) Correction factor

Figure 6.4. Measured results for the GTE D230K10 photodiode at 1532 nm, corrected for electrical reflections

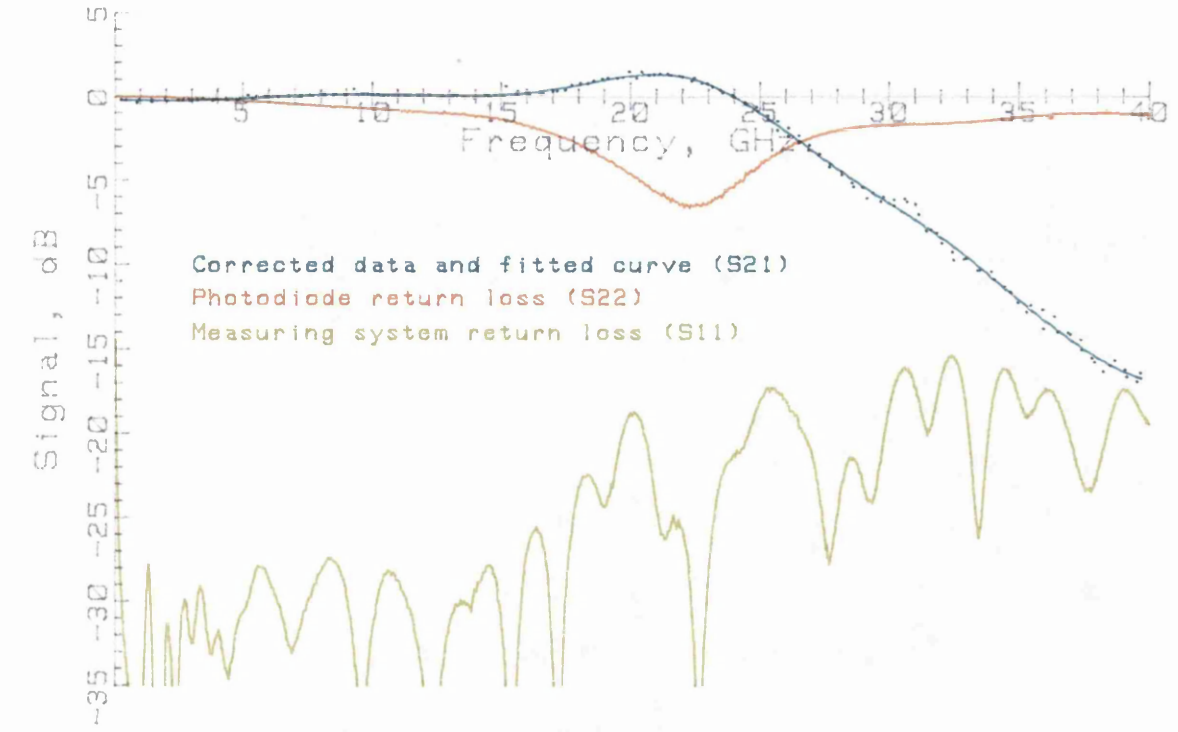

(a) Measured and corrected responses

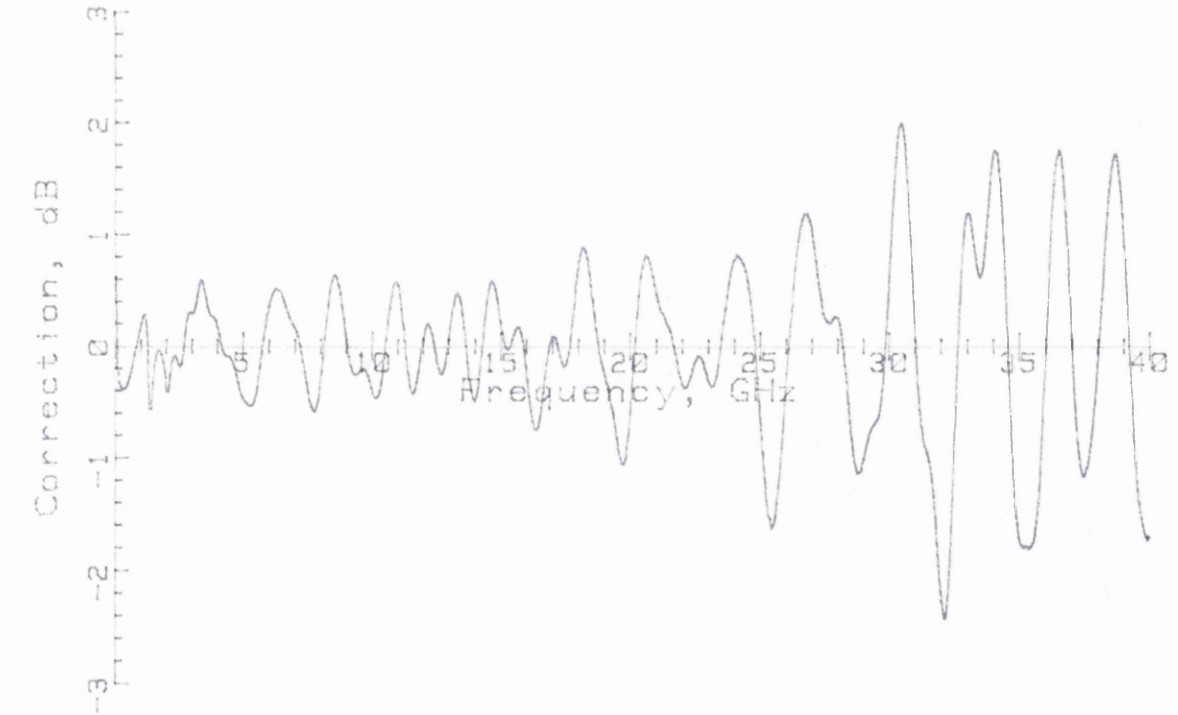

(b) Correction factor

Figure 6.5. Measured results for the GTE D230K12 photodiode at 1532 nm, corrected for electrical reflections

uncertainties have been calculated assuming an error of ±0.3 dB in the -3 dB level. If no corrections were made the error in the -3 dB level could be as great as ±1.1 dB, giving uncertainty limits of ±1.8 GHz. All the uncertainties are quoted at the 95% confidence level.

6.4. DISCUSSION AND CHAPTER CONCLUSION

The results show that a considerable improvement in the measurement uncertainties can be achieved by applying a correction factor derived from return loss measurements of both the device under test and the measurement system.

The corrections will not be exact for three reasons: firstly the accuracy of the reflection coefficients will depend on the accuracy of the measurement standards; secondly the measurements will not, in general, be performed under the same enviromental conditions (e.g. temperature and humidity) which may affect the results, especially at the higher frequencies; and finally the measurement frequencies of the optical and electrical measurements will differ slightly. The optical beat signal will have a spectral width of several tens of megahertz and the centre frequency may not be known exactly. This contrasts with the return loss measurement where the source may be a synthesizer.

The residual uncertainties due to these sources of error have not been quantified at this time and further work will be required to do this. The considerable improvement in the quality of the corrected results, compared with the original measurements, justifies the use of the more complicated procedure.

In the example chosen, the peak in the measured optical response occurs very close, in frequency, to the dip in the return loss for the two diodes. The dip is believed to be due to a resonance formed by the photodiode junction capacitance and the mounting inductance. It may therefore be possible to use both the return loss results and the optical measurements to fit values to a model of the device. This would allow a good estimate to be made for the *absolute* phase response of the device. Further work will be required to verify this theory and to determine the uncertainty limits that can be achieved.

7. DISCUSSION, COMPARISON OF TECHNIQUES AND CONCLUSION FOR PART 1

7.1. INTRODUCTION

In this chapter comparisons between the different techniques will be presented and the planned future research work to improve this important area of metrology will be outlined. In the previous chapters of this part of the thesis a number of different measurement techniques and methods to enhance the accuracy of the results have been described. Three novel methods for measuring photodiode frequency responses have been presented and a heterodyne system which returns both the magnitude and the phase responses of an unknown photodiode has been described.

7.2. COMPARISON OF MEASUREMENT TECHNIQUES

The comparison of measurement techniques is important as it gives confidence in results obtained with different systems. A comparison of different techniques also helps to identify systematic errors and weaknesses which might otherwise remain undetected.

A number of authors have compared different measurement methods: *Kawanishi et al*[10] has compared the heterodyne and comb harmonic methods and *Eichen et al*[46,47] have compared the FM sideband and the comb harmonic techniques.

In chapter 3 of this thesis a number of different heterodyne systems were compared using the AT&T and Plessey #20 photodiodes. The results indicated that a system using continuously tunable lasers was preferable to a system with external cavity lasers. The results also showed that systems based of DFB lasers and using a spectrum analyser as the r.f. detector were prone to serious systematic errors.

A comparison of the magnitude and phase responses of the Plessey #20 photodiode, measured by the vector heterodyne system and by deconvolution of pulsed laser diode measurements, was also presented in chapter 3. The agreement between the two techniques was reasonable. This is believed to be the first report of such a comparison.

7.3. COMPARISON OF THE INTEGRATED OPTIC MODULATOR (1.3 μm), FM SIDEBAND (1.3 μm) AND ROTATING POLARISATION HETERODYNE (1.53 μm) SYSTEMS

An informal intercomparison was performed with GTE Laboratories Inc., USA, to measure the performance of three GaInAs photodiodes. The measurements were performed using the FM sideband technique (1.3 μm) at GTE and by the Integrated Optic Modulator system (1.3 μm) and rotating polarisation DFB heterodyne system (1.53 μm) at NPL. These two systems are described in chapters 3 and 4 respectively and a brief account of the GTE system is given in chapter 3. The results measured using the heterodyne system were corrected for errors caused by electrical reflections (chapter 6). This considerably improved the smoothness of the results. The measurements made with the modulator system could not be corrected in this manner because the r.f. power was detected using a spectrum analyser. The electrical reflection coefficient of such an instrument can only be correctly measured if the network analyser and the spectrum analyser are tuned to the same frequency.

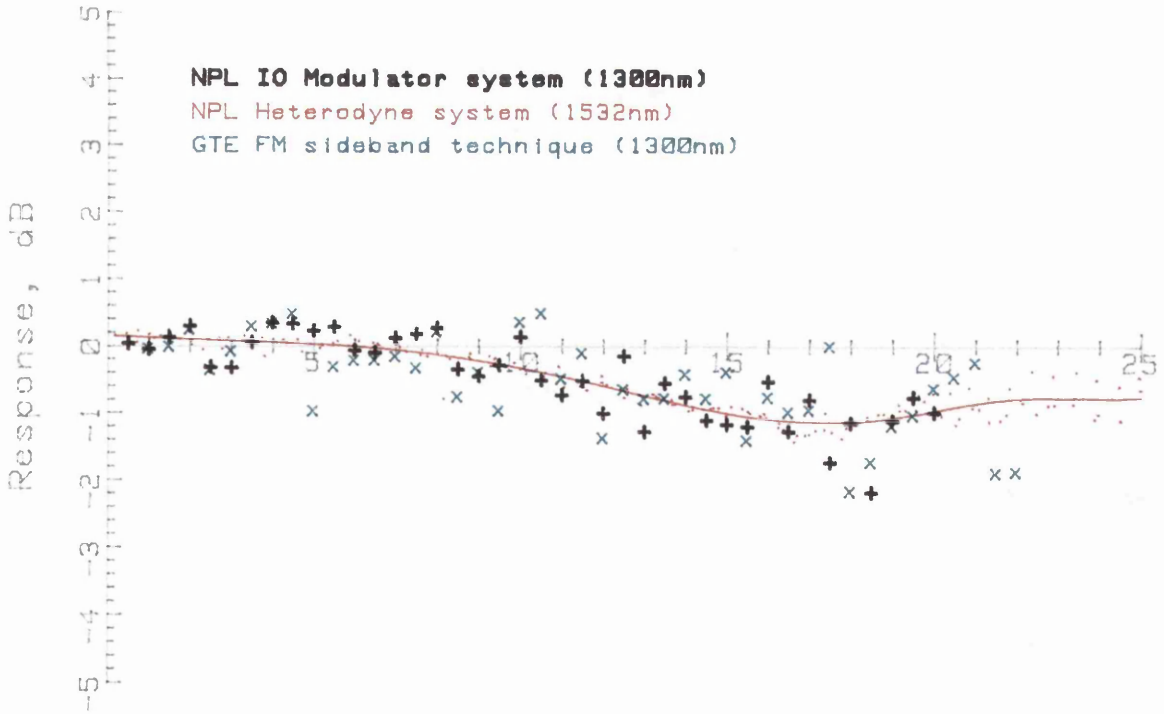

Figure 7.1. GTE D230k4 photodiode at 3 V bias, measured by the Integrated Optic Modulator (1.3 μm), FM sideband (1.3 μm) and Rotating Polarisation Heterodyne (1.53 μm) systems

The results obtained with the diodes, designated D230k4, D230k10 and

D230k12, are shown in figures 7.1 - 3. The frequency response of the D230k4 diode, measured with the heterodyne system extends to more than 40 GHz.

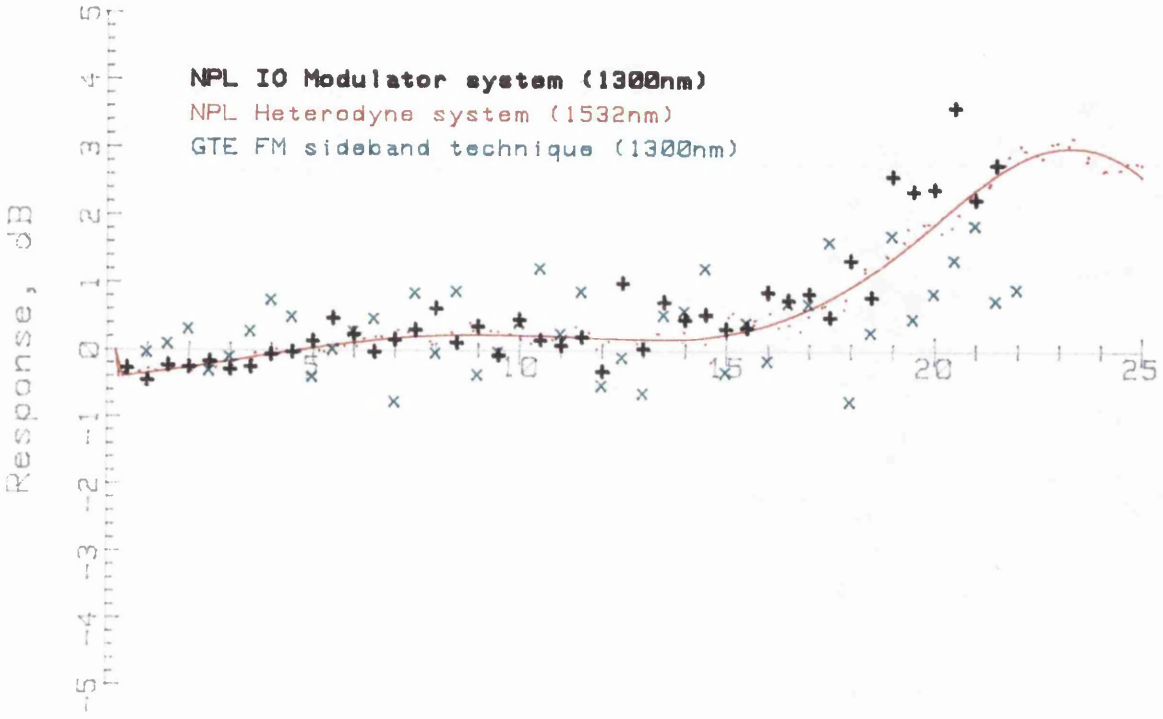

Figure 7.2. GTE D230k10 photodiode at 4 V bias, measured by the Integrated Optic Modulator (1.3 μm), FM sideband (1.3 μm) and Rotating Polarisation Heterodyne (1.53 μm) systems

The general agreement between the sets of results is very good but two points can be noted: firstly, the scatter on the results not corrected for electrical reflections is significantly greater than the scatter of the corrected results; and secondly, at high frequencies the results measured with the FM sideband technique are in general lower than those measured by the modulator system. This may be a systematic effect and should be investigated further.

In conclusion the comparison of the results shows that the methods agree to a good accuracy, with differences of less than ±1 dB typically, but the results also show the importance of correcting for electrical reflection errors.

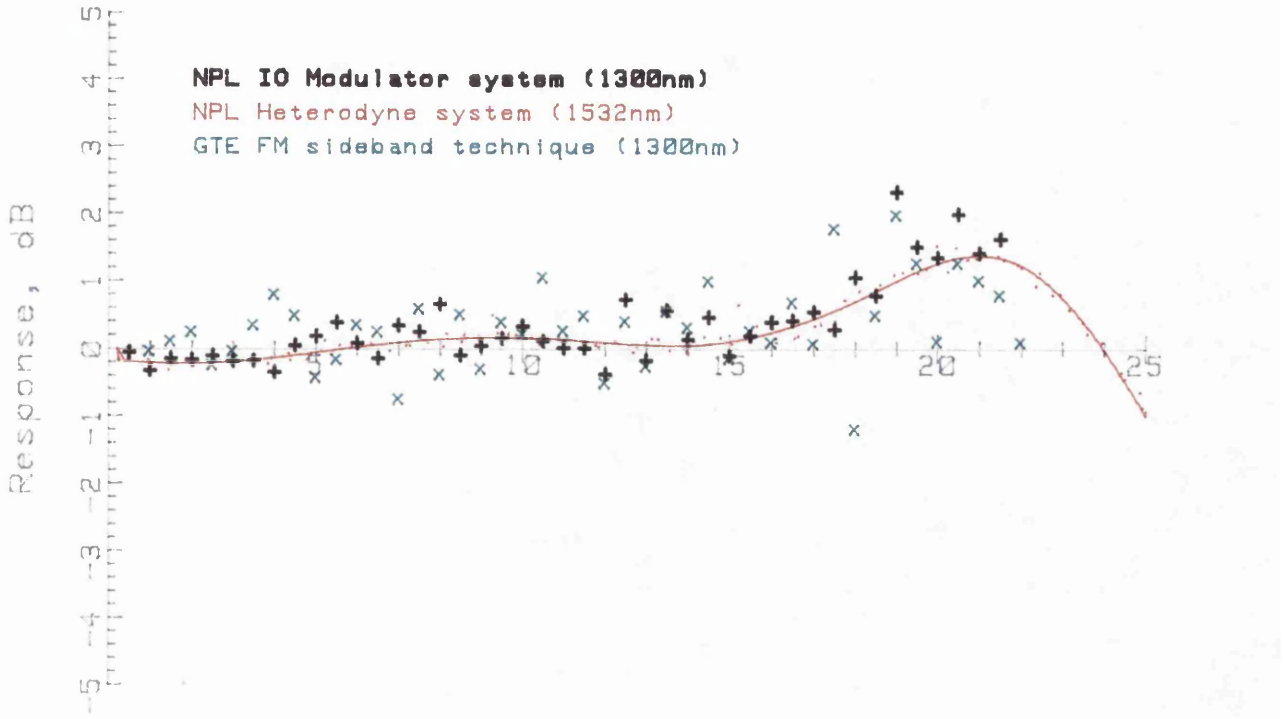

Figure 7.3. GTE D230k12 photodiode at 4 V bias, measured by the Integrated Optic Modulator (1.3 μm), FM sideband (1.3 μm) and Rotating Polarisation Heterodyne (1.53 μm) systems

7.4. FURTHER WORK

Further work will be required to improve the measurement systems described in this thesis. The details of the work required to improve each of these systems is given in the corresponding chapter conclusion. At a more fundamental level, the ultimate accuracy of the frequency domain systems is dependent on the accuracy of the r.f. power calibration. This is an area of metrology that will require attention if the absolute accuracy of measurements is to be reduced below ±0.5 dB. The power standards used at present are traceable to American national standards. It is intended that traceability to UK national standards should be obtained shortly so that the systems can be offered as a measurement service.

Measurement comparisons between different systems are important as they can be used to identify systematic errors in the measurement systems. The comparisons also give confidence in the different measurement techniques. Following the successful intercomparison with GTE inc, USA, a further international round-robin of photodiode frequency response

measurements has been organised. Eight participants in three countries will measure the frequency response of two GaInAs photodiodes. The measurements will be made at either 1.3 or 1.5 μm, depending on the systems available at each establishment. The measurements are expected to take approximately eight months.

8. REFERENCES FOR PART 1

1. *N Bracewell*: 'The Fourier Transform and its application ', 2nd edition, McGraw-Hill, ISBN 0-07-Y66196, 1978.

2. *G Eisenstein, R S Tucker, U Koren and S Korotky*: 'Active Modelocking characteristics of InGaAsP-Single Mode Fiber composite cavity lasers', IEEE J. of Quantum. Electron., Vol. **QE-22** (1), pp. 142 - 148, January 1986.

3. *C A Burrus, J E Bowers and R S Tucker*: 'Improved very high speed packaged InGaAs PIN Punch-Through photodiode', Electron. Letts., Vol. **21** (7), pp. 262 - 263, March 1985.

4. *D G Parker, P G Say and A M Hansom*: '110 GHz High-efficiency photodiodes fabricated from Indium Tin Oxide/GaAs', Electron. Letts., Vol. **23** (10), pp. 527 - 528, 1987.

5. *J G Edwards and R Jefferies*: 'Analysis and measurement of the speed and linearity of silicon photodiodes for measuring short laser pulses', J. of Phys. E, Vol. **6** pp. 841 - 853, 1973.

6. *L Piccari and P Spanno*: 'New method for measuring ultrawide frequency response of optical detectors', Electron. Letts., Vol. **18** (3), pp. 116 - 118, February 1982.

7. *K M Abramski*: 'Frequency response of photodetectors measured by means of heterodyne interferometric techniques of detection', Optica Applicata, Vol. **XIII** (3), pp. 223 - 229, 1983.

8. *H Blauvelt, G Thurmond, J Parsons, D Lewis and H Yen*: 'Fabrication and characterisation of GaAs Schottky barrier photodetectors for microwave fiber optic links', Appl. Phys. Letts., Vol. **45** (3), pp. 195 - 196, 1984.

9. *R D Esman and D L Rode*: 'Full beam asynchronous GaAs laser heterodyne', IEEE J. of Quantum. Electron., Vol. **QE-21** (1), pp. 3 - 5, 1985.

10. *S Kawanishi and M Saruwatari*: 'Wideband frequency response measurement of photodetectors using optical heterodyne detection technique', Electron. Letts., Vol. **22** (6), pp. 337 - 338, March 1986.

11. *R Schimpe, J E Bowers and T L Koch*: 'Characterisation of frequency response of 1.5 μm InGaAsP DFB laser diode and InGaAsP PIN photodiode by heterodyne measurement technique', Vol. 22 (9), pp. 453 - 454, April 1986.

12. *T S Tan, R L Jungerman and S Elliott*: 'Calibration of optical receivers and modulators using an optical heterodyne technique", IEEE MTT-S symposium.

13. *A J Moseley and A C Carter, D A Humphreys*: 'High speed InGaAs/InP photodiodes for application to 40 GHz", SPIE O-E Fiber/Lase'88 conference, Vol. 995, pp. 61 - 67, September 1988.

14. *M Makiuchi, O Wada, T Kumai, H Hamaguchi, O Aoki and Y Oikawa*: 'Small junction area GaInAs/InP pin photodiode with monolithic microlens', Electron. Letts., Vol. 24 (2), pp. 109 - 110, January 1988.

15. *T J Kane and R L Bayer*: 'Monolithic Unidirectional Single Mode Nd:YAG Ring Laser', Optics Letts., Vol. 10 (65), 1985.

16. *T J Kane, A C Nilsson and R L Byer*: 'Frequency Stability and Offset Locking of a Laser Diode Pumped Nd:YAG Monolithic Nonplanar Ring Oscillator', Optics Letts., Vol. 12 (175), 1987.

17. *K Otsuka, H Li and H R Telle*: 'CW Nd - lasers with broad tuning range', Optics Commun., Vol. 63 (1), pp. 55 - 60, July 1987.

18. *K R German and C R Pollack*: '$(F_2^+)_H$ color-centre laser operation in NaCl:OH with simultaneous 1.06 and 0.53 μm pumping', Optics Letts., Vol. 12 (7), pp. 474 - 476, July 1987.

19. *K Utaka, S Akiba, K Sakai and Y Matsushima*: 'λ/4-shifted InGaAs/InP DFB lasers', IEEE J. of Quantum. Electron., Vol. QE-22, pp. 1042 - 1051, July 1986.

20. *A J Collar, S J Clements, B R Butler, D J Moule, C J Armistead, J E A Whiteaway and A Rashid*: 'DFB lasers fabricated by electron beam lithography for high density WDM systems', ECOC'87 (Helsinki), Vol. I, pp. 70 - 73, September 1987.

21. *C E Zah, C Caneau, S G Menocal, P S D Lin, A S Gozdz, A Faviro, and T P Lee*: 'Narrow linewidth 1.3 μm DFB-DCPBH lasers with λ/4 shifted first-order gratings fabricated by electron beam lithography using a fast new resist', Electron. Letts., Vol. **24** (2), pp. 94 - 95, January 1988.

22. *Vahala, L C Chiu, S Margalin and A Yariv*: Appl. Phys. Letts., Vol. **42** (63), 1985.

23. *L D Westbrook*: 'Dispersion of linewidth-broadening factor in 1.5 μm laser diodes', Electron. Letts., Vol. **21** (22), pp. 1018 - 1019, October 1985.

24. *S Ogita, M Yano and H Imai*: 'Theoretical calculation of the linewidth enhancement factor of DFB lasers', Electron. Letts., Vol. 22 (11), pp. 580 - 581, May 1986.

25. *I F Lealman, D M Cooper, S Cole, A J Cockburn, P Spurdens and P W A McIlroy*: 'Properties of BH Distributed Feedback lasers grown by atmospheric MOVPE', SIOE'88 conference (Cardiff), Abstract only.

26. *K -Y Liou, N K Dutta and C A Burrus*: 'Linewidth - narrowed Distributed Feedback injection lasers with long cavity length and detuned Bragg wavelength', App. Phys. Letts., Vol. **50** (9), pp. 489 - 491, 1987.

31. *B Glance, O Scaramucci, K L Koch and J Stone*: 'Optical frequency synthesiser', Electron. Letts., Vol. **25** (17), pp. 1193 - 1195, August 1989.

27. *T L Koch and R A Linke*: 'Effects of nonlinear gain reduction on semiconductor laser wavelength chirping', Appl. Phys. Letts., Vol. **48** (10), pp. 613 - 615, March 1986.

28. *S Murata, I Mito and K Kobayashi*: 'Tuning ranges for 1.5 μm wavelength tunable DBR lasers', Electron. Letts., Vol. **24** (10), pp. 577 - 579, May 1988.

29. *T P Lee*: 'Narrow linewidth frequency tunable InGaAsP lasers for coherent communications applications', OE Fiber/Lase'88 conference (Boston), SPIE Vol. **988**, pp. 237 - 248, September 1988.

30. *S L Palfrey*: 'Device design for monolithic narrow linewidth semiconductor lasers', OE Fiber/Lase'88 conference (Boston), SPIE Vol. **988**, paper 34, September 1988.

32. *R Wyatt and W J Devlin*: '10 kHz linewidth 1.5 μm InGaAsP external cavity laser with 55 nm tuning range', Electron. Letts., Vol. **19** (3), pp. 110 - 112, February 1983.

33. *J Mellis, S A Al-Chalabi, K H Cameron, R Wyatt, J C Regnault, W J Devlin, and M C Brain*: 'Minature packaged external cavity laser with 50 GHz continuous electrical tuning range', Electron. Letts., Vol. **24**, pp. 988 - 989, August 1988.

34. *M de Labachelie, K Diomande, P Cerez*: 'Some applications of extended-cavity semiconductor lasers', Poster session, Fourth Symposium on Frequency Standards and Metrology, Ancona, Italy, September 1988.

35. *S Sampei, H Tsuchida, M Ohtsu and T Tako*: 'Frequency stabilization of AlGaAs semiconductor lasers with external grating feedback', Japanese J. of Appl. Phys., Vol. **21** (4), pp. L258 - L260, April 1983.

36. *P B Coates*: 'External cavity stabilization of gain - guided laser diodes for metrological purposes', J. Phys. E: Sci. Instrum., Vol. **21**, pp. 812 - 816, 1988.

37. *S K Korotky, E A Marcatili, G Eisenstein, J J Veselka, F Heismann and R C Alfreness*: 'Integrated optic, narrow linewidth laser', Appl. Phys. Letts., Vol. **49** (1), pp. 10 - 12, July 1986.

38. *C Park, J Hankey, P J Williams, N Weston and B T Debney*: 'DFB laser sources for coherent optical communication systems', IEE colloquium on 'High capacity fibre optic systems', Digest **1987/23**, paper 8, 1987.

39. *A R Chraplyvy et al*: 'Simple narrow linewidth 1.5 μm InGaAs DFB extended cavity laser', Electron. Letts., Vol. **22** (2), pp. 88 - 89, 1986.

40. *H R D Sunak and C Engbert*: 'Design of distributed feedback laser-based external cavity structures for coherent communications', OE Fiber/Lase'88 conference (Boston), SPIE Vol. **988**, pp. 250 - 258, September 1988.

41. *Hewlett Packard*: 'Test and measurement catalogue 1990', p. 122, 1990.

42. *A J Lucero, R W Tkach and R R M Derosier*: 'Distortion of the frequency modulation spectra of semiconductor lasers by weak optical feedback', Electron. Letts., Vol. **24** (6), pp. 337 - 338, March 1988.

43. *A R Chraplyvy, D Marcuse, R W Tkach*: 'Effects of Rayleigh backscattering from optical fibers on DFB laser wavelength', IEEE J. of Lightwave Tech., Vol. **LT4** (5), pp. 555 - 559, May 1988.

44. *R W Tkach and A R Chraplyvy*: 'Regimes of feedback effects in 1.5 μm Distributed feedback lasers', IEEE J. of Lightwave Tech., Vol. **LT4** (11), pp. 1655 - 1661, November 1988.

45. *D M Baney and W V Sorin*: 'Measurement of a modulated DFB laser spectrum using gated delayed self-homodyne techniques', Electron. Letts. **24** (11), pp. 669 - 670, May 1988.

46. *E Eichen and A Silletti*: 'Bandwidth measurements of ultra high frequency optical detectors using interferometric FM sideband technique', J. of Lightwave Tech., Vol. **LT5** (10), pp. 1377 - 1381, October 1987.

47. *E Eichen and A Silletti*: 'Nonlinear generation of high power millimeter wave optical intensity modulation ', O/E Fiber/Lase'88 conference (Boston), SPIE Vol. **995**, pp. 38 - 46, September 1988.

48. *M Ohtsu*: 'Realisation of ultra high coherence in semiconductor lasers by negative electrical feedback', J. of Lightwave Tech., Vol. **JLT-6** (2), pp. 245 - 256, February 1988.

49. *O Ishida, H Toba and Y Tohmori*: '0.04 Hz relative optical frequency stability in a 1.5 μm Distributed-Brag-Reflector (DBR) laser', Photonics Tech. Letts., Vol. **1** (12), pp. 449 - 451, December 1989.

50. *S Uehara*: 'Calibration of optical modulator frequency response with application to signal level control', Applied Optics, Vol. **17**, pp. 68 - 71, 1978.

51. *D D Hall and A Donaldson:* 'Advances in optical modulators for microwave transmission', IEE colloquium, 'Integrated Optics', 1989/93, paper 3, June 1989.

52. *D L Switzer and S P James*: 'A DC to 20 GHz externally modulated fibre-optic link', IEE colloquium, 'Optical control and generation of microwave and millimetre-wave signals', 1989/61, paper 1, April 1989.

53. *R G Walker, I Bennion and A C Carter*: 'Low-voltage 50 Ω, GaAs/AlGaAs travelling wave modulator with bandwidth exceeding 25 GHz', Electron. Letts., Vol. 25 (23), pp. 1549 - 1550, November 1989.

54. *GEC-Marconi advanced optical products*, Marconi Research centre, West Hanningfield Road, Great Baddow, Chelmsford, Essex, CM2 8HN, England.

55. *D W Dolfi, M Nazarathy and R L Jungerman*: '40 GHz electro-optic moduator with 7.5 V drive voltage', Electron. Letts., Vol. 24 (9), pp. 528 - 529, April 1988.

56. *Hewlett Packard*: 'Test and measurements catalogue 1990', p. 313.

57. *Tektronix*: '1990 catalogue', p. 72., 1990.

58. *D Henderson*: 'Measurement of the temporal response of a picosecond sampling oscilloscope by optoelectronic techniques', PhD Thesis, University College London, London University, July 1989.

59. *W M Grove*: 'Sampling for oscilloscopes and RF systems', IEEE Trans. MTT, Vol. **MTT-14**, pp. 629 - 635, 1966.

60. *J R Andrews*: 'Comparison of sampling oscilloscopes with <35 ps transition duration', Technical digest of the topical meeting on picosecond electronics and optoelectronics, Incline Village, Nevada, USA, 1987.

61. *G Frye*: 'A new approach to fast gate design', Tektronix service scope, Tektronix inc, Beaverton, Oregon, USA, 1970.

62. For a discussion on a commonly used sampling oscilloscope see, for example, 'S-4 sampling head instruction manual', sections 3.2 to 3.4, Tektronix inc, Beaverton, Oregon, USA.

63. *B K Garside and R E Park*: 'Lasers on the fast track: achieving picosecond and subpicosecond pulses', Photonics spectra, August 1982.

64. *K Y Lau*: 'Gain switching of semiconductor injection lasers', App. Phys. Lett., Vol. 52 (4), pp. 257 - 259, January 1988.

65. *D Henderson and J M Williams*: 'Notes on the use of the Tektronix S-53 trigger recogniser', NPL memorandum, **DES-55**, 1986.

66. *J R Andrews and W L Gans*: 'Pulsed wavemeter timing reference for sampling oscilloscope calibrations', IEEE Trans. Instrum. Meas., Vol. **IM-24**, p. 82, 1975.

67. *N S Nahman and M E Guillaume*: 'Deconvolution of Time Domain Waveforms in the presence of noise', NBS Tech. note, 1047, October 1981.

68. *P Paulus and D Jäger*: 'New correlation technique for measuring short electrical pulses with picosecond time resolution', App. Phys. Lett., Vol. 48 (22), pp. 1550 - 1551, June 1986.

69. *Hewlett Packard*: 'Fundamentals of RF and microwave power measurements', Aplication note **64-1**, August 1977.

70. *F F Kuo*: 'Network analysis and synthesis', 2nd edition, John Wiley & sons, Chapter 14, 1966.

71. *Hewlett Packard*: Instrument training course, 8510A + 24D.

72. *Hewlett Packard*: 'HP8566A spectrum analyser operating and service manual', p I-13, March 1980.

73. *M Cox*: 'Practical spline approximation', NPL report, **DITC 1/82**, ISSN 0143-7348, February 1982.

PART 2

NUMERICAL TECHNIQUES TO IMPROVE THE ACCURACY OF PICOSECOND ELECTRICAL MEASUREMENTS

1. INTRODUCTION

The introduction of computer controlled instrumentation over the past fifteen years has considerably improved measurement science. In the area of picosecond electrical metrology, the ability to capture a waveform and store it on a computer has allowed the use of numerical techniques to improve the accuracy of the result. The work carried out by the waveform metrology group at the National Institute of Standards & Technology (NIST), formerly the National Bureau of Standards (NBS), has had a considerable impact in this area. In this part of the thesis numerical techniques to improve accuracy and interpretability of photodiode measurements are presented.

Photodiode measurements made using different pulsed laser diode sources may be difficult to compare because the laser pulse shapes vary. The measured waveform will be the convolution of the instrument, laser and detector responses. Deconvolution is a technique which separates the response of the device being tested form the response of the instrument. In chapter 2 deconvolution techniques are used to transform the laser pulse shape and instrumental response to a near Gaussian, so that the results can be readily compared. The method has been extended to allow the simultaneous deconvolution of multiple sets of data.

In chapter 3 a novel measurement strategy has been used to determine the uncertainty between the trigger and measured signal. This uncertainty, known as jitter, distorts the measured waveform in a manner that cannot be removed by averaging. The distortion of the waveform by the noise and jitter has been assessed using synthetic data. This analysis serves two purposes: firstly to show the effect of the noise and jitter in a qualitative manner, and secondly to provide a known reference so that algorithms to remove the jitter can be assessed. An algorithm which corrects the distortions introduced by the jitter is presented. This technique has been used to remove the effects of jitter from both synthetic and measured data sets.

2. DECONVOLUTION OF SIGNALS IN THE PRESENCE OF NOISE

2.1. INTRODUCTION

A measurement system may contain elements that are not ideal and tend to mask the response of the device being tested. These effects cannot be completely eliminated but can be reduced by the use of signal processing techniques. The measured parameter will be a convolution of the true function with the instrument response as shown in equation 1:

$$z(t) = \int_{-\infty}^{t} x(t - \tau)y(\tau)\, d\tau \qquad \text{(eq. 1)}$$

where z(t) is the measured response; y(t) is the instrument function and x(t) is the true response.

This may be written in a more convenient shorthand notation (eq. 2):

$$z = x^{*}y \qquad \text{(eq. 2)}$$

where * denotes the convolution operation.

We are presented therefore with an integral equation problem. We wish to determine the response of the unknown device from the measured response z(t) and the instrument response y(t). The instrument response y(t) is known either from other measurements or from modelling.

Inverse convolution or deconvolution problems occur in a number of areas of physics and engineering. In this work the aim is to use deconvolution techniques to improve the measurement of photodiode temporal responses on a picosecond timescale. The resultant waveform will be more amenable to interpretation allowing comparisons with results obtained using different measurement systems to be performed.

The convolution operation has a tendancy to smooth the measured response making the solution of equation 1 difficult. The estimate for the instrument response may also contain systematic errors which will further complicate the problem.

The deconvolution problem can be restated as the convolution of z with the inverse of y as defined in equations 3 and 4:

$$\delta = y^{*}w \qquad \text{(eq. 3)}$$

$$x = z^{*}w \qquad \text{(eq. 4)}$$

where δ is the Dirac impulse function and w is the inverse of the instrument response y.

Methods for directly generating the inverse filter function w have been proposed by *Bracewell*[1] and *S M Bozic*[2]. The solution for the true response x(t) may be unique; but the problem so presented would be ill-posed. Small perturbations of the measured or instrument responses will give rise to large changes in the solution. Direct deconvolution methods are therefore not a practical solution. This has been demonstrated by *N S Nahman*[3].

The inverse of the instrument function may not be mathematically possible, however the ill-posed problem can be converted to a well-posed problem with a well behaved solution by the use of an appropriate regularisation filter. The concept of regularisation of ill-posed problems and the mathematical considerations for dealing with inverse problems have been discussed in the literature[4] [5] [6] [7].

In signal processing terms the ill-posed inverse w is replaced by a stable filtering function v defined in equation 5.

$$r = y^{*}v \qquad \text{(eq. 5)}$$

where v is the well behaved filtering function and r is the regularising filter which is a good approximation to a Dirac function.

A good estimate of the true response x will be obtained by convolving the measured result with the filter function (equation 6).

$$\tilde{x} = z^{*}v \qquad \text{(eq. 6)}$$

where $\tilde{x}$ is the estimate for the true response x.

2.2. DECONVOLUTION TECHNIQUES

A number of techniques have been used to perform the deconvolution process. The principle of operation of the main methods will be described here.

Gaussian approximation

The Gaussian approximation is used generally in electronics and optoelectronics. It assumes that the pulse responses are Gaussian in shape and therefore the full width at half maximum (FWHM) of the unknown pulse can be calculated from the full widths at half maximum of the measures and system responses as shown in equation 7:

$$FWHM_x = \sqrt{(FWHM_z^2 - FWHM_y^2)} \qquad \text{(eq. 7)}$$

where $FWHM_x$, $FWHM_y$ and $FWHM_z$ are the full widths at half maximum of the unknown, system and measured responses respectively.

This method is not a true deconvolution and is subject to serious errors[8], because the pulse responses will deviate from the Gaussian shape. This can be illustrated with a simple example: a measurement system with a constant frequency response from dc to 10 GHz and no response at higher frequencies is used to measure a similar band limited signal with a maximum frequency of 8 GHz. The frequency and time domain responses of the two signals are illustrated in figure 2.1.

The FWHMs of the system and measured responses are 60.3 ps and 75.4 ps respectively. The FWHM of the unknown response, calculated using equation 7, will be 45.3 ps. The true FWHM of the unknown signal is 75.4 ps, in agreement with the measured response. This is a particularly extreme example of the errors that can occur when the Gaussian approximation is used.

Trial convolution method

The trial convolution optimisation method[9], developed at NPL, uses a least squares optimisation technique to determine the best estimate for the unknown response. The shape of the unknown response can be described in terms of a physical model. The modelled function can be convolved with the measured instrument response and the result compared with the measured data. The model parameters are optimised to minimise

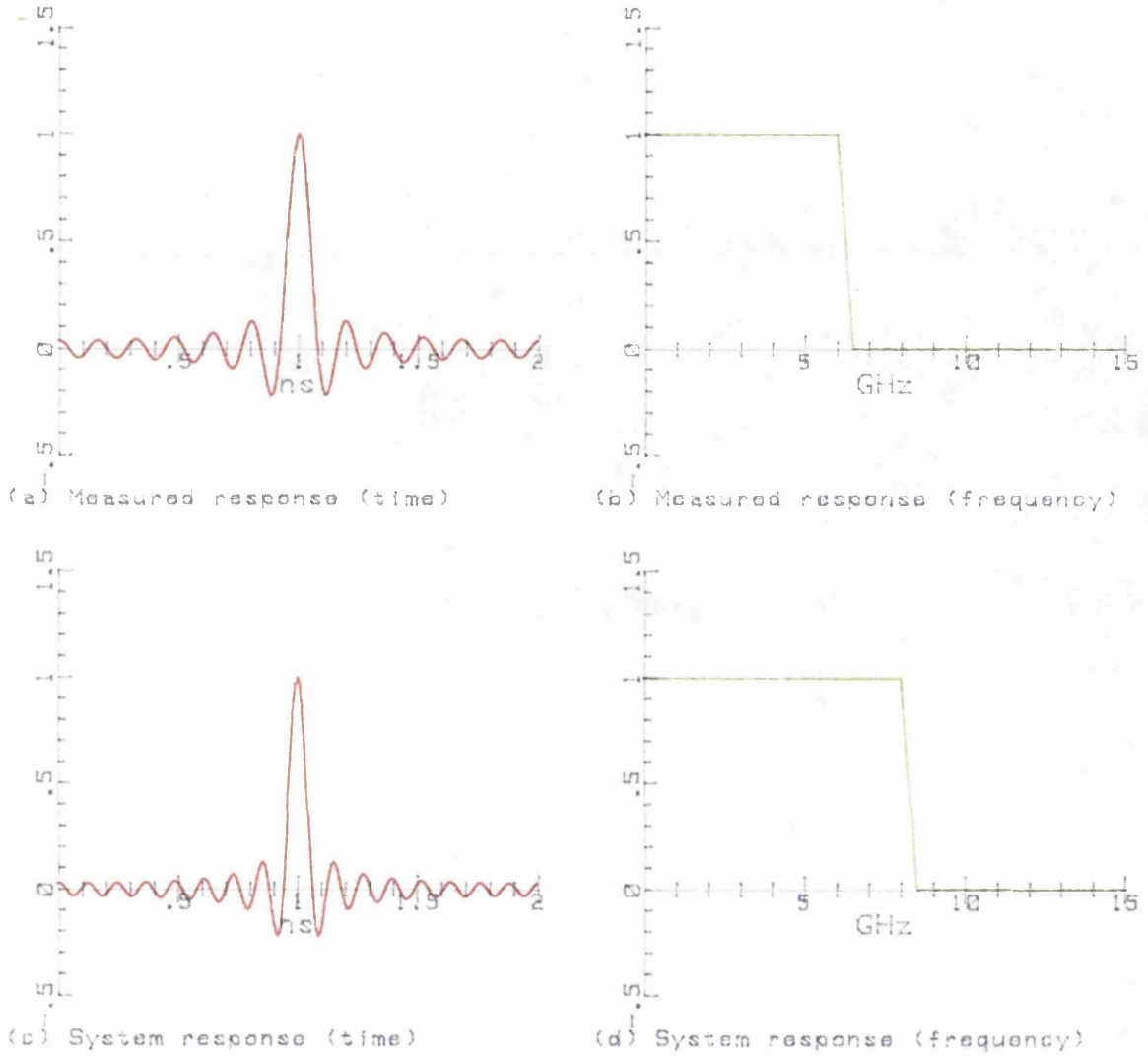

Figure 2.1. Example of errors introduced by Gaussian approximation

the error between the two curves. Because this is an integral method the noise in the result is reduced. In principle this allows measurements to be made of shorter pulses closer to the resolution limit of the system. The uncertainty of the result will depend on the closeness of the approximating function to the true shape. If the starting position is chosen incorrectly the method may find a local minimum rather than the global minimum of the error function.

A GaAlAs laser diode at 850 nm was measured using a Plessey GaInAs photodiode (CXL082) mounted in a fast photodiode holder developed at NPL (this author, unpublished work). The photodiode and sampling oscilloscope response had previously been measured using a dye laser

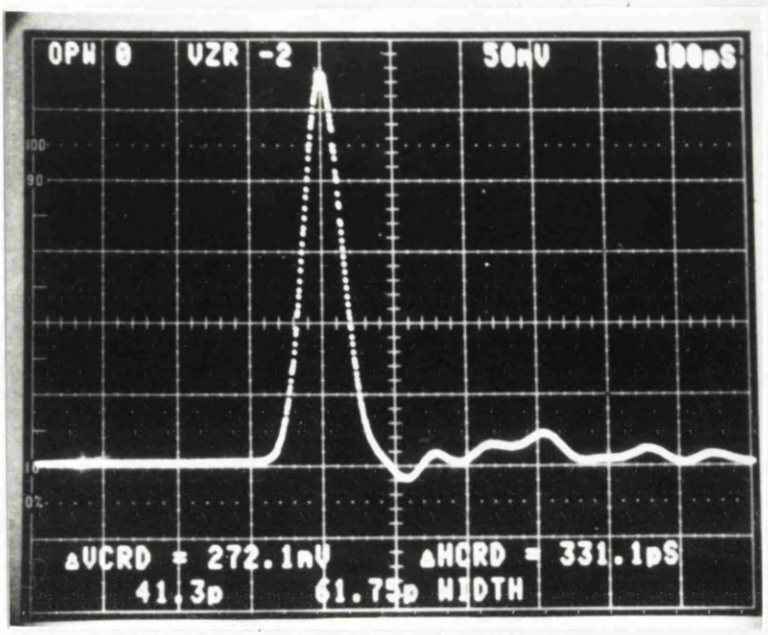

Figure 2.2. Response of photodiode at 830 nm (dye laser)

system at 830 nm giving pulses of <10 ps FWHM. For the purposes of this experiment it was assumed that the temporal response of the photodiode is the same at both wavelengths. The response measured with the dye laser is shown in figure 2.2 and has a FWHM of 65 ps.

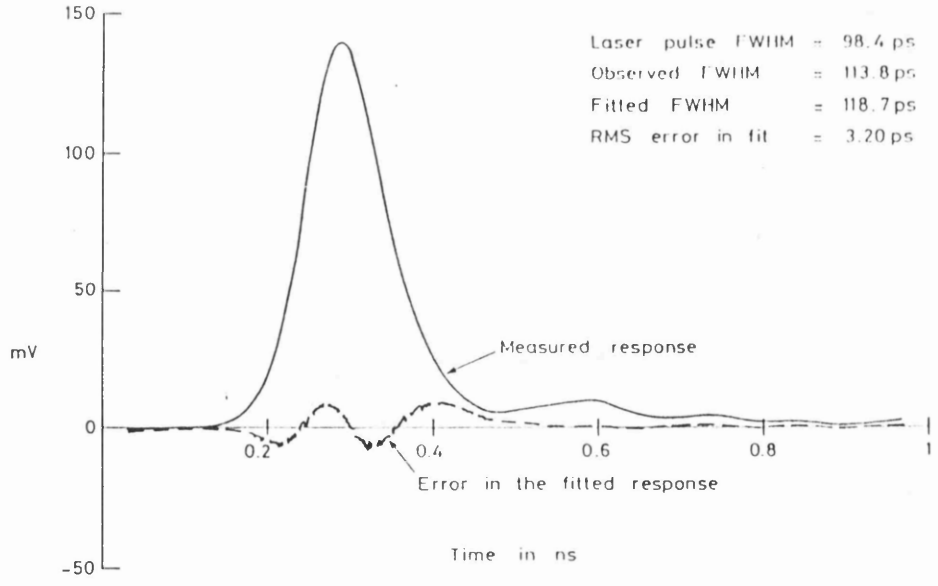

Figure 2.3. Response of photodiode at 850 nm (diode laser) showing fitted response and error

The measured response of the laser diode and detector gave a FWHM of 92 ps. The pulses from the semiconductor laser were assumed to be Gaussian and of approximately 66 ps duration, calculated using the

Gaussian approximation. This was used as a starting point for the optimising program. The best fit Gaussian pulse gave a minimum error for a FWHM of 67 ps. The measured response is shown in figure 2.3 together with the error between the measured and fitted responses.

The error between the measured and fitted responses shows a systematic and non-random deviation suggesting that either the temporal response of the photodiode is different at the two wavelengths, or that the laser pulse shape differs from the Gaussian approximation. This method is extremely powerful where a good model can be chosen.

Matrix methods

The convolution problem can be stated in a matrix formulation as shown in equation 8:

$$z = Ax \qquad \text{(eq. 8)}$$

where **A** is a convolution matrix formed from the instrument function y.

An exact inverse for the matrix **A** may not be possible, but a solution may be chosen that minimises the square of the residuals. The least squares solution will be given by equation 9:

$$\tilde{x} = [A^T A]^{-1} Az \qquad \text{(eq. 9)}$$

As the dimensions of the matrix **A** increase, the problem becomes increasingly ill-posed. The problem has been treated by *Sarkar et al*[4] who altered the problem from the minimisation of $\|Ax - z\|^2$ by adding a constraint $\|\hat{L}x\|^2$ where $\hat{L}$ is a suitably chosen linear operator. The function to be minimised is now given by equation 10:

$$\min_x \{\|Ax - z\|^2 + \mu^2\|\hat{L}x\|^2\} \qquad \text{(eq. 10)}$$

where μ is a constant chosen to control the degree of regularisation of the solution

The solution to this problem will be given by equation 11:

$$x = [A^T A + \mu^2 \hat{L}^T \hat{L}]^{-1} A^T z \qquad \text{(eq. 11)}$$

The type of constraint is dependent on the choice of linear operator $\hat{L}$.

If $\hat{L}$ is the identity matrix then this approach will yield a solution x that has a specified value for $\|x\|^2$. If a derivative operator is used then the result will have a specified degree of smoothness. This approach is known as the *Tykhonov regularisation scheme*[10, 11].

The major disadvantage of the method is that a large system of equations must be solved. This is very intensive of computer storage ($\propto n^2$) and computer time ($\propto n^3$). The inversion of the matrix in equation 11 will give rise to serious cumulative errors in the result. A better approach is to solve equation 12 by Gaussian elimination:

$$(A^TA + \mu^2\hat{L}^T\hat{L})x = A^Tz \qquad \text{(eq. 12)}$$

The form of the regularising filter r required to give a stable result can be found by substituting the instrument response function y into equation 12 in place of the measured response as shown in equation 13.

$$(A^TA + \mu^2\hat{L}^T\hat{L})r = A^Ty \qquad \text{(eq. 13)}$$

The matrix method presented requires the solution of a large system of linear simultaneous equations. This technique will not be considered further here.

Relaxation method

The matrix method described in the previous section is extremely storage intensive. An iterative method was originally proposed by *van Cittert*[12] in 1931 to correct for instrumental distortion. The method has been described by *P A Jansson*[13] and *A F Jones*[14]. The process is iterative and the solution waveform is improved at each cycle. To achieve increased speed over relaxation is used. The method has been widely used in spectroscopy[15], antenna problems[16], and for the deconvolution of time domain signals[3]. This method will not be considered further here.

Transformation methods

Transforms can be found that will convert the convolution integral into a more convenient operation such as a multiplication or an addition. The result can then be filtered in the transform domain. The deconvolved result will be obtained by performing the inverse transform

on the filtered signal.

Homomorphic transform systems have been used for the deconvolution of seismic data[17] and for high speed time domain measurements[18]. The transform used to perform the deconvolution operations consisted of three parts as shown in figure 2.4.

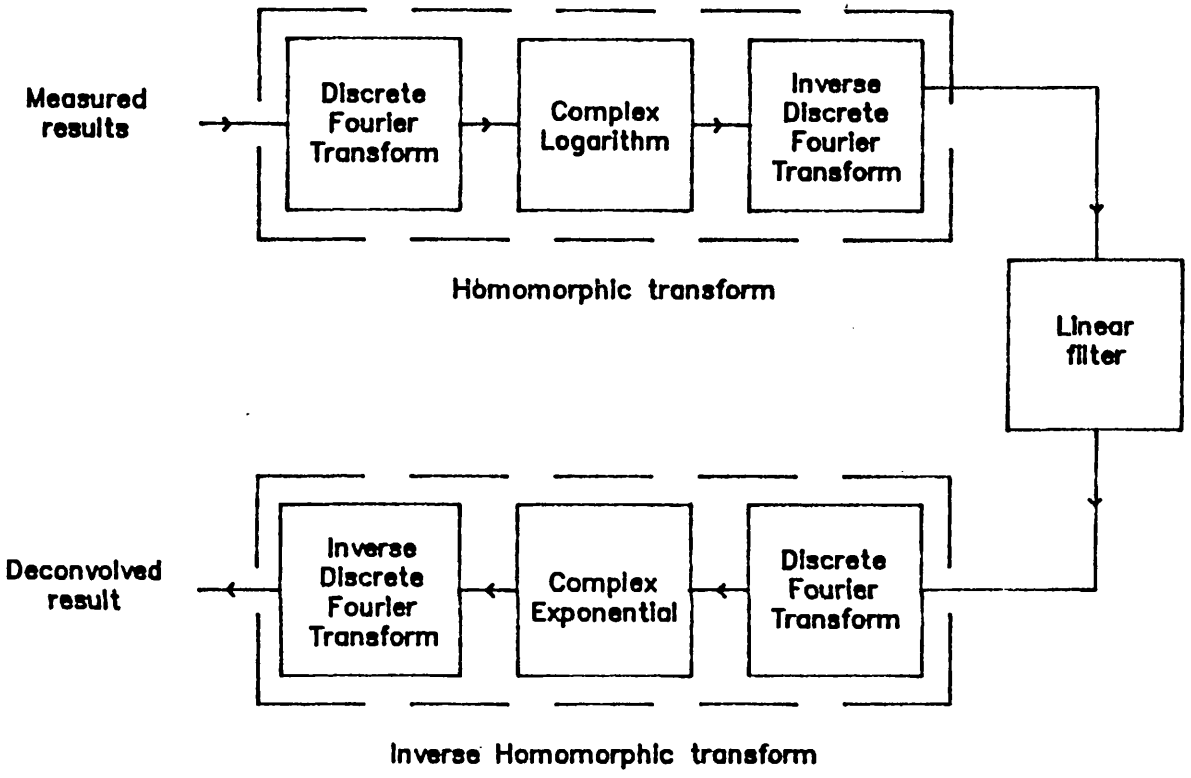

Figure 2.4. Homomorphic transform method.

The interpretation of the complex transform domain (cepstrum) waveform is not clear, but the operation of the transform is straightforward. The convolution operation is converted to an addition in the transform domain. The technique has been used with linear filters and is successful, provided that the correct filter can be found. This method will not be considered further here.

Some integral transforms, notably Fourier and Laplace, have the important property that a convolution in the untransformed domain becomes a multiplication in the transform domain and vice versa. This is shown by equations 14 and 15 for a Fourier transform system:

$$F(x(t)*y(t)) = X(j\omega)Y(j\omega) \qquad \text{(eq. 14)}$$

$$F(x(t)y(t)) = X(j\omega)*Y(j\omega) \qquad \text{(eq. 15)}$$

where $F(x(t)) = \frac{1}{2\pi j}\int_{-\infty}^{\infty} x(t)\ \text{Exp}\ -j\omega t\ dt$

The deconvolution operation will therefore be the division of the two signals. A suitable filter will have to be used to ensure the stability of the result.

The measured responses will be discrete and time limited. Therefore the Z transform and discrete fourier transform (DFT), which are the analogues of the Laplace and Fourier transforms, can be used. The Fast Fourier Transform[19] (FFT) exploits the symetry properties of the DFT, where the number of points is a power of two. The number of complex multiplications are reduced from 2^{2n} for the DFT to $n2^{n+1}$, considerably improving the processing speed for the transform and inverse transform operations. Deconvolution methods based on the fourier transform have been used for picosecond time domain measurements by *Nahman*[3] using a nonlinear regularisation filter to obtain a stable result. This method will be outlined in the next section.

2.3. NBS DECONVOLUTION METHOD

The deconvolution method developed by *Nahman and Guillame* at the National Bureau of Standards (NBS) will be described briefly here. The algorithm was developed to improve the accuracy of picosecond time domain measurements and forms the basis of the deconvolution method developed for photodiode measurements.

Theory of the NBS algorithm

The filter required to minimise the effects of noise should be chosen to give the most accurate results. The errors introduced by the filter should therefore be minimised. The filter has been chosen to maximise the smoothness of the signal and to minimise the errors introduced into the measured results.

As a shorthand notation the time domain and frequency domain signals will be represented implicitly by the lower case and upper case symbols only i.e. $x(t) \equiv x$ and $X(j\omega) \equiv X$.

The errors introduced into the original measurement by the filter can be determined by deconvolving the two signals and then reconvolving the

result with the measured system response. The error E can then be described as follows (equation 16):

$$E = \sum_{i=1}^{n} |Z_i|^2 |1 - R_i|^2 \qquad \text{(eq. 16)}$$

where E is the error term; Z is the measured signal; and R is the filter.

The smoothness of the signal has been interpreted as the power contained in the second derivative of the deconvolved result. The signals are measured at discrete time points. The $\frac{\partial^2}{\partial t^2}$ operator can be approximated by a central difference operator (δ).

Where $\delta(f_i) = f_{i-1} - 2f_i + f_{i+1}$, and i is the point of interest.

In the frequency domain the second difference operator becomes (17):

$$C = 2(\cos \frac{\pi i}{n} - 1) \qquad \text{(eq. 17)}$$

where i is the harmonic number; and n is the number of points in the transform. The smoothness parameter S is given by equation 18:

$$S = \sum_{i=1}^{n} | C_i X_i |^2 \qquad \text{(eq. 18)}$$

where X is the deconvolved signal with noise.

The filter was chosen to minimise the error E and maximise the smoothness of the result. An operator controlled parameter γ was chosen to control the degree of smoothing. The total error power P, which was minimised, is given in equation 19:

$$P = E + \gamma S \qquad \text{(eq. 19)}$$

The resultant optimal filter has the form (equation 20):

$$R = \frac{|Y^2|}{(|Y|^2 + \gamma |C|^2)} \qquad \text{(eq. 20)}$$

The deconvolution now takes the form shown in equation 21:

$$X = \frac{Z}{Y} R = \frac{ZY^*}{(|Y|^2 + \gamma |C|^2)} \qquad \text{(eq. 21)}$$

where Y^* is the complex conjugate of Y; and γ is a multiplicative constant chosen by the operator to control the amount of smoothing. γ must be greater than zero.

The magnification of the noise by the deconvolution process has been limited by the filter function.

Evaluation of the NBS deconvolution method

To test the effectiveness of the NBS deconvolution method the impulse response of a 20 GHz distributed amplifier was measured using a sampling oscilloscope with a nominal 14 GHz bandwidth. The results were deconvolved to remove the sampling scope response and compared with measurements made using a HP8510 vector network analyser at up to 26.5 GHz. The magnitude response of the amplifier, measured using the vector network analyser, is shown in figure 2.5.

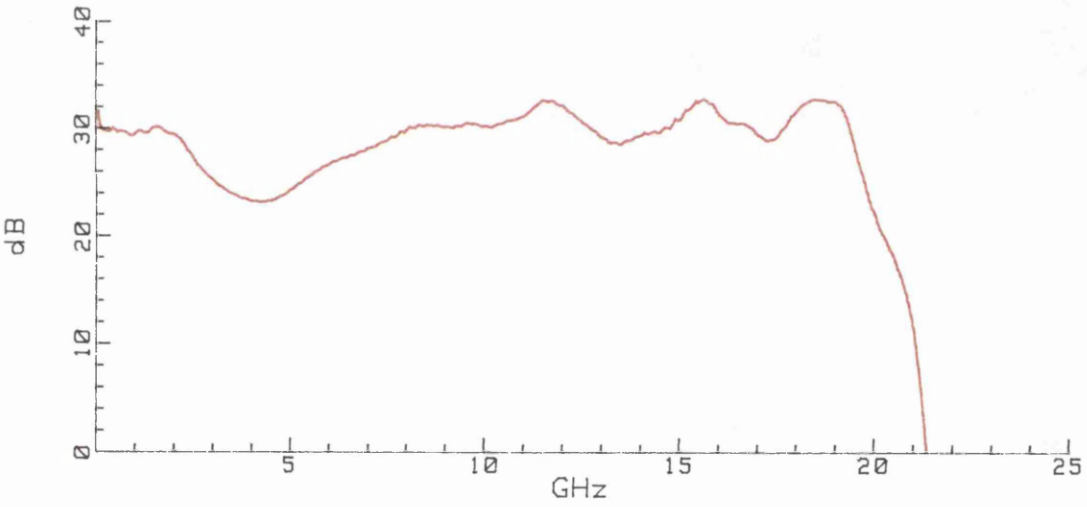

Figure 2.5. Magnitude response of the distributed amplifier used to test the deconvolution method

The deconvolution method is only suitable for use with impulse responses and so a differentiating capacitor was used with a Tektronix S-52 step generator to form an impulse of 29 ps FWHM. The resultant pulse, shown in figure 2.6(a), contains ringing and secondary pulses which will mask the true response of the amplifier. The measured amplifier response is shown in figure 2.6(b).

After deconvolution the measured impulse response is shown in figure 2.7 together with the time domain response derived from the

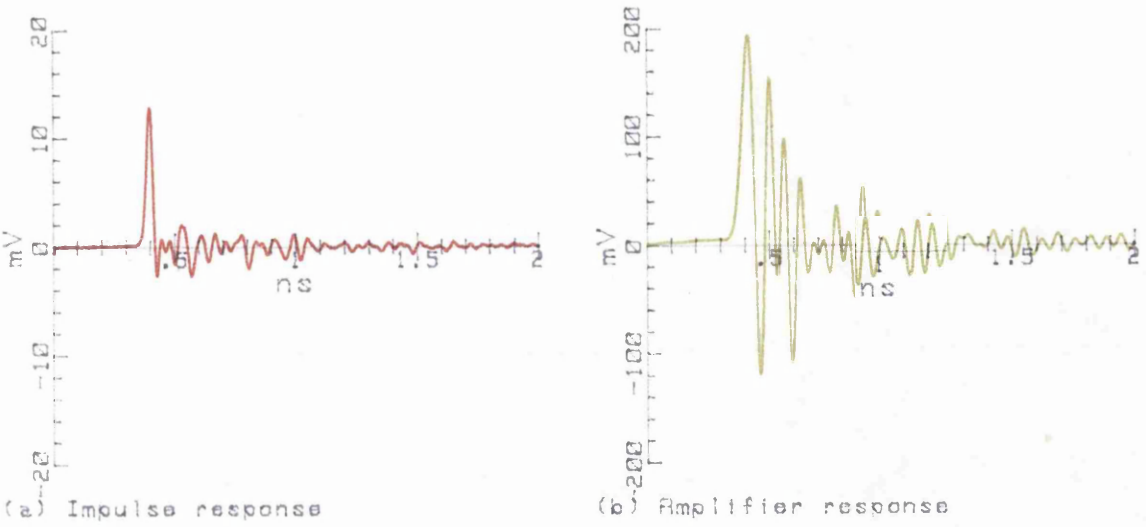

Figure 2.6. (a) Impulse formed by differentiating capacitor and S-52 pulse generator and (b) Measured amplifier response.

vector network analyser measurements. The two responses show only small differences in the ringing. The deconvolution method can therefore be successfully used to extract signals from beyond the normal usable range of the sampling oscilloscope.

The results presented here show that the deconvolution method works well. There are however two drawbacks with this method: firstly the parameter γ, which controls the level of smoothing, operates in the frequency domain so the result of the deconvolution will depend on the skill of the user; secondly the filter function R will vary from measurement to measurement, and is not amenable to simple interpretation.

2.4. SIGNIFICANCE OF THE FILTER FUNCTION

The deconvolved result X consists of the true pulse shape X' with a noise function N_x added and convolved with the filter function R as shown in equation 22.

$$X = R(X' + N_x) \qquad \text{(eq. 22)}$$

It is not possible to obtain the impulse response X' because the problem is ill-posed. The best estimate for the unknown response X' can be found by giving both the deconvolved result and the filter function. It is important that the filter function R can be interpreted because

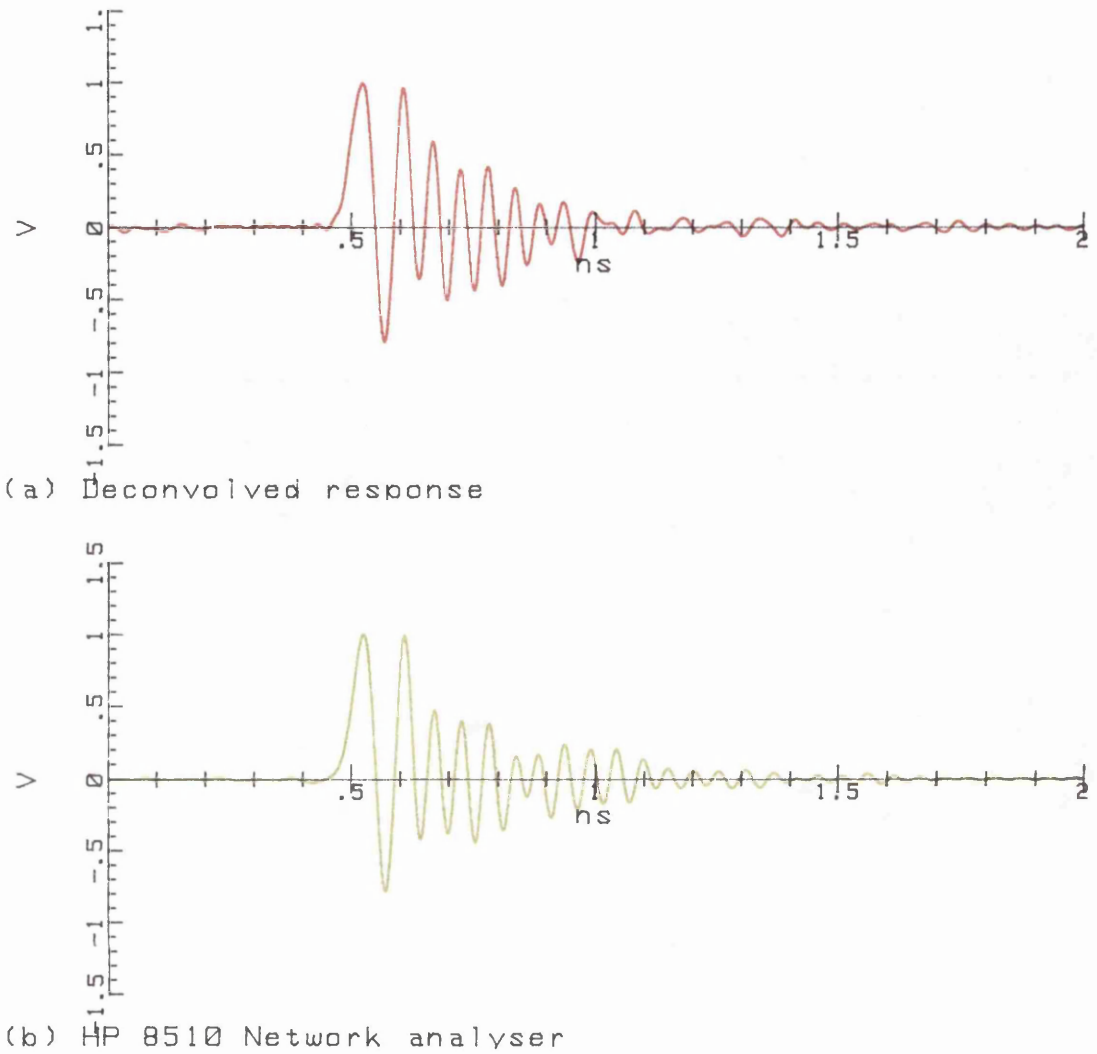

Figure 2.7. Deconvolved amplifier response (a) and response measured using vector network analyser (b)

the deconvolved result is the convolution of the true response and the filter. The filter function, at the optimum value for γ, is shown in both the frequency domain (figure 2.8) and in the time domain (figure 2.9). In the frequency domain the cutoff is quite sharp, allowing results to be interpreted at up to the cutoff frequency.

In the time domain the sharp frequency cutoff gives rise to a sinc(x) like response. The resultant filter function will also vary for different choices of γ making a comparison of deconvolved results difficult.

A modified deconvolution method, which allows interpretation and comparison of results, is therefore required for use with transfer standard photodiodes. A suitable regularisation scheme is developed in this work.

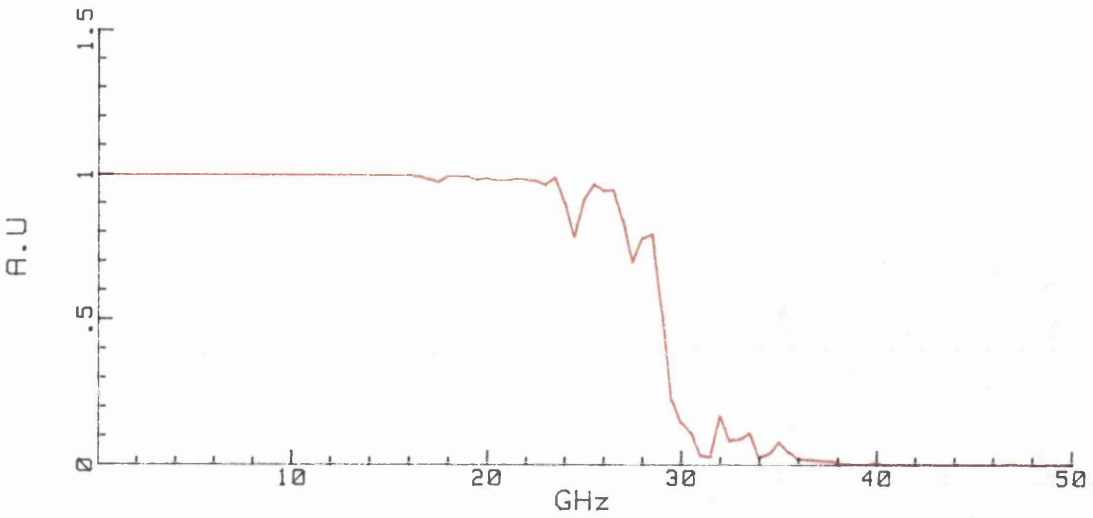

Figure 2.8. Response of the filter in the frequency domain

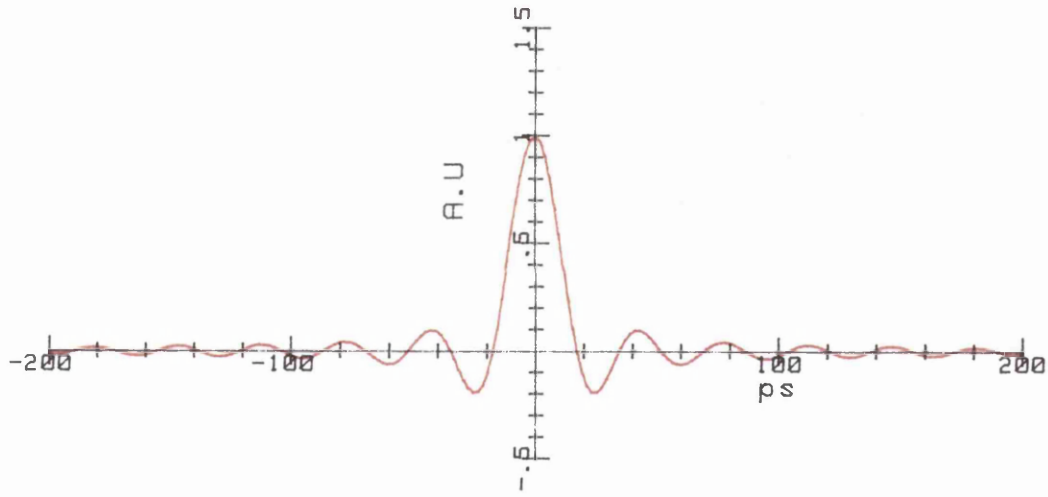

Figure 2.9. Response of the filter in the time domain

2.5. SMOOTHING FUNCTION

In the NBS method the smoothing function C, corresponding to $\frac{\partial^2}{\partial t^2}$ in the time domain, was approximated by a simple function derived from the second difference operator. In a continuous fourier transform the operation $\frac{\partial}{\partial t}$ in the time domain corresponds to a multiplication by $j\omega$ in the frequency domain. Therefore $|\frac{\partial^2}{\partial t^2}|^2$ would correspond to ω^4. For the discrete Fourier transform this would be equivalent to $(\frac{\pi i}{n})^4$. The simple expansion used by NBS will contain components due to higher derivatives. These can be eliminated by introducing further second difference operators for $i \pm 2$, $i \pm 3$ ... This gives rise to a

smoothing function of the form shown in equation 23:

$$C_i = \sum_{j=1}^{m} a_j \left(\cos\frac{ij\pi}{n} - 1\right) \qquad \text{(eq. 23)}$$

where a_j is the coefficient for each second difference operator; m is the number of terms; i is the harmonic number; and n is the number of harmonics.

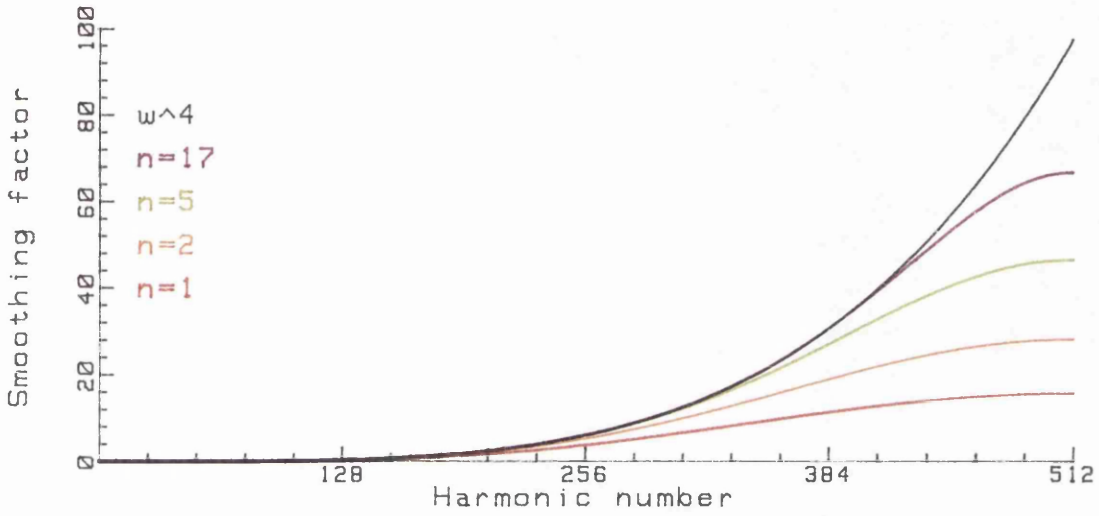

Figure 2.10. Variation of smoothing operator for different values of m

The higher order derivatives will be cancelled up to the $2m + 2^{th}$. Figure 2.10 shows the variation of $|C|^2$ for various values of m and gives a comparison with the $(\frac{\pi i}{n})^4$ approximation. The approximation is good and only introduces errors close to the Nyquist frequency. For this reason the simple approximation has been adopted for the smoothing function. In preference to the second difference operator used in the NBS method.

2.6. DECONVOLUTION METHOD FOR USE WITH TRANSFER STANDARD PHOTODIODES

A deconvolution method is required for use with transfer standard photodiodes for pulse response measurements. The method should be unambiguous in its use and not depend on the skill of the operator. The regularisation filter function, which acts as the equivalent excitation, should be a suitable known function or a good approximation to a known function, so that comparisons can be made between different sets of measurements. The filter function derived for the deconvolution

method in section 2.3 has a response similar to sinc(x) and would therefore be unsuitable for use as the equivalent excitation for photodiode measurements, because it would infer negative light levels which are physically unrealistic.

Deconvolution method

A Gaussian is generally used in optoelectronic measurements to model pulse shapes and is easily interpreted. It would be suitable for use as a regularisation filter. However, if the Gaussian filter were used on its own, either insufficient smoothing would be obtained for a suitable width of pulse, or too wide a Gaussian pulse would have to be used to allow easy interpretation of the results. To overcome this problem an deconvolution approach similar to the NBS method, discussed in section §2.3, has been adopted.

The regularisation filter consists of two parts: a Gaussian pulse G defined by the user and a second filter R' to stabilise the result. The composite filter R is given by equation 24:

$$R = R'G \qquad \text{(eq. 24)}$$

The regularisation filter R will be a good approximation to the Gaussian filter, allowing measurements performed using different systems to be compared. The differences between the Gaussian and the combined filter R give rise to an error term defined in equation 25.

$$E_g = \sum_{i=1}^{n} |G_i(1 - R_i')|^2 \qquad \text{(eq. 25)}$$

where E_g is the total error power introduced by the stabilising filter into the Gaussian.

The stabilising filter R' will give rise to errors in the measured response. The an error term defined in equation 26:

$$E_s = \sum_{i=1}^{n} |Z_i(1 - R_i')|^2 \qquad \text{(eq. 26)}$$

where E_s is the total error power introduced by the stabilising filter into the measured signal.

The stabilising filter should be chosen to minimise the errors introduced into the result and maximise the smoothness of the result. The filter must also be linked to the Gaussian error term so that only a single parameter is required.

The response of the photodiode used as the reference must be included otherwise errors will be introduced in the result. The deconvolved result, including the response of the reference device, will be given by equation 27:

$$X = \frac{Z\ Y_r G\ R'}{Y} \qquad \text{(eq. 27)}$$

where Y_r is the response of the reference device.

Optimal stabilisation filter

The errors introduced in the original data - the error in the Gaussian and the smoothness of the result - are considered to be of equal importance. The three terms are combined with equal weight to give a single error term P_1, defined in equation 28:

$$P_1 = \alpha E_s + \beta E_g + \gamma S \qquad \text{(eq. 28)}$$

The weighting parameters α,β and γ are defined in equations 29, 30 and 31.

$$\alpha = \frac{1}{\sum_{i=1}^{n} |Z_i|^2} \qquad \text{(eq. 29)}$$

$$\beta = \frac{1}{\sum_{i=1}^{n} |G_i|^2} \qquad \text{(eq. 30)}$$

$$\gamma = \frac{1}{\sum_{i=1}^{n} |X_i|^2} \qquad \text{(eq. 31)}$$

The filter R' can be found by differentiating the error term P_1 with respect to each frequency component of the filter response, and setting the result equal to zero. The optimal filter R' is given in equation 32:

$$R' = \frac{|Y|^2\ (\alpha|Z|^2+\beta|G|^2)}{|Y|^2(\alpha|Z|^2+\beta|G|^2) + \gamma|C\ G\ Z\ Y_r|^2} \qquad \text{(eq. 32)}$$

The parameter γ must be found iteratively and a Newton method has been used successfully.

This deconvolution method has the advantage that it is no longer dependent on the skill of the operator. Also the near Gaussian filter, which is equivalent to the excitation, allows results to be easily compared. If too narrow a Gaussian filter is chosen then the errors introduced in the Gaussian (E_g) may dominate the deconvolution process.

2.7. ASSESSMENT OF THE GAUSSIAN DECONVOLUTION METHOD

The performance of the deconvolution method described in the previous section has been assessed using measurements of the temporal responses of two photodiodes using three pulsed semiconductor lasers.

The first of the photodiodes is a GaInAs research photodiode, designated #20, from Plessey. This device has a 45 µm diameter active area and has a 3 dB frequency of roughly 14 GHz. The diode has been mounted in a specially modified NPL designed (this author, unpublished work) low inductance photodiode holder.

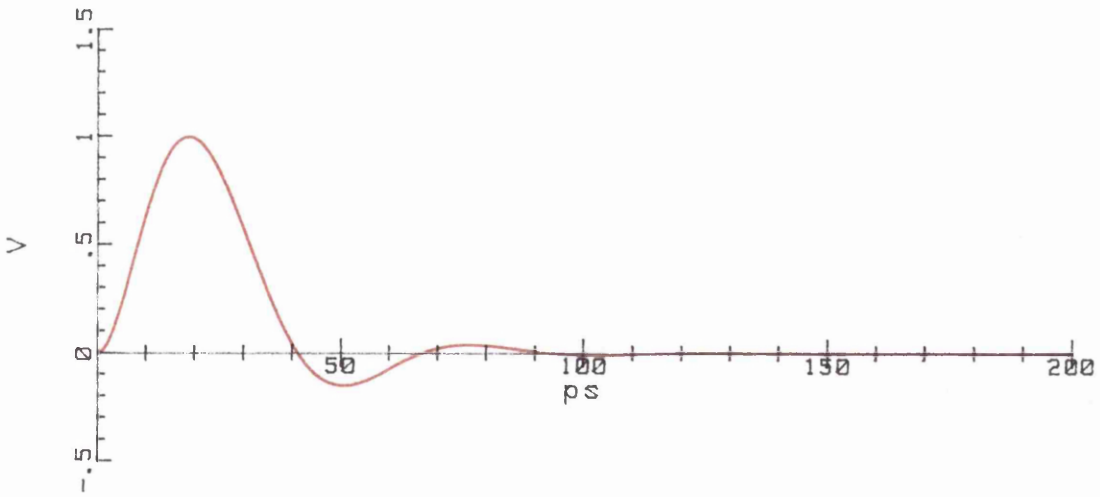

Figure 2.11. Theoretically modelled response of the AT&T diode

The second photodiode is a 25 µm diameter device provided by AT&T Bell laboratories[20], which is mounted in a modified Hewlett-Packard HP33330C detector diode package. Measurements have been made of this diode's performance and are described in part 1 of this thesis. The 3 dB frequency is about 19 GHz. A simple model of the response, believed to be accurate to 21 GHz, has been used to correct for the magnitude and

and phase response of the AT&T diode. Figure 2.11 shows the theoretically modelled response of this device.

The sources used for the experiment were two Optoelectronics Ltd PLS10 lasers operating at 1324 nm and 1323 nm, and a Lasertron QLPX laser operating at 1270 nm. The lasers are driven by a short high current pulse of sub-nanosecond duration. A theoretical analysis of the response of a semiconductor laser to a short electrical pulse[21,22] has shown that for an ideal drive pulse the laser can be made to produce a single optical pulse of < 100 ps duration. However if the electrical pulse is too long multiple optical pulsing occurs. The PLS10 laser exhibits this phenomenon. The spacing and shape of the pulses depends on the bias voltage.

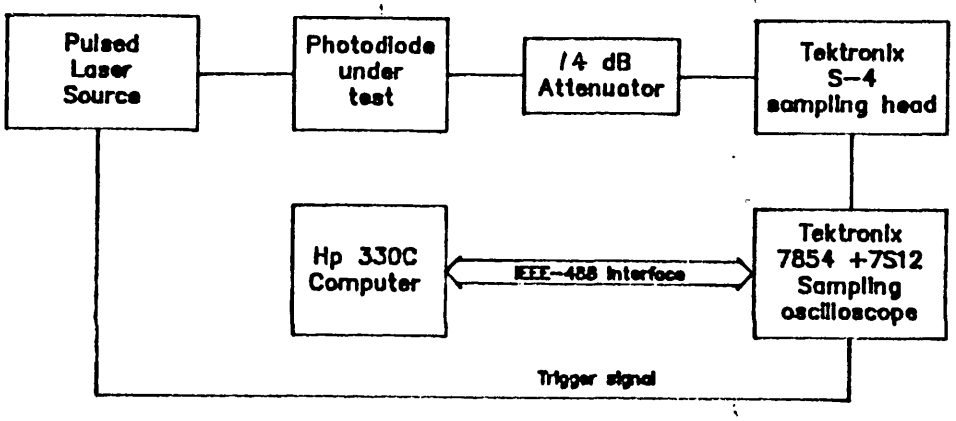

Figure 2.12. System to measure photodiode responses for deconvolution

The layout of the measurement system is shown in figure 2.12. A X5 (14 dB) attenuator was included to remove the effects of any electrical reflections from the measurement system. A measurement was made with the optical path blocked and this was subtracted from the measured results to remove the effects of trigger breakthrough. Each data set consisted of 1024 data points. An average of 100 measurements was taken at each point to reduce the effects of noise.

The results measured with the three lasers are shown figures 2.13 a - *f*. Multiple pulsing is clearly visible in two of the measurements. The results obtained with the Plessey photodiode show some ringing but the extent of this is not clear because the effect is masked by the laser response.

The results have been deconvolved using a Gaussian parameter of 25 ps

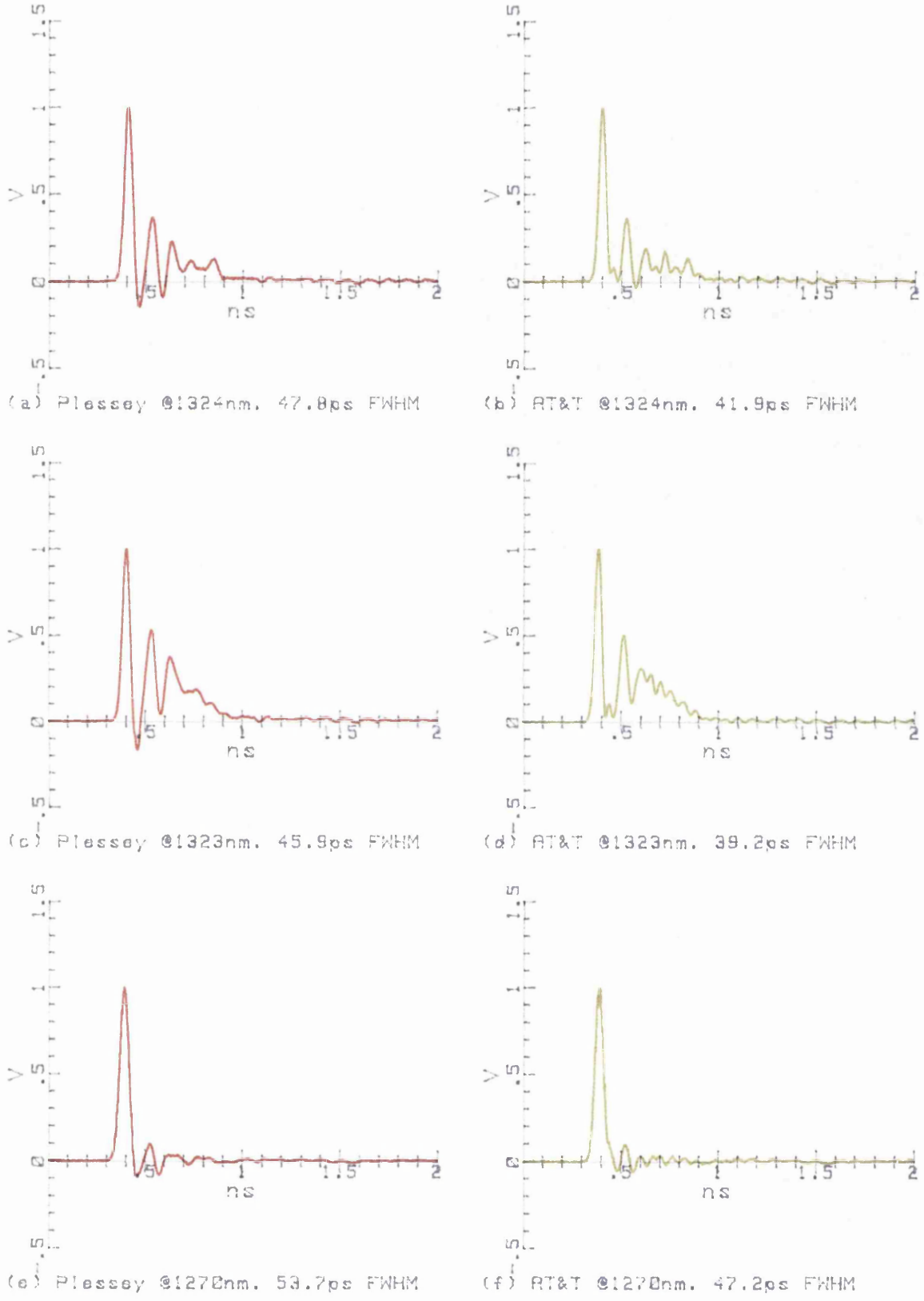

Figure 2.13. Measured results using different lasers.

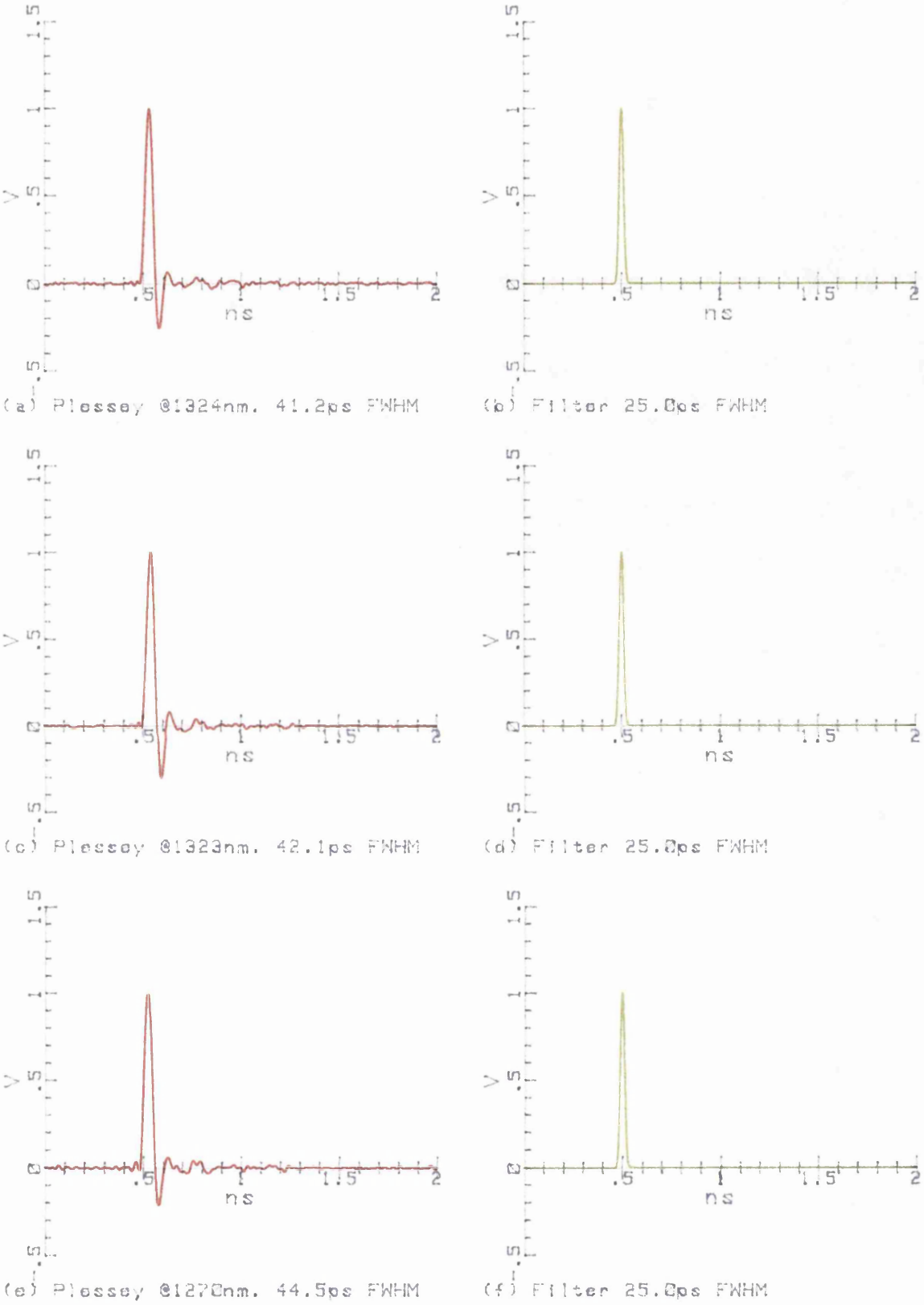

Figure 2.14. Deconvolved results using different lasers.

FWHM. The areas of the deconvolved results have been normalised for ease of comparison. The time relation between each of the deconvolved pulses is not known and so the position of the peaks have been aligned by introducing a delay into each of the results. The deconvolved results obtained are shown in figure 2.14 (a - c) together with their respective filter functions (d - f). The deconvolution method gives similar results with filter functions that are close to the original Gaussian.

2.8. DECONVOLUTION OF MULTIPLE DATA SETS

The deconvolution methods discussed so far have used a single set of measurement results per deconvolution. If a number of measurements are made using different exciting sources then an improvement in the accuracy of the result can be obtained by performing the deconvolution on all of the measured results together, rather than performing the deconvolutions separately and then averaging the results.

The magnitude of the power spectra of the three laser diodes used in the previous section are shown in figure 2.15 together with the mean response. Each of the lasers exhibits minima, due to multiple pulsing, but these occur at different frequencies.

The common dip in the power spectra at 10 - 11 GHz is believed to be a systematic error caused by the sampling oscilloscope. The mean response is considerably smoother, reducing the requirements for the regularisation filter to give a stable deconvolved result.

If a number of measurements are made each will have an associated arbitrary signal level and delay relative to a reference point. It is therefore necessary to normalise the signals and correct for the different delays so that all of the measurement sets are made with respect to a common reference.

Delay correction

To compensate for the arbitrary delays in the measurements, each of the data sets is separately deconvolved and one of these results is chosen as a reference. Initially the corrections for each of the data sets were determined by performing a cross-correlation between the deconvolved result and the reference. The position of the cross-correlation peak gave the delay correction required. This method

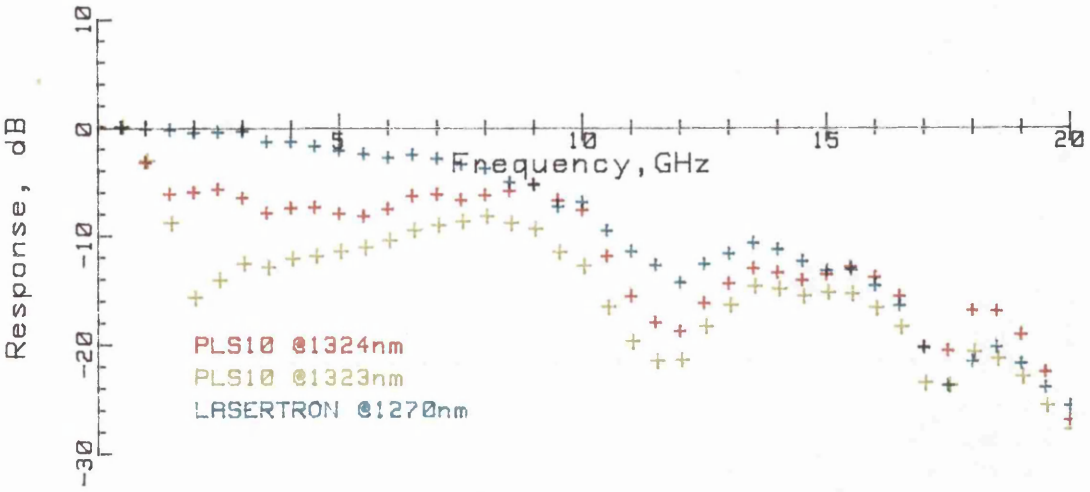

Figure 2.15. Power spectra measured using three pulsed laser diode sources

is rather slow because of the need to transform the results back into the time domain. An alternative approach, based on an adaptive time-drift compensation technique[23] (Appendix 1), has now been adopted.

Least squares deconvolution

The simplest approach to the deconvolution is to seek a solution that will minimise the errors introduced into the result. A least squares analysis, minimising the error E_1 defined in equation 33, gives rise to a simple expression for the deconvolved signal (equation 34).

$$E_1 = \sum_{i=1}^{n} \sum_{j=1}^{m} |Z_{ij} - Y_{ij} X_i (\theta_j)^i|^2 \qquad \text{(eq. 33)}$$

where E_1 is the error to be minimised; and θ is a delay correction parameter to ensure that the measurements are made with respect to a common reference.

$$X_i = \frac{\sum_{j=1}^{m} Z_{ij} Y^*_{ij} (\theta_j)^i}{\sum_{j=1}^{m} Y_{ij} Y^*_{ij}} \qquad \text{(eq. 34)}$$

where X is the least squares solution.

This solution would be perfectly acceptable provided that the errors were random. However, the power spectra shown in figure 2.15 show that systematic errors are present. Stabilising constraints may therefore be required as the problem is ill-posed.

If the least squares analysis is extended to minimise the errors and maximise the smoothness of the result the deconvolved signal will be given by equation 35 and the filter response will be given by equation 36.

$$X_i = \frac{\sum_{j=1}^{m} Z_{ij} Y^*_{ij} (\Theta_j)^i}{(\sum_{j=1}^{m} Y_{ij} Y^*_{ij}) + \gamma |C|^2} \qquad \text{(eq. 35)}$$

where γ is a parameter, selected by the operator, to control the degree of smoothing.

$$R_i = \frac{\sum_{j=1}^{m} Y_{ij} Y^*_{ij}}{(\sum_{j=1}^{m} Y_{ij} Y^*_{ij}) + \gamma |C|^2} \qquad \text{(eq. 36)}$$

The deconvolved result and filter are very similar to those obtained by the NBS method for a single result (see section §2.3).

To simplify the analysis it is necessary to redefine the deconvolution (equation 33) in terms of a weighted mean measured response $\bar{Z}$ and a weighted mean system response $\bar{Y}$, as shown in equation 37:

$$X_i = \frac{\bar{Z}_i}{\bar{Y}_i} \qquad \text{(eq. 37)}$$

where

$$\bar{Y}_i \bar{Y}^*_i = \sum_{j=1}^{m} Y_{ij} Y^*_{ij} \qquad \text{(eq. 38)}$$

An analysis to find the optimal filter that minimises the errors introduced into the weighted mean data, and maximises the smoothness of the result (see section §2.3) yields identical results to equations 35 and 36. The Gaussian deconvolution method, described in section §2.6, can be extended for use with multiple measurement sets

in a similar manner. The measured responses Z and Y are replaced by the weighted mean responses $\bar{Z}$ and $\bar{Y}$ and the analysis proceeds as before.

Estimation of Errors

The errors due to variation of the laser sources are estimated in a similar manner to the calculation of the standard error of the mean. The standard error of the mean is normally given by equation 39:

$$SEM_x^2 = \frac{\sum_{j=1}^{m} (x_j - \bar{x})^2}{m(m-1)} \qquad \text{(eq. 39)}$$

However, this can be rewritten in a more convenient form (equation 40).

$$SEM_x^2 = \frac{m-1}{m} \sum_{j=1}^{m} (\bar{x}_j - \bar{x})^2 \qquad \text{(eq. 40)}$$

where

$$\bar{x}_j = \frac{1}{m-1}\left(\left(\sum_{k=1}^{m} x_k\right) - x_j\right) \qquad \text{(eq. 41)}$$

To estimate the errors in the result, the weighted average deconvolved result $\bar{X}_j$ are calculated for each of the measurements. These results are then transformed back into the time domain, and the standard error of the mean is calculated at each time point using equations 40 and 41. If the results were required in the frequency domain then a similar procedure, without the fourier transform step, could be adopted.

Assessment of the deconvolution method

A total of fifty measurements were made using the AT&T photodiode and the 40 μm diameter Plessey research photodiode #20 using a number of pulsed semiconductor lasers at a nominal wavelength of 1.3 μm. From previous measurements it is apparent that the photodiode has a faster response than the sampling oscilloscope. A summary of the measurement results is given in table 2.1. All measurements were made on a timescale 200 ps per division.

The deconvolved results are shown in figure 2.16(a) for the multiple deconvolution method giving the mean value and showing the 95% confidence limit. The Gaussian part of the regularisation filter was chosen to be 20 ps FWHM, corresponding to a 3 dB frequency of 15 GHz. The regularisation filter is shown in figure 2.16(b).

The frequency response, determined from the deconvolved signal, is shown in figure 2.17 together with the response measured by the comb harmonic method described in part 1 of this thesis. The overall agreement is good, except at higher frequencies where the results obtained by the deconvolution method do not fall off quite as fast as those measured by the comb harmonic technique.

Table 2.1 Measured and deconvolved results for the Plessey #20 photodiode at 1300 nm

Laser source	Measured FWHM AT&T (ps)	Measured FWHM Plessey (ps)	Deconvolved FWHM (ps)
Optoelectronics PLS10 @1324 nm, 144V	41.6	47.9	40.7
Optoelectronics PLS10 @1324 nm, 143V	41.9	48.0	40.4
Optoelectronics PLS10 @1324 nm, 142V	43.1	48.8	40.3
Optoelectronics PLS10 @1324 nm, 140V	46.0	51.9	40.1
Optoelectronics PLS10 @1323 nm, 144V	39.5	46.1	40.4
Optoelectronics PLS10 @1323 nm, 142V	40.5	46.5	39.8
Optoelectronics PLS10 @1323 nm, 140V	40.3	47.0	40.8
Optoelectronics PLS10 @1323 nm, 138V	42.1	48.0	39.8
Lasertron QPLX @1270 nm	46.7	54.2	41.6
Lasertron QPLX @1328 nm	60.6	63.1	38.4
All measurements	-	-	40.5

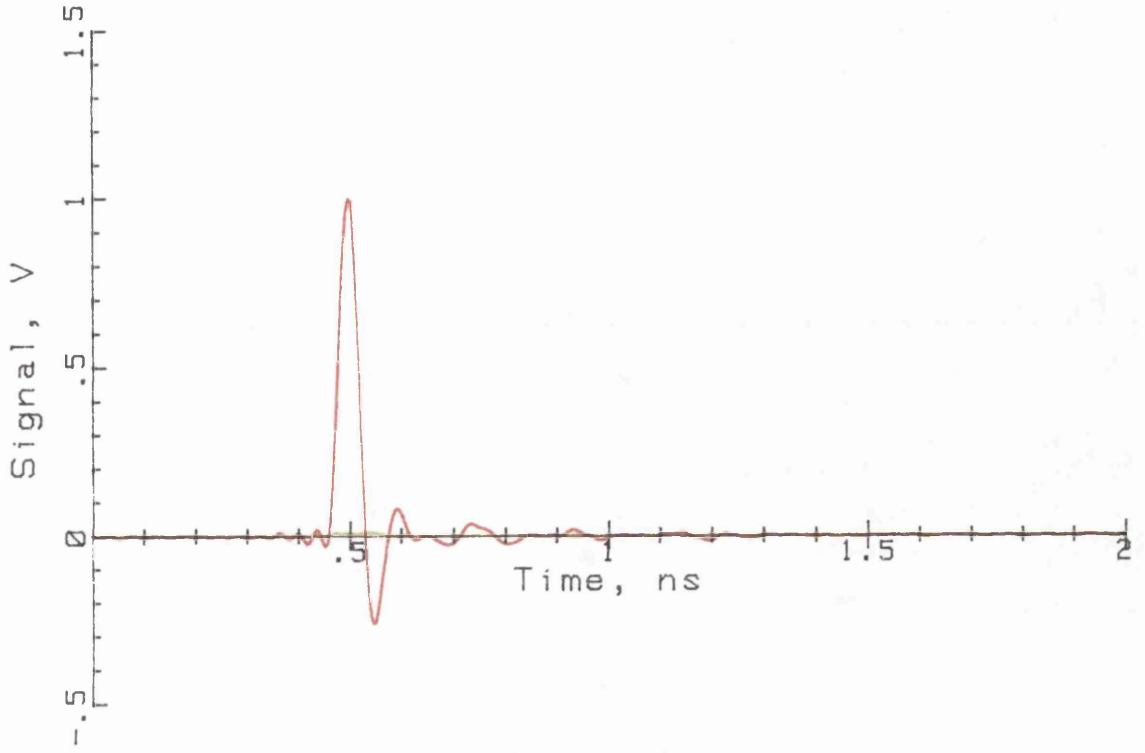

(a) Plessey diode. 40.5ps FWHM

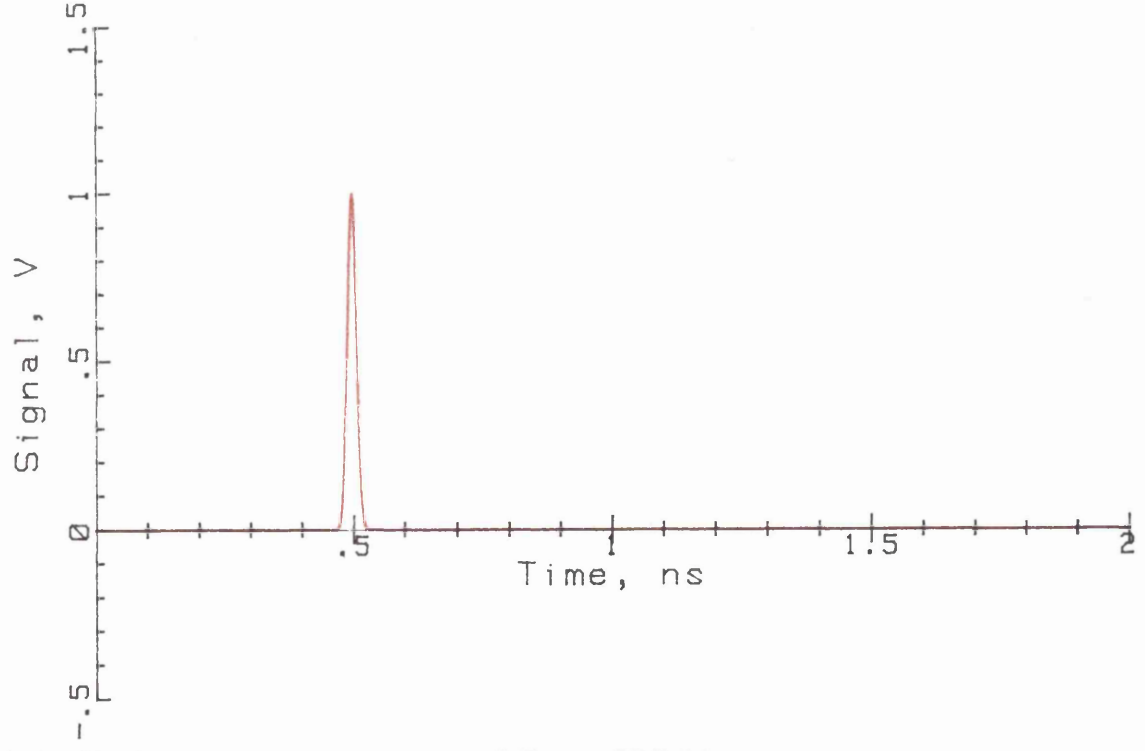

(b) Filter response. 20ps FWHM

Figure 2.16. Deconvolved response and filter

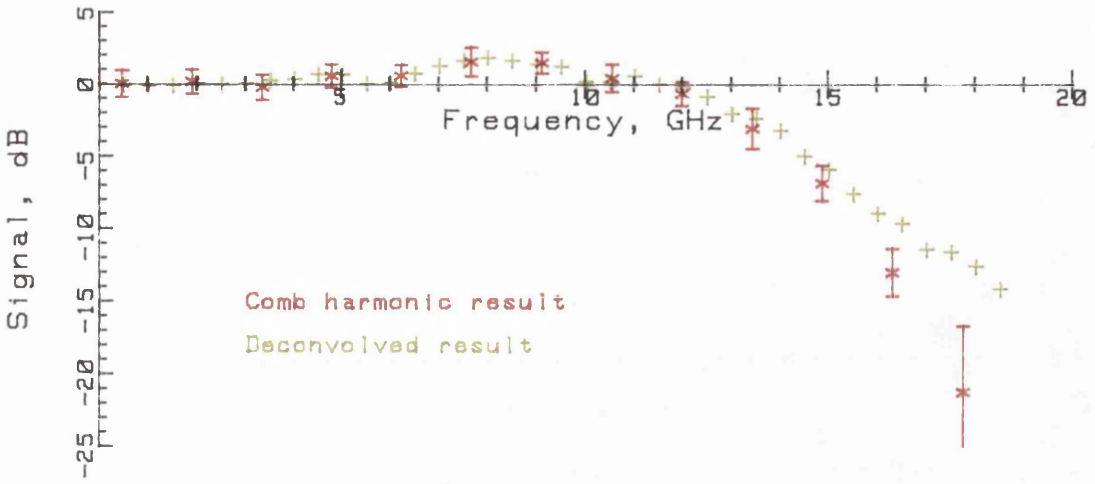

Figure 2.17. Frequency response of the Plessey #20 diode measured by the comb harmonic and deconvolution methods

2.9. CHAPTER SUMMARY

The concept of deconvolution has been discussed and a variety of deconvolution techniques have been described. In this work the Fourier transform deconvolution method developed by *Nahman and Guillame* has been adapted to allow the comparison of photodiodes measured using different laser sources. The significance of the filter function has been discussed. The deconvolution algorithm has been extended to allow multiple sets of measurements to be combined to give a single deconvolved result. The methods developed here give clear and easily interpreted results and are suitable for use by non-specialist users.

3. REDUCTION OF JITTER IN MEASURED SIGNALS

3.1. INTRODUCTION

Measurements made using a sampling oscilloscope will contain noise both on the signal and on the trigger inputs. The noise on the signal input is often due in part to that sampling process and can be reduced to an acceptable level by averaging many measurements. Noise on the trigger input gives rise to an uncertainty in time, between the measured signal and the trigger, as illustrated in figure 3.1.

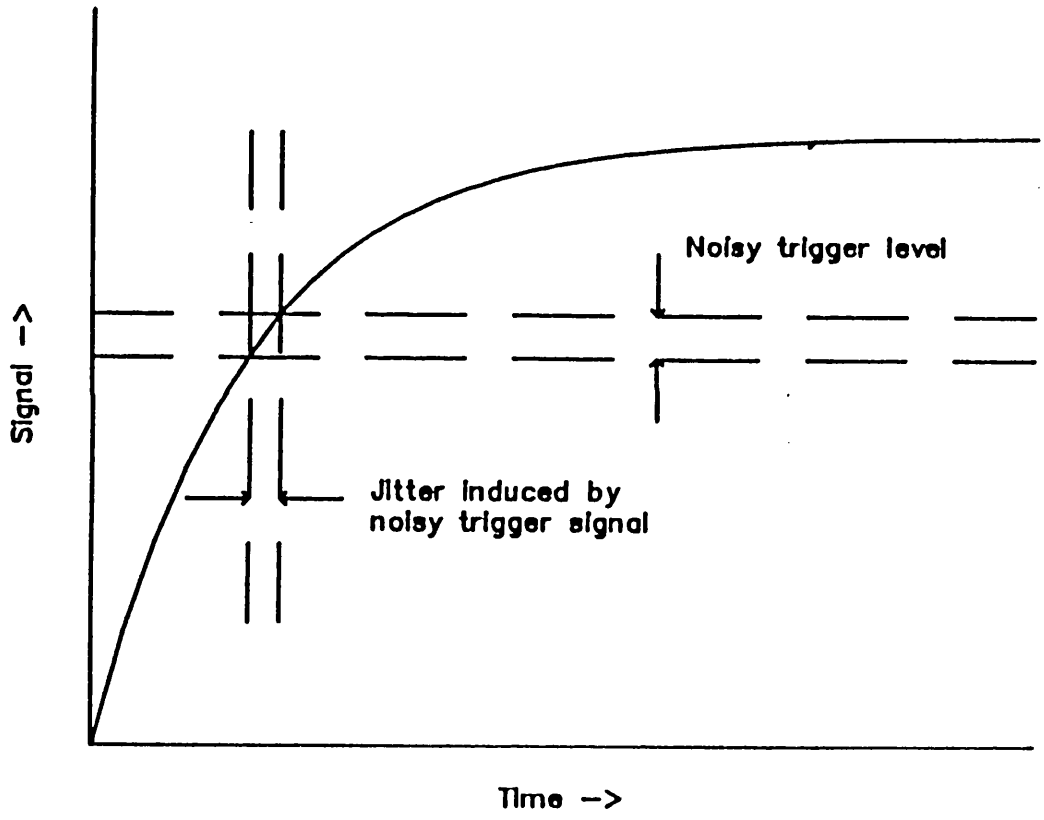

Figure 3.1. Origin of the Jitter effect

This effect, called jitter, causes a distortion of the original signal which cannot be removed by averaging. The measured signal, for an infinite number of samples, is the convolution of the true signal and the probability density function of the jitter (equation 1):

$$g(t) = \int_{-\infty}^{\infty} \phi(\tau)\ f(t-\tau)\ d\tau \qquad \text{(eq. 1)}$$

where g(t) is the mean of the measured signal; f(t) is the original signal; and ϕ is the probability density distribution of the jitter.

The effects of jitter have been studied by *W Ganz*[24] at the National Bureau of Standards and a method for correction of jittered signals has been tested using their Automatic Pulse Measurement system[25].

In this chapter the effects of jitter and noise on a waveform are explored using simulated data; and an algorithm for removing the effects of jitter is described. Two methods for measuring jittered signals are described and the results are processed to remove the jitter.

3.2. EFFECT OF JITTER ON VARIANCE AND EXPECTED VALUE OF THE MEASURED SIGNAL

The measured signal will have a variance function $\sigma^2(t)$ which will be a function of the original signal and the probability density distribution of the jitter as shown in equation 2. This can be written in a more convenient form (equation 3):

$$\sigma^2(t) = \int_{-\infty}^{\infty} \phi(\tau)(f(t)-f(t-\tau))^2 d\tau \qquad \text{(eq. 2)}$$

$$\sigma^2(t) = f^2(t) - 2f(t)g(t) + \int_{-\infty}^{\infty} \phi(\tau)f^2(t-\tau)\, d\tau \qquad \text{(eq. 3)}$$

where g(t) is the jittered response; and f(t) is the original response.

The effect of jitter on the expected value and variance of a measured signal can be assessed by a adding noise and jitter to a known response. The deconvolved response of the Plessey #20 diode (figure 2.16 from the previous chapter) has been used. This waveform has a a FWHM of 40.5 ps. At each temporal point the number of samples was chosen to be 1024. The noise and jitter probability density functions are both Gaussian. The mean value and standard deviation at each temporal point can be plotted together with the original signal. The effects of noise only (50 mV rms), jitter only (25 ps FWHM) and

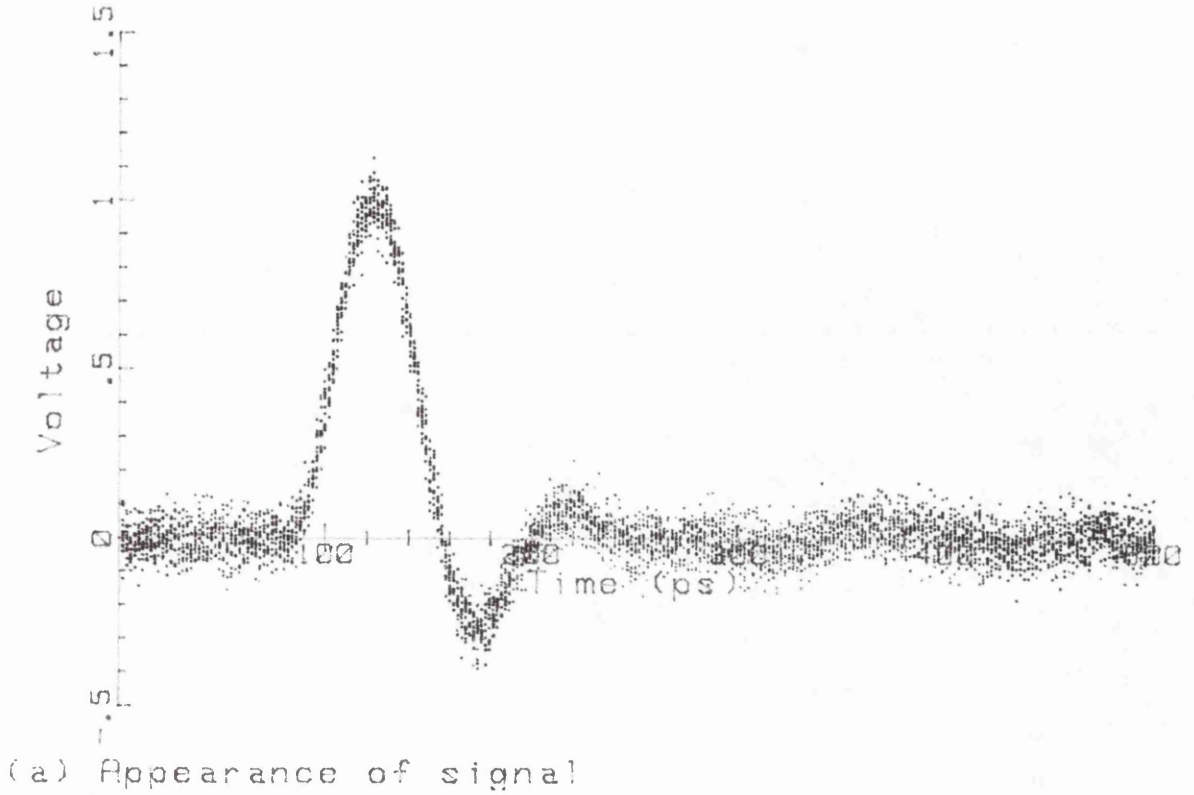

(a) Appearance of signal

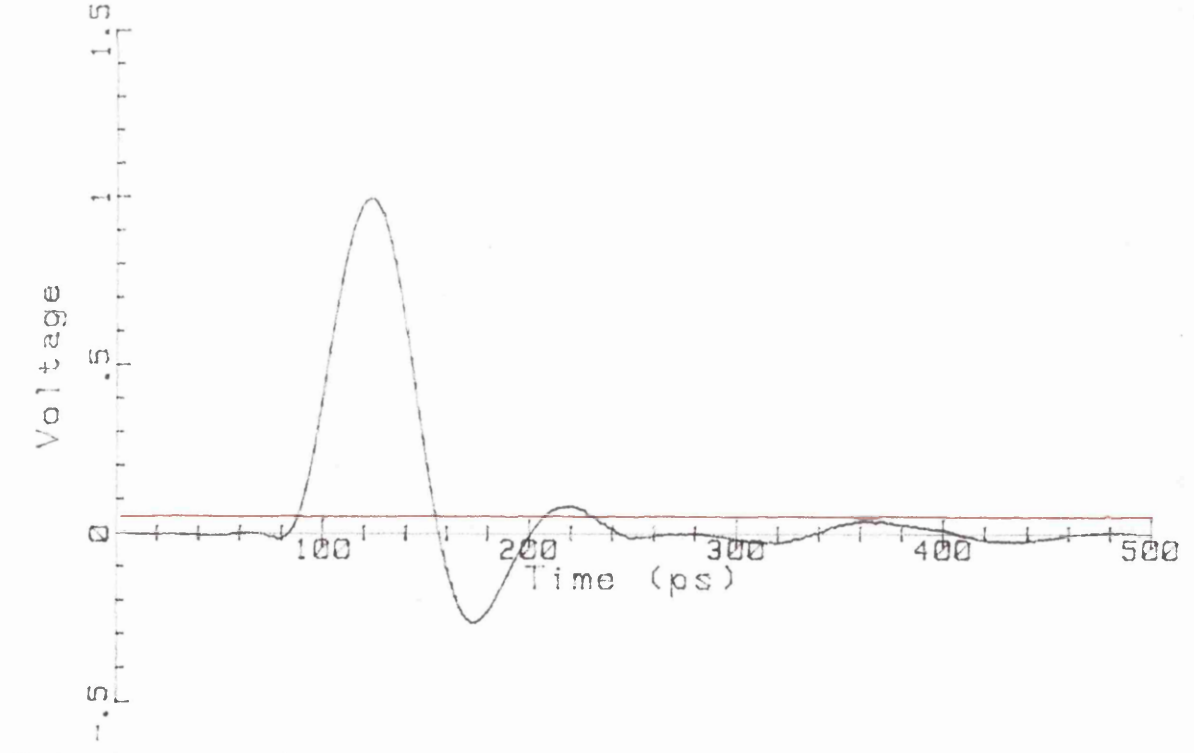

(b) Mean and standard deviation

Figure 3.2. Effect of 50 mV rms noise on the signal

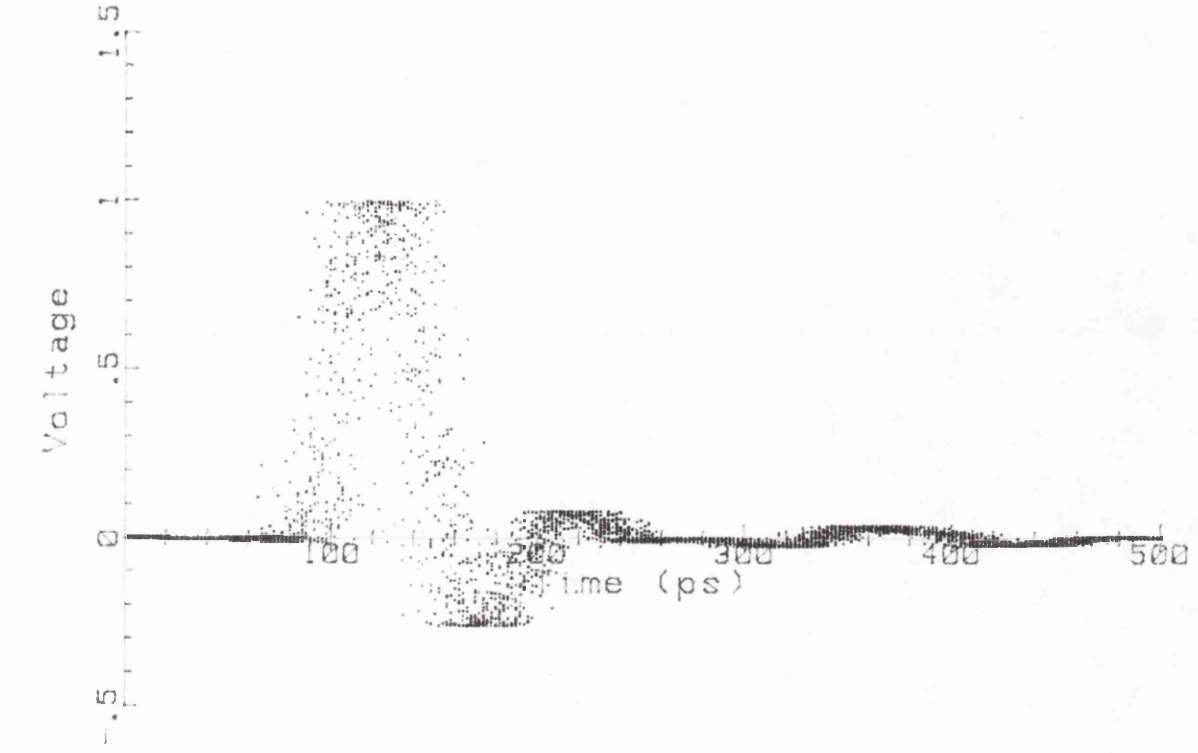

(a) Appearance of signal

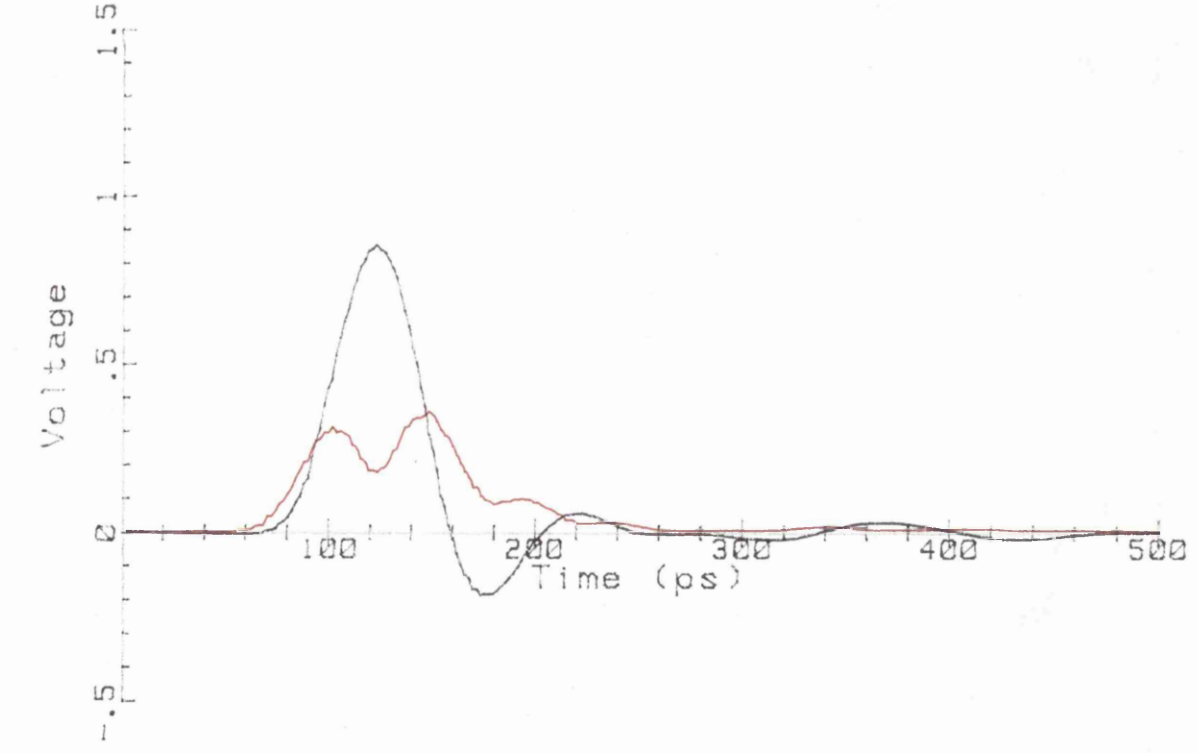

(b) Mean and standard deviation

Figure 3.3. Effect of 25 ps FWHM Jitter on the signal

(a) Appearance of signal

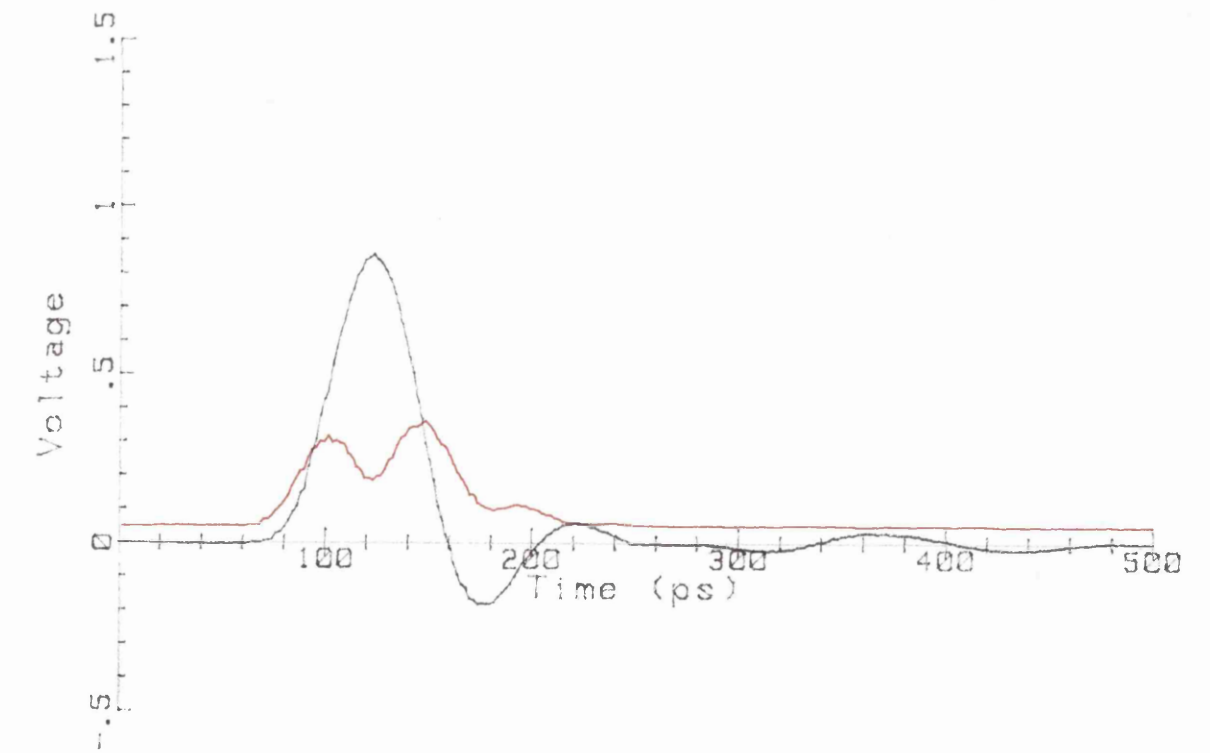

(b) Mean and standard deviation

Figure 3.4. Effect of 50 mV rms noise + 25 ps FWHM Jitter on the signal

both noise and jitter (50 mV rms + 25 ps FWHM) are shown in figures 3.2, 3.3 and 3.4 respectively. Each figure is divided into two parts: part (a) shows a fraction of the data (16 samples) so that the effects can be gauged, and part (b) shows the mean and standard deviation of the signal at each point.

Figure 3.2 shows that the effects of noise can be removed by averaging; this result is expected. Figures 3.3 and 3.4 show that the jitter has introduced a distortion of the measured signal that is independent of the added noise. The standard deviation of the jittered signals is not constant as a function of time; though the standard deviation curves plotted in figures 3.3 and 3.4 differ slightly.

In the previous example the mean and standard deviation were plotted. The standard deviation was chosen for the plot in preference to the variance because this allowed a direct comparison with the mean. The effects of noise and jitter are statistically independent and therefore the measured variance will comprise of two terms (equation 4):

$$\sigma_m^2(t) = \sigma_j^2(t) + \sigma_n^2(t) \qquad \text{(eq. 4)}$$

where $\sigma_m^2(t)$ is the measured variance; $\sigma_j^2(t)$ is the jitter contribution; and $\sigma_n^2(t)$ is the noise contribution.

The noise contribution will be approximately constant, limited by the number of samples, and will therefore give an offset to the results. The shape of the variance function is the key to the removal of the jitter.

Signal dependent jitter

The jitter described in the previous example was statistically independent of the signal amplitude. If the amplitude of the signal contains a noise component then the measured standard deviation will be a function of the pulse shape. This is illustrated in figure 3.5 using the diode response example with an amplitude variation of 100 mV rms at the peak (10%).

If the trigger signal for the sampling oscilloscope is derived from the signal being measured then fluctuations in the signal amplitude will give rise to variations in the triggering point. This is shown in figure 3.6.

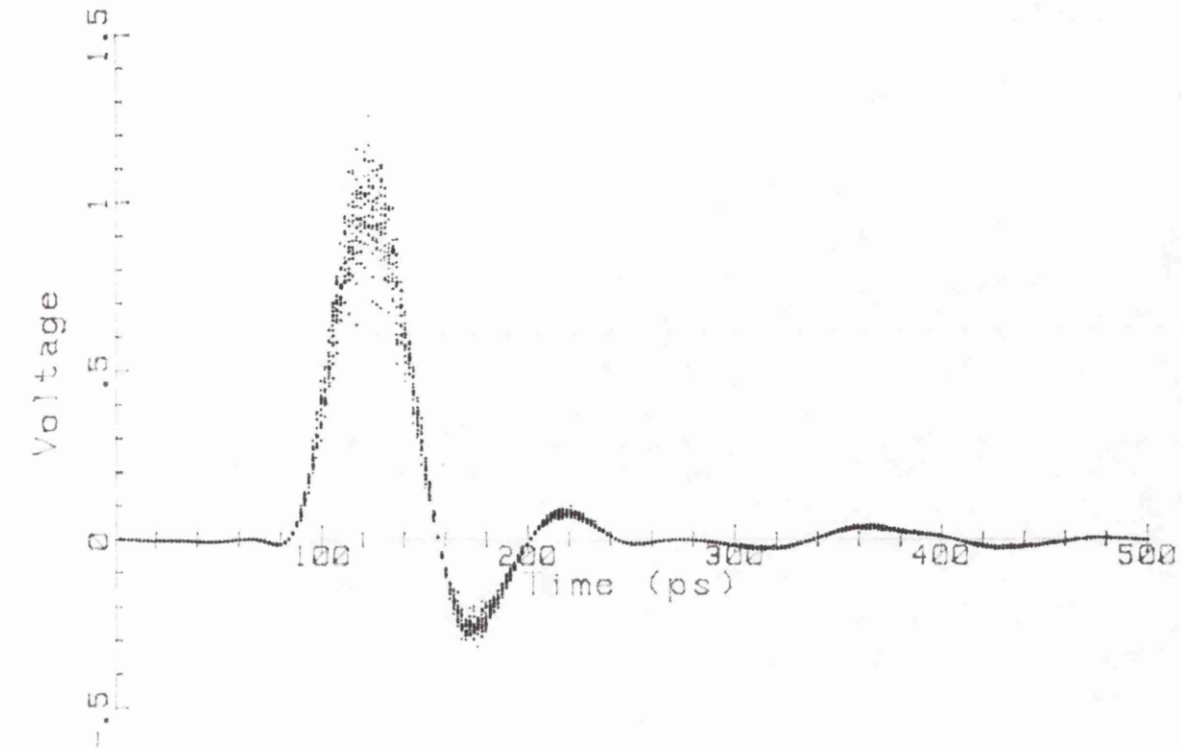

(a) Appearance of signal

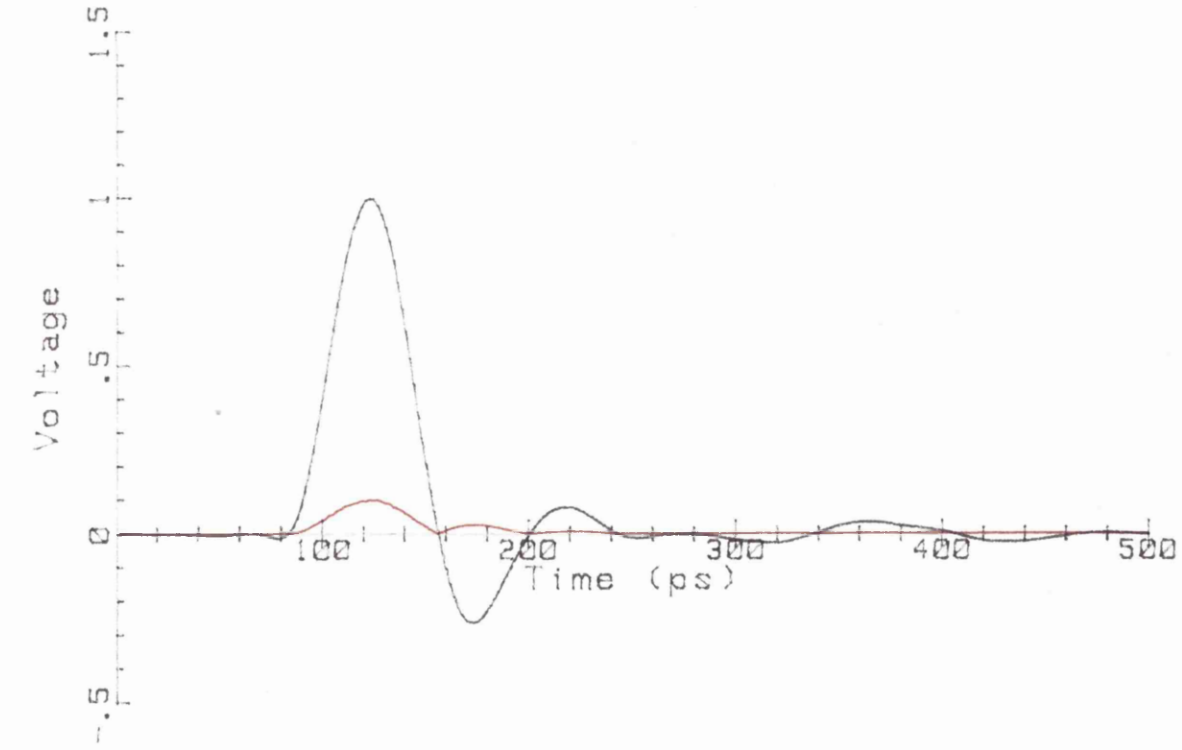

(b) Mean and standard deviation

Figure 3.5. Amplitude dependent noise

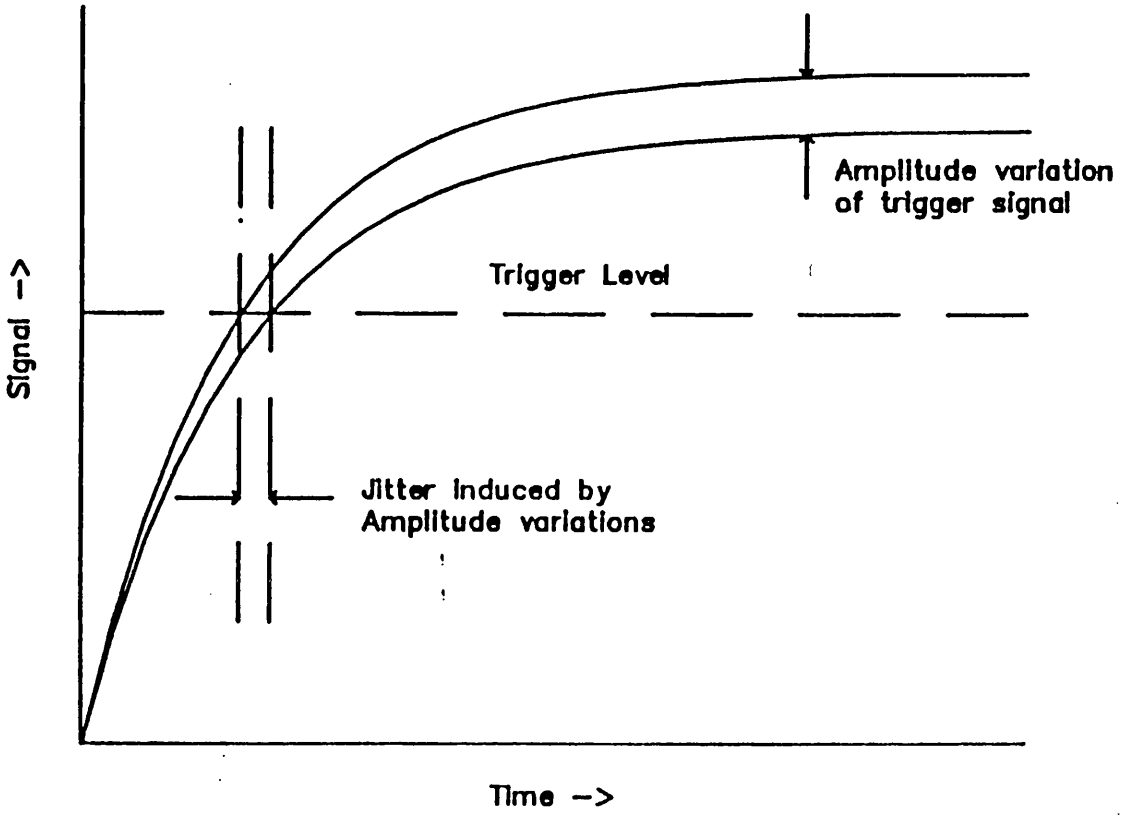

Figure 3.6. Amplitude variation induced jitter

If the variations in the trigger signal are correlated with the variations in the amplitude of the signal this will give rise to a systematic jitter. This systematic jitter is illustrated using the waveform example with a linear dependence of the trigger time on the trigger signal amplitude. The result is shown in figure 3.7. In this example the amplitude variations and jitter were exactly correlated though; in practice this would not be the case.

In this example the mean and standard deviation show some asymetry when compared with the results shown in figure 3.3. The mean and variance can be calculated by modifying equations 1 and 2 as shown in equations 5 and 6:

$$g(t) = \int_{-\infty}^{\infty} \phi(\tau)(1+A\tau)\, f(t-\tau)\, d\tau \qquad \text{(eq. 5)}$$

$$\sigma^2(t) = \int_{-\infty}^{\infty} \phi(\tau)(f(t)-(1+a\tau)f(t-\tau))^2 d\tau \qquad \text{(eq. 6)}$$

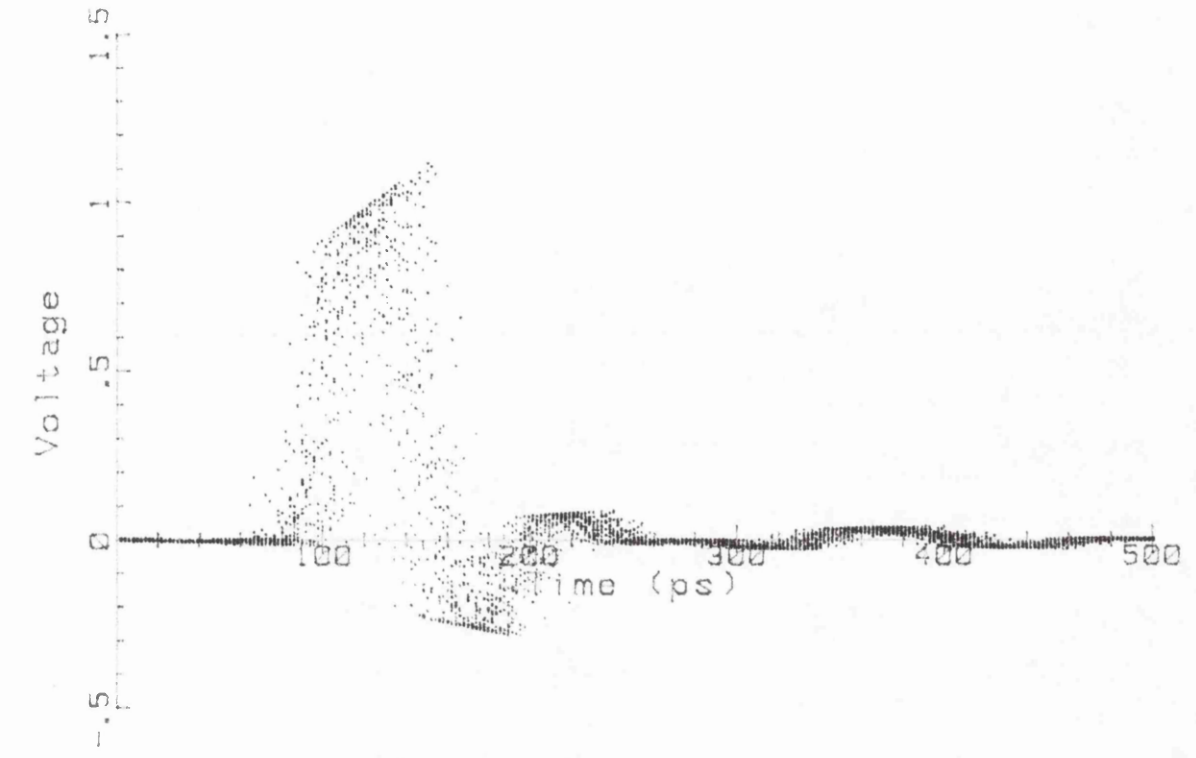

(a) Appearance of signal

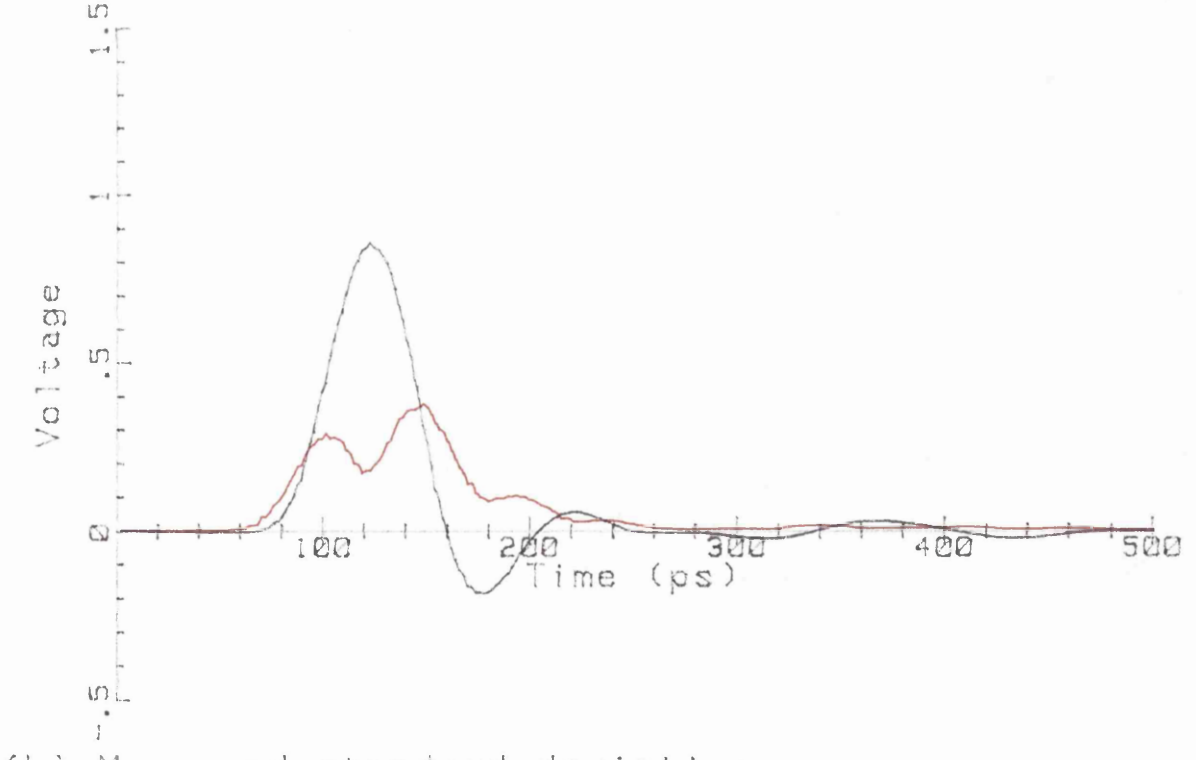

(b) Mean and standard deviation

Figure 3.7. Effect of amplitude induced jitter

where A is the rms amplitude variation of the signal.

Systematic jitter will not be considered further in this analysis, nevertheless the techniques described in the following section can be used to remove this type of jitter.

3.3. REMOVAL OF THE EFFECTS OF JITTER BY A DECONVOLUTION TECHNIQUE

The deconvolution techniques discussed in the previous chapter can be used to make an estimate $f_e(t)$ for the unjittered signal response, from the measured signal $g_m(t)$, provided the probability distribution of the jitter $\phi_j(t)$ is known. The estimate for the unjittered signal $f_e(t)$ can then be used to calculate an estimate for the variance $\sigma_e^2(t)$. The measured variance will contain contributions, due to both jitter and noise, which are statistically independent. The noise contribution will be constant at each point. If the estimated variance $\sigma_e^2(t)$ is compared with the measured variance $\sigma_m^2(t)$ the difference between the shape of two curves can be used to determine the accuracy of the estimate of the jitter (equation 7):

$$E(t) = \sigma_m^2 - \sigma_e^2 \qquad \text{(eq. 7)}$$

where σ_m^2 is the variance of the measured signal; σ_e^2 is the variance calculated from the de-jitterd estimate of the signal.

If the estimate for the jitter and the deconvolved signal is good, then the error function E(t) will be a constant. A suitable figure of merit for the quality of fit is therefore the variance of the values of E(t) at each measurement point. The variance has been chosen in preference to the sum of squares as it removes the effect of the noise. The best value for the jitter parameter will give the lowest variance of the error.

To perform the deconvolution the jitter has been assumed to have a Gaussian probability density distribution. The NBS fourier transform deconvolution technique, described in the previous chapter, has been chosen, because the stabilising filter is optimal and introduces the minimum error into the result. This method requires a smoothing parameter γ to be supplied by the user. Too low a value for γ will give rise to excessive noise in the deconvolved result, which will in turn increase the estimated value of the variance function $\sigma_e^2(t)$. Too high a

value for γ will give an over filtered result, with an incorrect estimate for $\sigma_\epsilon^2(t)$. To improve the smoothness of the mean signal a bicubic spline[26] was fitted to the measured data prior to the deconvolution.

To find the optimum value of the jitter and smoothing parameters a simple search algorithm has been used. Both parameters must be positive and so the logarithm of the value was optimised. A Newton method was used to find the optimum jitter parameter. This is not an ideal choice of algorithm because it is dependent on the choice of starting point. If too low a value is chosen then the routine converges to zero jitter where the error is a maximum. The search for the optimum choice of smoothing parameter was performed by evaluating the error for a number of values and selecting the minimum. The step size was then refined to improve the accuracy. The initial value for the jitter can be estimated in the following manner. If the jitter is assumed to be small then a Taylor series expansion of the region about the measurement point yields the following equation, neglecting higher order terms:

$$\sigma_m^2 = \sigma_j^2 \left(\frac{d\ f(t)}{dt}\right)^2 \qquad \text{(eq. 8)}$$

If the gradient of the measured signal $\left(\frac{d\ g(t)}{dt}\right)$ is assumed to be a reasonable approximation to the true gradient, then this expression can be used to yield an initial estimate for the jitter. The contribution to the measured variance due to noise (σ_n^2) can be estimated on a part of the signal, where the gradient is low. The accuracy of the estimate can be improved by weighting the result proportional to the square of the gradient. The estimate for the jitter parameter $\sigma_{j(est)}^2$ is given by equation 9:

$$\sigma_{j(est)}^2 = \frac{\sum_{i=1}^{n} (\sigma_m^2(i) - \sigma_n^2)\left(\frac{d\ g_i}{dt}\right)^2}{\left(\sum_{i=1}^{n} \left(\frac{d\ g_i}{dt}\right)^4\right)} \qquad \text{(eq. 9)}$$

where n is the number of points; and $\sigma_m^2(i)$ is the variance of the signal measured at the i^{th} point.

The derivative of the mean response can be calculated directly from the fitted spline function. This greatly improves the smoothness of the result.

3.4. EVALUATION OF THE JITTER REMOVAL ALGORITHM USING SYNTHETIC DATA

The performance of the jitter removal algorithm was assessed using the simulated jitter data described in section 3.2. The signal with 25 ps FWHM jitter and 50 mV noise (figure 3.4) was chosen. Initially the starting values were chosen by hand to assess the operation of the optimisation routine. With starting values for the jitter of greater than 19 ps FWHM, the routine converged to find a minimum jitter of 24.4 ps FWHM. The estimated jitter is lower than the true jitter (25 ps). This is a systematic effect caused by the deconvolution process. The initial estimate of the jitter parameter found by equation 9 gave a value of 26.6 ps, which was a satisfactory starting point for the optimisation routine.

The results from the de-jittering routine are shown in figure 3.8. Part (a) shows the jittered data, the result after processing and the error between the original (unjittered) data and the de-jittered data. In part (b) the variance of the jittered data (σ_m^2) and the variance calculated from the de-jittered data (σ_e^2) are plotted together with the error between these two curves. The agreement between the two curves is good but shows a slight systematic error attributed to the deconvolution process. The de-jittering technique, tested with synthetically jittered data, works well. Some systematic errors, caused in this case by the deconvolution routine, will lead to a low estimate for the jitter.

The variation of the initial estimate and final value of the jitter parameter was investigated for jittered signals in the range 15 - 50 ps FWHM. The initial estimate was always higher than the true jitter and the final value was generally lower than the true value as shown in figure 3.9. The low estimate for the jitter parameter gave an incomplete removal of the jitter and hence a lowering of the peak signal. This effect is plotted in figure 3.10.

3.5. MEASUREMENT OF JITTER USING A DIGITISING SAMPLING OSCILLOSCOPE

The response of a Laser Diode Source and detector exhibiting jitter was measured using a Tektronix 11802 digital sampling oscilloscope. The experimental layout is shown in figure 3.11. An optical triggering arrangement was required because the electrical triggering was too unstable. This may introduce some additional systematic errors because

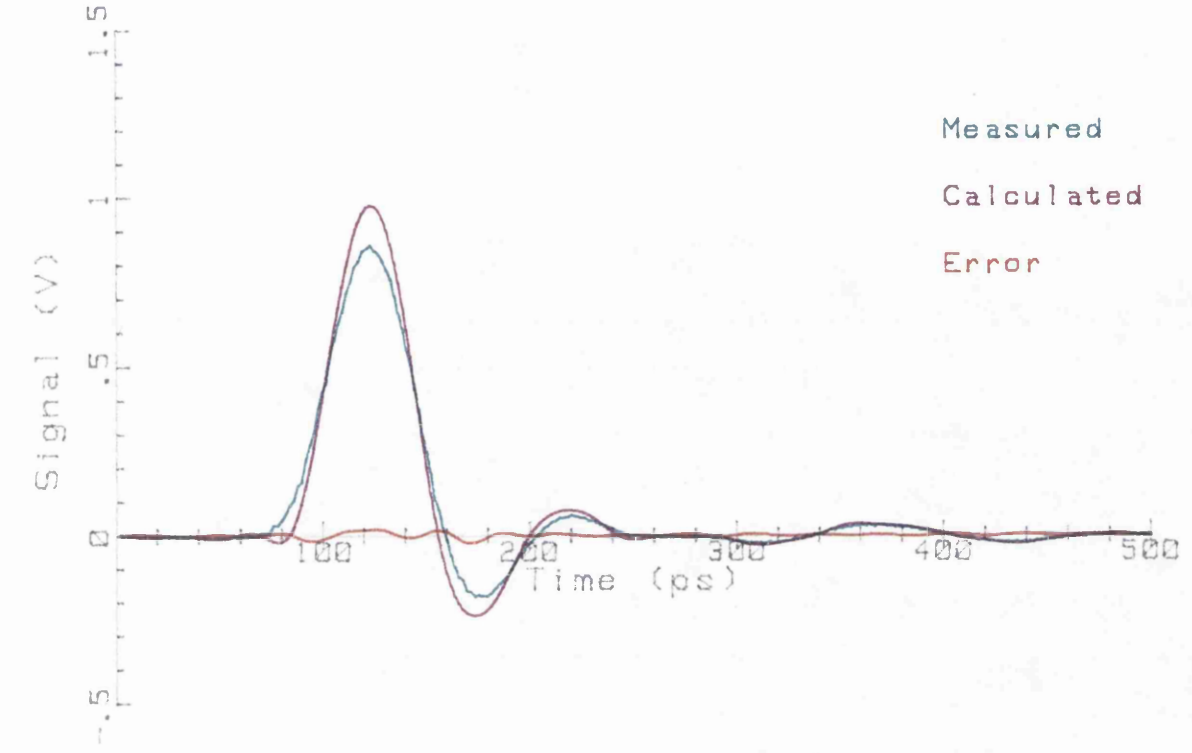

(a) Measured and calculated signals

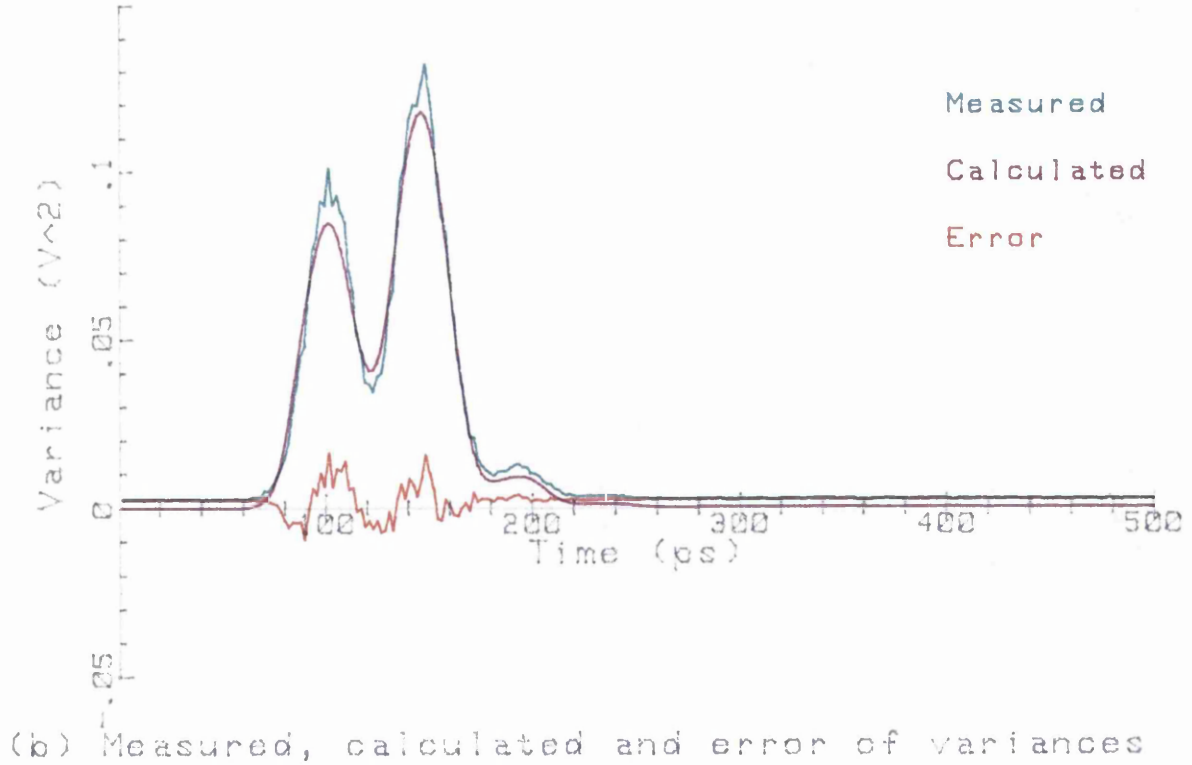

(b) Measured, calculated and error of variances

Figure 3.8. Removal of jitter from synthetically jittered data

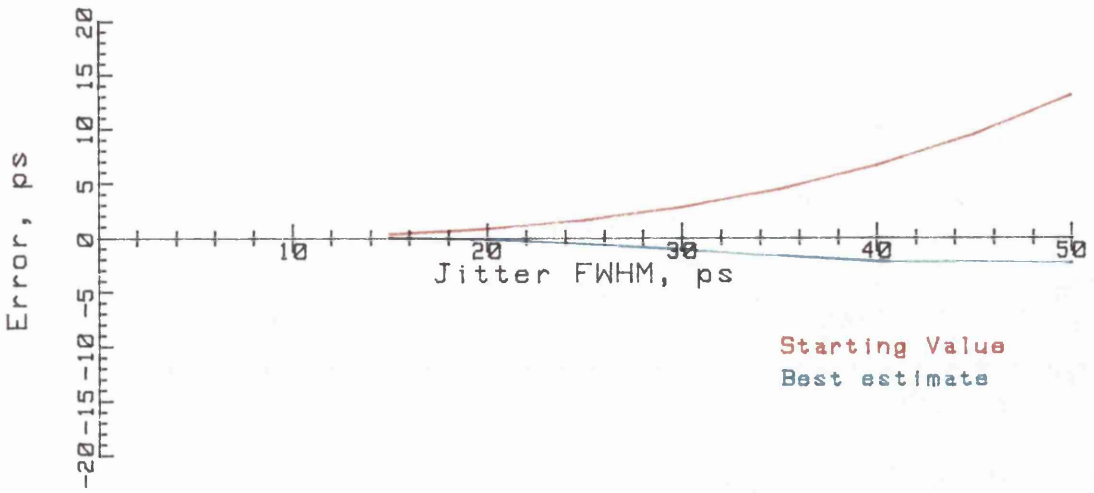

Figure 3.9. Errors in the initial estimate and final value of the jitter parameter

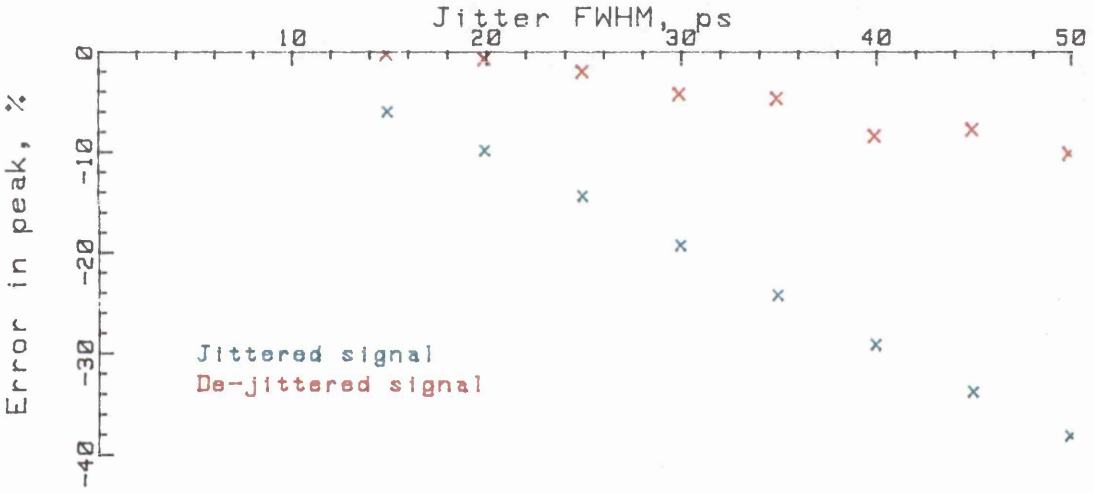

Figure 3.10. Reduction of the peak signal by incomplete removal of the jitter

of jitter correlated to amplitude fluctuations of the laser, described in section §3.2.

A total of 512 measurements were made. Each measurement consisted of a single sweep of 2048 points which were then sent to the computer using the IEEE-488 interface. This data acquisition technique takes roughly one second per set of measurement points. The amplitude stability of the laser is good but it is reasonable to expect that over a long period some drift would occur. A drift in the position of the pulse will have a similar effect to that of jitter, except that it is a

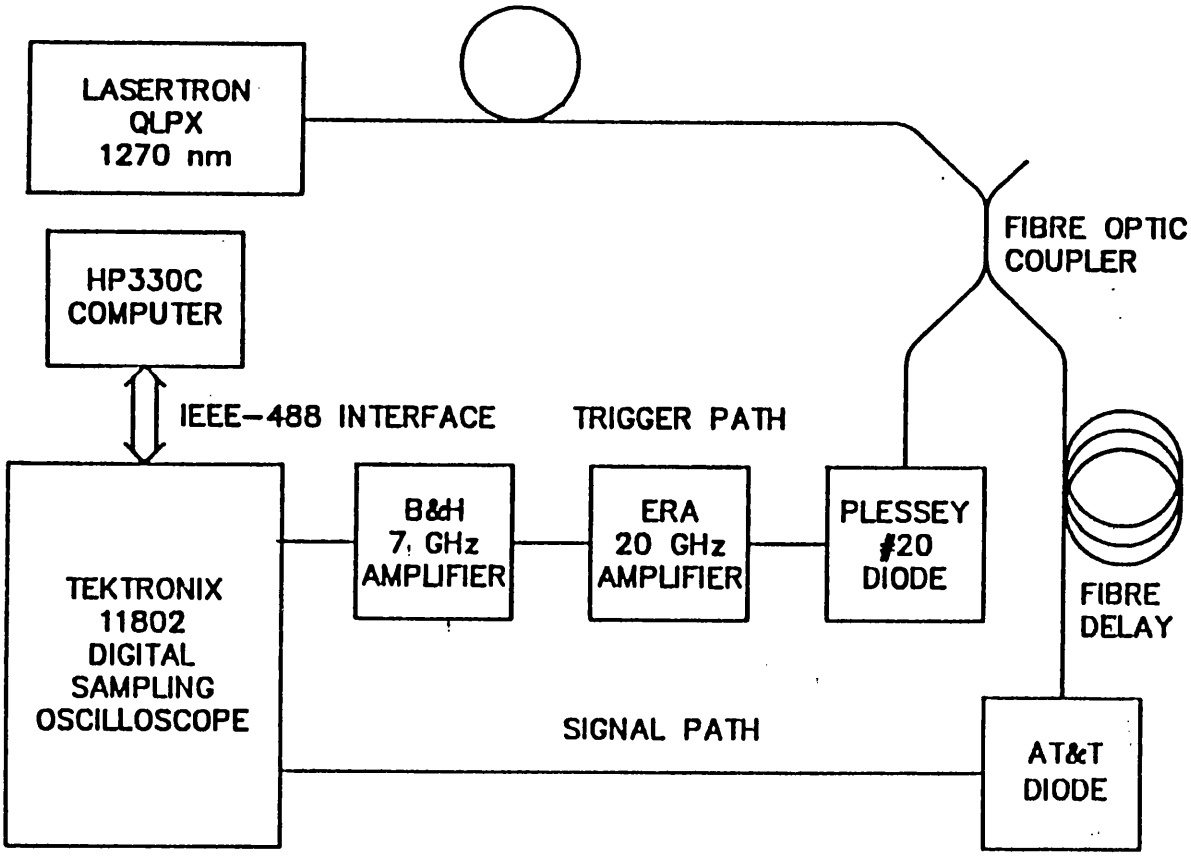

Figure 3.11. Experimental layout to measure jittered signals

systematic effect. The effect of drift can be compensated by applying an artificial drift, numerically, when processing the data. The drift was calculated as a function of the measurement number, using the modified adaptive drift compensation scheme described in the previous chapter (section 2.8). To avoid introducing errors by overcompensating the drift a bicubic spline was fitted to the results. This smooths the fluctuations due to noise and gives a better estimate of the overall drift. The measured drift and fitted spline are shown in figure 3.12.

A sample of the jittered data, corrected for drift, is shown in figure 3.13. The mean data is deconvolved to produce the estimate for the unjitterd signal. To improve the smoothness of the mean signal, a bicubic spline was fitted to the drift corrected mean. The FWHM of the mean corrected signal was 58 ps FWHM. The results were de-jittered and the best estimate for the jitter was 36 ps with a de-jittered signal of 48.8 ps FWHM. The mean of the measured and de-jittered signals are shown in figure 3.14(a). The measured and estimated variances are shown in figure 3.14(b), together with the error between the two curves. The measured and calculated variances show some dissagreement.

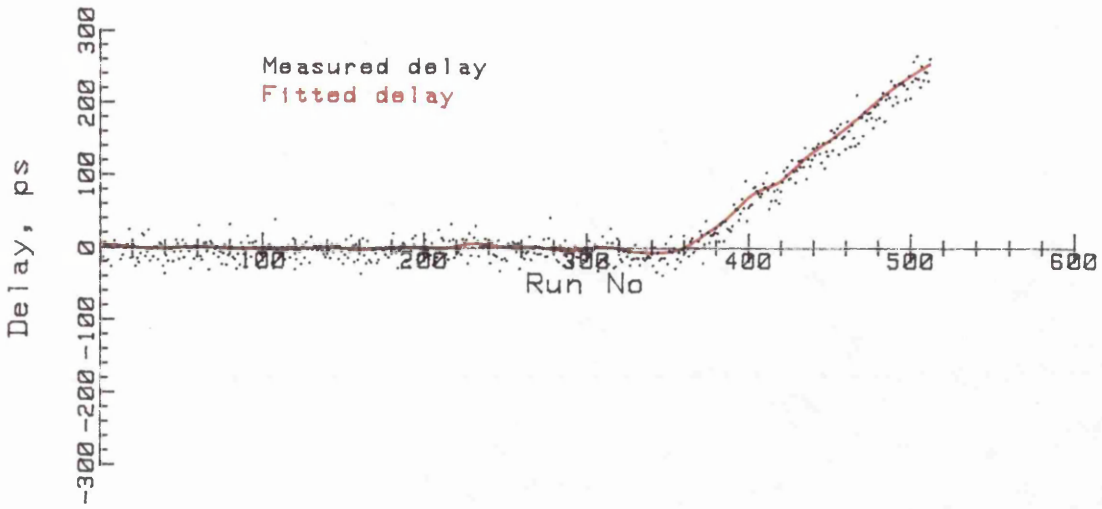

Figure 3.12. Drift of the jittered signal during the measurement

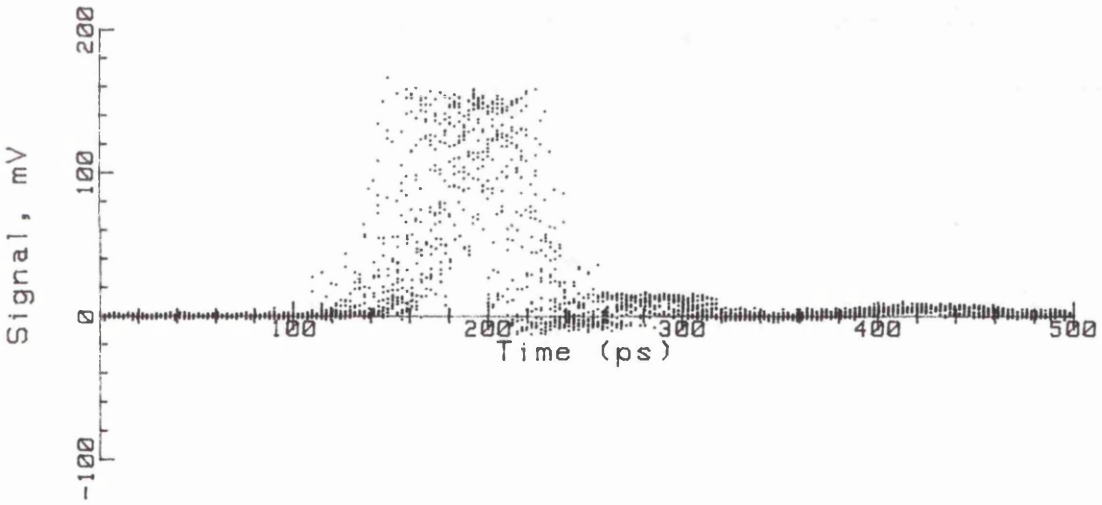

Figure 3.13. Jittered data (16 sets) measured using a sampling oscilloscope

This may be because the statistics of the jitter are not Gaussian.

3.6. MEASUREMENTS OF JITTERED SIGNALS USING DIGITAL VOLTMETERS

The measurement method used in the previous section was limited by the time taken to acquire the data. If the same technique were employed with the previous generation of sampling oscilloscopes the time to transfer the data to the computer would be prohibitive. Alternative faster techniques are therefore required to measure jittered signals using these instruments.

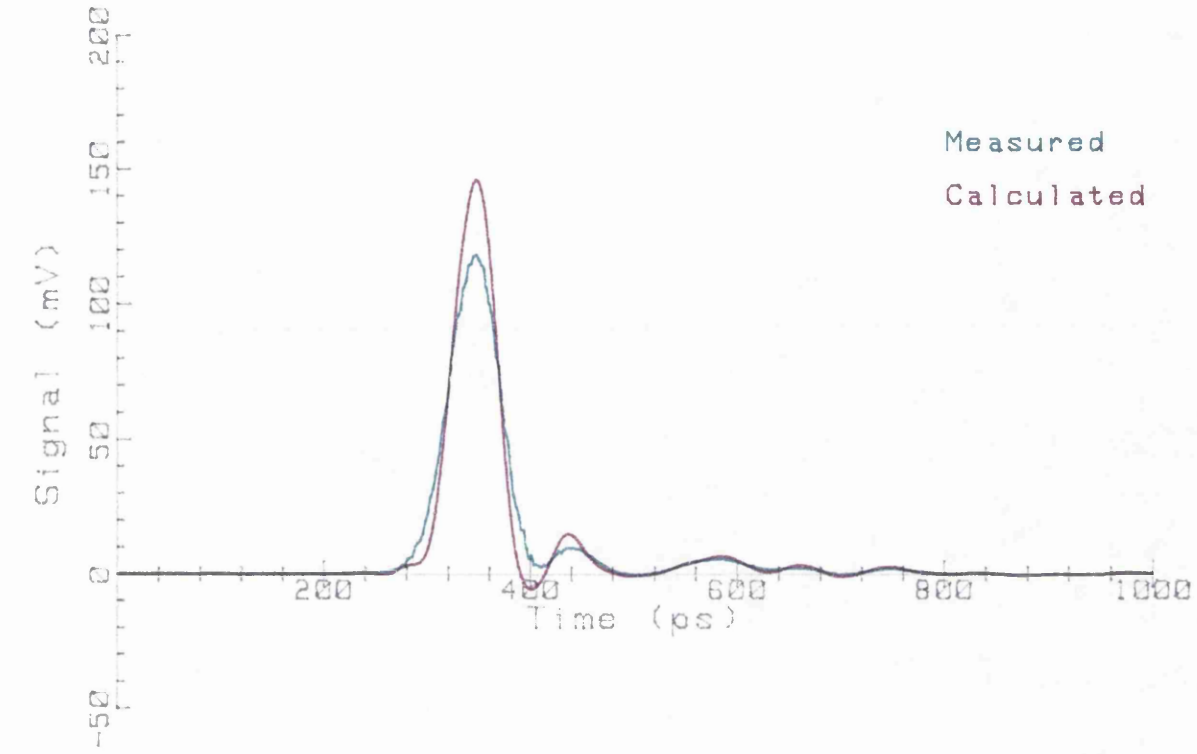

(a) Measured and calculated signals

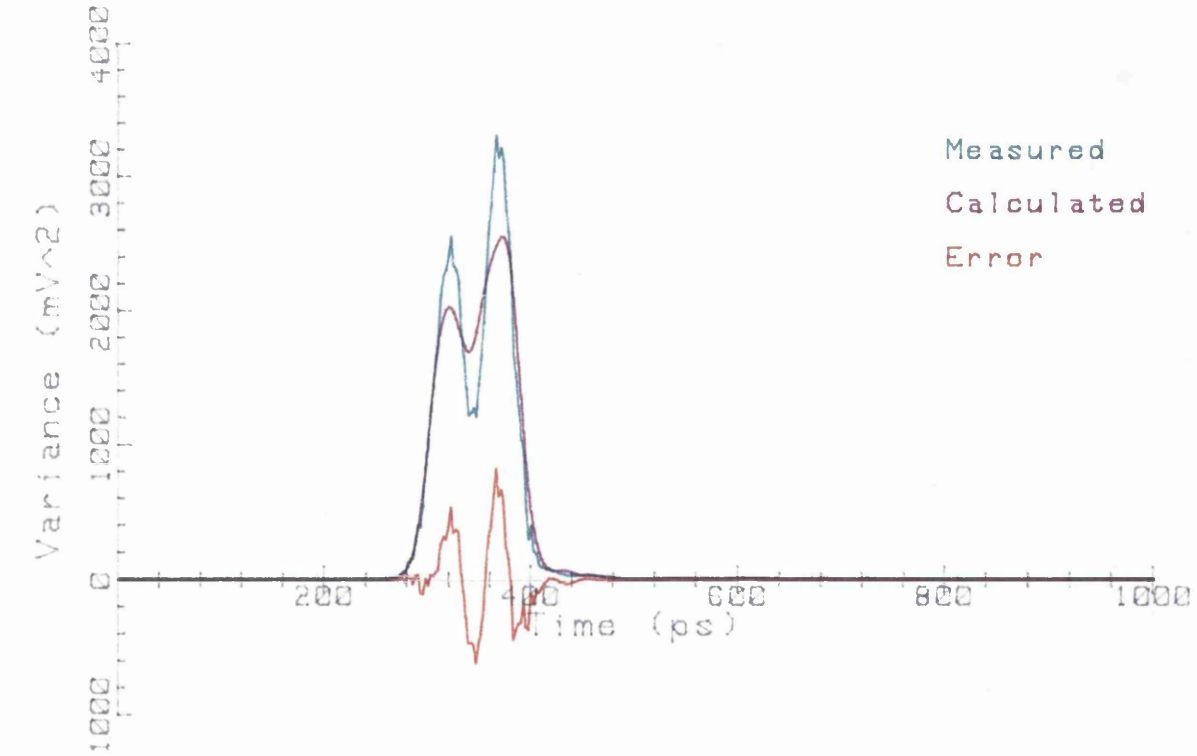

(b) Measured, calculated and error of variances

Figure 3.14. Removal of jitter from sampling oscilloscope measurements

Digital voltmeters (dvm) with 'true rms' measurement capabilities for ac can be used to measure the standard deviation directly, because this corresponds to the rms voltage, corrected for the dc level. By employing two dvms the mean and standard deviation can be measured as the dc and ac components of the signal. The frequency response of a typical true rms dvm, Fluke model 8840A, extends from 45 Hz to over 10 kHz. No correction for the dc level is required and the standard deviation can be measured directly as the ac component of the signal.

The maximum internal triggering rate for a Tektronix 7S12 or 7S11/7T11 sampling system is roughly 40 kHz. This is greater than the maximum frequency response of the voltmeter and may lead to low readings. To test the effect of trigger rate on the measured rms voltage a noise source was measured at a variety of trigger rates. Figure 3.15 shows the variation of the measured rms voltage as a function of trigger rate. The error bars correspond to 95% confidence intervals determined from the number of measurements at each point. The results indicate that at high frequencies the measured ac component will be low. This can be corrected by scaling. Nevertheless, a systematic effect caused by a change in the statistical distribution of the noise may occur at the peak of the signal. This cannot be corrected but the effect is expected to be negligable. The disadvantage of employing two separate instruments to measure the mean and the standard deviation is that errors of calibration between the two instruments may give rise to incorrect estimates for these parameters.

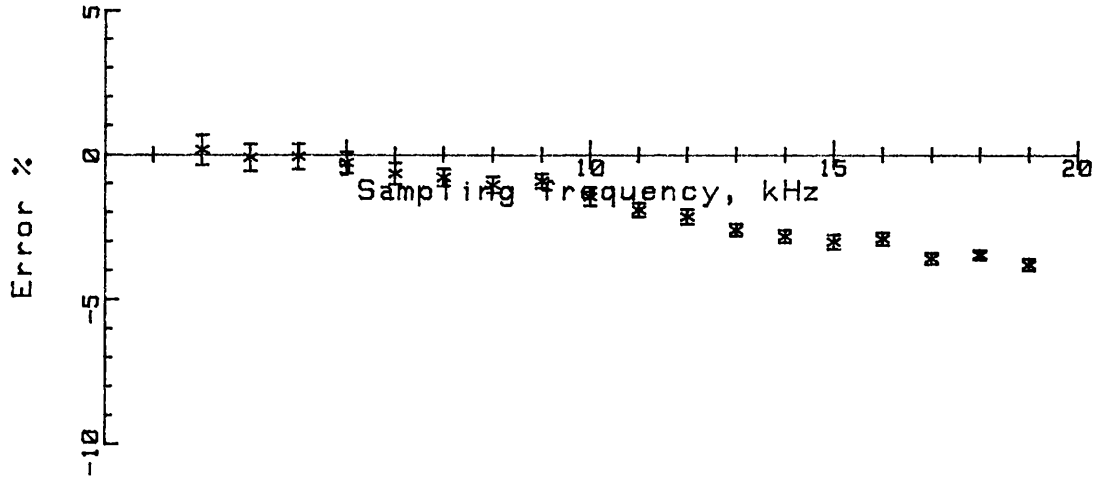

Figure 3.15. Error in the measured AC signal with sampling rate

Assessment of the method

A measurement has been made of the Lasertron pulse laser diode source at 1270 nm. The measurement system is shown schematically in Figure 3.16. The sampler is controlled by applying an external control voltage of 0 - 10.24 V from a programmable power supply (HP6632A). A time base calibration was not performed in this case and a value of 100 ps/V was assumed, this will be accurate to within ± 5%. A low pass filter with 100 ms time constant was included in the dc path to improve the noise performance.

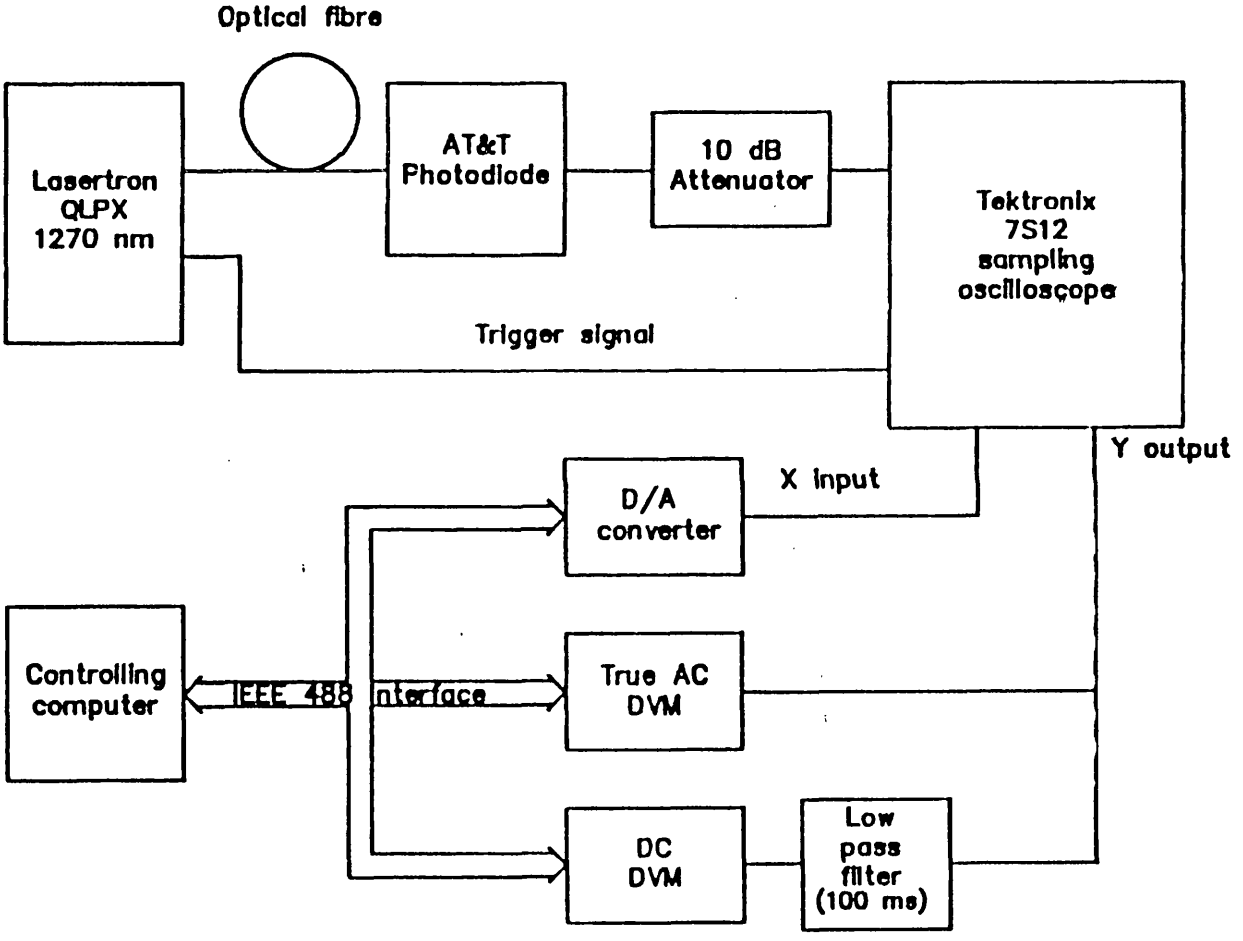

Figure 3.16. Measurement of jittered signals using digital voltmeters

The Fluke digital voltmeters used for the experiment have three measurement rates: 2.5, 50 and 100 readings per second, which can be programmed over the IEEE-488 interface. Measurements made on the slow reading rate give a smooth result with little noise. Measurements made at the medium reading rate show considerable noise for a single sample. The noise could be reduced by averaging though this gave little improvement over the lower reading rate. Measurements at the highest

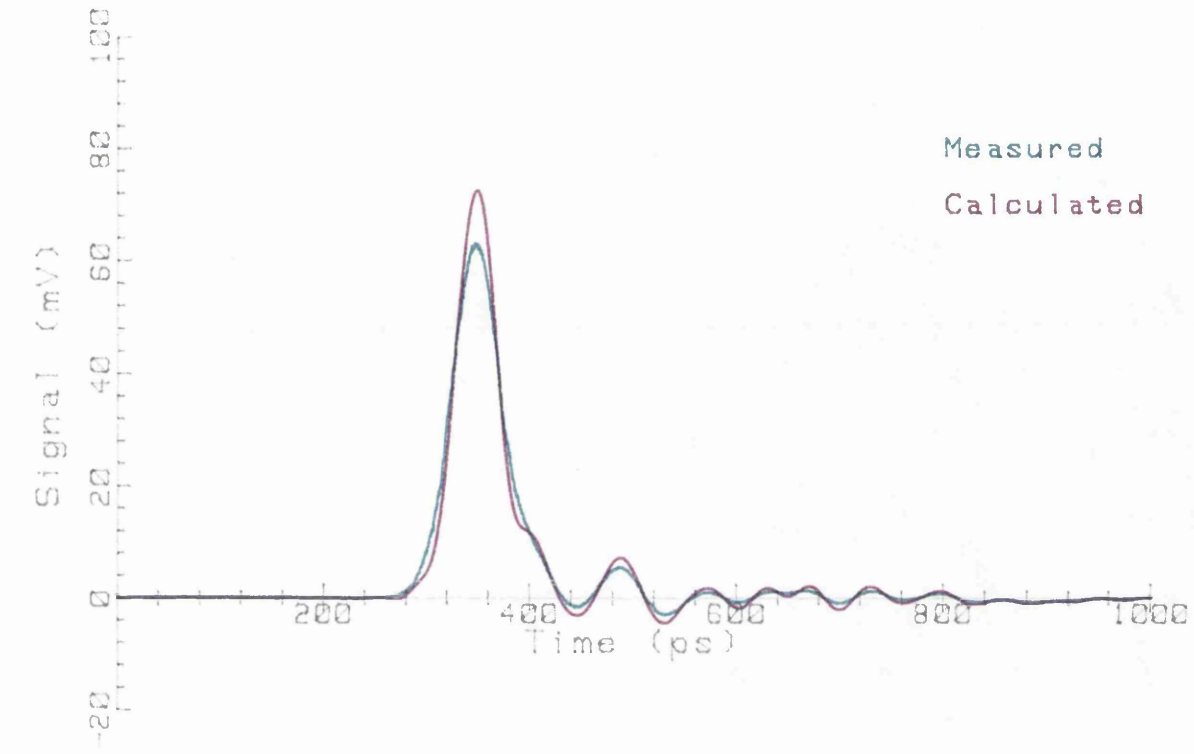

(a) Measured and calculated signals

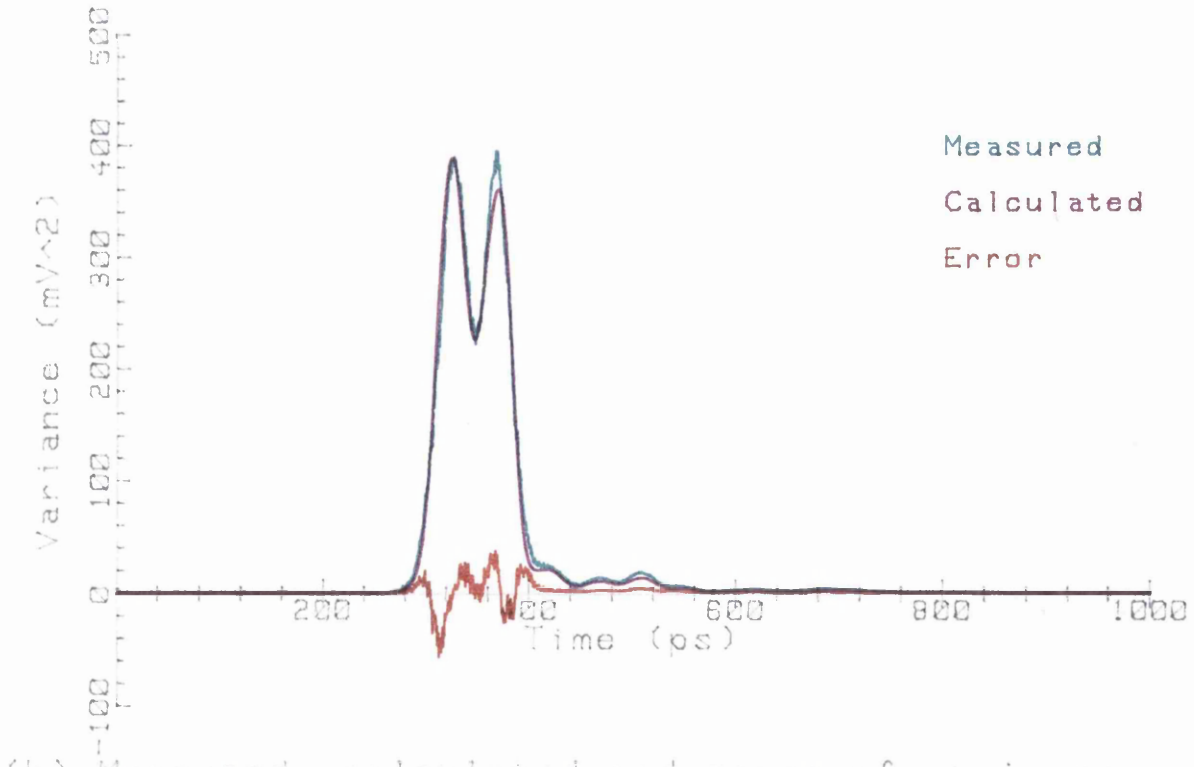

(b) Measured, calculated and error of variances

Figure 3.17. Measured and de-jittered response of the Lasertron diode, slow measurement rate

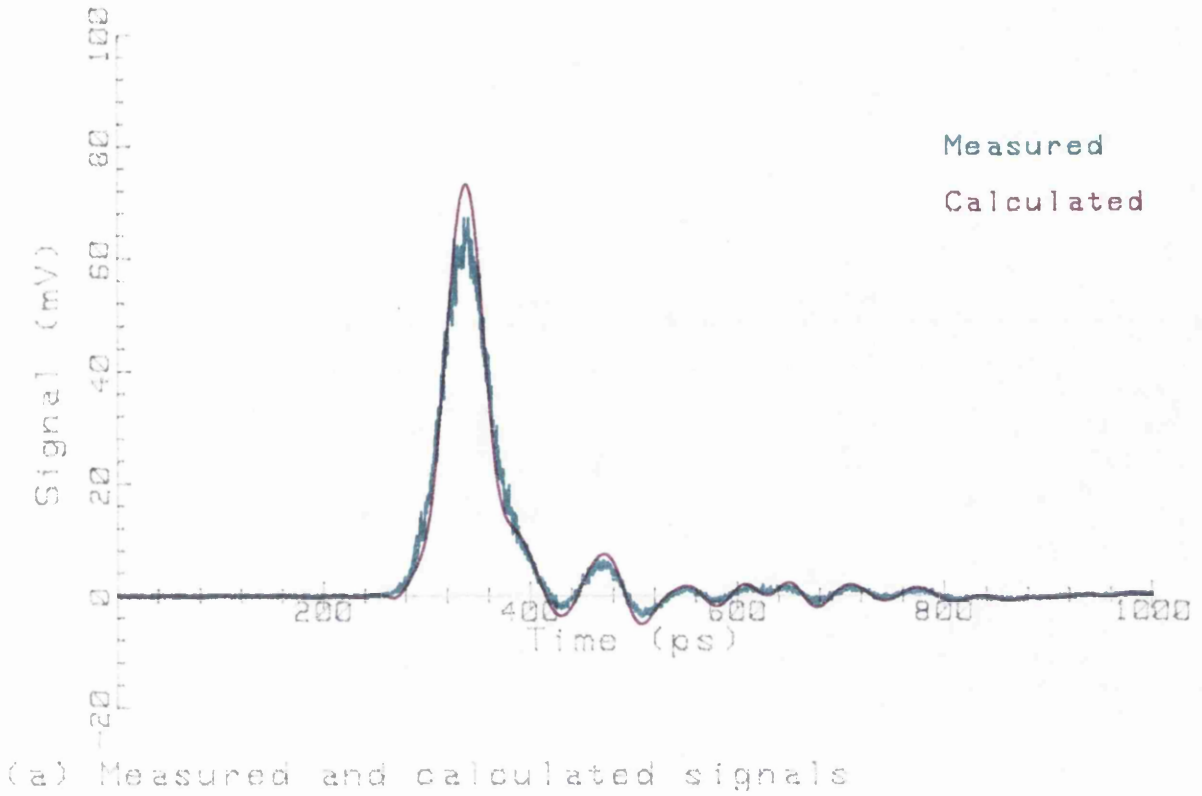

(a) Measured and calculated signals

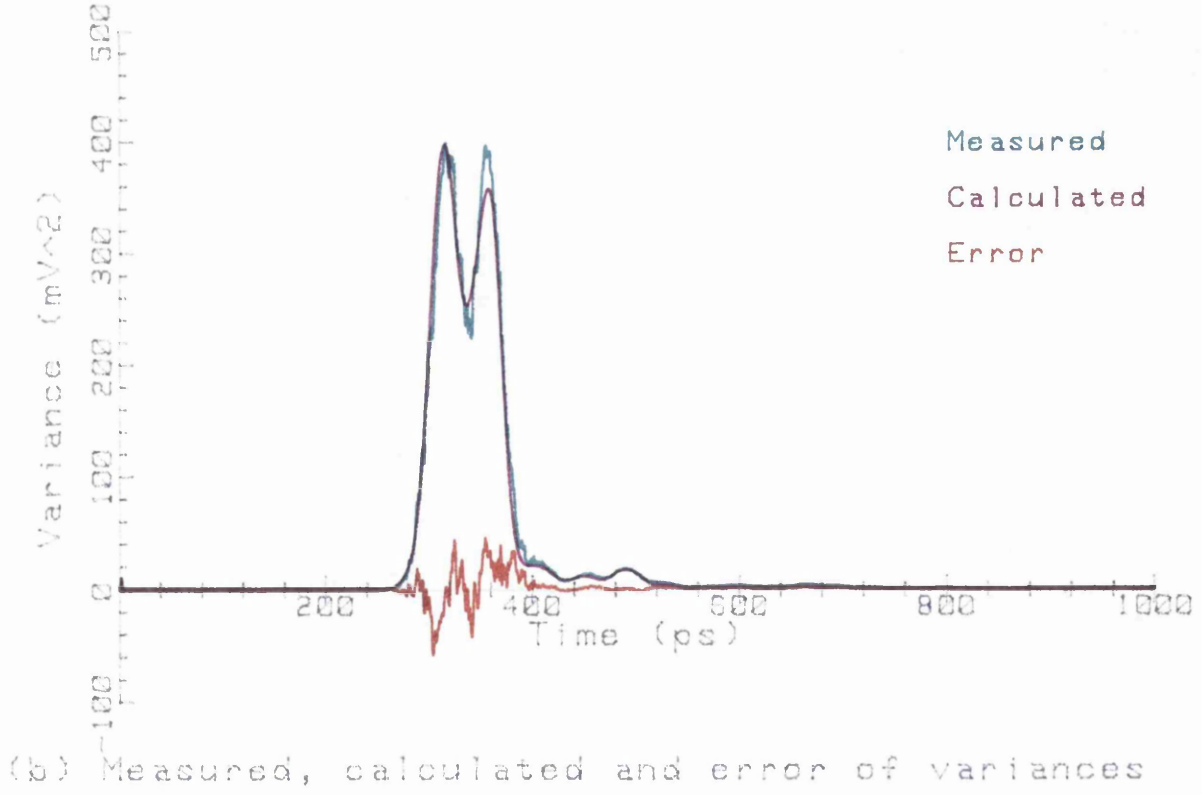

(b) Measured, calculated and error of variances

Figure 3.18. Measured and de-jittered response of the Lasertron diode, medium measurement rate

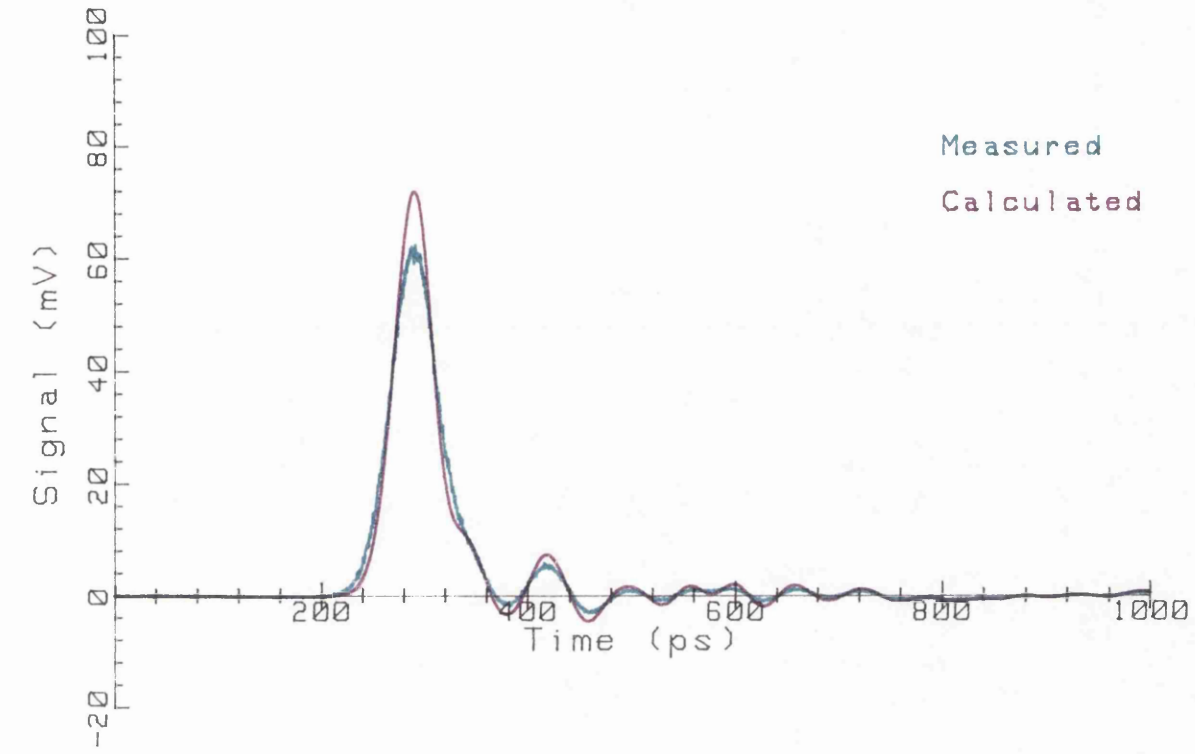

(a) Measured and calculated signals

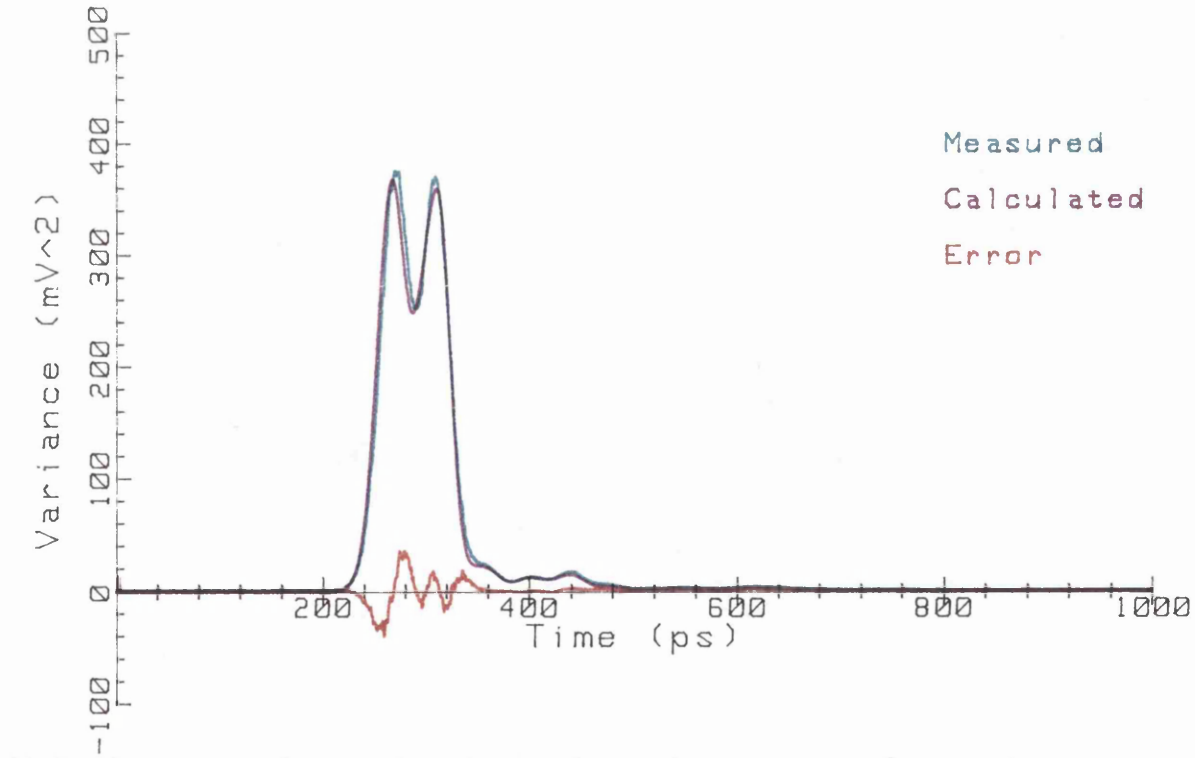

(b) Measured, calculated and error of variances

Figure 3.19. Measured and de-jittered response of the Lasertron diode, average of 10 results, medium measurement rate

reading rate were too noisy to be of use.

The three sets of measurements, corrected for the reading rate error, have been processed to remove the jitter. The results are shown in figures 3.17, 3.18 and 3.19, together with the de-jittered response and the measured and estimated variances. A summary of all the results is given in table 3.1.

Table 3.1 Summary of the measured and de-jittered results

Measurement parameters		Measured results		De-jittered results		
Reading rate	No of averages	FWHM (ps)	Peak signal (mV)	Jitter FWHM (ps)	FWHM (ps)	Peak signal (mV)
slow	1	54.3	62.7	27.4	46.2	72.5
fast	1	50.8	67.3	27.0	44.2	73.3
fast	10	53.5	61.4	27.2	44.4	72.0

The de-jittered results for the three measurements show a good fit between the measured and estimated variance functions. The higher noise on figure 3.18 did not affect the result greatly. At present the routine to remove the jitter is fairly slow, limited by the time to perform the Fourier transforms. The use of dedicated hardware to perform the transforms would greatly improve the speed of the algorithm, allowing near real-time measurement and processing of jittered signals.

The data aquisition method presented here is simple and cheap to implement. The method will contain some systematic errors caused by differences in calibration between the ac and dc voltmeters, and by the bandwidth of the ac voltmeter.

3.7. CHAPTER SUMMARY

In this chapter the effects of noise, jitter, amplitude noise and amplitude noise correlated jitter have been assessed using synthetic data. A novel algorithm for the reduction of the effects of the jitter

has been presented. This algorithm has been evaluated using synthetically jittered data.

Measurement techniques suitable for the latest generation of digital sampling oscilloscopes and the previous generation of analogue sampling oscilloscopes have been described. Potential sources of systematic errors in these methods have been identified. The signals measured by these methods have been processed to remove the effects of jitter. The results show acceptably low errors between the calculated and measured variance functions, suggesting that the de-jittered signal is a good approximation to the original.

4. DISCUSSION AND FURTHER WORK

In chapter 2 the concept of deconvolution was discussed and a variety of techniques described. A fourier transform method, developed by *Nahman* and *Guillame* has been adapted to simplify the comparison of photodiodes measured using different pulsed laser diode sources. The deconvolution algorithm has been extended to allow multiple sets of measurements to be combined to give a single deconvolved result. The methods developed here give a clear and easily interpreted result suitable for use by non-specialists.

Work in this area will continue as an algorithm which estimates the value of a missing or uncertain point is required. Such a technique would be useful for overcoming systematic errors in the measurement system.

In chapter 3 the effects of noise, jitter, amplitude noise and amplitude noise correlated jitter have been assessed using synthetic data. A novel algorithm for the reduction of the effects of the jitter has been evaluated using the synthetically jittered data. Measurement techniques suitable for the latest generation of digital sampling oscilloscopes and the previous generation of analogue sampling oscilloscopes have been described. Potential sources of systematic errors in these methods have been identified. The signals measured by these methods have been processed to remove the effects of jitter. The results show acceptably low errors suggesting that the de-jittered signal is a good approximation to the original.

The algorithm currently used assumes that the statistics of the jitter are known. If the distribution of the measured values at each temporal point is known then it may be possible to determine the jitter probability density distribution. It is hoped that further work in this area may lead to an improved algorithm for the removal of the jitter.

5. REFERENCES FOR PART 2

1. *R N Bracewell*: 'The Fourier transform and its applications' McGraw-Hill, ISBN 0-07-Y66196-0, 1978.

2. *S M Bozic*: 'Digital and Kalman filtering', Edward Arnold ISBN 0 7131 3410 0, 1979.

3. *N S Nahman* and *M E Guillaume*:'Deconvolution of time domain waveforms in the presence of noise', NBS Technical note 1047, October 1981.

4. *T K Sarkar, D D Weiner* and *V K Jain*: 'Some mathematical considerations in dealing with inverse problems', IEEE Trans. on Antennas and Prop., Vol. **AP-29** (2), pp. 373 - 379, March 1981.

5. *A N Tikonov* and *V Y Arsenin*: 'Solutions of ill-posed problems', New York: Wiley 1977.

6. *I Stackgold*: 'Greens functions and boundary value problems', New York: Wiley 1979.

7. *B R Hunt*: 'A theorem on the difficulty of numerical deconvolution', IEEE Trans. Audio Electroacoust., Vol. **AU-20**, pp. 94 - 95, 1972.

8. *R S Cram* and *A J Caravone*: 'Deconvolution as a feasible alternative to the root-sum-squares rule for non-Gaussian transition duration analysis', IEEE Trans. on Instrumen. and Meas., Vol. **IM-30** (1), pp. 63 - 66, March 1981.

9. *D Henderson, A G Roddie, J G Edwards and H M Jones*: 'A deconvolution technique using least-squares model-fitting and its application to optical pulse measurements', NPL report **DES 87**, ISSN 0143 - 7305, March 1988.

10. *M M Lavrentiev*: 'Some improperly posed problems of mathematical physics', Tracts in natural philosophy, Vol. II, Berlin, Germany: Springer-Verlag, 1967.

11. *J H Franklin*: 'On Tikhonov's method for ill-posed problems', Math. Comput., Vol. **28**, pp. 889 - 907, October 1974.

12. *P H van Cittert*: Z. Physic, Vol. **60**, p. 298, 1931.

13. *P A Jansson, R H Hunt* and *E K Plyler*: 'Resolution enhancement of spectra', J. of Opt. Soc. of America, Vol. **60** (5), pp. 596 - 599, May 1970.

14. *A F Jones* and *D L Missell*:'The problem of error in deconvolution', J. Phys. A: Gen. Phys., Vol. **3**, pp. 462 - 472, 1970.

15. *G Halsey* and *W E Blass*: 'Deconvolution of ir spectra in real time', App. Optics, Vol. **16** (2), pp. 286 - 288, February 1977.

16. *T K Sarkar, F I Tseng, S M Rao, S A Dianat* and *B Z Hollmann*: 'Deconvolution of impulse response from time limited input and output: Theory and experiment', IEEE Trans. on Instrumen. and Meas., Vol. **IM-34** (4), pp. 541 - 546, December 1985.

17. *V Karya* and *H D Holden*: 'Deconvolution of seismic data - an overview', IEEE Trans. on Geoscience electron., Vol. **GE-16** (2), pp. 95 - 98, April 1978.

18. *S M Riad* and *N S Nahman*: 'Applications of the homomorphic transformation to time domain measurement problems', NBSIR 78-81, June 1978.

19. *J W Cooley* and *J W Tukey*: 'Math. Comput.', Vol. **19**, pp. 297 - 301, April 1965.

20. *C A Burrus, J E Bowers* and *R S Tucker*: 'Improved very-high-speed packaged InGaAs PIN punch-through photodiode', Electron. Letts., Vol. **21** (7), pp. 262 - 263, March 1985.

21. *B K Garside*: 'Lasers on the fast track', Photonics Spectra, 1982.

22. *B K Garside* and *R E Park*: 'Ultrashort pulses from semiconductor diode lasers', Optics and Laser Tech., pp. 91 - 94, April 1983.

23. *H Meckelburg* and *K Matkey*: 'A highly sensitive microwave sampling system with adaptive time-drift compensation', IEEE Trans. on Instrumen. and Meas., Vol. **IM-34** (3), pp. 427 - 430, September 1985.

24. *W L Ganz*: 'The measurement and deconvolution of time jitter in equivalent-time waveform samplers', IEEE Trans. on Instrum. and meas., Vol. **IM-32** (1), March 1983.

25. *W L Ganz* and *J R Andrews*: 'Time domain network analyser for measurements of RF and microwave components', NBS tech. note 672, September 1975.

26. *M G Cox*: 'Practical spline approximation', NPL report DITC 1/82, ISSN 0143 - 7348, February 1982.

PART 3

DEVELOPMENT OF A GaInAs PHOTODIODE SUITABLE FOR USE AS A TRANSFER STANDARD AT 1.3 - 1.5 μm

1. INTRODUCTION AND OVERVIEW OF THE TRANSFER STANDARD PHOTODIODE PROJECT

1.1. INTRODUCTION

The previous two parts of this thesis concentrated on the techniques to measure the performance of an unknown device, both directly and by using a fast photodiode with well known temporal response as a reference device. This part of the thesis describes the research work to develop a fast photodiode and mount that can be used as the reference device. At the time this work was started GaInAs photodiodes were being developed for use in 1.3 μm long wavelength fibre-optic communication systems[1,2]. The speeds of the devices being reported was in the range 35 - 140 ps for the Full Width at Half Maximum parameter[3]. It was anticipated that the speed of response of these devices would increase and this would give rise to future measurement difficulties.

1.2. OVERVIEW OF THE PROGRAMME

A research programme was started at NPL to develop a fast photodiode and mount that would be suitable for use as a reference standard for high speed optoelectronic measurements. The requirements for this device, as perceived at the time, were as follows:

1. The device should have a bandwidth which is in excess of 20 GHz and the temporal response should be relatively free from ringing.
2. The diode and mount should be represented by a model to allow the impulse response to be estimated. Parameters for the model may be obtained from a detailed knowledge of the structure and from measurements of the device.
3. The operating spectral range should cover the two main wavelengths of interest for optical fibre communications, 1.3 and 1.55 microns.
4. The temporal response should be largely independent of variations of the bias voltage about the normal operating point.
5. The active area should be as large as practical and the speed of response should be independent of the position of the light spot on the active area.
6. The device should present a good impedance match to the measurement system so that the uncertainties introduced are minimised.

The manufacture of the photodiodes was carried out by industry under a extra-mural research contract, as NPL has no semiconductor fabrication facilities. The two firms approached were Plessey Research (Caswell) and STL. Plessey was chosen as this project was best fitted to their own programme at that time.

The research programme was divided into three stages:

1. The development of a suitable model for the device and the measurement of the optical properties of the GaInAs material and the identification of a suitable device structure.
2. Fabrication of test samples in a high speed package to test both the model and the package design.
3. Fabrication and assessment of the final devices.

The measurement of the optical properties of the GaInAs material, carried out as part of the first stage, was required because at that time no absorption coefficient data were available for the device modelling. The work is described in paper 1 referenced in appendix 2.

The modelling of the photodiode and mount was considered to be an important part of the programme. Modelling of the diode structure allows the important design parameters to be identified and optimised. The model may also be used to estimate the temporal response of the device from incomplete frequency domain measurements. Parameters for the modelling can be determined from the physical properties of the device, measured during the manufacture.

At the time this thesis was written the research programme had not been completed. The work covered is as follows: chapter 2 describes the choice of a suitable diode structure, chapter 3 describes the device modelling and chapter 4 describes the development work covered in the second and third parts of the project.

A separate collaborative project was undertaken with British Telecom Research Laboratories to mount a fast photodiode on to a commercial microstrip test fixture and test the device performance. This work is described in chapter 5.

2. CHOICE OF A SUITABLE DEVICE STRUCTURE

2.1. INTRODUCTION

The choice of the device structure can affect the performance and suitability of the photodiode for a particular application. It is therefore necessary to choose the device structure that will give the best response in that application. Plessey make GaInAs pin photodiodes in two designs, a device where the light enters through the top contact and a device where the light enters through the substrate. In this chapter the advantages and disadvantages of the two available photodiode structures have been compared.

2.2. CHOICE OF DEVICE STRUCTURE AND SIZE

The two structures available are: a top entry device (figure 2.1) in which the light enters through the p^+ region; and a substrate entry device (figure 2.2) in which the light must pass through the indium phosphide substrate before entering the active region. The growth and preparation of the GaInAs/InP wafers would be identical for both structures.

Because of the high cost of mask fabrication it was decided near the beginning of the programme that where possible existing masks should be used. Two mask sets giving circular active regions of 30 - 35 or 40 - 45 microns diameter were chosen. Although speed was an important consideration, it was felt that if the device were too small it would be difficult to use.

Advantages and disadvantages of the top light entry structure

The top light entry device has the advantage of an extended wavelength range. Measurements, described in part 2 of this thesis, have been made on this type of device at 830 nm using a dye laser. A second advantage of this structure is that the majority of the current is carried by the more mobile electrons and so a lower operating bias voltage should be possible.

The photodiode chip must be connected to the external circuit. The number of bond-wires, their diameter and length will determine the overall inductance which can be varied to achieve the optimum response.

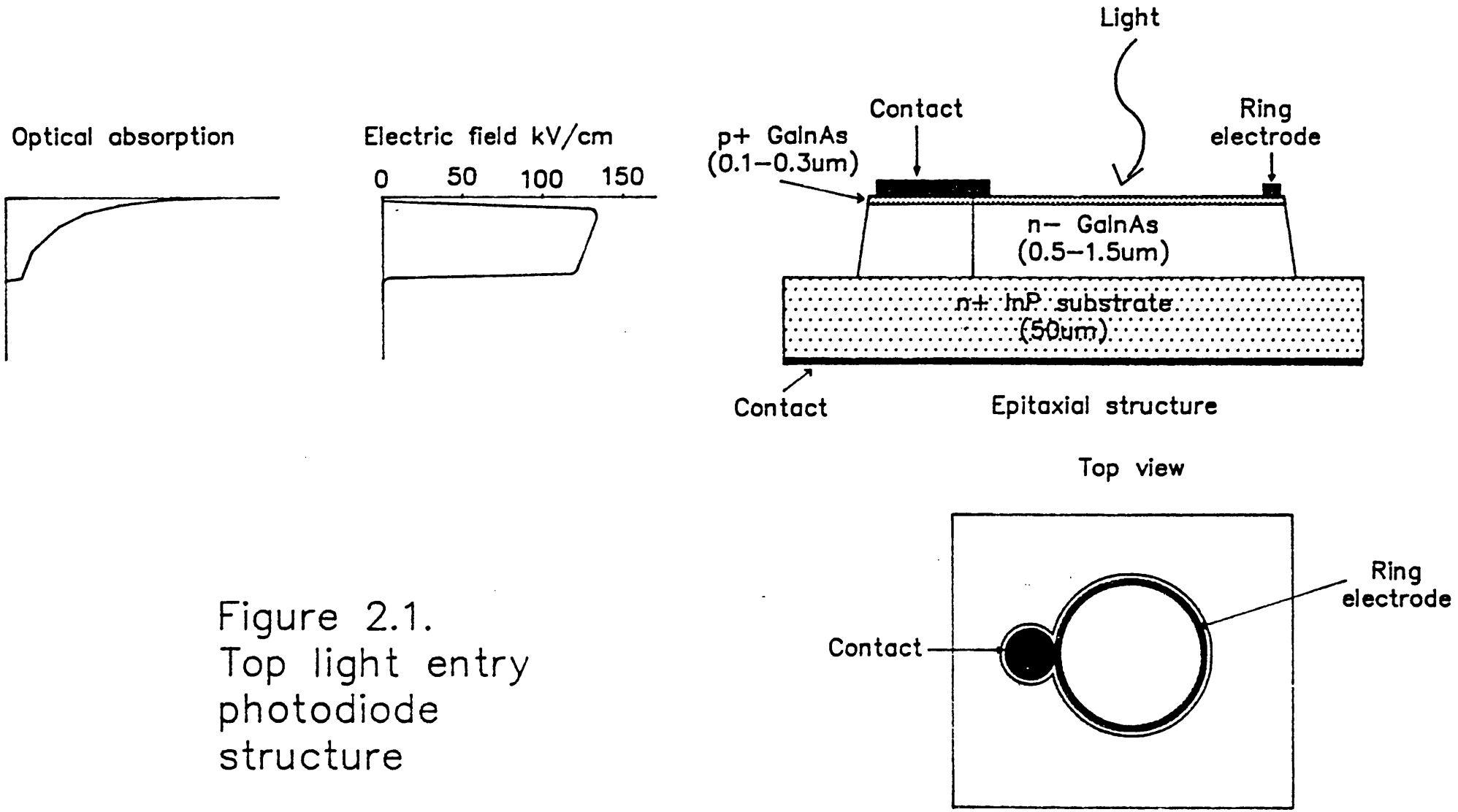

Figure 2.1.
Top light entry
photodiode
structure

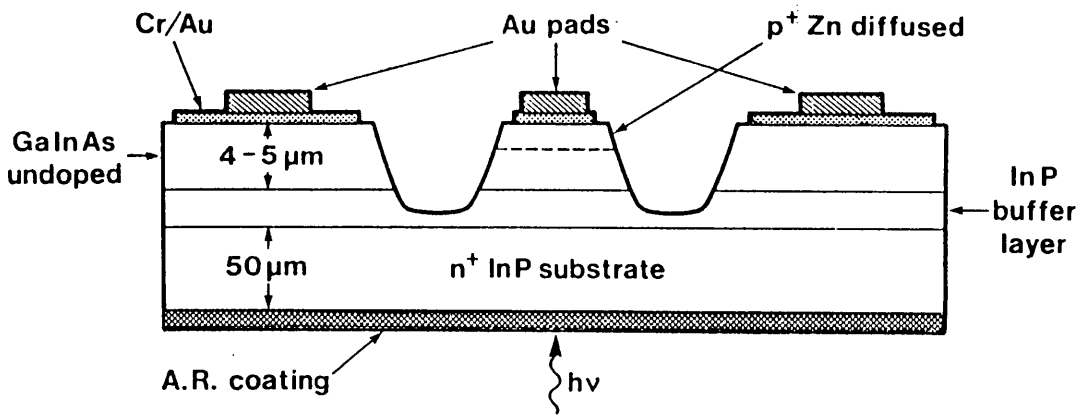

Figure 2.2. Substrate light entry photodiode structure

The effects of the mounting inductance on the predicted device performance have been modelled. These results are presented in the next chapter.

A major disadvantage of this structure is the need for a bonding pad so that the diode can be connected to the external circuit. The size of the pad is determined by mechanical constraints. If the area is too small then it will not be possible successfully to attach a wire to the pad. A 40 µm diameter bond pad would contribute an extra 150 fF to a diode with an depletion width of 1.0 µm, greatly slowing its speed of response. High speed GaAs photodiodes, where the bonding pad is considerably larger than the active area, have been fabricated using semi-insulating material and air-bridge techniques to reduce the capacitance[4]. However, these techniques were not available when this decision was made.

The other main disadvantage is that the speed of response may depend on the position of the light on the active area. Photogenerated carriers in the p^+ region will move by diffusion due to carrier concentration gradients, rather than drift due to electric fields. These carriers will therefore contribute less to the high frequency performance of the device than the carriers generated in the high field regions of the device. The p^+ layer must therefore be made thin so that the light will be absorbed mainly in the depleted region of the device. This gives rise to a positional dependence of the response speed, caused by the high sheet resistance of the thin p^+ region. Some manufacturers have overcome this problem by growing a cap layer of indium phosphide

material to reduce the sheet resistance. This approach is successful but it restricts the operational wavelength range of the device.

Advantages and disadvantages of the substrate light entry structure

The operating wavelength of the substrate light entry structure is limited by the transmission of the InP and InGaAs materials to between 0.95 and 1.65 μm. This is ideal for the optical fibre communications windows at 1.3 and 1.55 μm but does not allow the use of the short optical pulses available from a dye laser.

The top contact of device is metallised, giving a temporal response that is independent of position. Connection can be made directly to the device active area, removing the need for a separate bond pad. Alternatively the diode can be mounted in a *flip-chip* configuration[5]. The former arrangement allows some variation of the mounting inductance. The latter method gives a repeatable, low inductance but contributes extra stray capacitance.

The light entering the device makes two passes through the active region because it is reflected from the metalisation on the top contact. This is a considerable advantage over the top light entry design as it allows thinner epitaxial growth layers to be used to achieve the same sensitivity. Some interference will occur between the forward and reflected travelling optical waves. However, this effect can be neglected because the device structure will not be completely uniform on the scale of the optical wavelength within the material ($\lambda/2 \simeq 110$ nm).

The majority of the current is carried by the less mobile holes because the peak optical absorption occurs near the heterojunction. The holes have, on average, a greater distance to travel to reach the undepleted p-type material than the electrons travelling to the region of undepleted n-type material. The peak optical absorption is also not coincident with the peak electric fields in this structure. To compensate for these effects a higher bias voltage must be adopted. At lower bias voltages there is the possibility of using the field dependence of the drift velocity for a non-linear mixing process. This effect is outlined in paper 4 referenced in appendix A2.

Choice of structure

The disadvantages of the top light entry structure are considered to be more serious than those of the substrate light entry structure for the transfer standard application. The possible position dependence of the response would make modelling difficult and could introduce serious problems with measurements. The speed of response would also be impaired by the extra capacitance caused by the bonding pad. For these reasons the substrate light entry structure has been chosen for modelling and optimisation.

3. MODELLING AND OPTIMISATION OF PHOTODIODES

3.1. INTRODUCTION

The development of a fast photodiode and mount requires compromises to be made between such parameters as size, speed and responsivity to produce the best design. The cost of fabricating a large number of different devices would be prohibitively high and so a theoretical model must be used to describe the photodiode responses.

In this chapter a small signal model of the chosen structure has been described. The model has been checked for accuracy by comparison with measurements made on a photodiode of known parameters. The model has been used to optimise the photodiode structure so that the the bandwidth and the responsivity are maximised.

3.2. THE CHOICE PHOTODIODE MODEL

The model used for the optimisation of the fast photodiode structure must be able to be run for a reasonable length of time (200 ps or more). A large number of runs must be performed so that the effects of various parameters can be investigated. The types of model fall into two classes: large signal and small signal simulations.

In a large signal simulation, the optical signal, diode structure and external circuitry must be modelled simultaneously. Such a model assumes non-linearity and so any change of the parameters requires the program to be re-run.

A further disadvantage is that the carrier concentrations in the undepleted regions must also be modelled. In the undepleted material, the carrier concentrations will be high and so the time increment, which must be shorter than the dielectric relaxation time, will have to be very small (<15 fs) to ensure stability. The dielectric relaxation time, given by equation 1, is the time constant for the correction of an imbalance in the local carrier concentration:

$$\tau_R = \frac{\epsilon}{q\mu_n n} \qquad \text{(eq. 1)}$$

where τ_R is the dielectric relaxation time in n-type material; q is the electronic charge; μ_n is the electron mobility; n is the electron density; and ϵ is the permittivity of the material.

The electric field throughout the device must also be calculated at each timestep. If a large number of parameter changes is required this type of model becomes extremely expensive.

In general the signals on a photodiode are small and do not perturb the internal field distributions significantly. It is therefore reasonable to use a small signal model in which the flow of the photocarriers is not allowed to affect the field distributions. The advantages of such a model are twofold: firstly the model is linear and so the overall device response can be calculated from the current response, due to the flow of carriers within the structure, and the network response by convolution (equation 2); secondly the calculation of the field dependent carrier transport coefficients need only be performed once at the beginning of the program:

$$V(t) = \int_0^t I(\tau)\, Z(t - \tau)\, d\tau \qquad \text{(eq. 2)}$$

where V(t) is the response of the device; I(t) is the current response of the structure; and Z(t) is the response of the network formed by the diode and the mount.

A small signal model has been chosen to simulate the photodiode and mount performance. This allows the modelling of the epitaxial structure and the optimisation of the mounting structure to be performed separately.

Analytical models have been used to describe the current flow in photodiodes, but these were thought to be too limited for this application.

A finite difference approach has been chosen to describe the current flow within the epitaxial structure. The results from this model are then used to determine the overall response of the packaged device by equivalent circuit modelling.

3.3 MODELLING OF THE CURRENT RESPONSE

A one dimensional explicit finite difference model has been chosen to describe the current flow. The use of a single dimension to model a three dimensional device is justified because the active area is large compared to the depletion width, removing any edge effects. The response speed is independent of position because the p^+/metal contact covers the whole active area.

Carrier transport

The flow of carriers within the structure is governed by the classical continuity equations. The continuity equations for holes and electrons in a one dimensional approximation are as follows:

$$\frac{\partial n}{\partial t} = \frac{1}{q}\frac{\partial J_n}{\partial x} + G_n - U \qquad \text{(eq. 3)}$$

$$\frac{\partial p}{\partial t} = -\frac{1}{q}\frac{\partial J_p}{\partial x} + G_p - U \qquad \text{(eq. 4)}$$

where J_n and J_p are the electron and hole current densities; G is the generation rate; and U is the recombination rate.

In this application the generation of carriers will be due to the absorption of light and therefore G_n and G_p will be equal. The contribution of the recombination rate U has been ignored as the carrier lifetime is several nanoseconds which is considerably longer than the timescale of this model. The electron and hole current densities are given by equations 5 and 6:

$$J_n = q\mu_n E + q\frac{\partial D_n n}{\partial x} \qquad \text{(eq. 5)}$$

$$J_p = q\mu_p E - q\frac{\partial D_p p}{\partial x} \qquad \text{(eq. 6)}$$

where μ_n and μ_p are the electron and hole mobilities. The diffusion coefficients for the electrons and holes, D_n and D_p, are determined using the Einstein relation (equation 7):

$$D = \frac{\mu kT}{q} \qquad \text{(eq. 7)}$$

where D is the diffusion coefficient; k is the Boltzmann constant; and T is the lattice temperature.

The assumption of constant electron and hole mobilities breaks down at the high fields present within the depleted region of the photodiode. The average velocity/field characteristics for GaInAs and other III-V materials has been measured at fields of up to 100 kV/cm by *T H Windhorn*[6,7]. The characteristics have also been extensively modelled using Monte-Carlo simulation techniques by *Littlejohn et al*[8,9]. The measured drift velocities have been fitted to a simple function (equation 8) so that the drift velocities within the depletion region can be modelled. At the time this part of the work was done, no high field measurements of the hole drift velocities had been reported. A simple approximation[10], shown in equation 10, was used to model the saturation of the hole drift velocity:

$$v_e(E) = - \frac{\mu_1 E}{(1 + \alpha E.E)} - \frac{\mu_2 E}{\sqrt{(1 + \beta E.E)}} \qquad \text{(eq. 8)}$$

where $v_e(E)$ is the field dependent drift velocity for electrons; α and β are constants chosen to give the best fit to the data;

$$\mu_e = \mu_1 + \mu_2 \qquad \text{(eq. 9)}$$

where μ is the low field electron mobility;

$$v_h(E) = \frac{\mu_h E}{(1 + |\frac{\mu_h E}{v_s}|)} \qquad \text{(eq. 10)}$$

where $v_h(E)$ is the field dependent hole drift velocity; μ_h is the hole low field mobility; and v_s is the saturated drift velocity.

This is a crude approximation as it assumes that the carriers will instantaneously reach the average drift velocity. Simulations of the carrier dynamics of GaAs (a related compound) by the Monte-Carlo method, show that, on the timescales of interest, the approximation is reasonable[19]. The values for the coefficients of the electron and hole drift velocities used in this work are given in table 3.1.

Table 3.1. Parameters used for the field dependent drift velocities

Description	Symbol	Value	Units
Low field electron mobility	μ_e	9500	cm^2/Vs
Parameters for the model of the field dependent drift velocity	μ_1	9303.3	cm^2/Vs
	μ_2	196.7	cm^2/Vs
	α	6.285×10^{-8}	cm^2/V^2
	β	1.548×10^{-9}	cm^2/V^2
Low field hole mobility	μ_h	300	cm^2/Vs
Saturated drift velocity	V_s	5×10^6	cm/s

More recently measurements of the hole and electron drift velocities have been made by *P Hill et al*[28] over the range 66 - 197 kV/cm. These results are shown in figure 3.1, together with the approximating functions and the measurements by *Windhorn*. The agreement between the original data *(Windhorn)* and the fitted curve is good, with a rms error at each point of 1.85×10^5 cm/s. The later measurements give slightly higher values than those used for the modelling and so the theoretical results may be slightly pessimistic.

The Einstein relation, shown in equation 7, gives the low field diffusion coefficient. If this value is used throughout the model then serious problems will occur because the high electron mobility gives rise to a large diffusion coefficient which dominates the carrier transport equations even in the depleted region where the electric field is high.

To overcome this problem the constant diffusion coefficients have been replaced by field dependent relations, equations 11 and 12:

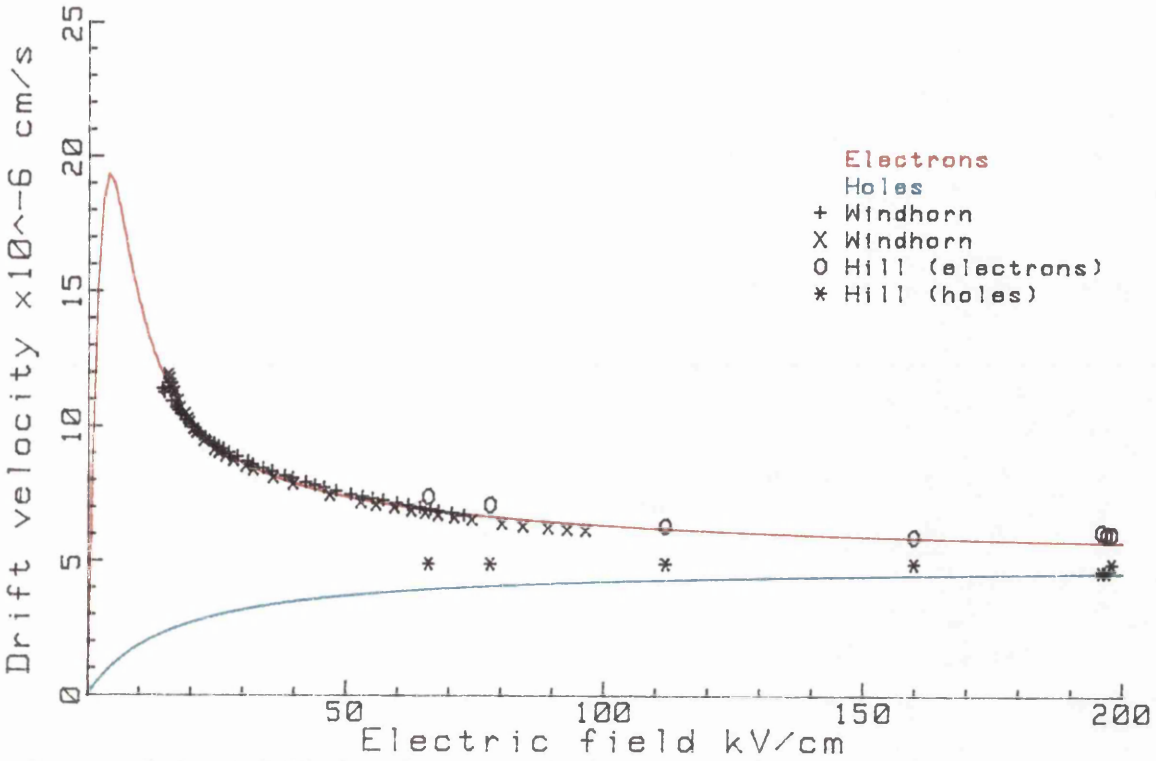

Figure 3.1. Modelled and measured electron and hole drift velocities in GaInAs

$$D_e(E) = \left|\frac{kTv_e(E)}{qE}\right| \qquad \text{(eq. 11)}$$

for electrons and

$$D_h(E) = \left|\frac{kTv_h(E)}{qE}\right| \qquad \text{(eq. 12)}$$

for holes. $D_e(E)$ and $D_h(E)$ are the field dependent diffusion coefficients.

Field dependent diffusion coefficients have been measured in a similar material, gallium arsenide, by *Fawcett & Rees*[10]. Their results show similar high field behaviour and suggest that this approximation is reasonable.

Treatment of the heterojunction

The depletion region of the diode may extend into the InP material. Photoelectrons generated in the GaInAs absorbing region will have to cross the heterojunction in order to reach the undepleted n-type material. In this model the effects of the heterojunction have been

largely ignored. However, the model allows the carrier transport equations to be modified in the following manner: a constant factor has been included, corresponding to for the probability that a carrier can cross to the next spatial point; within a material this factor would be unity for both carrier types and in both directions. However, at the heterojunction, different factors could be chosen for the two directions of travel and for the two species of carrier. The electric field calculations correct for the different material permitivitty within the structure.

Finite difference representation of the carrier flow

The finite difference approximation uses a Taylor series expansion to give an estimate for the derivatives of the carrier concentrations in space and time. This assumes that the carrier concentration is a continuous and single valued function with continuous derivatives. The Taylor series expansion for the electron density about a point is shown in equation 13.

$$n(x+\Delta x) = n(x) + \Delta x \frac{\partial n}{\partial x} + \frac{\Delta x^2}{2!} \frac{\partial^2 n}{\partial x^2} + \frac{\Delta x^3}{3!} \frac{\partial^3 n}{\partial x^3} + \ldots \qquad \text{(eq. 13)}$$

If the series is truncated so that only the first two or three terms are considered then approximations for the first and second derivatives can readily be obtained:

$$\frac{\partial n}{\partial x} = \frac{n(x+\Delta x) - n(x)}{\Delta x} + O_1 \qquad \text{(eq. 14)}$$

and

$$\frac{\partial^2 n}{\partial x^2} = \frac{n(x-\Delta x) - 2n(x) + n(x+\Delta x)}{\Delta x} + O_2 \qquad \text{(eq. 15)}$$

where O_1 and O_2 are error terms due to the truncation of the series.

The temporal derivatives of the carrier concentration can be obtained by a similar procedure.

Truncation is the major source of error in the finite difference model. The errors in the representation of the first derivative of the carrier density will be proportional to the step size. If the spatial derivative were described by the following relation:

$$\frac{\partial n}{\partial x} \simeq \frac{n(x+\Delta x) - n(x-\Delta x)}{2\Delta x} \qquad \text{(eq. 16)}$$

then the errors would be proportional to Δx^2. Unfortunately this scheme has been shown to be unconditionally unstable by *P A Blakey*[11]

Model structure

In the model the flow of holes and electrons are treated separately. The epitaxial layer and part of the substrate has been represented as two interleaved sets of layers. These contain the carrier concentrations and the carrier transport coefficients respectively. Within each layer the values are assumed to be constant. The structure is shown in figure 3.2.

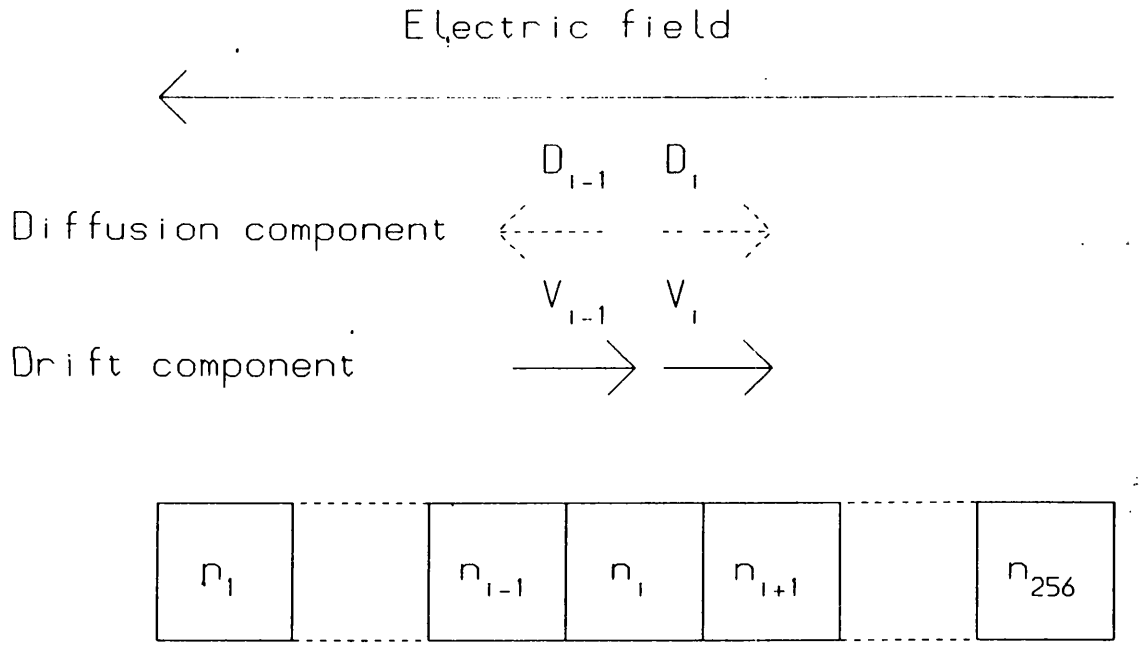

Figure 3.2. Finite difference model of the photodiode

The spatial structure is the same for both holes and electrons but the timesteps Δt_e and Δt_h are different with $\Delta t_h = k\,\Delta t_e$, where k is an integer. The reason for the different timestep values is that the lower mobility of the holes allows the model to remain stable with a longer timestep than that allowed for electrons.

Numerical stability

The criterion for stability is simple, the number of carriers moved from one layer to the next in one timestep should not exceed those originally present in that layer. Dielectric relaxation does not affect this model because the static electric fields are not perturbed by the

photogenerated carriers. The nonlinear drift velocity characteristic makes the rigorous testing of the stability difficult during the data preparation phase. Two simple criteria have been chosen as a quick test of the stability. These tests are for the stability in the undepleted n-type material (equation 17) where diffusion effects dominate and for the holes in the high field region where the drift velocity is the dominant effect (equation 18):

$$\Delta t_e \leq \frac{\Delta x^2}{2D_e} \qquad \text{(eq. 17)}$$

and

$$\Delta t_h \leq \frac{\Delta x}{V_{sat}} \qquad \text{(eq. 18)}$$

where D_e is the low field diffusion coefficient for electrons and V_{sat} is the saturated drift velocity.

The program to determine the current response calculates the transport coefficients and then checks that they meet the stability criterion at all points.

Pseudo-diffusion

The finite difference approximation to a partial derivative will contain higher order terms. If only the second derivative terms are considered the effect is to introduce a pseudo-diffusion component which behaves as an increased diffusion coefficient. The finite difference representation of the continuity equation for electrons, shown in equation 19, has been expanded to include the second derivative terms (equation 20):

$$\frac{n(t+\Delta t) - n(t)}{\Delta t} = V_e \frac{n(x+\Delta x) - n(x)}{\Delta x} \qquad \text{(eq. 19)}$$

where V_e is the drift velocity for the electrons;

$$\frac{\partial n}{\partial t} = V_e \frac{\partial n}{\partial x} + (\Delta x - V_e \Delta t)\frac{V_e}{2} \frac{\partial^2 n}{\partial x^2} \qquad \text{(eq. 20)}$$

The diffusion effect will be zero when the drift velocity is either zero or such that all the carriers move from one layer to the next at

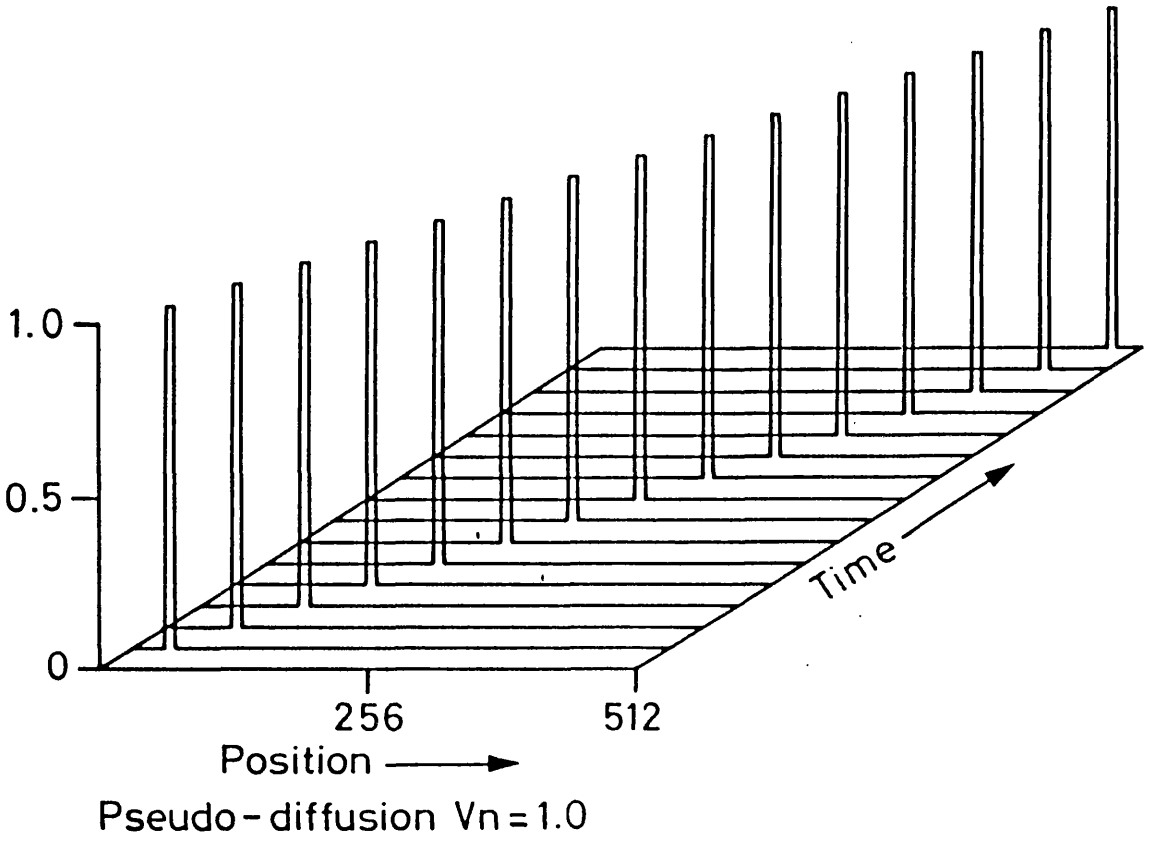

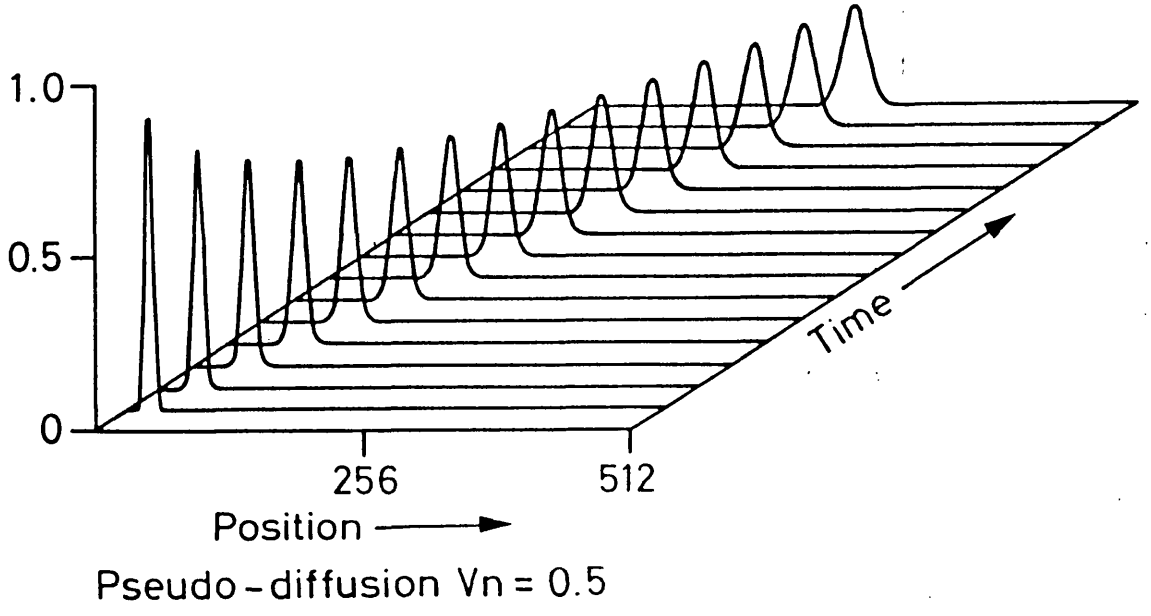

Figure 3.3. Effect of Pseudo-diffusion on drift

each timestep. The error due to this effect will be a maximum when half of the carriers move to the next layer at each timestep. To illustrate this effect the transport of a packet of charge through a finite difference scheme has been considered. Two examples with normalised drift velocities, defined in equation 21, of one and a half are shown in figure 3.3.

$$V_{norm} = \left(\frac{V\Delta t}{\Delta x}\right) \qquad \text{(eq. 21)}$$

where V_{norm} is the normalised drift velocity.

The pseudo-diffusion effect can be compensated by reducing the value of the original diffusion coefficient except where the pseudo-diffusion is greater. If a negative diffusion coefficient were introduced the model would become unstable and so a value of zero must be used.

Treatment of the contacts

The p^+ contact and the InP substrate end layers have been assumed to trap all carriers. At the p^+ ohmic contact the minority carrier concentration will be held at its equilibrium value by the increased recombination effects caused by the high local doping. At the final modelled layer of the substrate it was assumed that both electrons and holes would be lost into the substrate by diffusion.

Equations governing the flow of carriers

The flow of electrons and holes from one layer to the next are given by simple relations designed to ensure that the model is conservative and stable. The diffusion component of the carrier flow (for electrons) will be given by equation 22:

$$\Delta n_j(\text{diff}) = D_{j-1}(n_{j-1}\theta^1_{j-1} - n_j\theta^2_{j-1}) + D_j(n_{j+1}\theta^2_j - n_j\theta^1_j) \qquad \text{(eq. 22)}$$

where n is the carrier density in the box, the subscripts denote position; D is the normalised diffusion coefficient, corrected for pseudo-diffusion effects; and θ^1 and θ^2 are the probabilities that the carriers can cross from a lower number box to a higher and vice-versa.

The contribution due to drift is more complex as the direction of the drift must be taken into account to ensure numerical stability. Four combinations of drift direction are possible although two of these are highly unlikely. These are shown in the following relations:

$$\Delta n_j(\text{drift}) = n_{j-1}\theta^1_{j-1}V_{j-1} - n_j\theta^1_jV_j \qquad \text{(eq. 23)}$$

where the both the normalised drift parameters (V) are positive.

$$\Delta n_j(\text{drift}) = n_j(\theta^2_{j-1}V_{j-1} - \theta^1_jV_j) \qquad \text{(eq. 24)}$$

where V_{j-1} is negative and V_j is positive.

$$\Delta n_j(\text{drift})\ n_{j-1}\theta^1_{j-1}V_{j-1} - n_{j+1}\theta^2_jV_j \qquad \text{(eq. 25)}$$

where V_{j-1} is positive and V_j is negative.

$$\Delta n_j(\text{drift}) = n_j\theta^2_{j-1}V_{j-1} - n_{j+1}\theta^2_jV_j \qquad \text{(eq. 26)}$$

where the both the normalised drift parameters (V) are negative.

The carrier density in the box can be calculated from the drift and diffusion components as shown in equation 27:

$$n_j(t+\Delta t) = n_j(t) + \Delta n_j(\text{diff}) + \Delta n_j(\text{drift}) \qquad \text{(eq. 27)}$$

where $n(t+\Delta t)$ is the carrier density in the box after one time increment of Δt.

The equations for the transport of the holes will be identical as the equation set takes into account the direction of flow of the carriers.

Current response of photodiode

The photodiode under bias contains three regions: an undepleted (highly conductive) p^+ region; a depleted (insulating) n^- region; and an undepleted (highly conductive) n^+ region. The structure is therefore very similar to a capacitor. The flow of current in the external circuit due to the photogenerated carriers causes the potential across the diode to vary, altering the depleted width slightly. Returning to the capacitor analogy, the change in the depletion width is negligible and therefore the potential across the photodiode induced by the photogenerated carriers is equivalent to a charge on the plates of the capacitor formed by the depletion width. The current response can be calculated from the potential induced by the photogenerated carriers using the relation (equation 28):

$$I(t) = C\frac{dV(t)}{dt} \qquad \text{(eq. 28)}$$

where C is the capacitance of the diode.

The initial distribution of photocarriers is generated using the absorption coefficients for the n^- and p^+ GaInAs materials and assuming exponential absorption. The light passes through the diode initially and is then reflected back again from the metallic top contact. The density of carriers in a layer is proportional to the sum of the forward and reverse losses in that layer. Interference effects caused by the coherence of the light reflected from the metal contact have been ignored in this analysis.

The potential induced by the drift and diffusion of the photogenerated carriers can be calculated by numerically integrating the fields produced by their presence (equations 29 and 30). The majority photogenerated carriers, i.e. electrons in the region of undepleted n-type material and holes in the region of undepleted p-type material, are assumed to lie at the edge of their respective depletion regions:

$$E_i = E_{i-1} + \frac{2q(p-n)\Delta x}{(\epsilon_{i-1} + \epsilon_i)} \qquad \text{(eq. 29)}$$

where E is the electric field and $E_1 = 0$; q is the electronic charge; ϵ is the permitivitty of the material and n and p are the photogenerated carrier densities of the electrons and holes respectively.

$$V = \frac{\Delta x}{2} \sum_{i=1}^{n-1} (E_i + E_{i+1}) \qquad \text{(eq. 30)}$$

The charge density can be calculated using the potential and the capacitance per cm^2. In this model the charge at the final timestep is normalised to unity so that the current response $(\frac{dQ}{dt})$ will be an impulse response with unity area.

Network response

The lumped circuit network (figure 3.4) has been used to model the effects of bondwire inductance, contact resistance, load resistance and the capacitances due to the depletion width and stray effects. The position of the stray capacitance is not known and so can be introduced

separately as C_2. The load resistance will be either 25 Ω or 50 Ω depending on whether or not the mount is reverse terminated. In a reverse terminated mount any signals reflected by the measurement system will see a near perfect 50 Ω termination of the diode mount, reducing further reflections. The disadvantage is a reduced signal from the diode caused by the current being divided equally between the measurement system and the terminating load.

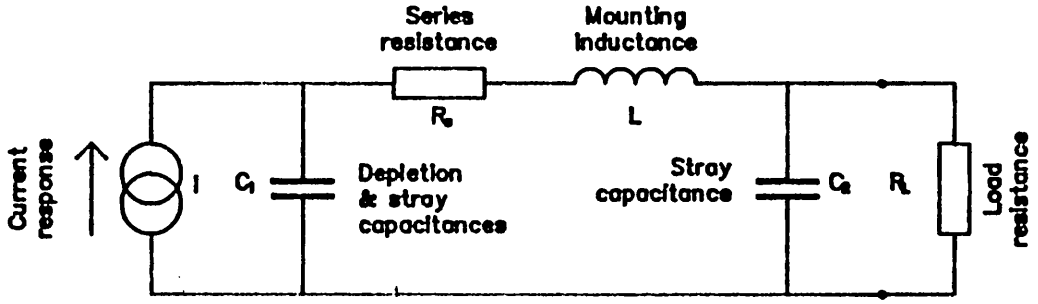

Figure 3.4. Network description of the photodiode

The lower load impedance seen by the diode increases its response speed but also makes the design more sensitive to the inductance of the bondwire. Circuit analysis of the network gives the following expression (equation 31) for the frequency response.

$$Z(j\omega) = \frac{R_2}{((1-(LC_1 + R_1R_2C_1C_2)\omega^2)+j\omega((R_1C_1+R_2(C_1+C_2))-LC_1C_2R_2\omega^2))}$$

(eq. 31)

Later in the programme a more sophisticated method of analysing the network was adopted to allow the introduction of circuit elements such as delays and the reflection from connectors. In the new approach each element in the circuit was treated as a one, two or three port network. The reflected signal from each network and the transmitted signal through each network can be calculated as at any frequency. In this analysis, scattering parameters were used because they are the most convenient method for representing a microwave network. A good introduction to scattering parameters is given by *Kuo*.

The scattering parameters for two simple networks, shown in figure 3.5, have been considered here. The first is a series impedance which will have a reflection coefficient given by:

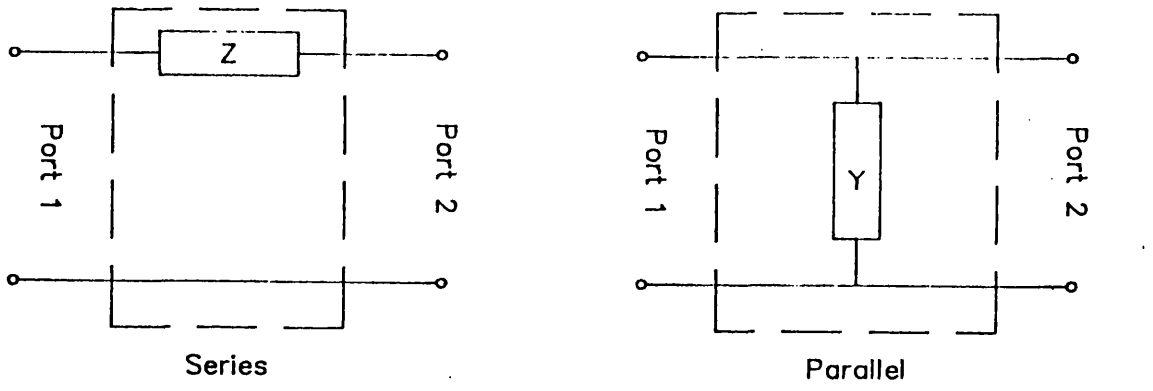

Figure 3.5 S-parameter representation of a network

$$S_{s11} = \frac{Z}{(Z + Z_o)} \qquad \text{(eq. 32)}$$

and a through transmission given by:

$$S_{s21} = 1 - S_{s11} \qquad \text{(eq. 33)}$$

where S_{s11} is the reflected signal; S_{s21} is the forward transmitted signal; Z is the series impedance and Z_o is the line impedance (50 Ω).

The second network is a parallel conductance Y which will have a reflection coefficient given by equation 34:

$$S_{p11} = \frac{-YZ_o}{(2 + YZ_o)} \qquad \text{(eq. 34)}$$

and a through transmission given by:

$$S_{p21} = 1 - S_{p11} \qquad \text{(eq. 35)}$$

A complicated representation of the diode circuit response could be built up by combining the networks as shown in figure 3.6 and equations 36 - 39.

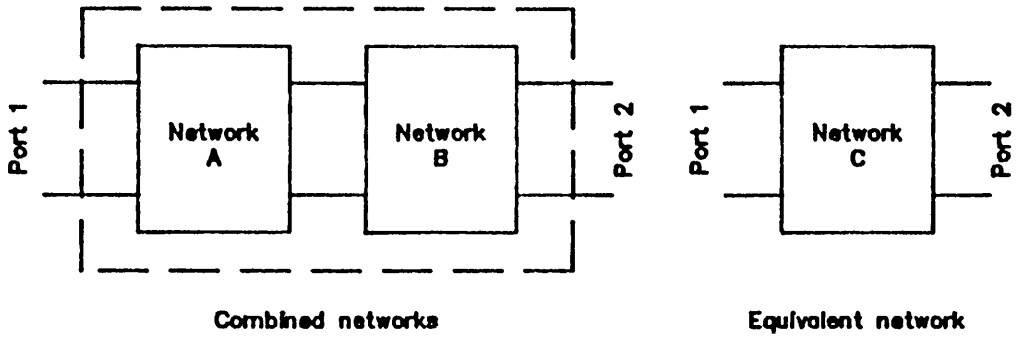

Figure 3.6 Combination of S-parameter networks

$$S_{11c} = S_{11a} + \frac{S_{11b}S_{21a}S_{12a}}{(1-S_{22a}S_{11b})} \qquad \text{(eq. 36)}$$

$$S_{21c} = \frac{S_{21a}S_{21b}}{(1-S_{22a}S_{11b})} \qquad \text{(eq. 37)}$$

$$S_{12c} = \frac{S_{12a}S_{12b}}{(1-S_{22a}S_{11b})} \qquad \text{(eq. 38)}$$

$$S_{22c} = S_{22b} + \frac{S_{22a}S_{12b}S_{21b}}{(1-S_{22a}S_{11b})} \qquad \text{(eq. 39)}$$

3.4. PARAMETERS AND INITIAL CONDITIONS FOR THE PHOTODIODE MODEL

The parameters for the network response will depend strongly on how the photodiode is mounted. The values of stray capacitance and inductance will be very small and so cannot be measured directly. These values can be estimated by measuring the electrical reflection coefficient (S_{11}) with a vector network analyser and then fitting a model to the measured results[12]. Unfortunately when this work was performed facilities of this type were not available at NPL. An estimate of 70 fF was be made for the stray capacitance, based on the physical size of the chip. The true value may lie anywhere in the range 40 - 100 fF and is comparable with the depletion capacitance. The mount inductance was expected to be less than 2 nH.

The diode current response is affected by the distribution of the optically generated carriers, the electric field profile within the depleted region and the electron and hole drift velocities and diffusion coefficients.

The distribution of the optically injected carriers can be determined using the measured absorption coefficients for GaInAs, paper 1 by this author, referenced in appendix 2. Different values have been used for the n^- and p^+ regions of the device. The values for the absorption coefficients, at a wavelength of 1.3 μm, are 1.16×10^4 cm^{-1} and 1.55×10^4 cm^{-1} for the n^- and p^+ type materials respectively. The reason for the higher value in the p^+ material is not understood. In the model the number of electron-hole pairs injected is proportional to the total light absorbed in the element.

The electric field profile for a particular bias voltage can be determined if the doping profile is known. The surface doping level is in the range 10^{18} - 10^{19} cm^{-3} and the depth of the junction is controlled to be roughly 1 μm. Later in the programme, Plessey developed a shallow diffusion technique which gave junction depths of the order of 0.3 μm. The p^+ region of the device is made by zinc diffusion. The theoretical doping profile is the gaussian error function. In practice the profile will differ because not all the dopant material will fall onto active lattice sites. In this model the p^+ doping level has been assumed to be constant at 10^{18} cm^{-3}.

A small fraction of the zinc dopant material will have penetrated beyond the junction and will compensate the residual n^- doping to give a lower effective value. By measuring the capacitance of the junction as a function of bias voltage it is possible to make a good estimate of the doping profile with thicker devices. As the bias voltage is increased the width of the depleted region increases. Using the relation (equation 40) it is possible to determine the local carrier concentration and hence estimate the doping profile of the device.

$$C = \frac{dQ}{dV} \qquad \text{(eq. 40)}$$

where C is the capacitance; and Q is the charge

A measured CV plot, where the doping profiles have been calculated, is shown in figure 3.7. The apparent sharp rise and dip of the carrier concentration at the heterojunction (1) is not indicative of the local doping profile. The electrons in the indium phosphide material are at a higher energy than those in the neighbouring gallium indium arsenide. Consequently electrons moving by diffusion from the indium phosphide

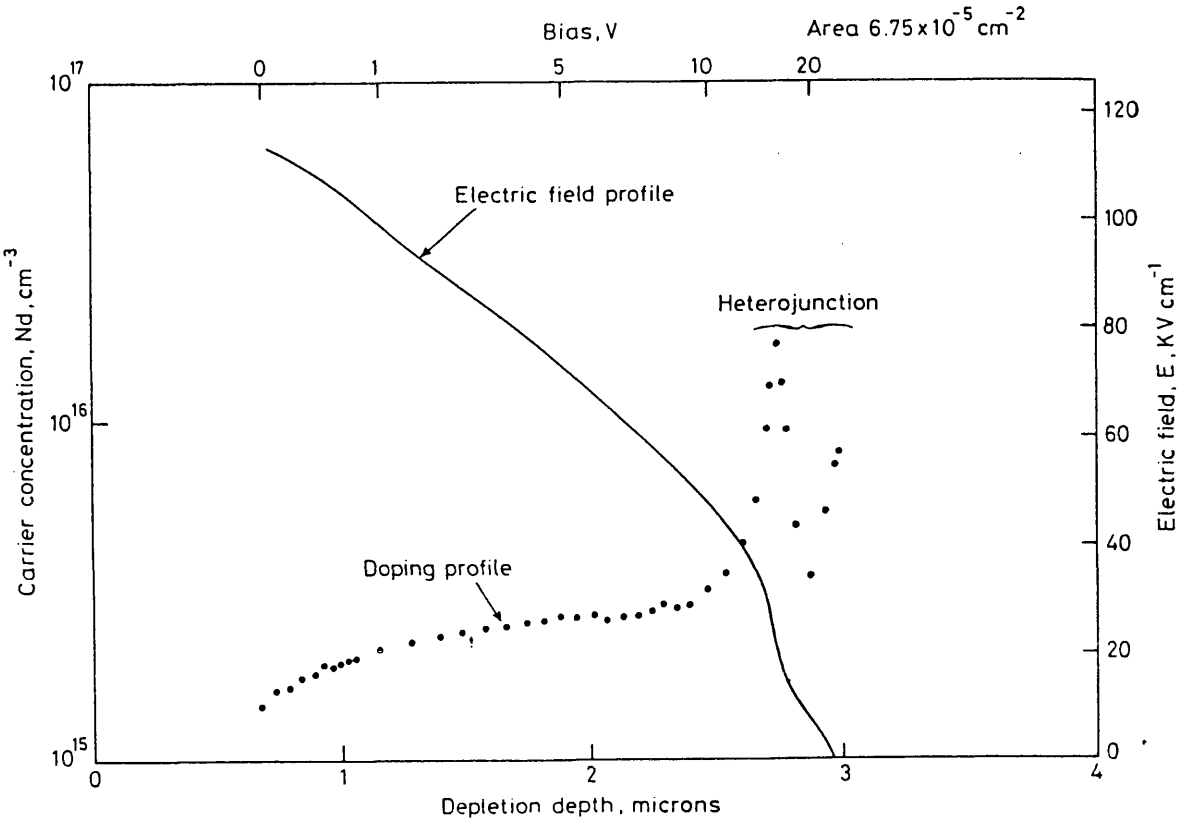

Figure 3.7. Carrier density distribution calculated from C-V profile

into the gallium indium arsenide can do so but; in the opposite direction they will experience a potential barrier. Around the heterojunction the charge imbalance will give rise to a local high field region and an equilibrium will be set up. In the depleted photodiode all the electrons will have been swept out and so only the fixed charges due to the dopants will remain. It has been assumed that no significant diffusion occurs between the GaInAs and InP layers during the material growth.

3.5. MODELLING PROGRAMS

The photodiode modelling proceeds in two phases: the modelling of the flow of charge in the epitaxial structure, and the modelling of the diode response as a convolution of the current and network responses. To make a cost effective use of computer resources, both space and time, the model has been implemented in four stages: data preparation; modelling of the current response; data compression and a suite of modelling programs to give time domain, frequency domain, or contour plots of the resultant response. The division of the task into separate

programs has allowed the use of batch and interactive programs where appropriate, as shown in figure 3.8.

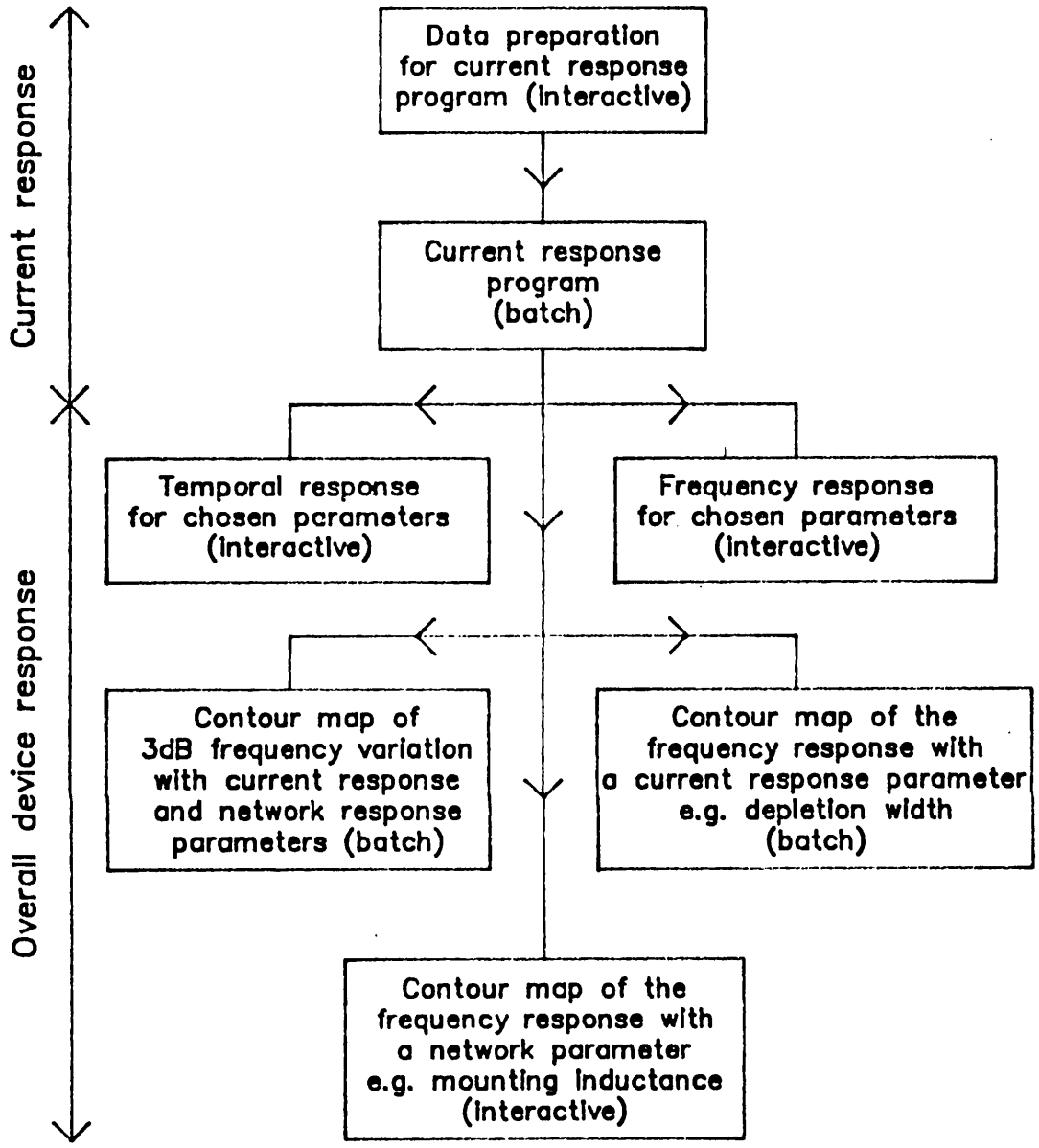

Figure 3.8. Photodiode modelling programs

NPL Facilities

The NPL computing facility used an ICL 2976 at the time this work was carried out. Three Fortran compilers were available for general users: F1, G and Fortran 77. The F1 compiler (Fortran IV) carried out the bulk of the checking during the compilation and has few run time checks. Both the G (Fortran IV) and the Fortran 77 compilers carried out a number of checks during run time. This made them slow for use with a long batch program. The difference between the run time of F1 and G compiled

programs was considerable. A data set containing 41 runs of a 3.4 μm epitaxial thickness device (216 spatial points) with 1024 temporal points was run on the modelling program. Using the F1 compiler the program took 2300 seconds (56 seconds per run) but using the G compiler the time taken was 8600 seconds (210 seconds per complete run), almost a factor of four difference.

The Fortran G compiler was required for use with the Ghost 80 graphical software to allow interactive modelling of the device performance. In this application the programs were relatively short and the slower running speed was relatively unimportant.

Data preparation

The data preparation program is interactive and generates a data file for the modelling program. This task would be tedious to carry out by hand and the possibility of errors would be high. Some checking of the original data is carried out at this stage, parameter choices that are obviously wrong or fail simple stability tests are rejected. Parameters such as the doping levels or the epitaxial layer thickness can be varied between a minimum and maximum value but the absorption coefficients, which do not vary linearly with wavelength, can be entered individually or be fixed at a particular value.

Current response program

The current response model was run as a batch program. A maximum of 51 structures could be modelled, each containing up to 256 spatial points and 1024 time values. The number of structures chosen was generally smaller and depended on the range over which parameters were being varied. At the start of the run the stability of the transport coefficients was checked, the program would stop if the stability conditions were violated.

Spline fitting

The output data file from the modelling program took roughly 15.5 kbytes per set of parameter changes making an average of 686 kbytes (41 runs) per run. The current response model gave the normalised charge response, the integral of the current response. The current response can be determined by a numerical differentiation process.

A spline[13] representation of a curve consists of a set of n degree

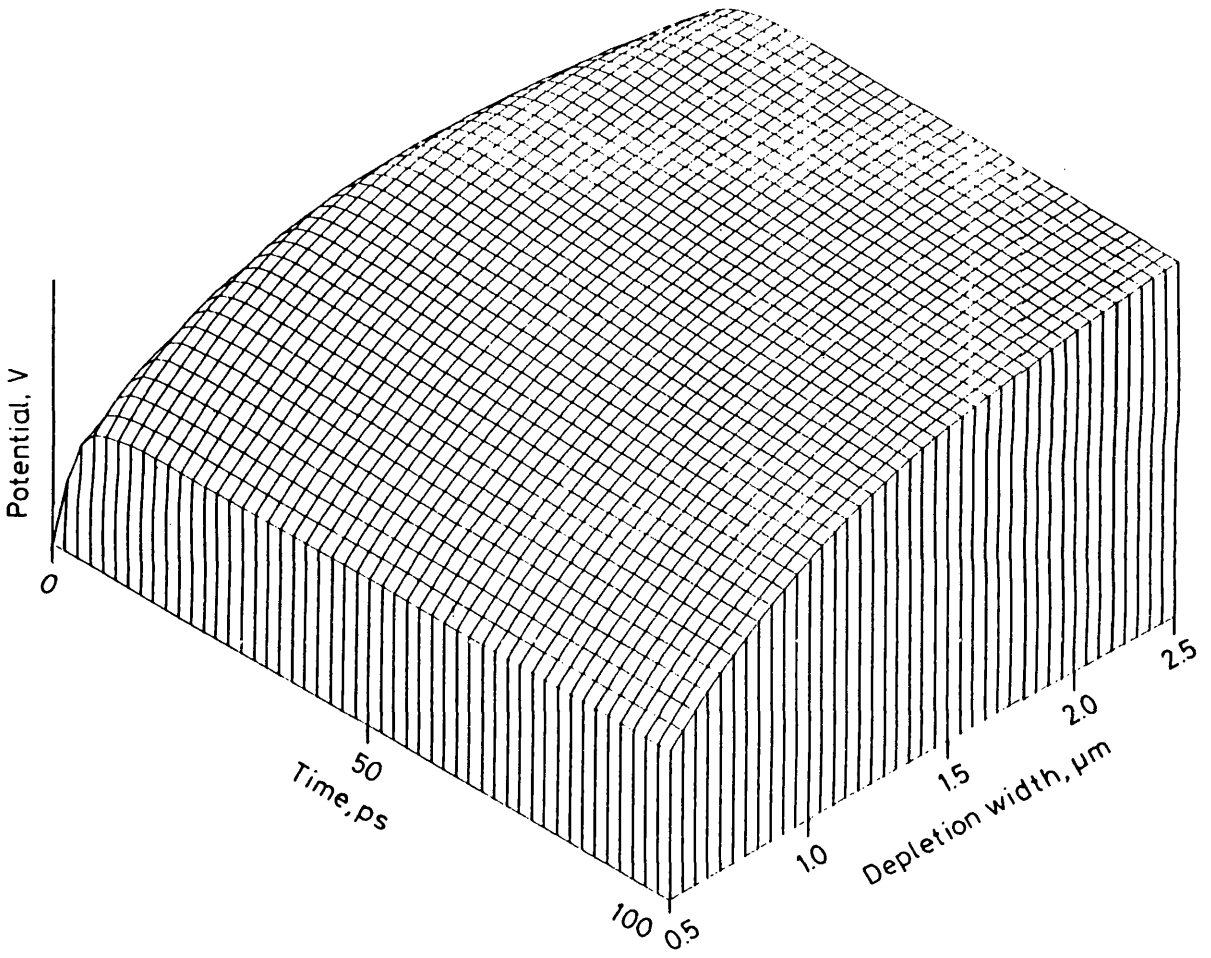

Figure 3.9. Spline fitted to the original data

polynomial arcs joined together at the ends (knots) with continuity in the values of the function and all derivatives to the $n - 1^{th}$. The spline uses a number of low degree polynomials to give a smooth curve, rather than resorting to a single polynomial or Tchebychev series containing a large number of terms and possibly introducing unwanted fluctuations into the result. The spline functions are piece-wise continuous polynomials and can therefore be differentiated analytically, allowing a more accurate representation of the current response than could be obtained by using a finite difference approximation.

A two dimensional spline was fitted to the charge response. On the time axis a bicubic spline was chosen, giving a quadratic spline representation of the current response after differentiation. The parameter axis was represented by a bicubic spline as this gave adequate results. The number of knots in the two axes of the spline were markedly different. The signal changes rapidly along the temporal axis and therefore a large number of knots (54) were required. On the other axis

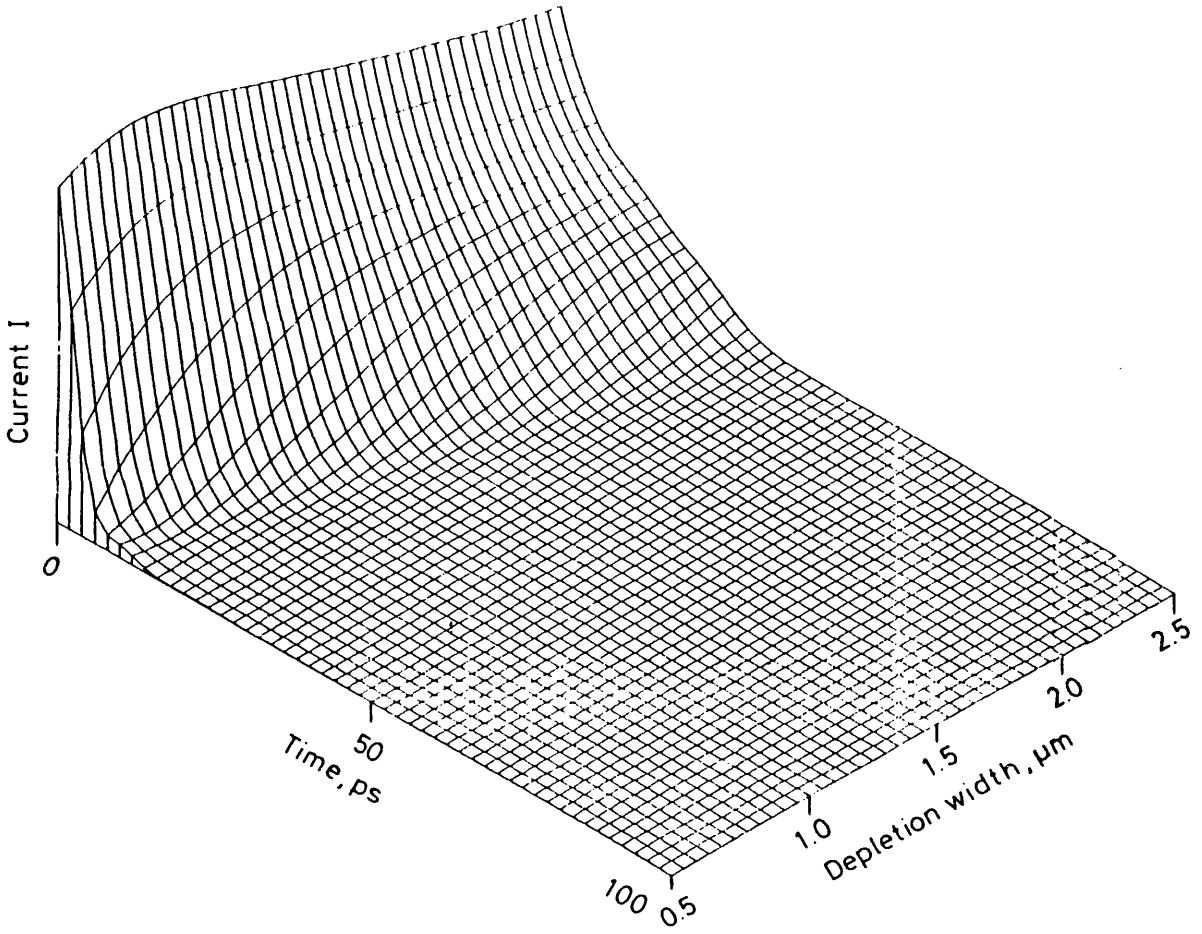

Figure 3.10. Spline fitted current response

the response varied more slowly and so few (6) knots were required. The positioning of these knots was carried out automatically[14]. All the routines used are available from the Division of Information Technology & Computing (DITC) Data Approximation and Subroutine Library (DASL) at NPL. An Isometric projection of the fit to the original data (the varation of the potential induced by the photocarriers) is shown in figure 3.9. The current response, derived from the original data, is shown in figure 3.10. The fitting of the splines reduces the size of the data set from 636 kbytes to 20 kbytes which is a considerable space saving.

3.6. VERIFICATION OF THE MODEL USING MEASURED RESULTS

In order to proceed with the development of an optimised diode it is important to know that the model chosen is accurate. Measurements were made of the performance of a prototype diode and mount. A fitting program was then used to find the best values of parameters such as the

Epitaxial layer thickness and the stray capacitance for which good estimates were available from measurements made during the manufacturing process.

Photodiode and mount

The Photodiode, designated K133a, is a substrate light entry PIN device with a 45 μm diameter circular active area. A photograph of the photodiode chip is shown in figure 3.11. In the upper part of the photograph, diode is shown mounted on the glass submount in the flip chip configuration. The lower part of the photograph shows the underside of the chip. The diode mesa and gold thermocompression bond-pads can be clearly seen. The diode was mounted on a low capacitance glass subcarrier and bonded onto a ceramic microwave package[15] by Plessey. The Epitaxial layer thickness of this device was measured at Plessey during the manufacturing process and is 3.2 ±0.1 μm. The total capacitance of the diode and ceramic mount was measured as 140 fF at 15 V bias. The internal series resistance of the diode was not measured but is normally within the range 5 - 10Ω.

The diode was mounted between the centre and outside of a coaxial line. A modified form of the NPL fast photodiode mount (this author, unpublished work) was used as this gave excellent decoupling of the bias supply.

The measurement system

The measurement system, shown in figure 3.12, consisted of a Tektronix sampling system and an Optoelectronics Ltd PLS 10 laser diode at 1324 nm as the source.

The laser suffers from multiple pulsing, described in part 1 and 2 of this thesis. An research photodiode from AT&T Bell laboratories[16], having a frequency response considerably in excess of that of the sampler, was used as a transfer standard to give the impulse response of the system. Measurements were made with the laser diode biased at 141, 142, 143 and 144 V using both the Bell and Plessey diodes. A 20 dB attenuator was used to remove any electrical reflections from the photodiode or the sampling head.

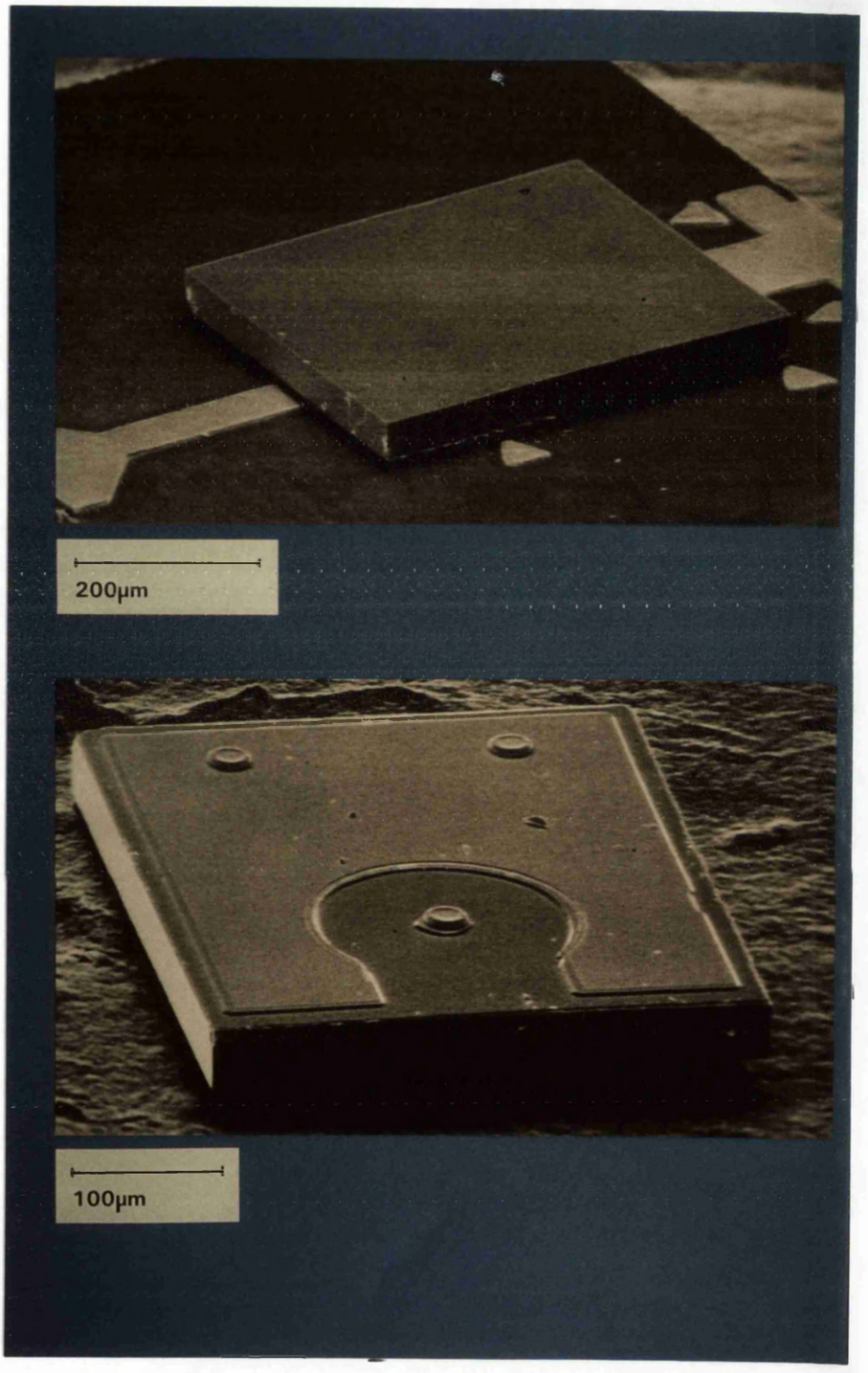

Figure 3.11. Plessey photodiode chip mounted on glass subcarrier (upper) and view of the etched mesa (lower)

Fitting program

A forward convolution fitting process was used to determine the accuracy of the model in preference to the deconvolution method described in

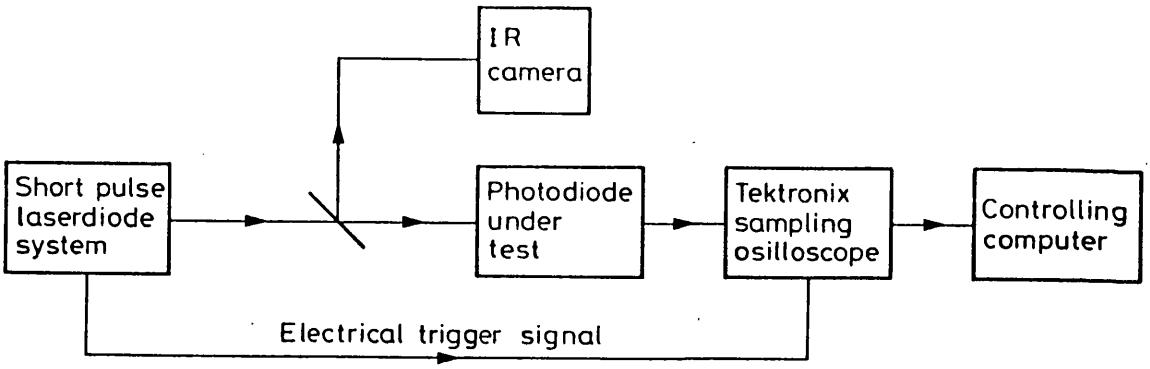

Figure 3.12. Layout of the system to measure the Plessey K133a photodiode at 1324 nm

part 2. This approach was taken because it eliminated the need for a filtering function to remove the effects caused by deconvolution of the noise. In the forward convolution method the model is convolved with the system impulse response and compared with the measured response. The parameters are varied until the sum of the squares of the difference between the two curves is at a minimum.

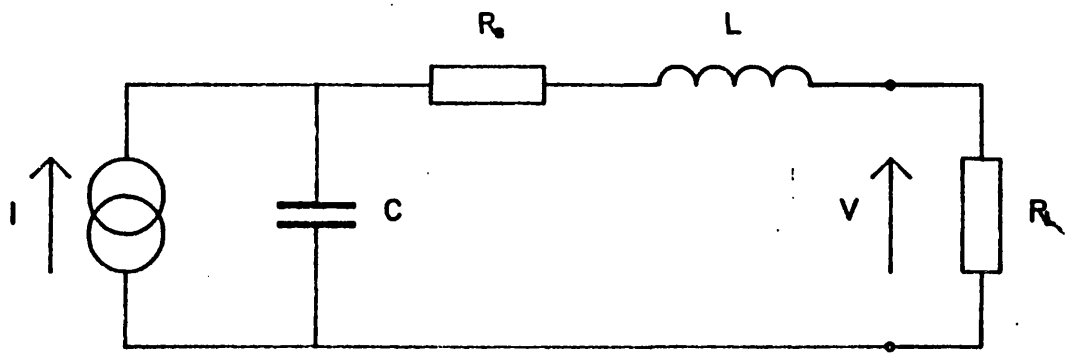

Figure 3.13. Network model of the photodiode

A simple network was used to describe the diode response (figure 3.13). The values of the parameters were constrained to lie within physically realisable limits. Table 3.2. shows the allowed range of the parameters and their starting values.

The minimisation routine used for the program was a *Linearly Constrained modified Newton algorithm Subroutine*[17] from the DITC Numerical Optimisation Subroutine Library (DNOSL).

Table 3.2. Starting values for the fitting program

Parameter	Minimum value	Maximum value	Starting value	Units
Stray capacitance	0.0	200.0	60.0	fF
Series resistance	0.0	20.0	5.0	Ω
Bondwire inductance	0.2	2.5	1.25	nH
Epitaxial layer thickness	2.8	3.6	3.2	μm
Time shift	-200.0	200.0	set for each run	ps
Scale factor	0.0	10.0	set for each run	-

Results from the fitting program

Figure 3.14 shows the measured responses of the Bell and Plessey diodes, the convolution of the Bell diode response with the model for the optimum choice of parameters and the accuracy of the fit obtained with the laser biased at 141 V. The final values of the parameters are shown with their mean and standard deviation in table 3.3. Good agreement has been found between the measured epitaxial layer thickness and the fitted result suggesting that the model is fairly accurate and can be used to predict the photodiode response.
The high inductance of the photodiode mount (≈1.3 nH) makes this mounting arrangement unsuitable form use with high speed diodes.

3.7. MODELLING RESULTS

The modelling programs have been used to investigate the effect of varying the mounting inductance, the stray capacitance, the device diameter and depletion width on the speed of response. A number of different programs have been developed to give time or frequency domain information about the diode response. In order to optimise the design a

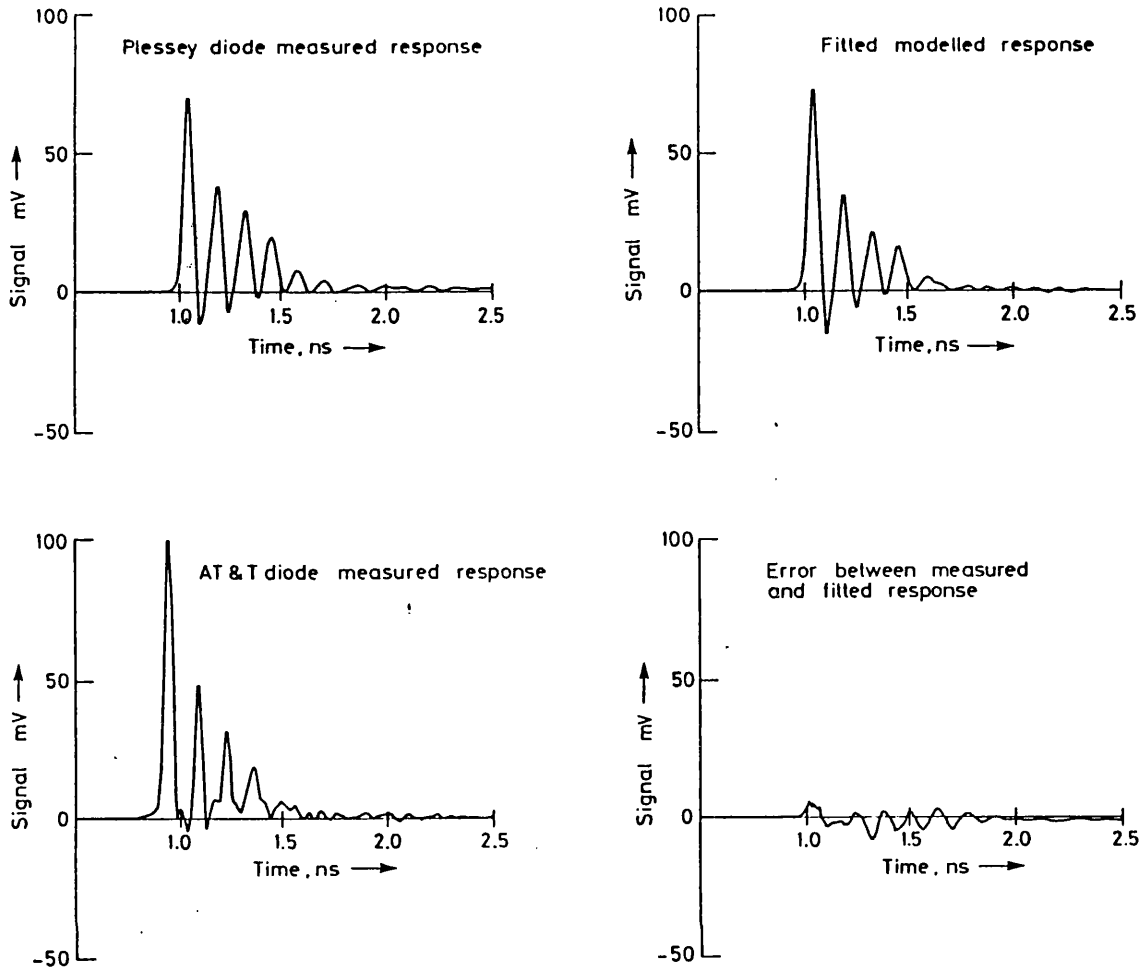

Figure 3.14. Measured, fitted responses and error

suitable parameter must be chosen to represent the diode performance. The two most commonly used parameters are the Full Width at Half Maximum (FWHM) in the time domain and the frequency at which the sensitivity of the diode is reduced by 3 dB (f_{-3dB}). These parameters make a good starting point but have limitations because of their inherent simplicity.

For a given device area, a change to the depletion width will alter both the transit time for the photogenerated carriers and the junction capacitance. If the depletion width is too small, the speed of response will be dominated by capacitive effects. If the depletion width is too large, the transit time for the photogenerated carriers will dominate. Clearly there must be an optimum depletion width for a given diameter device. The modelled results showing this relationship are presented in figure 3.15. The optimum depletion width for a 30 μm diameter device is approximately 0.8 μm.

Table 3.3. Results from the fitting program

Parameter	Optimum value for each run				Mean	Standard deviation	Units
Laser bias	141.0	142.0	143.0	144.0	-	-	V
Stray capacitance	92.6	105.5	118.3	88.1	101.1	13.6	fF
Series resistance	5.86	6.44	6.78	5.67	6.19	0.52	Ω
Bondwire inductance	1.28	1.27	1.23	1.32	1.28	0.04	nH
Epitaxial layer thickness	3.24	3.26	3.27	3.23	3.25	0.02	μm
Time shift	61.2	0.44	-15.9	-30.6	-	-	ps
Scale factor	0.80	0.59	0.82	0.70	-	-	-

The inductance of the mounting circuit can also be used to enhance the speed of response of the photodiode. This technique has been used by a number of authors to improve the photodiode performance[16,18]. Figure 3.16 shows the current response of structure, the response of the network and the overall response of the device. The resonance associated with the network response raises the overall response of the device and greatly improves the 3 dB frequency performance. At frequencies above this resonance the overall response of the photodiode drops rapidly. Some tailoring of the individual mounting inductance, or selection of the devices after manufacture, is required to achieve the best results.

The effect of the variation of the mounting inductance on the frequency response of a photodiode is shown in figure 3.17.

The temporal response of the photodiode is also of great importance as it allows the device to be used as a transfer standard for both vector and scalar measurements. Figure 3.18 shows the modelled response of an optimised photodiode with a FWHM of 17.9 ps and a f_{3dB} frequency of

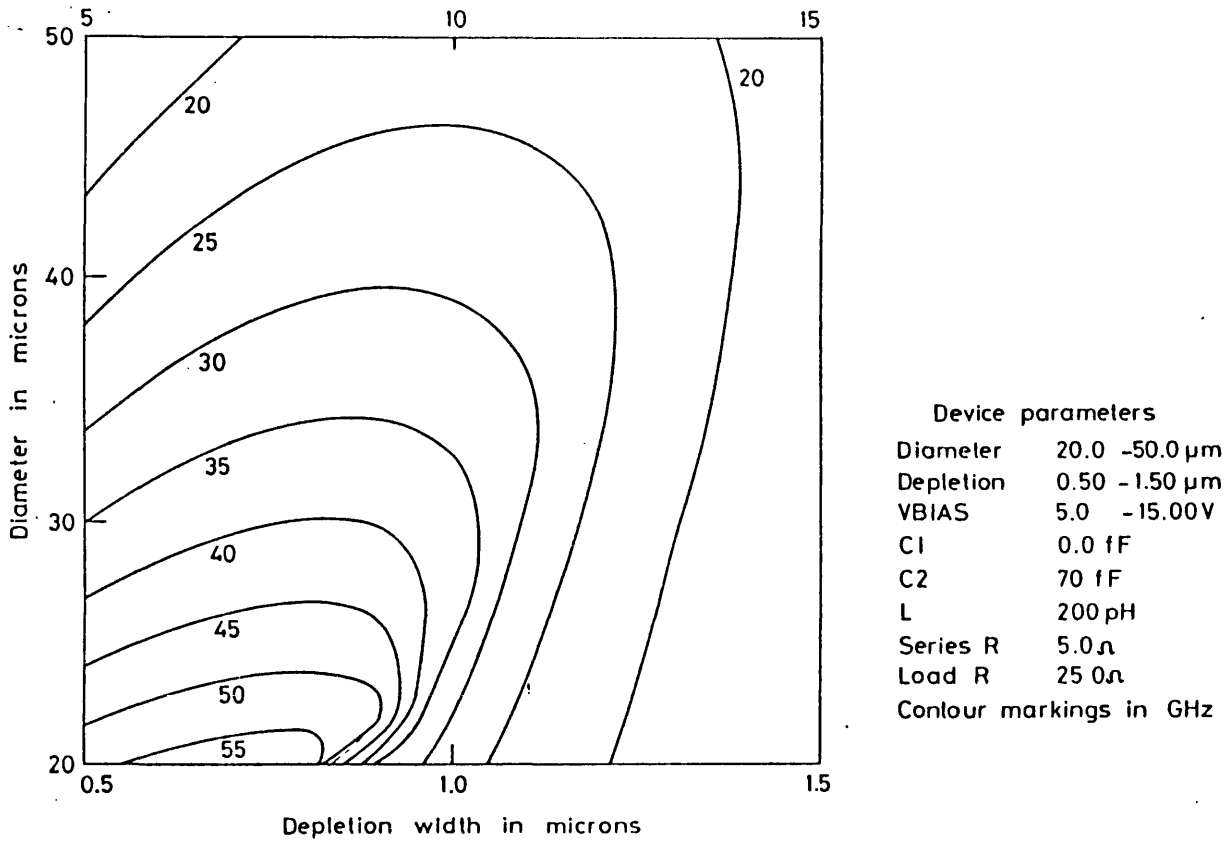

Figure 3.15. Contour map showing the variation of the photodiode f_{3dB} with depletion width and device diameter

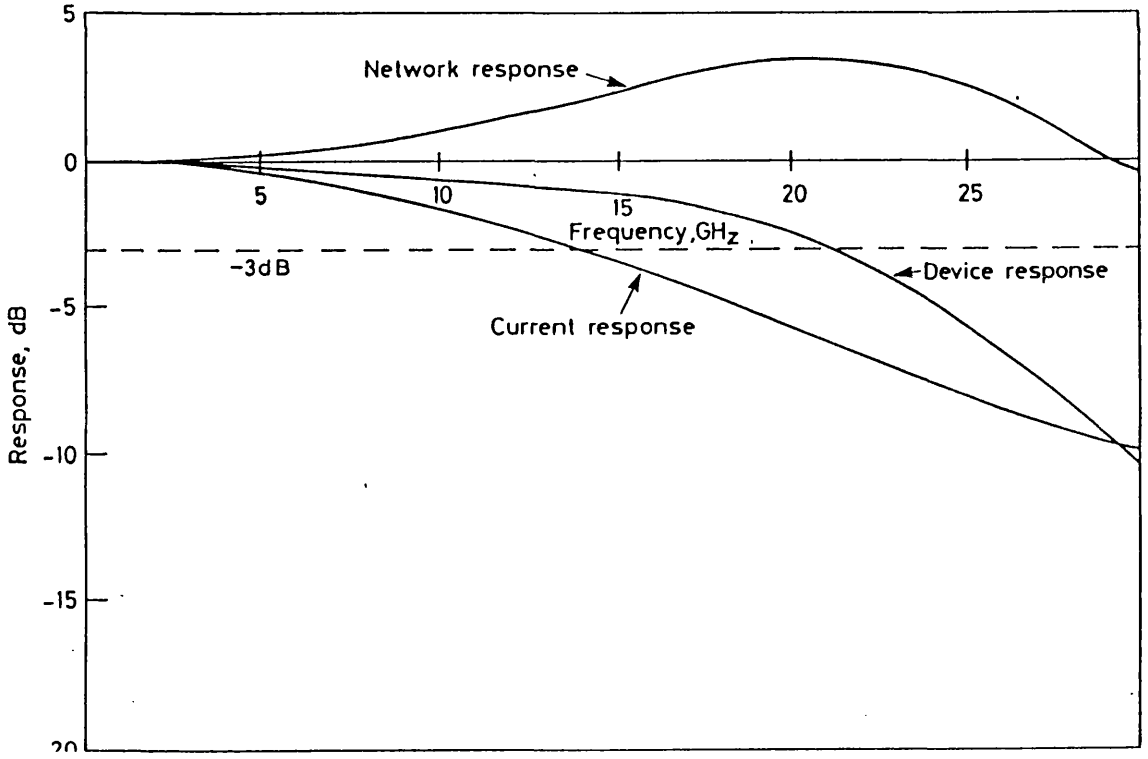

Figure 3.16. Variation of the components of the diode response with frequency

25.9 GHz. Unfortunately, few of the techniques available to measure

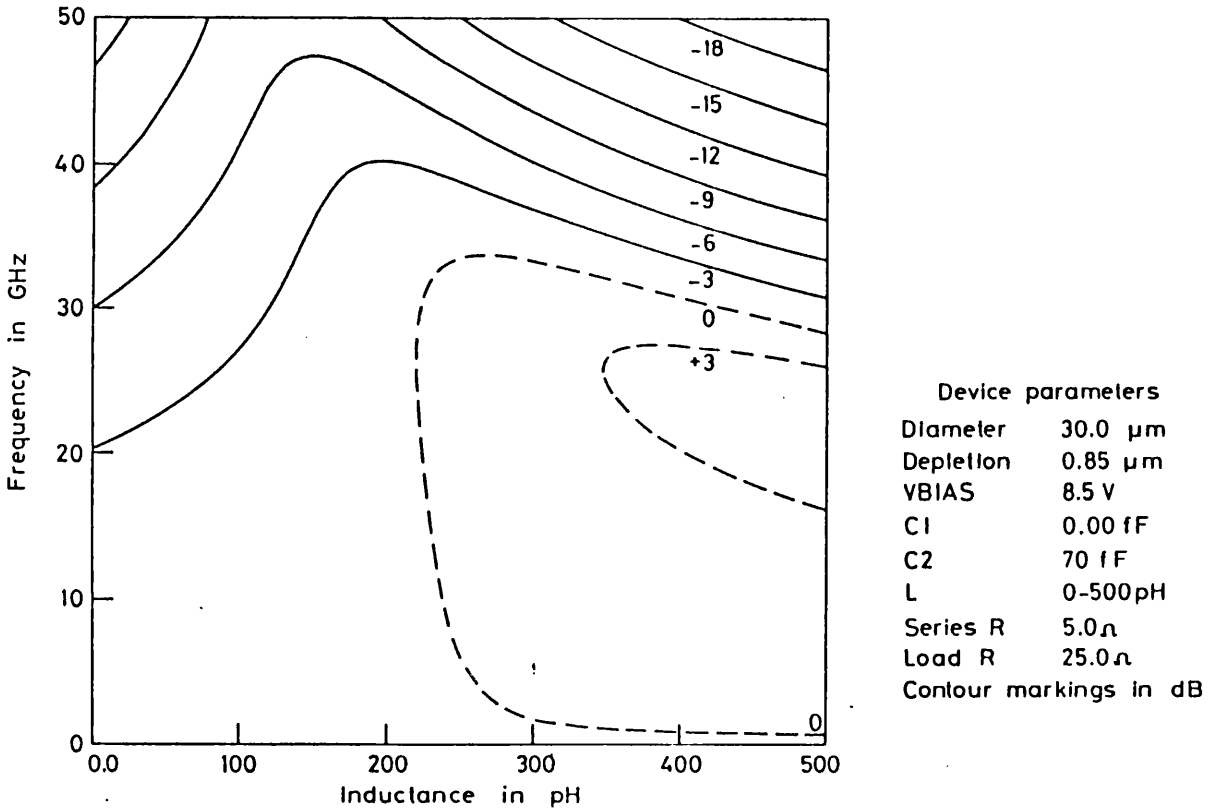

Figure 3.17. Variation of the frequency response with mounting inductance

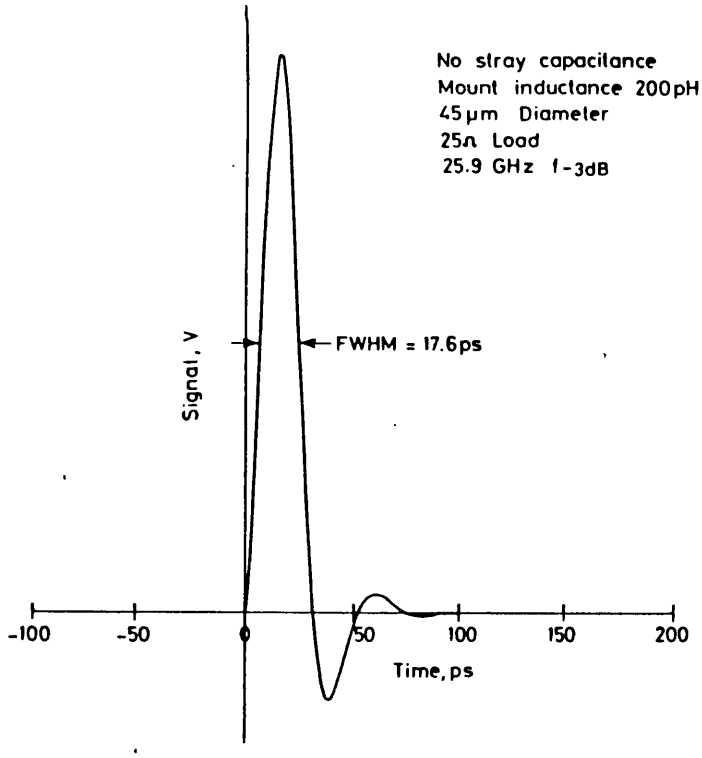

Figure 3.18. Temporal response of a 45 µm diameter, optimised photdiode

photodiodes with millimetre-wave bandwidths will allow the measurement of the temporal response. A possible solution would be to use a model of

the photodiode performance fitted to the measured parameters for that device. The measured scalar frequency response can be used in conjunction with vector measurements of the electrical reflection coefficient and a model of the device to estimate the response.

3.8. CHAPTER CONCLUSION

In this chapter the advantages and disadvantages of the available photodiode structures have been compared. The structure chosen for the optimised design will be of the substrate light entry type with an active region of 30 - 40 microns in diameter.

A linear small signal model of the photodiode has been described and the choice of the parameters for this model has been shown. The accuracy of the model has been tested using measurements of a device with a known structure. The effect of varying parameters on the device frequency response has been considered. The model has been used to estimate the optimum parameters for achieving the highest bandwidth and the largest area device.

4. DEVELOPMENT AND ASSESSMENT OF THE FAST PHOTODIODE AND MOUNT

4.1. INTRODUCTION

The choice of the mount design for a fast photodiode strongly affects the overall performance of the system. The design determines the load impedance, stray capacitance and inductance seen by the diode. In this chapter the main mounting configurations are compared, the design of a coplanar geometry prototype mount is described and the experimental results obtained with these designs are presented and discussed.

4.2. MOUNTING CONFIGURATIONS

The mount configuration chosen for a fast photodiode designed to be used as a transfer standard should have good high speed properties and should present a good impedance match for signals reflected from the measuring equipment. The second property is called reverse termination and can be achieved at the expense of some of the diode sensitivity. The importance of the reverse termination property can be seen from the following example. A measurement system with a return loss (reflection coefficient) of -15 dB, will give rise to errors of up to ± 1.5 dB due to reflections, when measuring an unterminated photodiode. If a reverse terminated photodiode having a maximum reflection coefficient of -10 dB is used the overall accuracy will be ± 0.5 dB. To obtain an equivalent performance with an unmatched diode the return loss of the measurement system would have to be improved by 10 dB. Alternatively the return losses of both components could be measured and a correction made to the results as shown in part 1 of this thesis. Reverse terminated packaged devices with frequency responses of greater than 20 GHz have been reported[16,19].

The main circuit arrangements used to mount photodiodes and photoconductors are shown in figure 4.1 a - d. The positions of the decoupling capacitors have been shown as these represent a potential source of problems for a high bandwidth design.

The first arrangement, shown in figure 4.1a, is the simplest and most commonly used design for a fast photodiode mount and was used for the initial assessment of the substrate light entry photodiode design. The load impedance presented to the diode is 50 Ω and all of the signal is launched into the line. This design is not reverse terminated and will

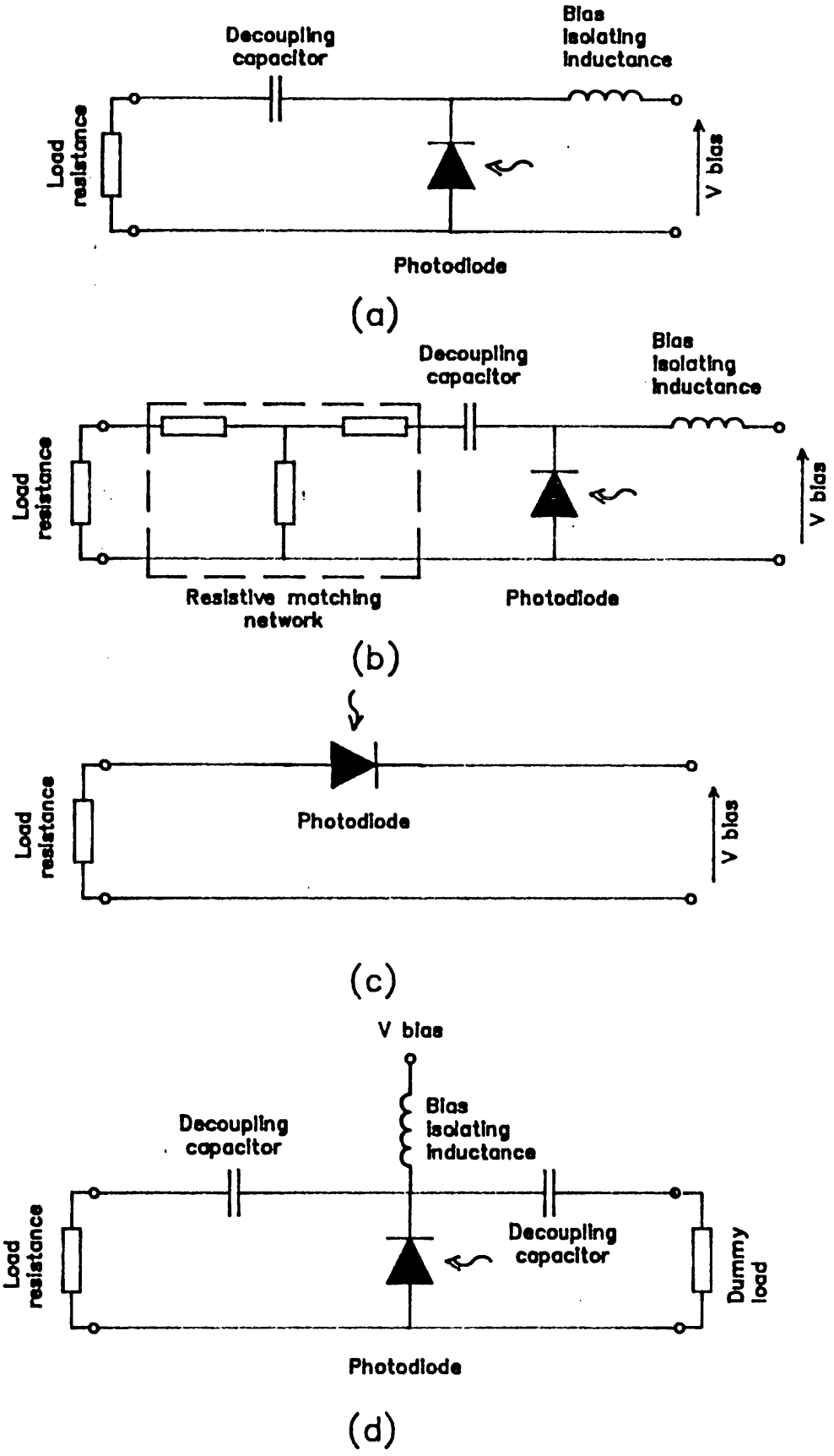

Figure 4.1. Possible photodiode mounting configurations

present a poor match for any signals reflected from the measurement system. Results obtained in the previous chapter, from the assessment of the substrate light entry photodiodes, suggested that the inductance of this type of mount could be as high as 1.3 nH. More recent results suggest that an inductance of about 300 pH can be obtained[18,12].

The second arrangement is a hybrid circuit consisting of a resistive network to match the diode to the transmission line. The circuit can be well matched to the 50 Ω line and hence overcomes the problems caused by reflections. The penalty of this approach is that half the signal will be lost to the matching network. The AT&T Bell laboratories photodiode[16] used in previous measurements is of this design. The diodes were mounted in a modified detector diode mount (HP33330C) which has a series resistance of roughly 50 Ω. The photodiode is therefore presented with a load impedance of 75 Ω which seriously restricts the allowable device area but allows a higher mount inductance to be tolerated. A 45 μm diode of the Plessey substrate entry design, optimised for speed, would have a 3 dB frequency of between 10 and 14 GHz in this type of mount.

The third mounting arrangement, shown in figure 4.1c, is well suited to coplanar[20] and microstrip[21] designs. The arrangement is most suitable where the detector is fabricated directly onto the substrate and the gap between the two lines is of the order of a few microns. The impedance presented to the photodiode is 100 Ω. The high load impedance puts tight constraints on the device capacitance. The arrangement is also not reverse terminated and will present a poor match for reflected signals. Biasing the device is simple and mismatches occuring at the bias connection can be removed to outside the temporal region of interest.

The fourth arrangement, shown in figure 4.1d, has the photodiode is placed across the transmission line. The diode is presented with a low load impedance of 25 Ω allowing a larger area device to be used. However the low load impedance will tighten the constraints on the allowable mounting inductance if resonant effects are to be avoided. The bias supply must also be decoupled at two points, increasing the complexity of the design. This mounting arrangement is reverse terminated and will give a reasonable match for reflected signals.

Two suitable options for mounting the photodiodes have been chosen from an assessment of the advantages and disadvantages of the four circuit configurations. These are the hybrid approach (b) and the mount where the diode is placed across the transmission line (d).

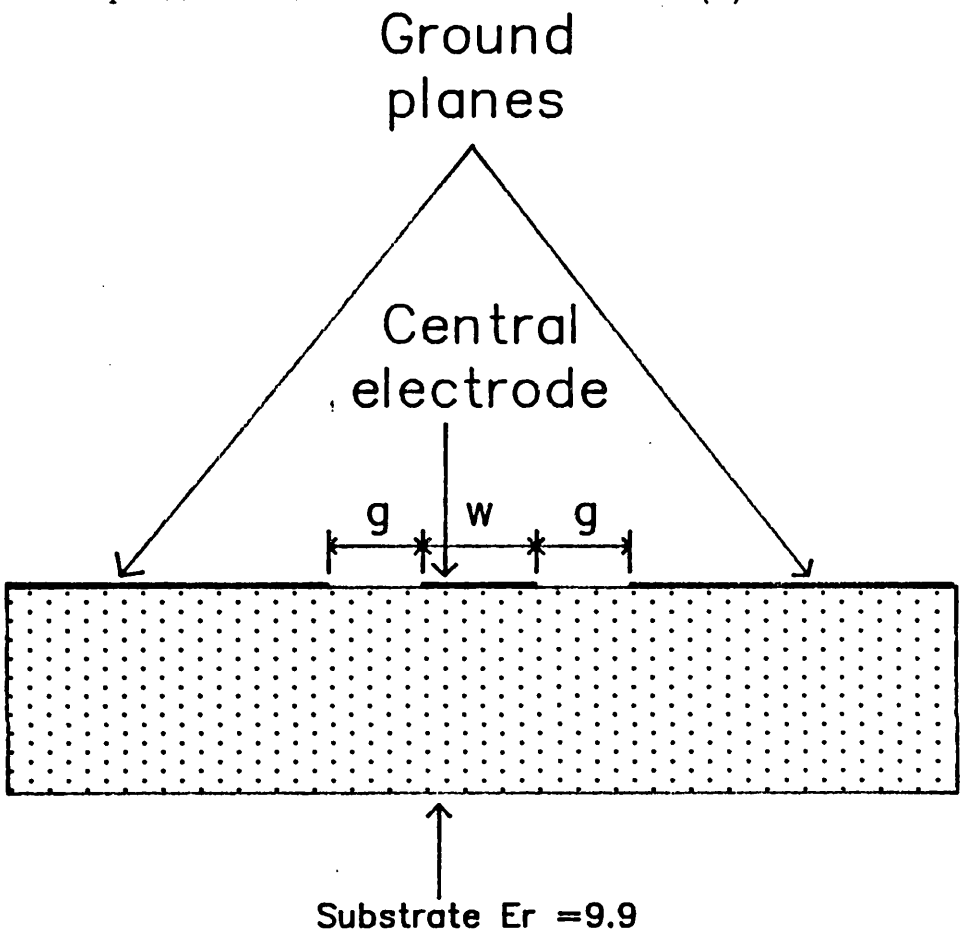

Figure 4.2. Balanced coplanar waveguide

The hybrid circuit offers the considerable advantage that the impedance presented to the diode can be tightly controlled. This would allow the series resistance to be optimised to maximise the frequency response but suppress resonant effects. Unfortunately the matching networks available in r.f. detector diode packages present an unacceptably high series resistance. The development of a specific thin film resistor network is feasible but beyond the scope of the current research.

Mounting the photodiode directly across the transmission line is feasible using the coplanar geometry, shown in figure 4.2. This has been chosen as the circuit arrangement for mounting the fast photodiodes.

4.4. CALCULATION OF THE COPLANAR WAVEGUIDE LINE IMPEDANCE

An approximation for the impedance of a transmission line can be calculated from the capacitance per unit length:

$$Z_o = \frac{\sqrt{\epsilon_r}}{cC_o} \qquad \text{(eq. 1)}$$

where Z_o is the impedance of the transmission line; ϵ_r is the relative permitivity of the medium; c is the speed of light and C_o is the capacitance per unit length of the line.

The capacitance of a balanced coplanar waveguide structure, shown in figure 4.3a, is determined by the substrate permittivity, the width of the central electrode (w) and the width of the gap (g) between the centre electrode and the earth planes.

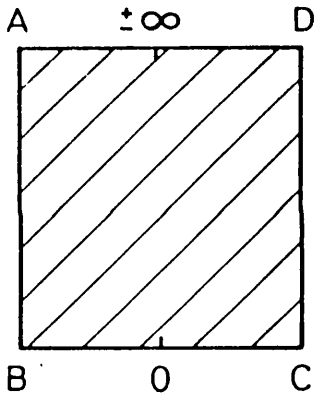

Transformed domain

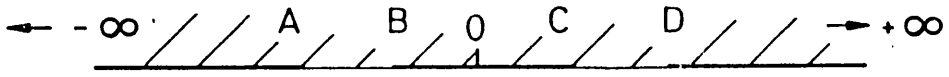

Untransformed domain

Figure 4.3. Conformal mapping to calculate the impedance of a coplanar waveguide

An elliptic integral conformal transformation[22] can be used to map the fields in the upper half of the structure into the inside of a rectangle as shown in figure 4.3b. The points A',B',C' and D' in the

rectangle correspond to the points A,B,C and D in the original structure. The problem is then converted to that of a simple parallel plate capacitor and therefore the impedance can be easily obtained. The analysis was later extended[23] to allow for a finite thickness of substrate but this assumes that the electric field is completely confined within the dielectric layer. The impedance estimated by this method will therefore always be slightly lower than the true value because the electric fields will not be completely confined within the substrate. A fortran subroutine was used to perform the transform[24].

It is likely that the mismatch in the electric and magnetic fields at the interface between the coaxial and the coplanar lines will give rise to a much larger reflection than that caused by a simple impedance mismatch.

4.5. Mk1 PROTOTYPE COPLANAR MOUNT DESIGN

A prototype mount with a 25.4 mm long coplanar section was designed to test the performance of the mount/diode combination. The flip-chip mounting of the photodiode is shown in figure 4.4. The bias was decoupled using four low inductance 33 pF chip capacitors[25].

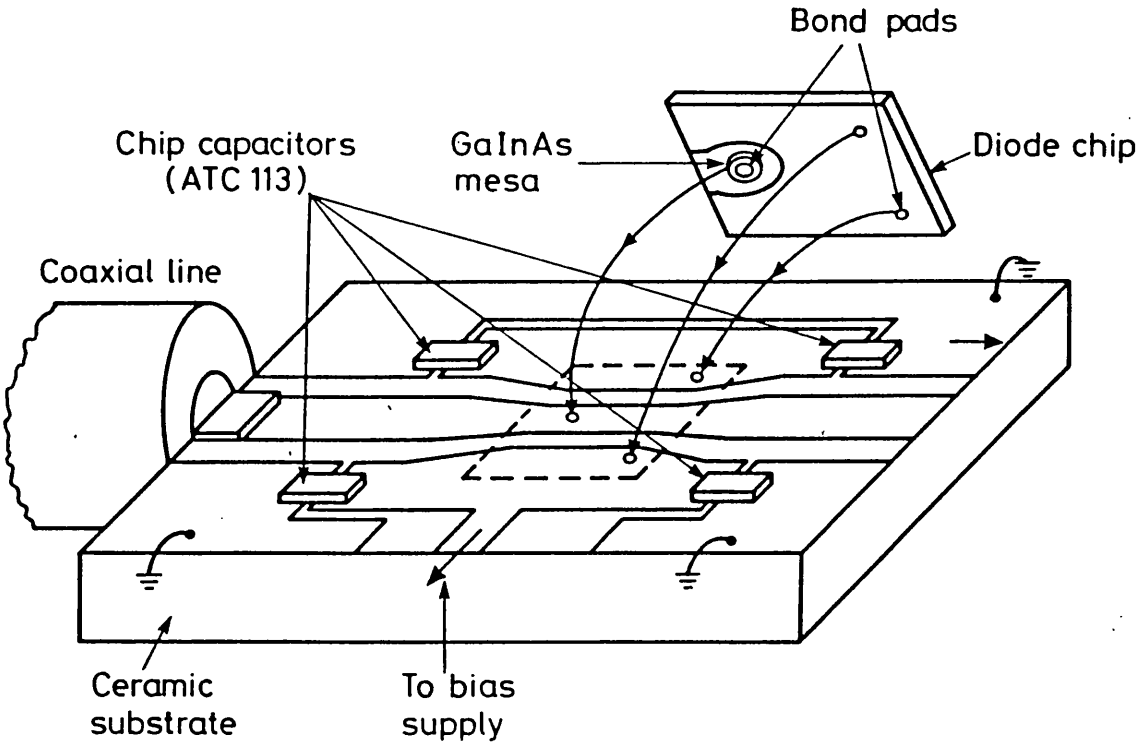

Figure 4.4. Flip chip mounting of photodiode on a coplanar waveguide

Graded coaxial/coplanar transitions at either end of the mount were included to improve the impedance match. The width of the central electrode was chosen to match that of the inner of the SMA connector

(0.8 mm) The mount is shown in figure 4.5.

The mount was fabricated on a standard polished 0.025" ceramic substrate using a lift-off technique and subsequently gold plated to a thickness of 5 μm. During the assembly process problems were encountered because the n^- region of the diode became shorted to the coplanar inner connector. This was attributed to preferential plating at the edges of the coplanar lines. The short circuit problem was overcome by etching back the gold in the region under the photodiode to a thickness of 0.2 μm before assembly. This will locally increase the resistance of the inner by 1 - 2 Ω. A photograph of the central section is shown in figure 4.6. The etched region is visible as a slightly darker portion of the central electrode.

A production diode was used to test the design. The chip design is the same as was used for the K133a photodiode described in the previous chapter. The device had a 45 μm diameter active area and a depletion width of roughly 2 μm at 25 V bias. The wide depleted region was caused by low doping of the n - type InP buffer layer.

The impedance characteristics of the coplanar mount were measured both for the bare mount and for the diode and mount. The reflection coefficients (S_{11}) were measured using a Hewlett Packard 8510A vector network analyser. The results, shown in figure 4.7, give a maximum value for the reflection coefficient of -17.5 dB for the mount alone and -10.7 dB for the diode and mount.

4.6. ASSESSMENT OF THE Mk1 PROTOTYPE COPLANAR MOUNTED PHOTODIODES

Two prototype mounts containing production diodes were made. One of these devices became short circuit during preliminary testing but the second device, designated CPW#2, functioned for some time. This diode eventually failed by becoming short circuit, drawing currents of several milliamps at 5 V bias. However, a considerable body of measurements were made by both time and frequency domain methods prior to the photodiode's demise.

Measurements using pulsed semiconductor lasers

A Lasertron QLPX source at 1270 nm and an Optoelectronics PLS10 laser at 1146 nm were used. the two lasers produced measured responses of 43 ps and 33 ps FWHM respectively when measured using the AT&T

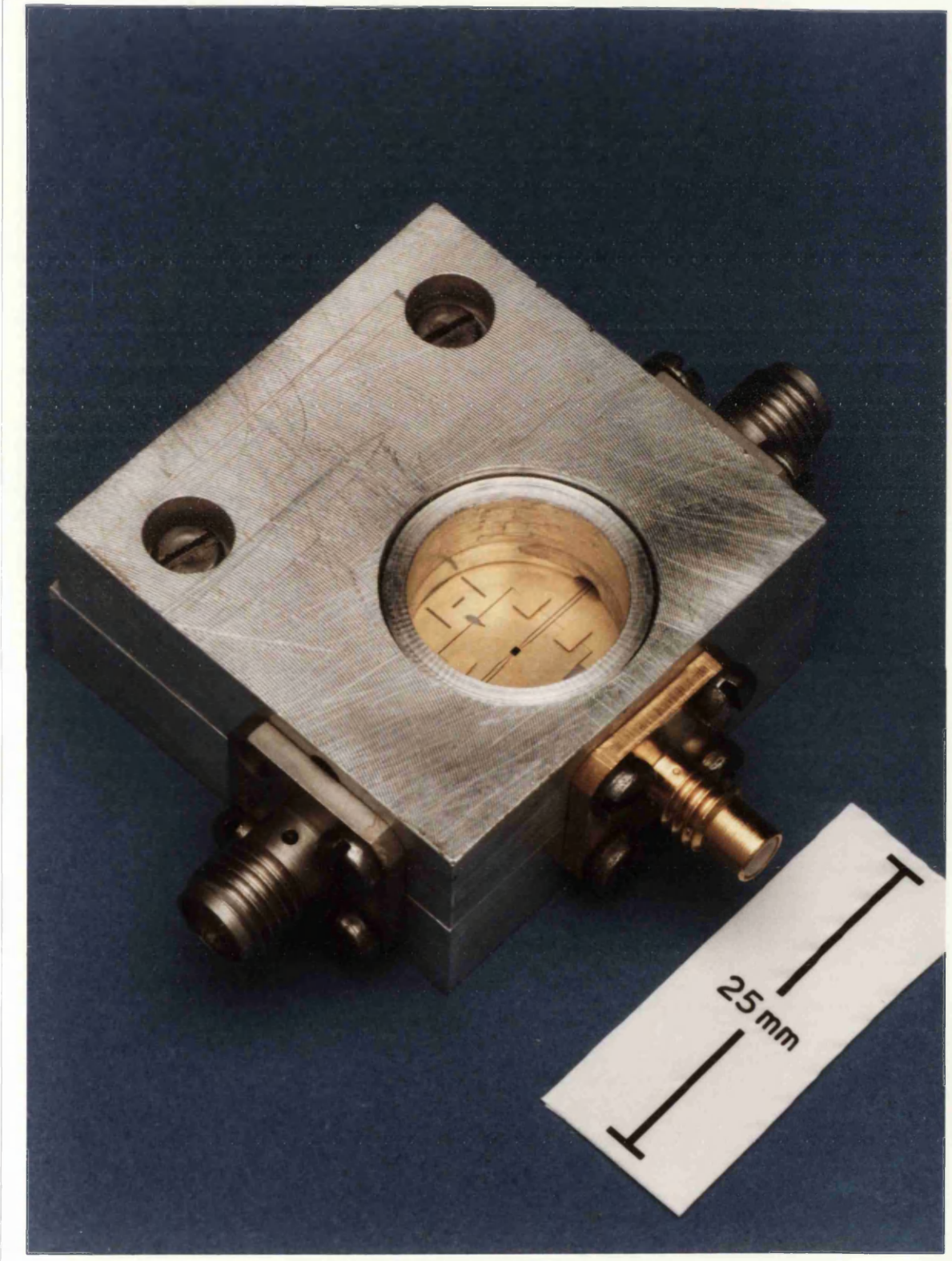

Figure 4.5. Mk1 prototype coplanar photodiode mount

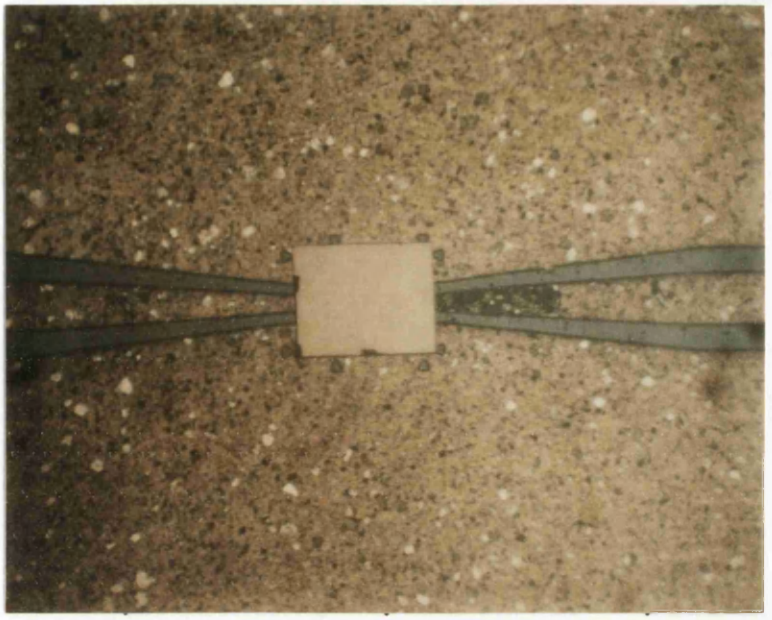

Figure 4.6. Centre section of Mk1 prototype coplanar photodiode mount

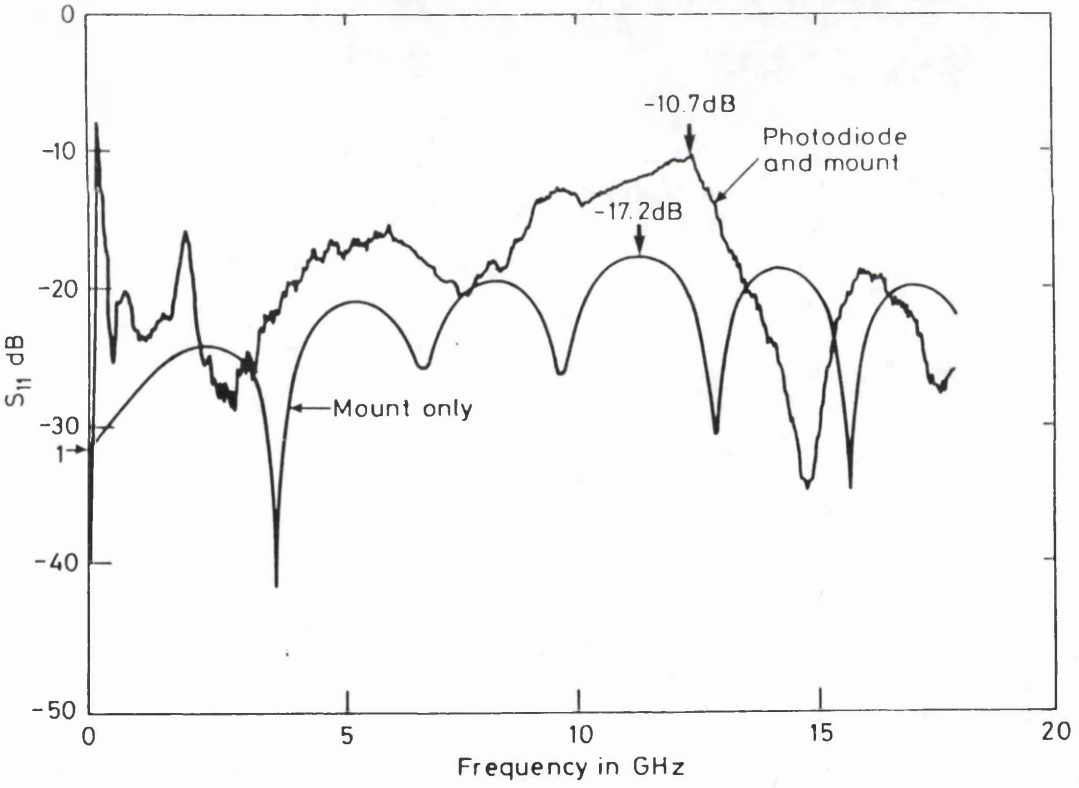

Figure 4.7. Reflection coefficient of the mount and photodiode

photodiode.

The PLS10 laser produces multiple pulses. The separation between the first two pulses is roughly 120 ps. This limits the time window that can be used for measurement. Figure 4.8 shows the response of the Plessey and AT&T diodes on a 50 ps/div timescale. The Plessey diode has

a longer fall time and little ringing is apparent from the trace. A summary of the results is given in table 4.1.

Table 4.1. Summary of the measured results at 1146 nm

Device	Risetime (ps)	Falltime (ps)	FWHM (ps)
AT&T	29	20	34
Plessey	29	40	41

The long fall time of the CPW#2 device has been attributed to the wide depletion region. The short rise time and the absence of significant ringing suggests that the coplanar mount has a low inductance.

The QLPX source produces a single pulse with no appreciable secondary pulsing. A comparison of the measured responses of the AT&T and the CPW#2 devices is shown in figure 4.9.

Measurements using the pulse compressed YAG laser

The pulse compressed YAG laser system consists of a modelocked Quantronix laser operating at 1.06 μm and a fibre/grating pulse compressor supplied by Imperial College. The repetition rate of the modelocked pulses was 76 MHz with an uncompressed FWHM of approximately 80 ps. The experimental layout is shown in figure 4.10.

Considerable difficulties were experienced with the YAG laser and as a result the pulse compressor was not ideally optimised. The unoptimised operation of the pulse compressor was such that only part of the energy in a pulse was compressed. The remaining fraction was broadened to form a wider pedestal. The optical pulse has been described by a simple model (equation 2).

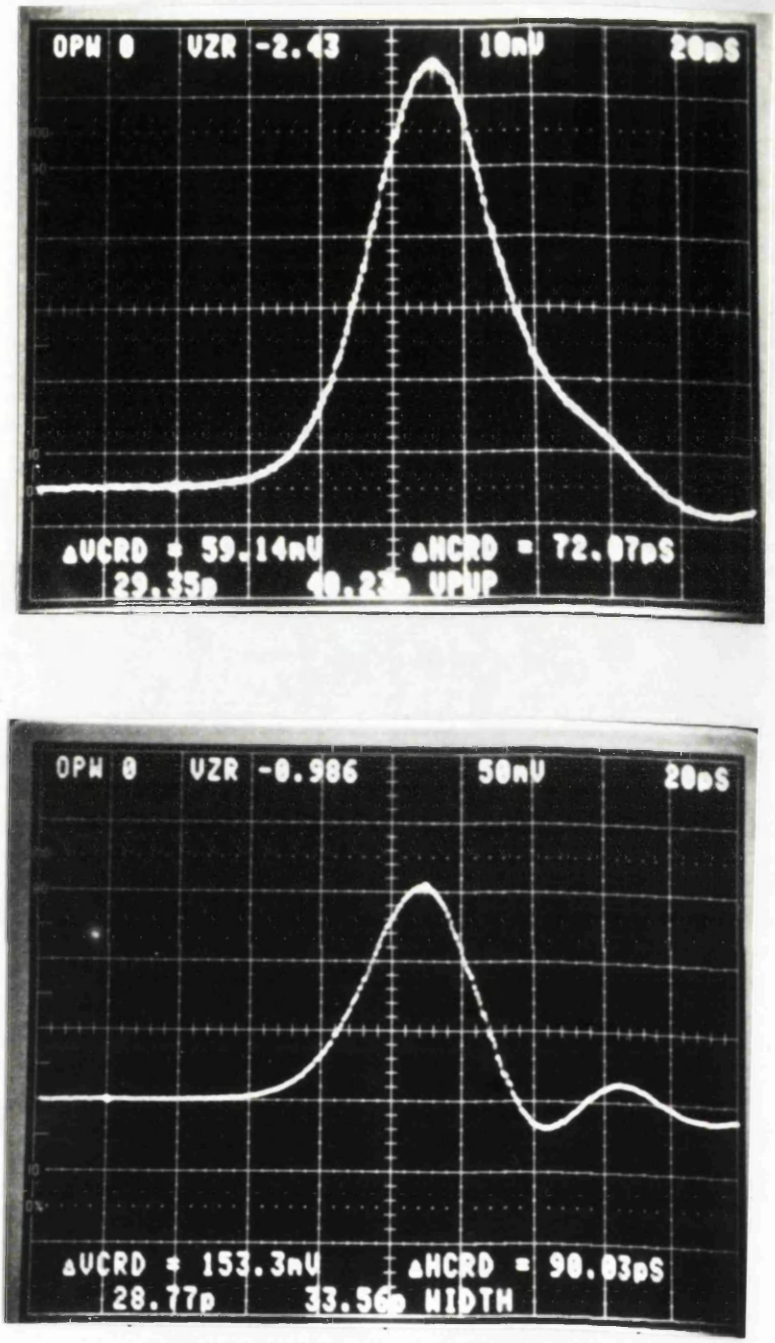

Figure 4.8. Measurement of the CPW#2 (upper) and AT&T (lower) photodiodes at 1146 nm

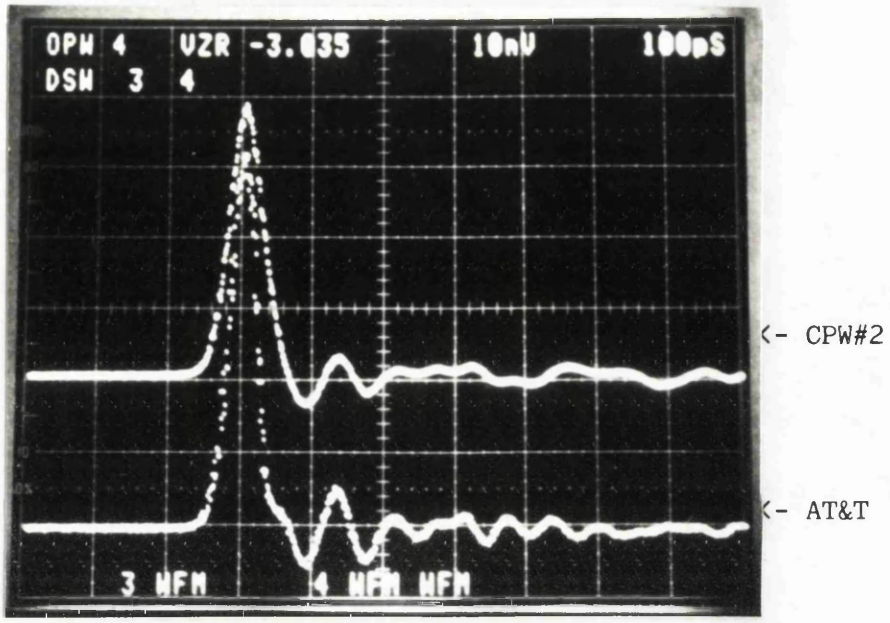

Figure 4.9. Measurement of the CPW#2 (upper) and AT&T (lower) photodiodes at 1270 nm

$$I(t) = I_o(A_1 \exp(-B_1 t^2) + A_2 \exp(-B_2 t^2)) \qquad \text{(eq. 2)}$$

where I(t) is the optical intensity in the pulse; I_o is the maximum optical intensity; A and B are constants determined by a fitting process

Measurements of the power spectrum of the comb of harmonics using the AT&T photodiode show this effect clearly (figure 4.11). The modelled function was fitted to the results measured with the AT&T photodiode over the range 0 - 10 GHz. The best fit corresponded to a pulse with Gaussian components 9 ps and 145 ps FWHM with 65% of the energy in the shorter pulse. The rms error in the fit was 0.26 dB.

The response of the CPW#2 diode was measured and the results were corrected for the spectrum analyser sensitivity, variations of the photocurrent and the modelled laser response shape, as shown in figure 4.12. The 3 dB frequency of this device has been estimated as 10.8 GHz at 25 V bias.

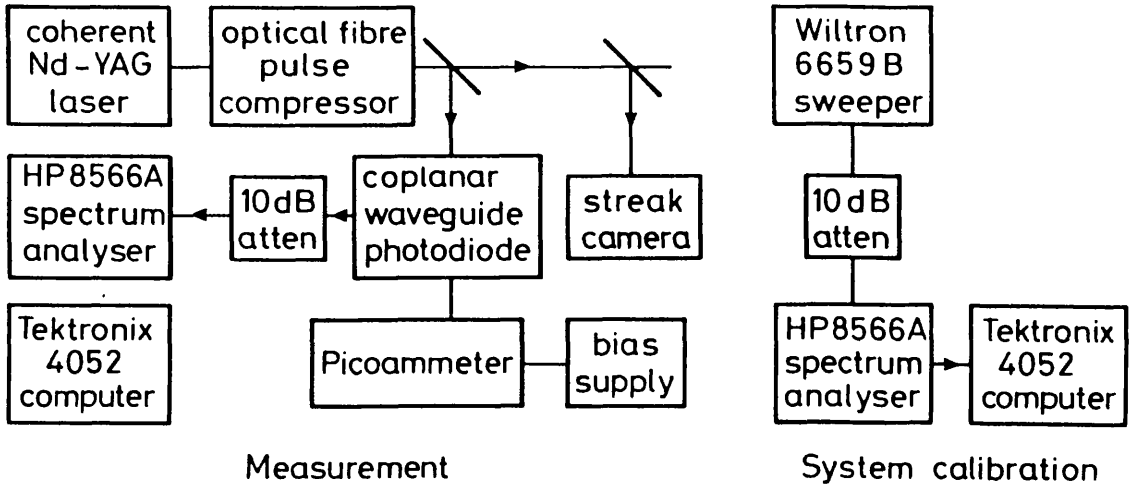

Figure 4.10. Experimental layout for measurements using the pulse compressed YAG laser at 1.06 μm

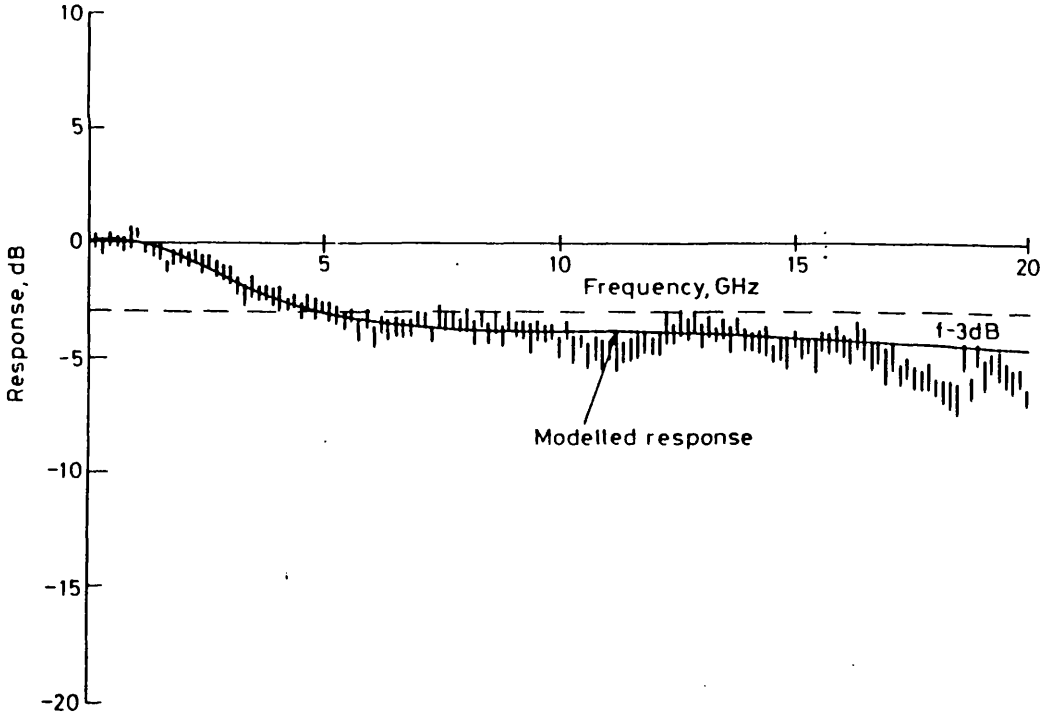

Figure 4.11. Measured and modelled response of the pulse compressed YAG laser pulses using the AT&T photodiode

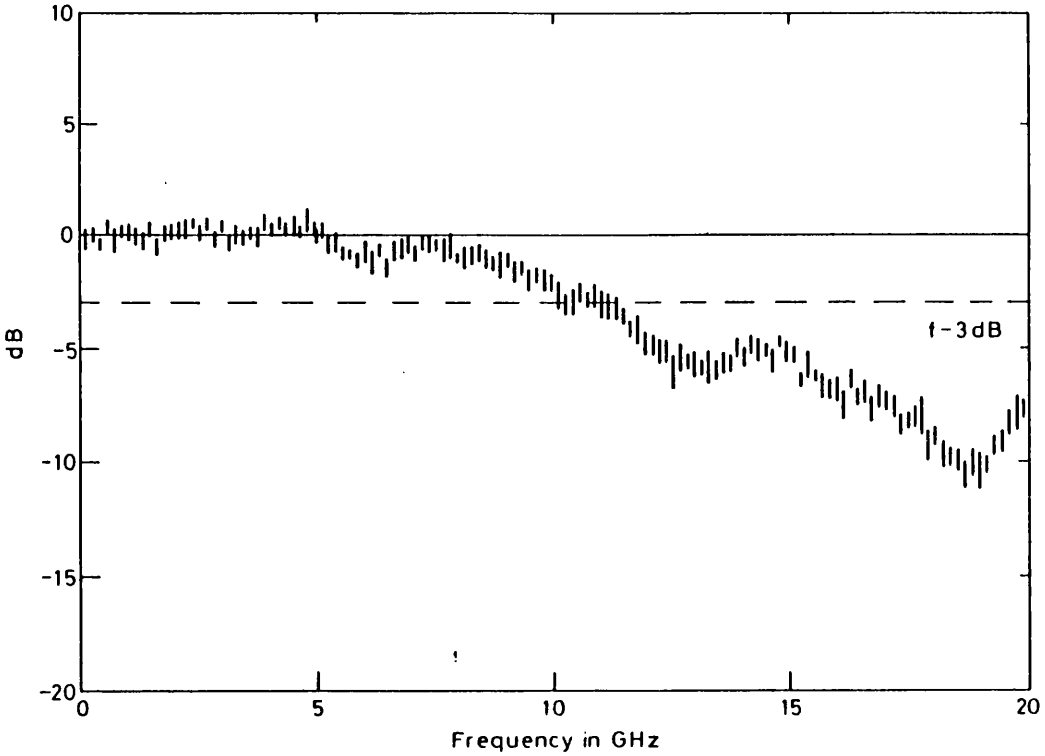

Figure 4.12. The corrected response of the Plessey CPW#2 photodiode using pulse compressed YAG laser pulses

Interpretation of the results

The results obtained for the CPW#2 device indicate a very low inductance for this mounting arrangement. An exact figure could not be obtained because the diode could not be modelled correctly. This is a considerable improvement over the 1.3 nH estimated for the coaxial mount.

4.7. DESIGN OF THE Mk2 COPLANAR MOUNT

A second prototype coplanar mount was designed using the knowledge gained with the Mk1 design. The graded coaxial/coplanar transition was abandoned to allow the overall length of line to be minimised.

Two decoupling strategies were tested: the first used the millimeter wave chip capacitors as before, this design gives 6.6 mm as the minimum practicable length of line; the second decoupling strategy allowed the line length to be reduced to 3.05 mm. Single layer millimeter wave chip capacitors[26] were mounted on their edge at the ends of the mount as shown diagramatically in figure 4.13. The inductance of this

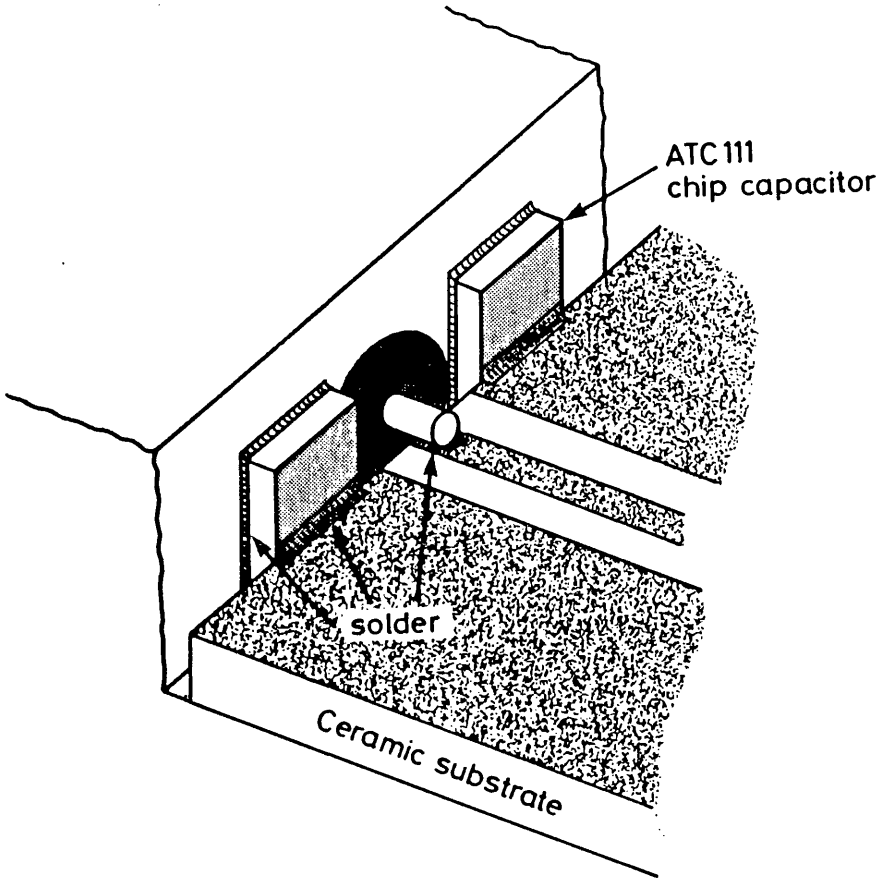

Figure 4.13. Decoupling arrangement using single layer mm-wave chip capacitors

arrangement should be very small but assembly is more difficult.

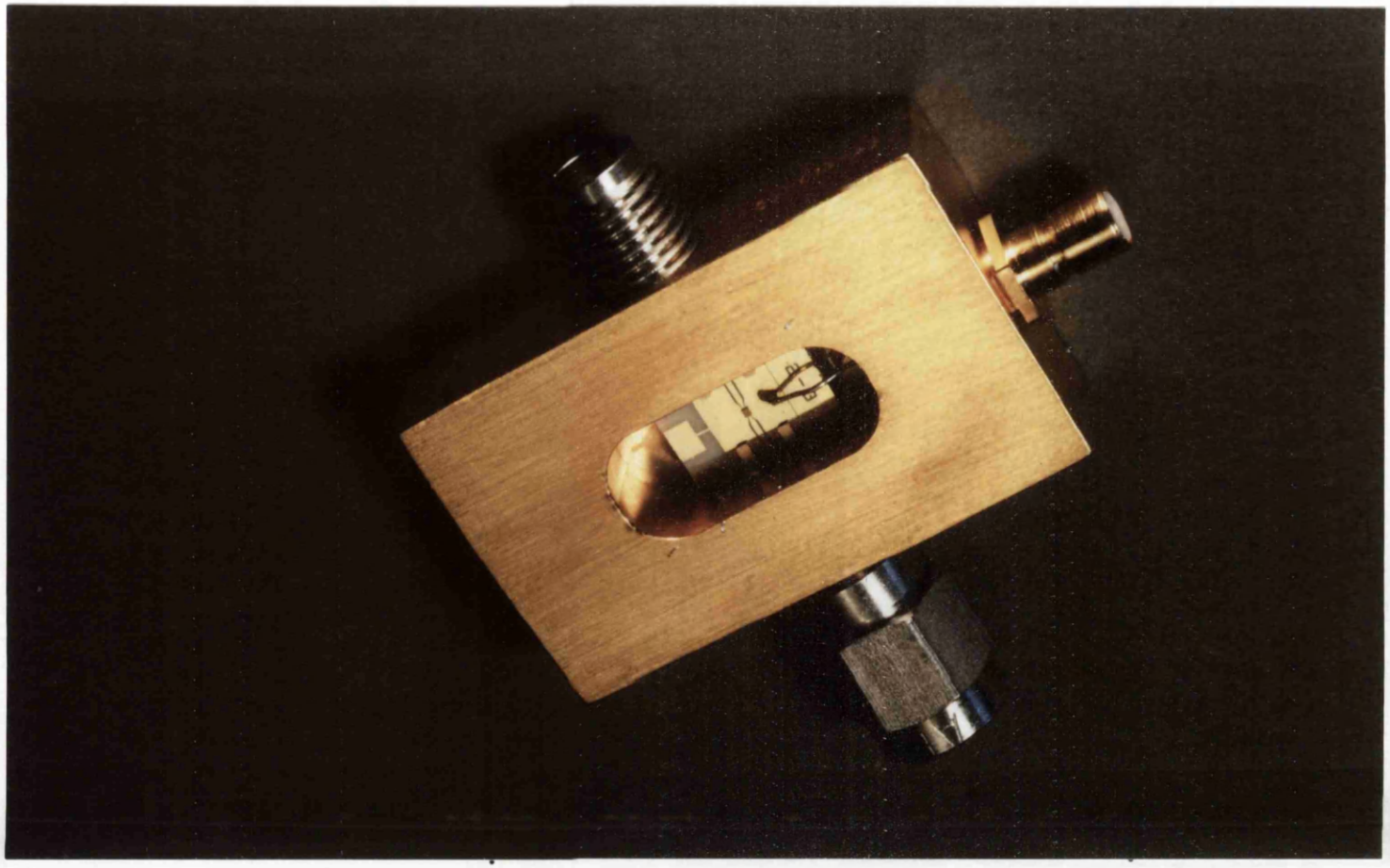

Figure 4.14. Photodiode mount with 6.6 mm long ceramic submount
(photograph courtesy of Plessey Research Caswell)

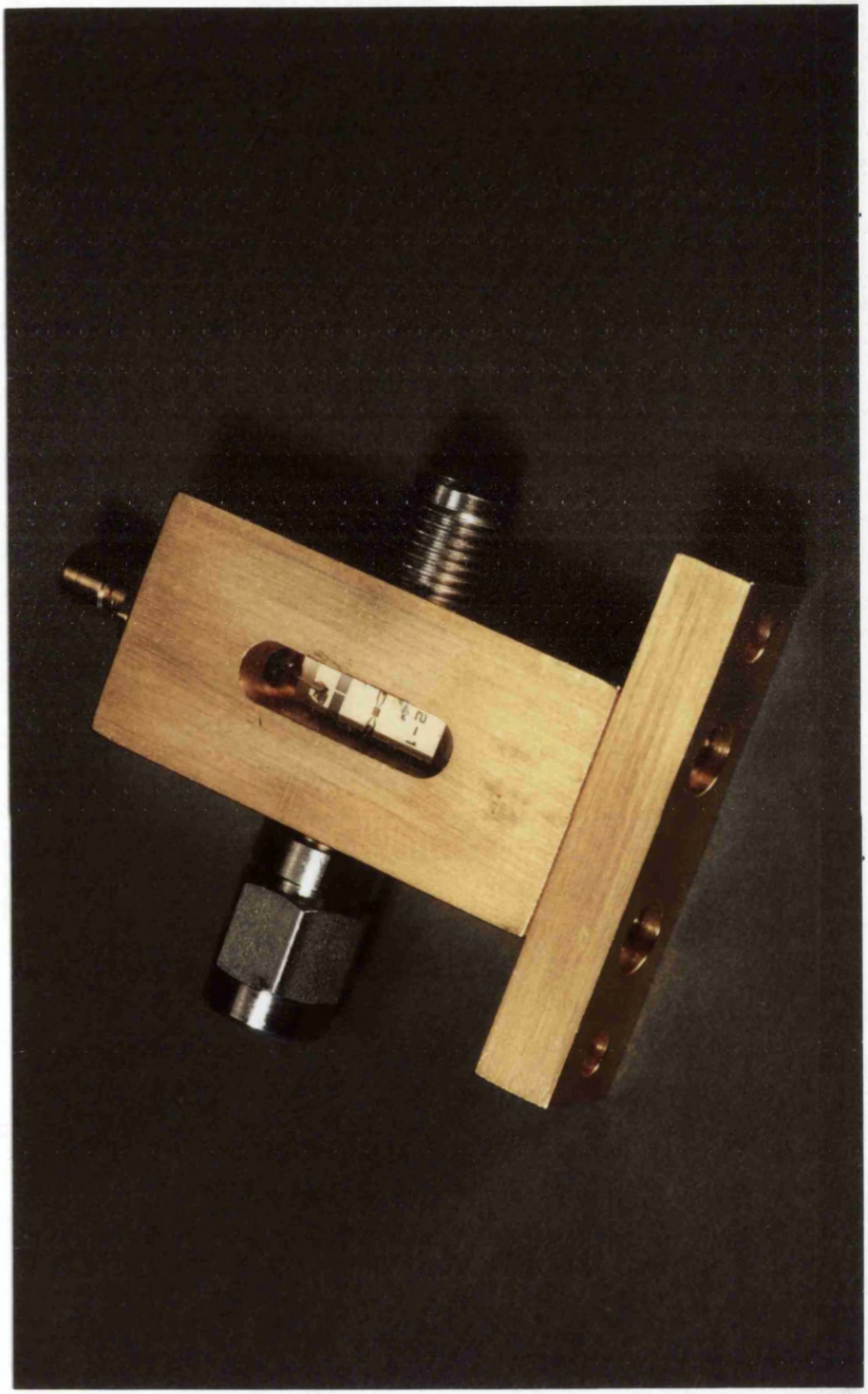

Figure 4.15. Photodiode mount with 3.05 mm long ceramic submount
(photograph courtesy of Plessey Research Caswell)

The coplanar line was designed to have a target gap/width ratio of 0.4474, corresponding to a 50 Ω line impedance on a ceramic substrate $\epsilon_r = 9.9$. The width of the central electrode at the ends of the line was chosen to be 304 μm to suit the K connectors. The central electrode width at the diode mesa has been chosen to be 70 μm. This is 20 - 30 μm wider than the photodiode mesa to allow some device placement

tolerance. The taper from 304 μm to 70 μm central electrode width occurs over a 500 μm long section of line.

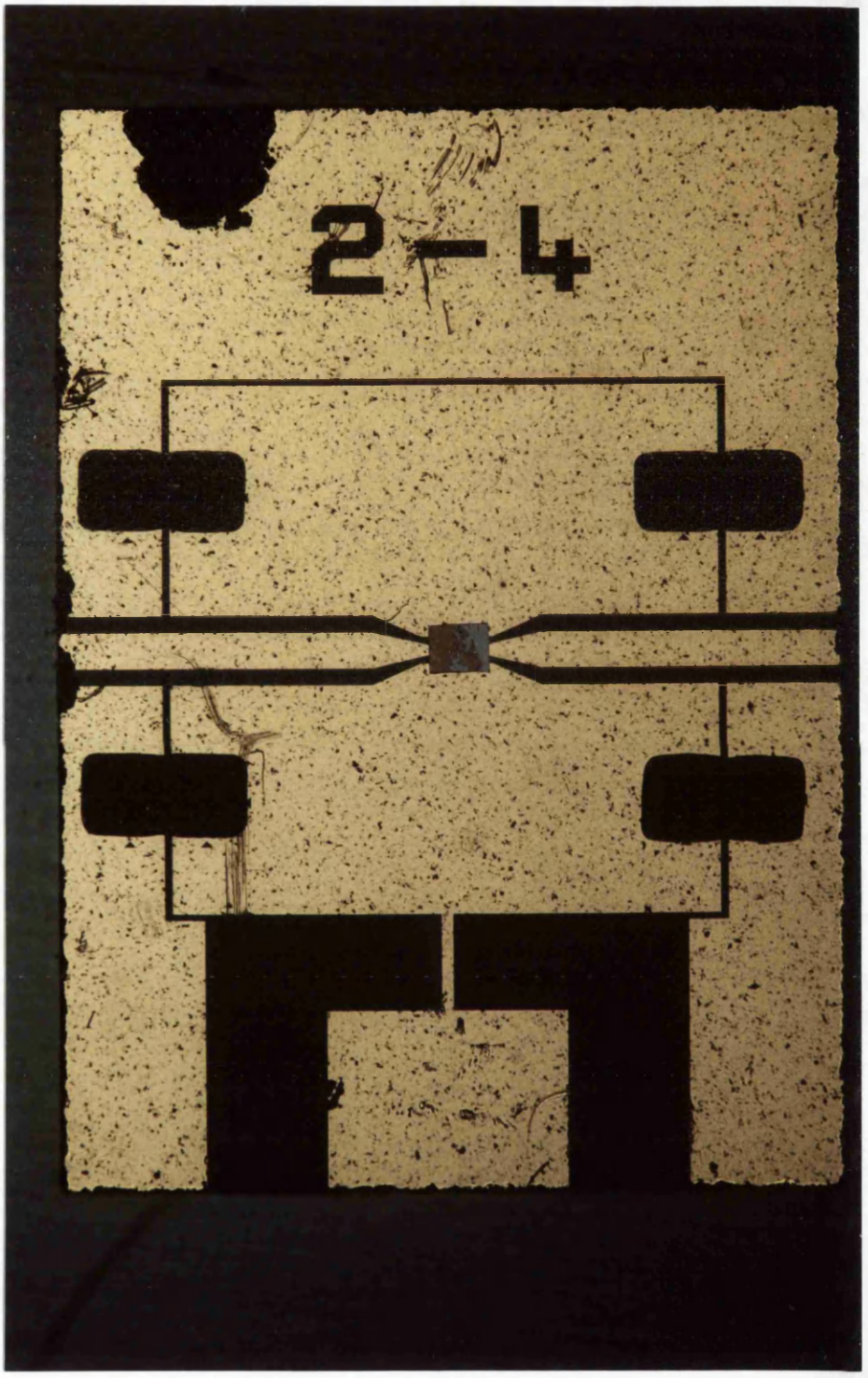

Figure 4.16. 6.6 mm long ceramic submount with chip capacitors and photodiode *(photograph courtesy of Plessey Research Caswell)*

The Wiltron K connector system has been adopted in preference to the SMA connectors previously used because the k connectors operate to a

higher frequency (46 GHz), giving the mount the potential for future development. The ability of the K connector system to be hermetically sealed is also of great importance because the devices are intended for eventual manufacture. Photographs of the mounted photodiodes are shown in figures 4.14 and 4.15.

The previous design suffered from short circuit problems caused by the fabrication process. The new designs are made using an ion beam milling process to overcome the shorting problem. The ceramic substrate is plated over the whole surface to a thickness of 5 μm. The gold is then etched to leave the desired pattern. The finished result has smooth line edges that are free from the ridges associated with the lift-off and plating process. The smooth edges should also improve the loss characteristics of the coplanar line at high frequencies.

The Mk2 prototype mount was designed to be assembled in two stages: first the diode and decoupling capacitors were to be assembled onto the ceramic mount which would then be inserted into the mount. Photographs of the ceramic substrates with the photodiodes mounted are shown in figures 4.16 and 4.17.

The assembly proved to be difficult because of the small sizes involved and the restrictions imposed on the choices of solders available. The K connector beads were soldered into place using a 260°C solder and the submount was assembled into the mount using a 180°C fluxless solder. Two problems were encountered: firstly a good soldered connection between the mount and the ceramic submount was difficult to obtain and secondly in at least one case the solder flow around the K connector bead was incomplete leading to failure of the K connector/central electrode connection. The former problem gave rise to ringing and some reflection of the electrical signals at the coaxial/coplanar transitions. The latter problem gave rise to large reflections due to the unterminated line.

4.8. ASSESSMENT OF THE Mk2 COPLANAR MOUNT DESIGNS

To assess the performance of the Mk II coplanar mount designs two optimised diodes were tested. The devices were measured using both time domain and frequency domain techniques. The AT&T photodiode was used as a reference for the time domain comparisons.

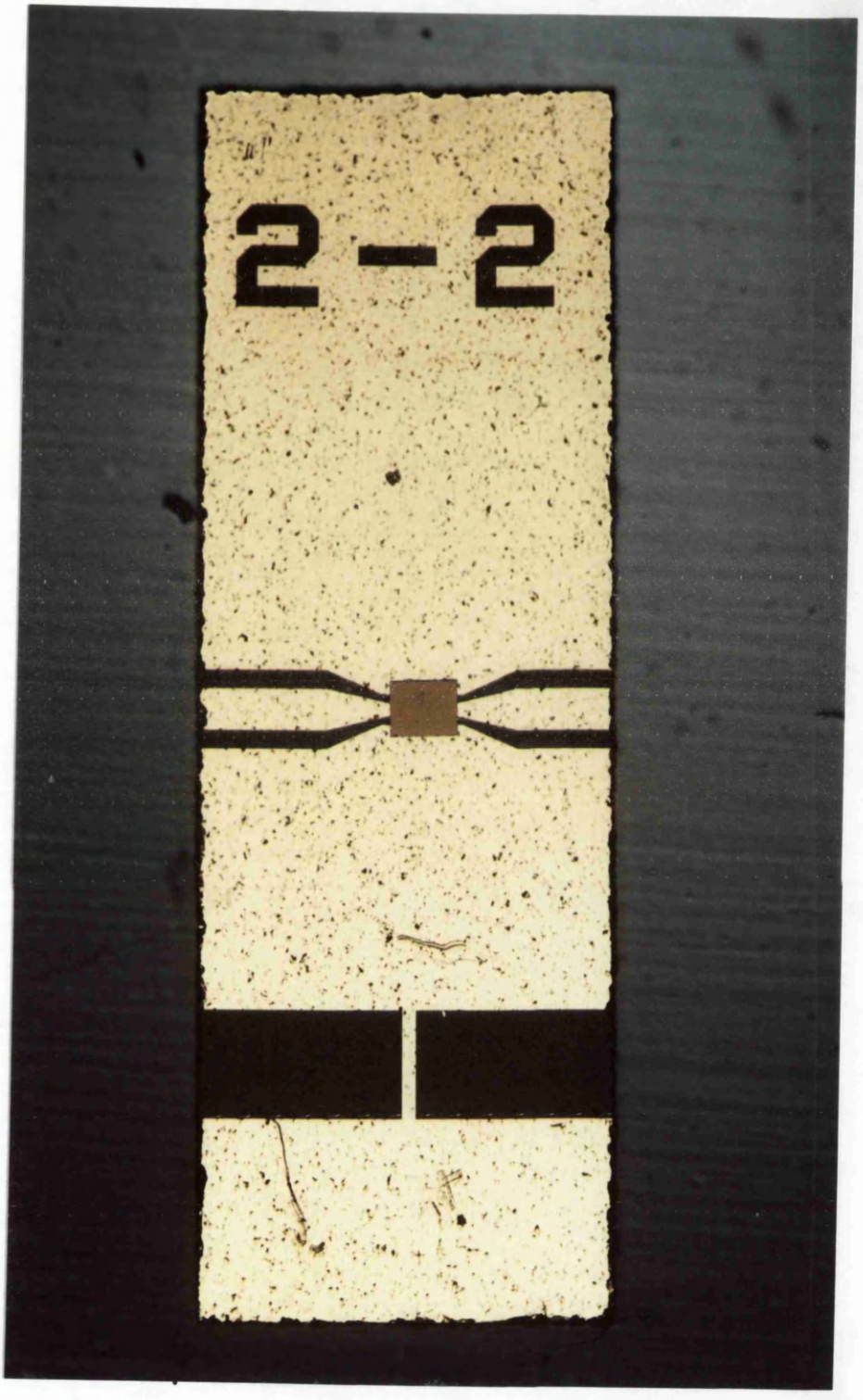

Figure 4.17. 3.05 mm long ceramic submount with photodiode
(photograph courtesy of Plessey Research Caswell)

Optimised photodiodes

Two 40 µm diameter diodes both from the same batch were used to assess the performance of the Mk II mounts. The diodes were grown by an atmospheric MOCVD process onto an unbuffered n^+ InP substrate with a

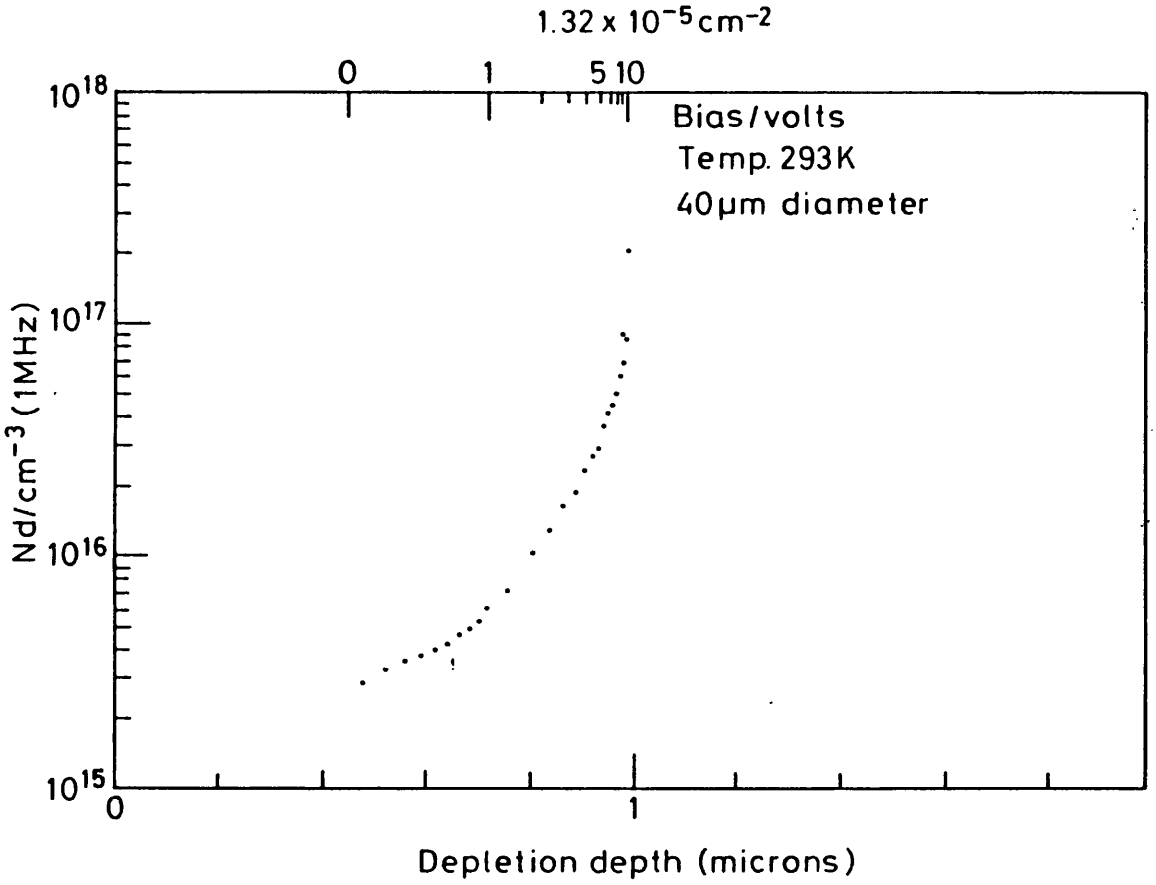

Figure 4.18. Measured C-V characteristics of the epitaxial layer

doping level of 10^{18} cm^{-3}. The lattice matched GaInAs epitaxial layer had an unintentional background level of 10^{15} cm^{-3}. The p-n junction was formed by shallow zinc diffusion giving a p^+ region roughly 0.3 μm thick. An unbuffered substrate was chosen to overcome problems caused by the depleted region extending into the InP substrate. A C-V profiling technique was used to determine the depletion width. The results are shown in figure 4.18 and indicate that the depleted region is roughly 0.95 μm wide and does not extend beyond the GaInAs/InP heterojunction. The diode is a near optimum device design assuming a stray capacitance of 70 fF and a mounting inductance of 200 pH.

The diodes mounted in the short and long coplanar mount variants have been designated 2#6 and 2#19 respectively. The breakdown voltage of these devices has been estimated as 15 V and good results have been obtained at 7.5 V bias corresponding to a peak electric field of 87 kV/cm. The diode leakage currents at 7.5 V bias, for the mounted chips, are about 10 nA indicating that the lattice match at the GaInAs/InP interface is good. A plot of the leakage current characteristic of the unmounted diode chip is shown in figure 4.19. At

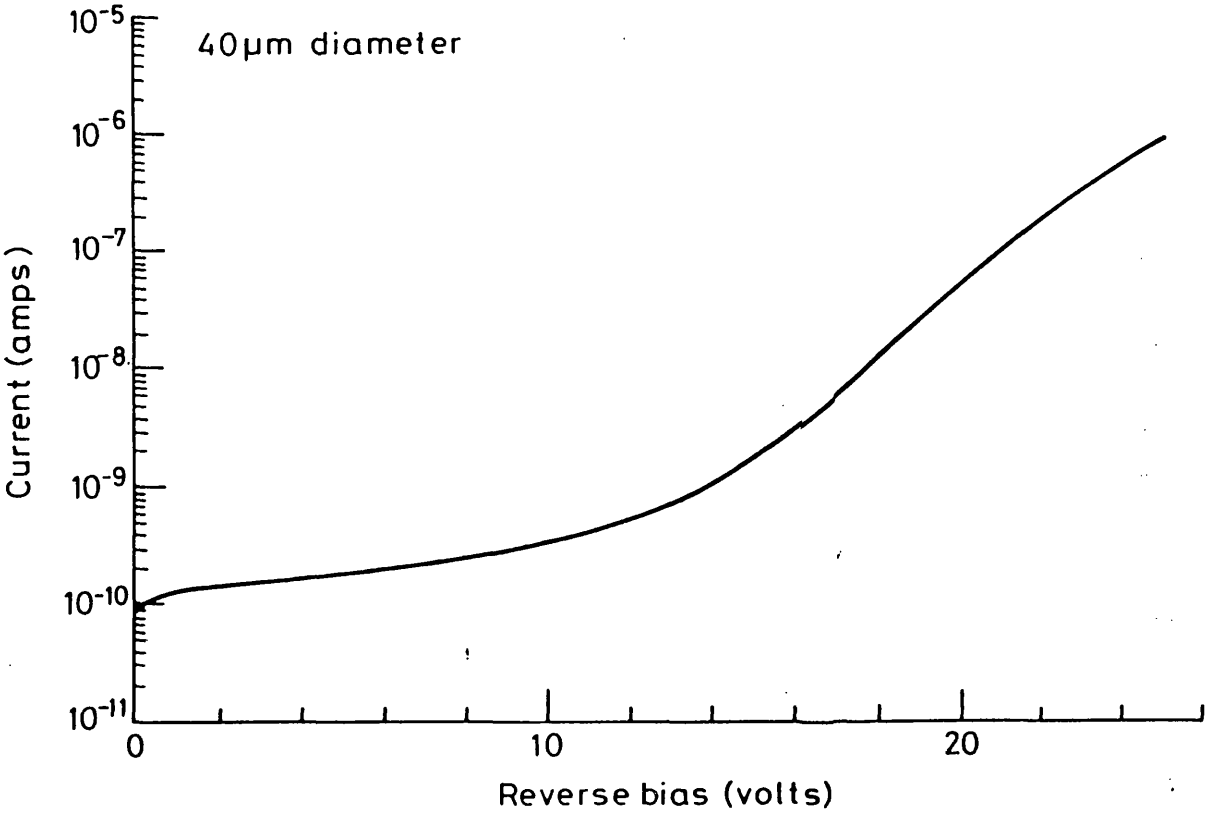

Figure 4.19. Measured leakage currents for the 0.95 μm depletion width photodiodes

voltages above 15 V the rapid increase in the leakage is due to tunnelling currents which occur at electric fields in excess of 150 kV/cm.

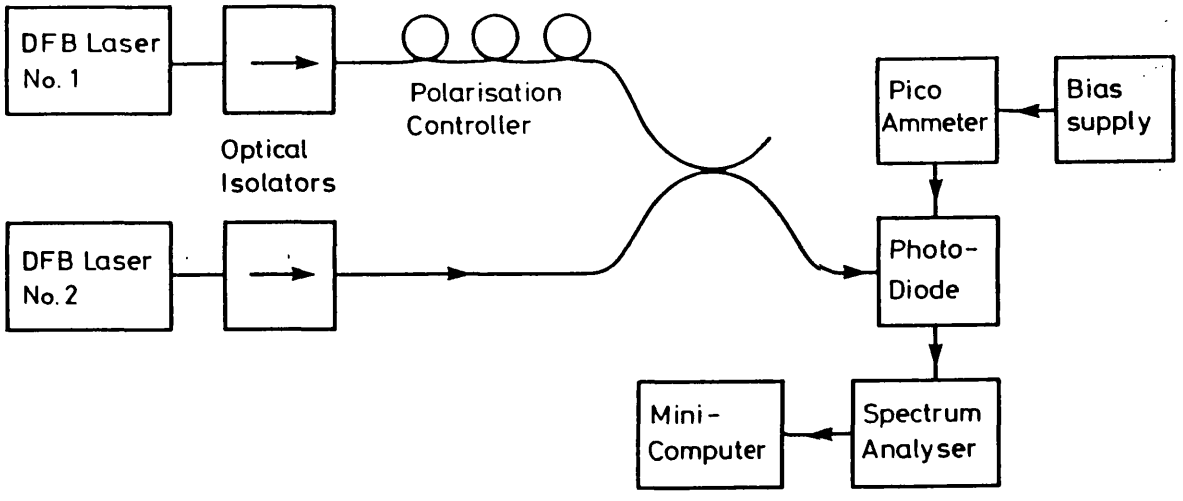

Figure 4.20. Heterodyne measurement system used to characterise the Mk2 photodiode and mount

Heterodyne measurement of the diode performance

The layout of the beat frequency measurement system is shown in figure 4.20. The two optically isolated DCPBH structure distributed feedback lasers had 550 μm long cavities. The important parameters are summarised in table 4.2. The frequency stability of the beat was limited by the voltage stability of the commercial power supplies used to drive the lasers. The measurement system contained some poor optical splices and the maximum photocurrent that could be obtained with the 40 μm diameter diodes was 36 μA.

Table 4.2. DFB laser performance parameters

DFB laser	1	2	
Optical power into fibre	100	100	μW
Optical isolator performance	>30	>30	dB
Linewidth	7	17	MHz
Temperature tuning	11	11	MHz/°C

The spectrum analyser was set to peak hold and the sweeping of the optical beat frequency was carried out by hand using temperature tuning. Figure 4.21 shows the results corrected for noise, amplifier gain, cable loss and spectrum analyser sensitivity, referenced against the sweeper response. The results have been edited to remove points at which very low measurements were made as these are not indicative of the device response. The results suggest a 3 dB frequency of 17 GHz which is lower than the value expected from the theoretical modelling results (22 - 27 GHz).

The diode 2#19 could not be measured satisfactorily because of a failure of the junction between the submount and the coaxial connector.

Assessment of the diodes using pulsed semiconductor lasers

The performance of the photodiodes were measured using three pulsed semiconductor lasers with nominal wavelengths of 1300 nm. The Optoelectronics PLS10 lasers at 1323 nm and 1324 nm produce multiple pulses, which limit the useful time window. The Lasertron source at 1270 nm gives a wider pulse with no significant after pulses. One hundred averages were taken for each measurement to reduce the sampling

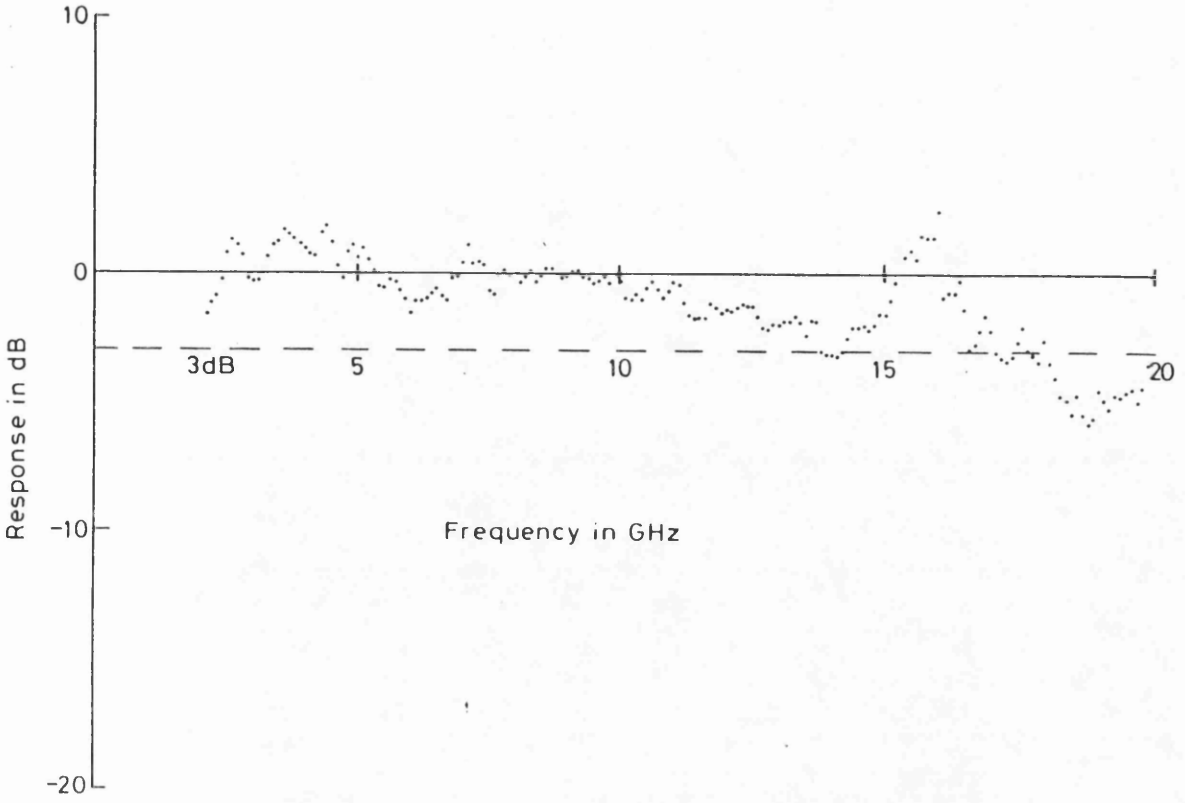

Figure 4.21. Measured response of Plessey 2#6 photodiode

noise and a zero subtraction was performed to remove any effects due to trigger breakthrough.

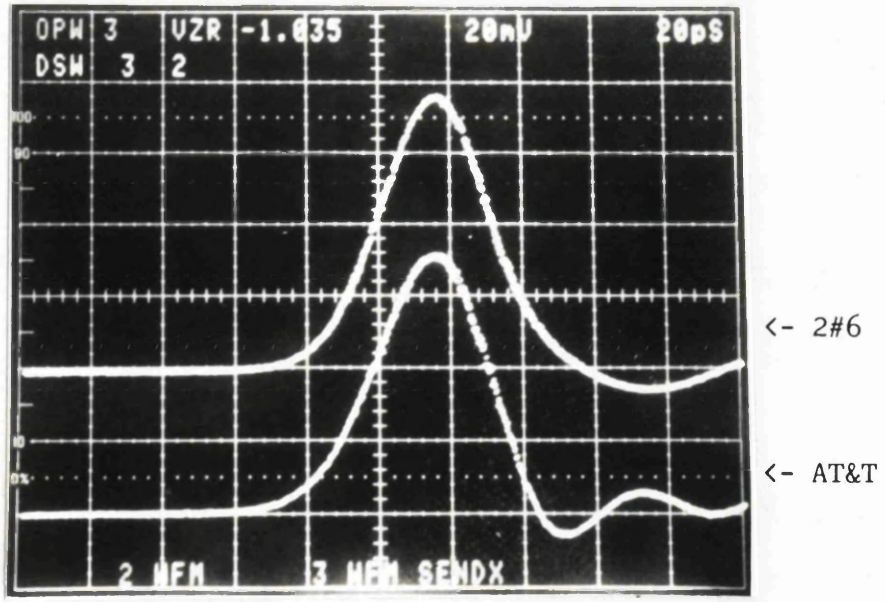

Figure 4.22. Temporal response of Plessey 2#6 (upper) and AT&T (lower) photodiodes at 1323 nm

The measured responses of the AT&T and Plessey diodes at 1323 nm are shown in figure 4.22. The more obvious feature is the difference in

the rise and fall characteristics of the two devices: the AT&T diode has a slower rise and sharper fall which can be attributed to the higher series resistance and mounting inductance of this device.

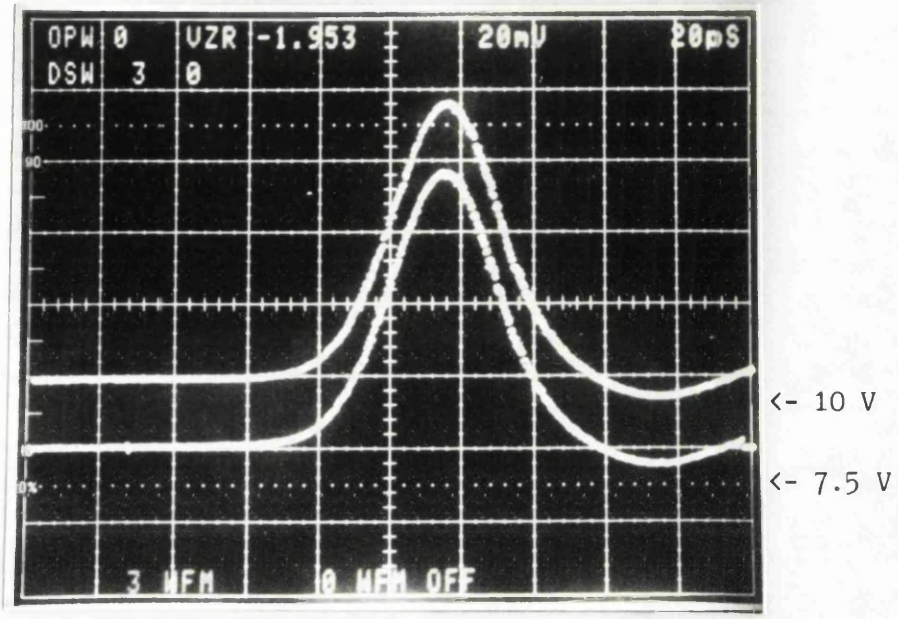

Figure 4.23. Temporal response of Plessey 2#6 at 1323 nm, 7.5 V bias (lower) and 10 V bias (upper)

The response of the Plessey device biased at 7.5 V and 10 V, corresponding to peak internal fields of 87 kV/cm and 112 kV/cm respectively, are shown in figure 4.23. No appreciable difference can be seen between the two curves which suggests that any change in the the diode response is beyond the limits of the measurement system.

The responses of the two photodiodes measured at 1270 nm with the Lasertron QLPX system are shown in figure 4.24 for a 100 ps/division timescale. The difference in the ringing for the two detectors is apparent but more heavily masked by the longer pulse. It can be seen that the laser is almost free from secondary pulsing and that there are no significant ringing effects for either device.

Measurements were made of both the Plessey 2#6 and 2#19 photodiodes at 1323 nm. The 2#19 device had a break in the connection between the coplanar submount and the K connector. This caused the signal to be reflected from the end of the line, rather than being properly terminated as shown in figure 4.25.

The 2#19 diode was returned to Plessey for repair. After the repair, the measured signal from this device was very similar to that of the

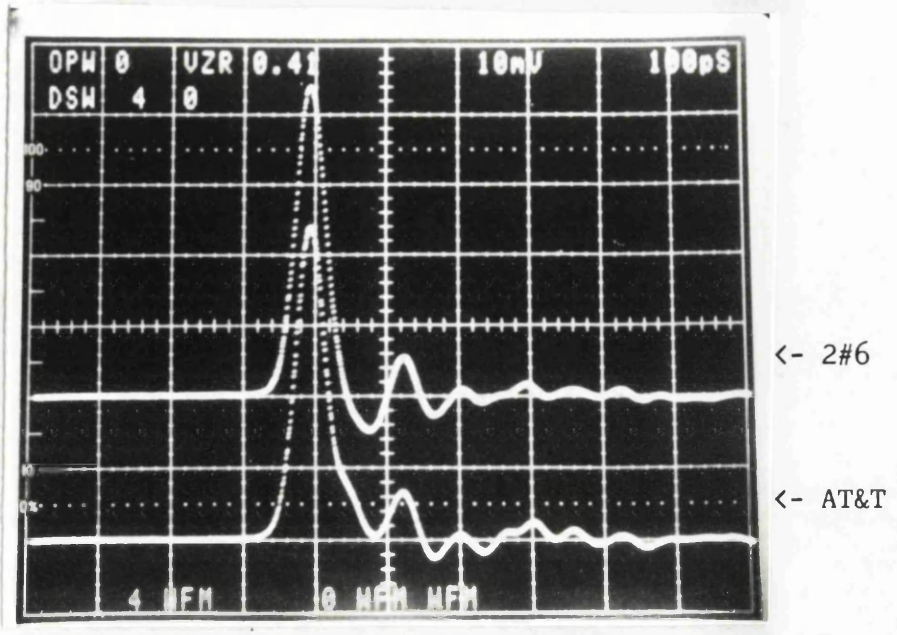

Figure 4.24. Temporal response of Plessey 2#6 (upper) and AT&T (lower) photodiodes at 1270 nm

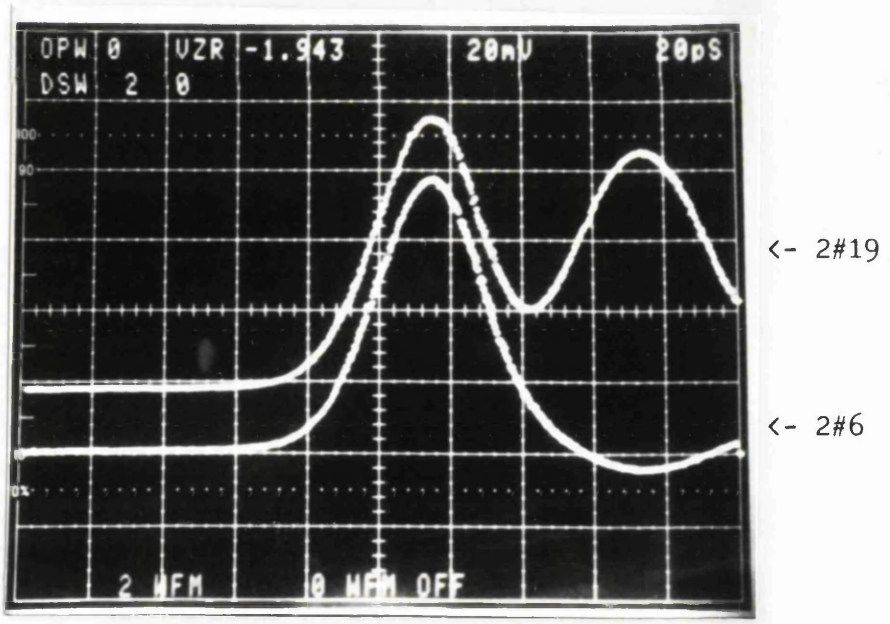

Figure 4.25. Temporal response of Plessey 2#19 (upper) and Plessey 2#6 (lower) photodiodes at 1323 nm

2#6 photodiode. Figure 4.26 shows the responses of the 2#19 (top), 2#6 (centre) and AT&T diodes at 1324 nm. The bump in the response at approximately 50 ps after the main peak can be attributed to a poor reflection from the coax/coplanar interface.

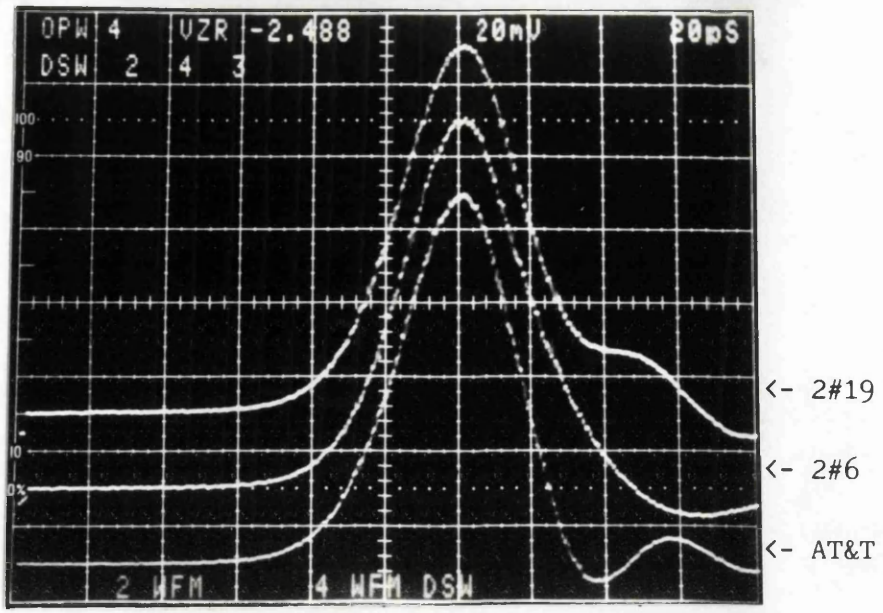

Figure 4.26. Temporal response of Plessey 2#19 (upper), 2#6 (centre) and AT&T (lower) photodiodes at 1324 nm

Measurement of the electrical reflection coefficients

Measurements of the electrical reflection from both diodes were made using a Tektronix Time Domain Reflectometry system (TDR). The results obtained with the 2#19 device at 7 V bias are shown in figure 4.27. The two peaks corresond to the reflections from the transitions at either end of the mount. The central dip is due to the diode capacitance. The reflection from the transition is approximately 10%. This is in broad agreement with the size of the reflection observed in the optical measurement (figure 4.26).

Measurements were also made of the reflections from the 2#6 device. In this case measurements were made both with and without the photodiode chip. The measured TDR signal with the diode is shown in figure 4.28. The removal of the diode chip did not significantly affect the measured peak signal. The photodiode chip was removed because the diode had become short circuited. The results suggest a peak reflected signal of approximately 8%.

Interpretation of the measured results

It is clear from these results that a significant improvement of the coax/coplanar transitions is required in order to achieve the desired performance. The results from the heterodyne experiment showed that the diode had a significantly lower frequency response than the modelled

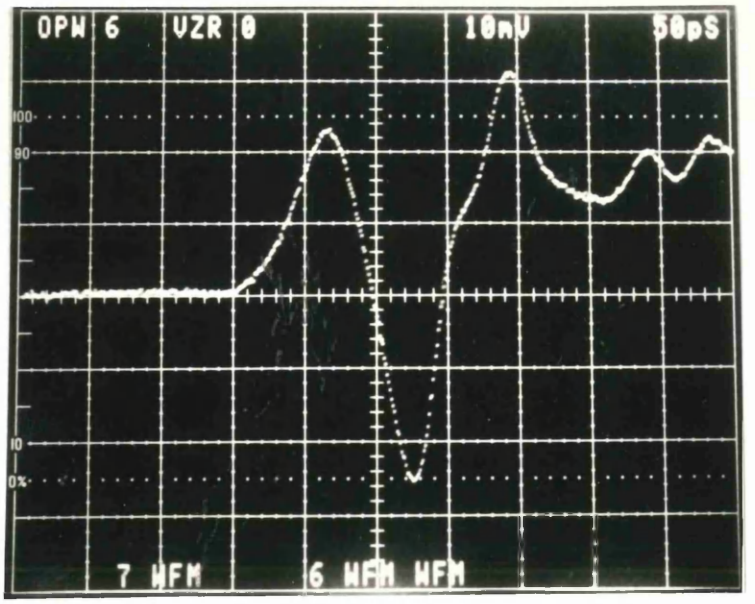

Figure 4.27. Reflected signal from 2#19 diode measured by time domain reflectometry

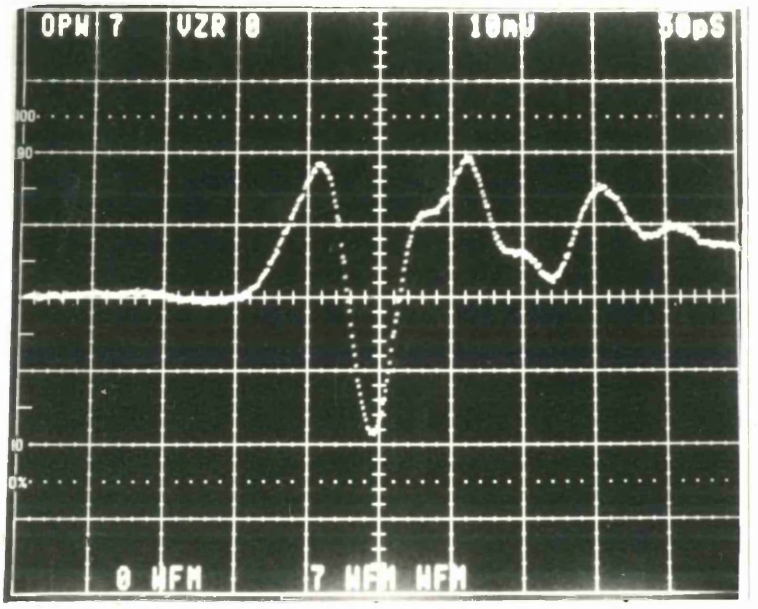

Figure 4.28. Reflected signal from the 2#6 diode at 7.5 V bias, measured by time domain reflectometry

results would suggest. The reason for this discrepancy is not fully understood. Two factors which may be responsible are the mounting inductance and the coax/coplanar transitions. The inductance of the mount may be too low. This would account for the longer falltime, compared to the AT&T device.

During the assembly, it was difficult to obtain a good electrical contact between the ceramic submount and the mount. The poor coax/coplanar transitions will give a frequency dependent reflection which will affect the overall performance of the mounted photodiode.

4.9. DESIGN OF THE Mk3 COPLANAR MOUNT

The previous generation of prototype mounts proved to be very difficult to assemble. The ceramic submount had to be inserted from the top and it was difficult to achieve a good soldered contact between the package and the submount. This was especially true for the shorter package design.

The mount was re-designed to overcome these faults and allow the submount to be inserted from underneath. This allows a good contact to be made between the package and the ground plane. A further advantage of this approach is that the diode position is well known, allowing the use of a passively positioned optical fibre to couple the light into the device. A photograph of the fibred and standard packages are shown in figure 4.29.

The bias decoupling arrangement and dimensions of the ceramic submount were identical to the 6.6 mm long device from the previous design, with an isolated section of the ground plane to provide the decoupling. In this version a different supplier of the decoupling capacitors was used.

Initial measurements of the device performance were made using a Heterodyne system described in paper 7 in appendix 2. This measurement system was subsequently greatly improved by using the rotating polaration heterodyne system described in part 1 of this thesis. The results measured for the 30 μm diode biased at 7 V are shown in figure 4.30, together with a measurement of the electrical coefficient for this device. The optical measurements (S_{21}) contain uncertainties of greater than ±1 dB at frequencies above 20 GHz because the r.f. detector was uncalibrated. The frequency response of this diode is very ragged, suggesting some resonance problems in the mount. The 3 dB frequency is about 18 GHz which is similar to the results obtained for the previous design.

A measurement of the electrical return loss (S_{22}) has been made at

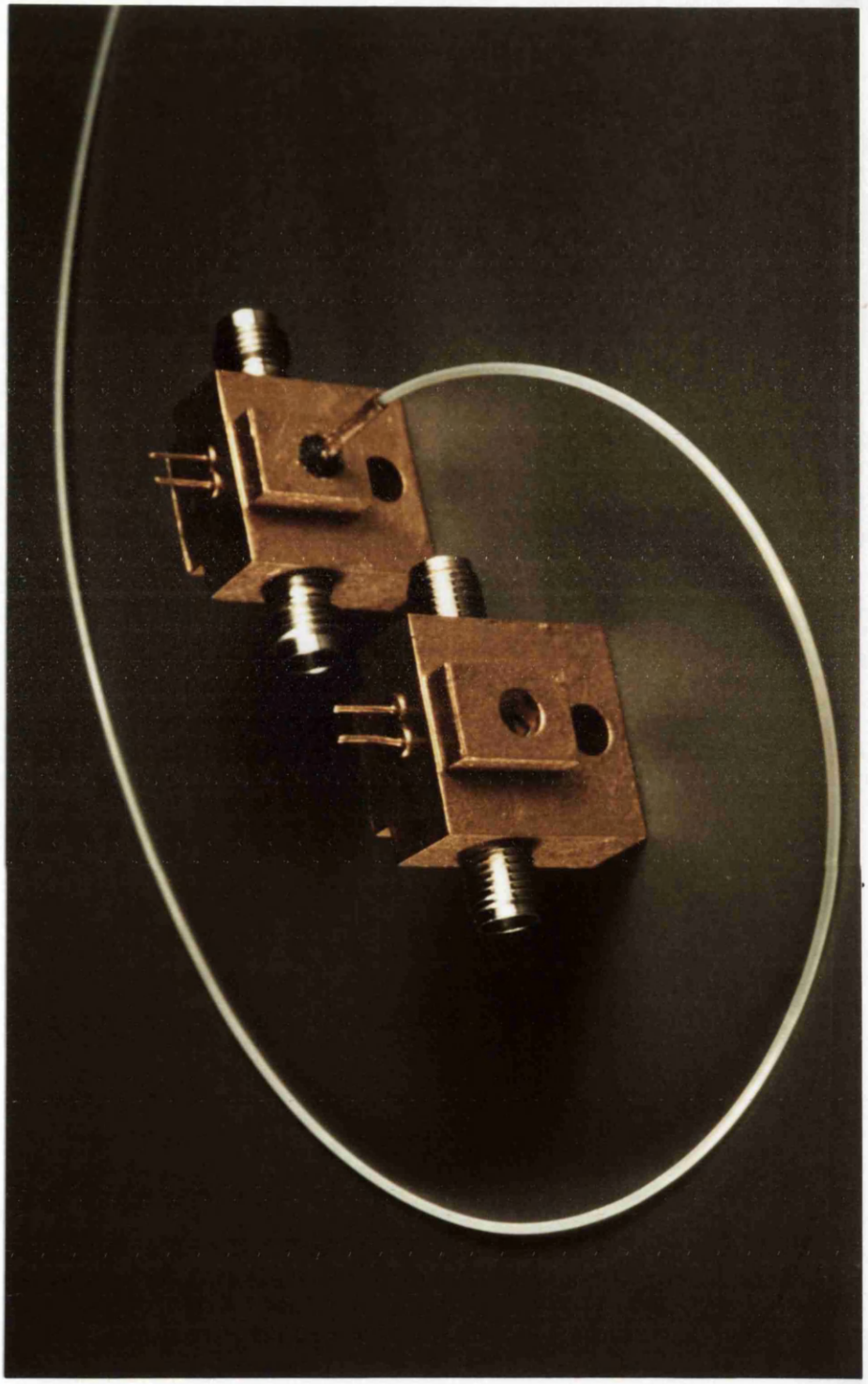

Figure 4.29. Mk3 photodiode package *(photograph courtesy of Plessey Research Caswell)*

frequencies of up to 40 GHz. The results are also presented in figure 4.30;. The diode shows a number of sharp resonances, spaced at roughly 10 GHz intervals. These are believed to be caused by the isolated central section of the diode earth plane not being properly decoupled. The dips in the measured response correspond well to the package resonances. Therefore to improve the overall performance it will be necessary to suppress these resonances.

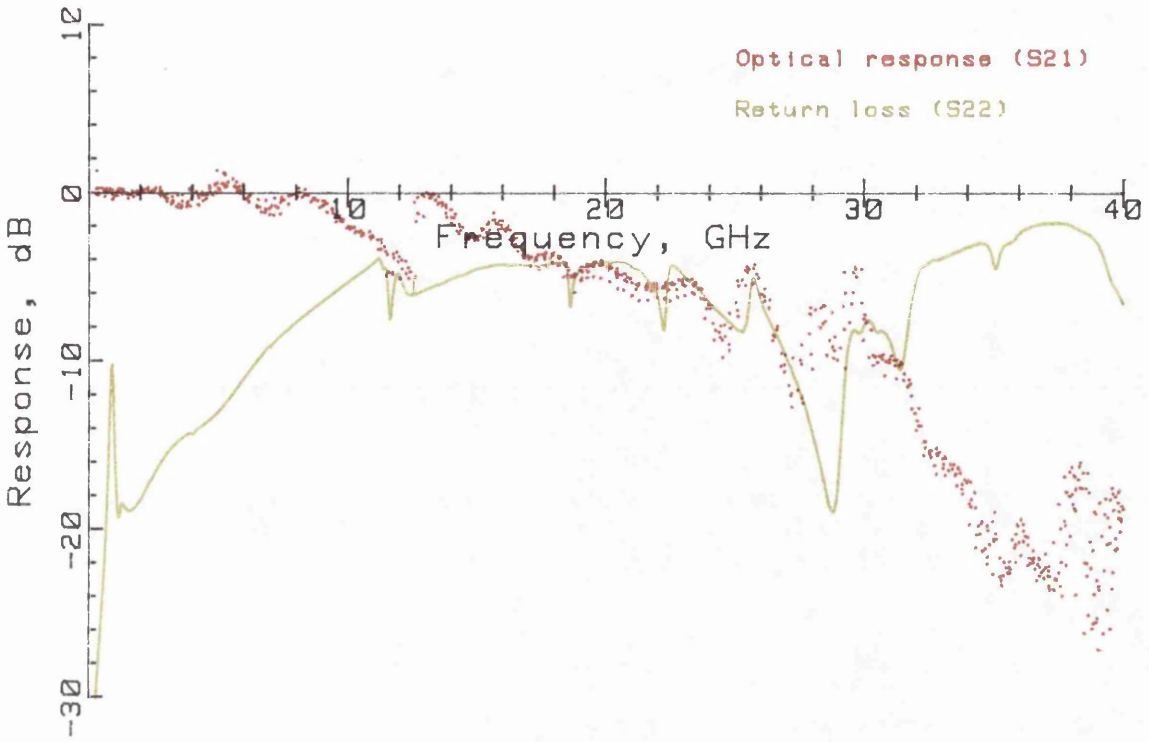

Figure 4.30. Measured response of the 30 μm diameter diode at 1532 nm

4.10. CHAPTER CONCLUSION AND DISCUSSION

In this chapter the different strategies for mounting fast photodiodes have been considered and the development of a fast pin structure photodiode, suitable for use as a risetime transfer standard, has been described. The mounting arrangement in which the diode is placed across the transmission line maximises both the speed of response and the active area at the expense of some sensitivity. This design has been chosen for the fast photodiode.

Three design iterations of the diode and mount have been described. The first design used an unoptimised diode mounted on a coplanar substrate. This device was rather slow because the photodiode had a wide depleted region. The process used to fabricate the coplanar line caused the diodes to become short circuit.

The second iteration produced successful devices with frequency responses of approximately 17 GHz for a 40 μm diameter device. This is believed to be the highest bandwidth reported for a device of this area. The problem of short circuits encountered in the previous iteration was overcome by using an ion milling process to make the waveguides. The edges of the waveguides were smooth and no longer shorted out the diode. The design of the mounts made them difficult to

assemble.

In the third iteration the package design was improved to ease the manufacturing problems. The devices of this design can be hermetically sealed and a fibre coupled variant has also been designed. The decoupling strategy chosen requires further attention as the device exhibits high Q package resonances. At the time this thesis was written these problems had not yet been overcome.

5. MICROSTRIP MOUNTED PHOTODIODE

5.1. INTRODUCTION

An informal project was undertaken in collaboration with British Telecom Research Laboratories to mount a research photodiode onto a commercially available microstrip test fixture and test the performance of the resultant device. The aim of the project was to evaluate both the mounting concept and to test the device.

5.2. PHOTODIODE STRUCTURE AND MOUNT

The photodiode used for the experiment was a top light entry design with a 30 μm diameter active area. The design of diode had been reported *D Wake*[12,27].

The mount used a commercial K-connector microstrip test fixture with the photodiode in the centre of the line. The diode was connected to two decoupling capacitors (ATC111) on either side of the line by multiple bondwires, as shown in figure 5.1.

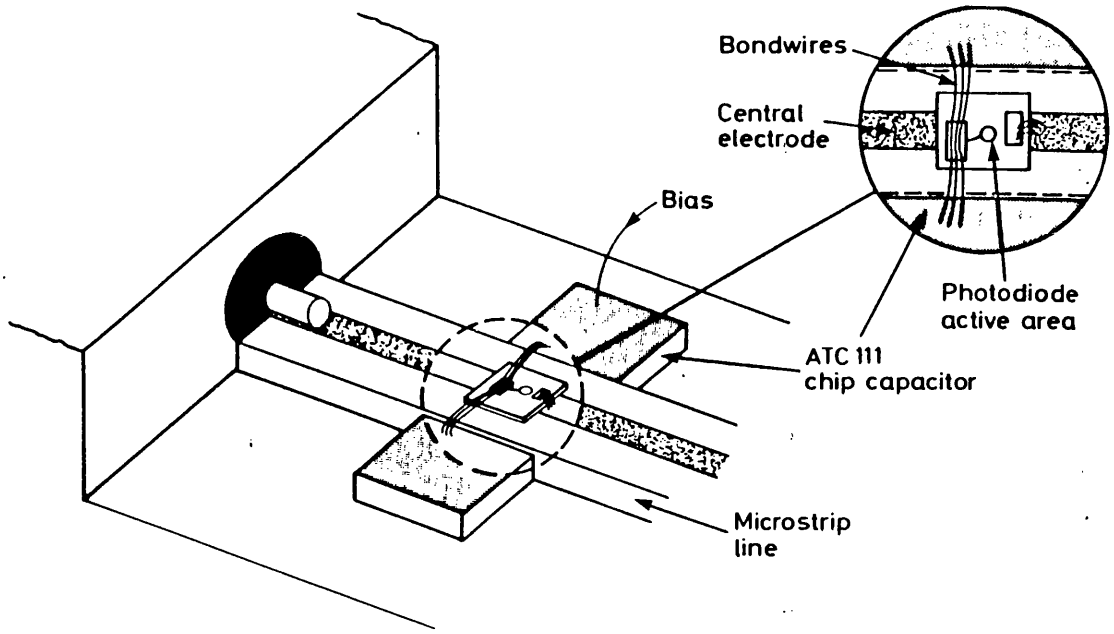

Figure 5.1. Microstrip mount for BTRL GaInAs photodiode

This arrangement allowed the diode to be biased from an external supply without having to use a bias tee. The diode chip was larger than the width of the line and this may introduce some extra stray capacitance.

The use of a top light entry device potentially allows extremely high speed detectors, with bandwidths in excess of 40 GHz, to be realised because the active area can be reduced to 20 μm diameter or less. The main limitation to the speed of response will be the stray capacitance. In this design the stray capacitance is reduced by using a semi-insulating substrate.

5.3. MODELLING OF THE BTRL DIODE RESPONSE

The response of the top light entry structure was modelled at a wavelength of 1.5 μm to estimate the expected response. The thickness of the p^+ diffusion was not known but has been estimated to be 0.8 μm. This is thick compared to the Plessey devices and may lead to an increase in the response at low frequencies. The depleted region was assumed to be approximately 0.8 μm thick. A contour plot of the modelled frequency response as a function of the mounting inductance is shown in figure 5.2.

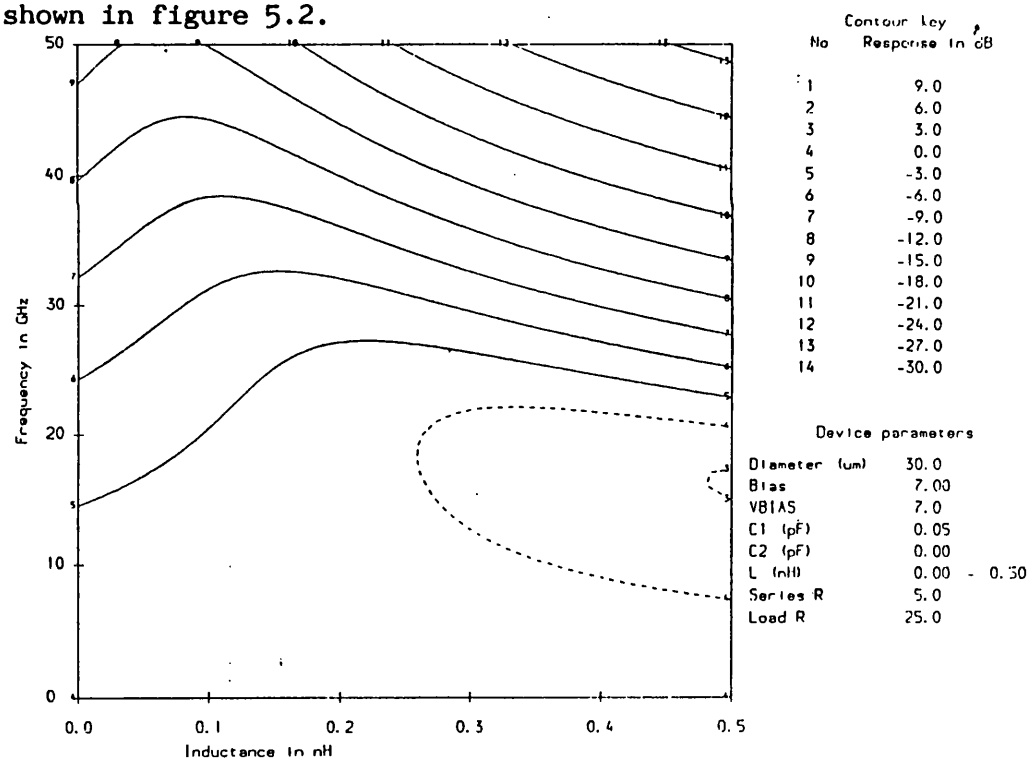

Figure 5.2. Modelled frequency response of the diode

The optimum choice of mounting inductance will give a 3 dB frequency of approximately 26 GHz, assuming a stray capacitance of 50 fF.

The electrical reflection coefficient S_{22} of the photodiode was measured over the range 45 MHz to 40 GHz using a Hewlett Packard 8510A vector network analyser. The results, shown in figure 5.3, indicate that this mounting scheme is free from high Q resonances.

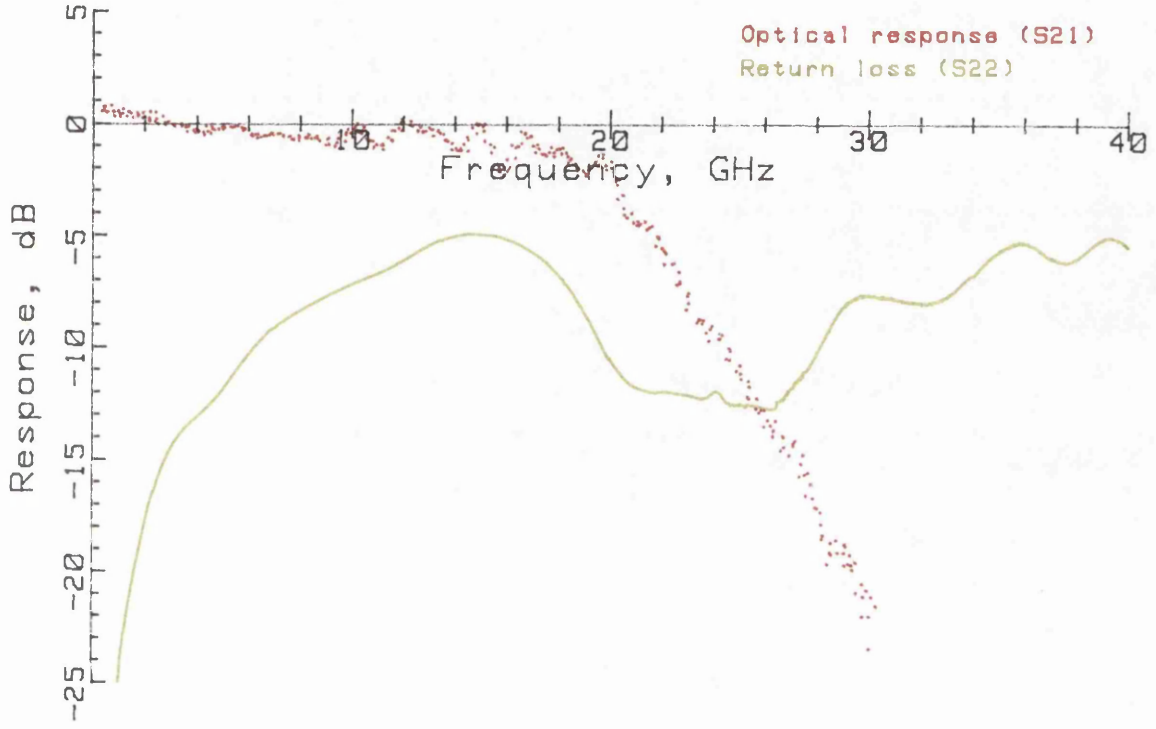

Figure 5.3. Optical response (1532 nm) and return loss measurements of the BTRL photodiode

Measurements of the bandwidth of this device were made using the rotating polarisation heterodyne system described in part 1 of this thesis. The results (figure 5.3) show that the diode exhibits some ripple in the response and has a 3 dB frequency of 20.5 GHz.

The measurements were made during the development of the system and no corrections were made for the electrical reflections between the photodiode and the measurement system. For this reason it is not clear whether the ripple in the result is due to reflections within the mount or between the measurement system and the photodiode. The speed of response is rather slower than predicted by the modelling. A possible cause of this discrepancy is that the stray capacitance of the mounting arrangement is higher than anticipated. Also, the series resistance in the device tested was higher than the value used in the model.

5.5. SUMMARY AND DISCUSSION

A fast photodiode mounted on a microstrip line has been tested. The device showed a good electrical reflection performance and was free from high Q resonances. Measurement of the optical performance gave a 3 dB frequency of 20.5 GHz, which was lower than expected from the modelling results. This device demonstrates that it should be possible to make very high bandwidth photodiodes, containing the bias circuitry and presenting an acceptable return loss to the measurement system, if the mount can be improved to reduce the parasitic effects.

6. CONCLUSION AND FURTHER WORK

In this part of the thesis the results of a collaborative research programme, to develop a fast photodiode for use as a reference device for high speed optoelectronic measurements, have been described. The aim of the programme was to produce a photodiode with a large active area, high bandwidth and good electrical properties that could be used, in conjunction with the techniques described in the previous two parts of this thesis, to characterise unknown devices.

The advantages and disadvantages of the two available diode structures were discussed in chapter 2. The main difference between the two designs is the direction from which the light enters the photodiode: in the first structure the light enters the device through the top contact and in the second structure the light enters through the substrate. A flip-chip mounted, substrate light entry device has been identified as offering the greatest advantages for this application.

A suite of programs to model the photodiode response was described in chapter 3. The aim of the modelling work was to identify the critical design parameters so that the photodiode structure could be optimised. A small signal model, based on a finite difference approach, was chosen to describe the flow of current in the photodiode structure. The results could then be used with a circuit representation of the device to estimate the overall response. The model was checked against the measured performance of a diode with a known structure. It will be necessary to re-check the model to improve its accuracy when new higher speed devices become available.

In chapter 4 the different strategies for mounting fast photodiodes have been considered and the development of a fast pin structure photodiode, suitable for use as a risetime transfer standard, has been described. The mounting arrangement in which the diode is placed across the transmission line maximises both the speed of response and the active area at the expense of some sensitivity. This design has been chosen for the fast photodiode.

Three design iterations of the diode and mount have been described. The first design used an unoptimised diode mounted on a coplanar substrate. This device was rather slow because the photodiode had a wide depleted region. The process used to fabricate the coplanar line caused the

diodes to become short circuit.

The second iteration produced successful devices with frequency responses of approximately 17 GHz for a 40 μm diameter device. This is believed to be the highest bandwidth reported for a device of this area. The short circuit problem encountered in the previous iteration was overcome by using an ion milling process to make the waveguides. The edges of the waveguides were smooth and no longer shorted out the diode. The design of the mounts made them difficult to assemble.

In the third iteration the package design was improved to ease the manufacturing problems. The devices of this design can be hermetically sealed and a fibre coupled variant has also been designed. The decoupling strategy chosen requires further attention as the device exhibits high Q package resonances. At the time this thesis was written these problems had not yet been overcome.

Chapter 5 described an informal project in collaboration with British Telecom Research Laboratories to mount and test a fast pin photodiode onto a commercially available microstrip test fixture. The resultant device had a 3 dB frequency of 20.5 GHz and was free from any high Q resonances. The frequency response was lower than theoretical predictions but this can be attribured to excess stray capacitance. This design of device offers the potential for photodiodes with frequency responses in excess of 40 GHz provided the mounting parasitics can be improved. This device demonstrated that a photodiode can be successfully mounted across a transmission line, thus gaining the advantages of improved speed of response and improved electrical reflection coefficient.

Future work

Future work will be required to make accurate estimates of the temporal responses of the high speed devices from incomplete measurement results and a knowledge of the device structure. The measurement results that can readily be obtained are the magnitude of the optical to electrical response (S_{21}) and the vector electrical reflection coefficient (S_{22}). This work will have applications in the areas of waveform metrology and picosecond electrical measurements.

Further work will be required to complete the photodiode project with Plessey. The package resonances present in the third design will have

to be overcome so that the device will be suitable for the reference application. Looking further ahead, it may be necessary to repeat the procedure and develop a photodiode and mount for use as a reference device at frequencies of up to 40 GHz.

The optoelectronic mixing effect predicted from the modelling results will have considerable potential for future frequency standards for coherent optical communications. It is hoped that a project can be started to develop devices with a good conversion efficiency for this application.

7. REFERENCES FOR PART 3

1. *R F Leheny, R E Nahory and M A Pollack*: '$In_{0.53}Ga_{0.47}As$ photodiodes for long wavelength fibre-optic systems', Electron. Lett., Vol. 15, pp. 713 - 715, October 1979.

2. *T P Lee, C A Burrus and A G Dentai*: 'InGaAs/InP p-i-n photodiodes for lightwave communications at the 0.95 - 1.65 μm wavelength ', IEEE J. of Qantum. Electron., Vol. QE-17 (2), pp. 232 - 238, February 1981.

3. *K Li, E Rezek and H D Law*: 'InGaAs pin photodiode fabricated on a semi-insulating InP substrate for monolithic integration', Electron. Lett., Vol. 20 (5), pp. 196 - 198, March 1984.

4. *T P Pearsall (Ed)*: 'GaInAsP Alloy Semiconductors', Wiley, ISBN 0 471 10119 2, 1982.

5. *D G Parker*: 'The theory, fabrication and assessment of ultra high speed photodiodes', GEC journal of research, Vol. 6 (2), pp. 106 - 117, 1988.

6. *R S Sussman, R M Ash, A J Moseley and R C Goodfellow*: 'Ultra low capacitance flip chip bonded GaInAs photodiode', Electron. Lett., Vol. 21, pp. 573 - 575, 1985.

7. *T H Windhorn, L W Cook and G E Stillman*: 'The electron drift velocities in $In_{0.53}Ga_{0.47}As$ at 300 K', Electron. Device Lett., Vol. 3, pp. 18 - 20, 1982.

8. *T H Windhorn, L W Cook and G E Stillman*: 'Electron drift velocites in $In_{0.53}Ga_{0.47}As$ at very high fields', IEDM Technical Digest, pp. 641 - 644, 1981.

9. *M A Littlejohn, J R Hauser and T H Glisson*: 'Velocity-field characteristics of $Ga_{1-x}In_xP_{1-y}As_y$ quaternary alloys', App. Phys. Lett., Vol. 30, pp. 242 - 244, March 1977.

10. *C M Snowden*: 'Semiconductor device modelling', Peter Peregrinus Ltd. (London), ISBN 0 86341 130 4, chapter 8, 1988.

11. *P A Blakey*: 'A study of the output power capabilities of avalanche diode oscillators', PhD Thesis, University College London, March 1976.

12. *D Wake, L C Blank, R H Walling and I D Henning*: 'Top illuminated InGaAs/InP PIN-photodiode with a 3dB bandwidth in excess of 26 GHz', ECOC'87 Vol. III (postdeadline papers), pp. 67 - 69, September 1987.

13. *M G Cox*: 'Practical spline approximation', NPL report DITC 1/82.

14. *P M Harris*: 'The use of splines in the modelling of a photodiode response', NPL report **DITC 88/87**.

15. Rhode Island Electronic Ceramics, Beam lead package, DWG. No. 3-3032.

16. *C A Burrus, J E Bowers and R S Tucker*: 'Improved very-high-speed packaged InGaAs PIN punch-through photodiode', Electron. Letts., Vol. **21** (7), pp. 262 - 263, March 1985.

17. *P E Gill, W Murray, S M Pickering and E M Long*: 'Subroutine LCQNDF', Ref. No. E4/38/1/Fortran/10/86, 1986.

18. *J E Bowers and C A Burrus*: 'InGaAs PIN photodetectors with modulation response to millimetre wavelengths', Electron. Letts., Vol. **18**, pp. 812 - 814, August 1985.

19. *J Schlafer and L Ulbricht*: 'Packaging techniques for broadband microwave optoelectronic components', SPIE conference **995**, 'High frequency analogue communications', Ed. P Sierak, pp. 48 - 52., September 1988.

20. *P Schmid and H Melchior*: 'Coplanar flip-chip mounting technique for picosecond devices', Rev. Sci. Instrum., Vol. **55** (11), pp. 1854 - 1858, November 1984.

21. *P R Smith, D H Auston, A M Johnson, and W M Augustyniak*: 'Picosecond photoconductivity in radiation-damaged silicon-on-sapphire films', App. Phys. Lett., Vol. **38** (1), pp. 47 - 50, January 1981.

22. *P Cheng*: 'Coplanar waveguide: a surface strip transmission line suitable for nonreciprocal gyromagnetic device applications', IEEE Trans. Microwave Theory and Tech., Vol. **MTT-17**, pp. 1087 - 1090, 1969.

23. *V F Hana and D Thebault*: 'Theoretical and experimental investigation of asymetric coplanar waveguides', IEEE Trans. Microwave Theory and Tech., Vol. **MTT-32**, pp. 1649 - 1651, 1984.

25. American Technical Ceramics, ATC113 'Twincap'.

26. American Technical Ceramics, ATC111.

27. *D Wake, L C Blank, R H Walling, I D Henning*: 'Top-illuminated InGaAs/InP p-i-n photodiodes with a 3-dB bandwidth in excess of 26 GHz', IEEE Electron. Device Letts., Vol. **EDL-9** (5), pp. 226 - 228, May 1988.

28. P Hill, J Schlafer, W Powazinik, M Urban, E Eichen, R Olshanski: 'Measurements of hole velocity in n-type InGaAs', App. Phys. Letts., Vol. 50 (18), pp. 1260 - 1262, May 1987.

CONCLUDING REMARKS

AIMS

The aims of the work covered in this thesis were threefold: to provide improved metrological techniques for the measurement of high bandwidth optoelectronic devices; to develop numerical methods which will increase the accuracy of the measured results; and finally, to develop devices which can be used as calibration artifacts to disseminate standards for temporal and frequency response measurements.

The first two of these targets have been successfully met. At present, the collaborative programme with Plessey to make the transfer standard devices is incomplete. However, the transfer standard principle has been successfully demonstrated.

ACHIEVEMENTS OF PART 1

The first part of this thesis was concerned with the development and assessment of accurate measurement techniques for optoelectronic devices.

In chapter 2, the comb harmonic method was used to measure the frequency response of an unknown photodiode at up to 18 GHz using a well characterised photodiode as a transfer standard reference. Over this frequency range the r.f. power in the comb drops by more than 40 dB. The results were compared with measurements made using pulsed laser diodes and the same transfer standard reference. The two sets of results agree, to within the uncertainty limits, at frequencies of up to 15 GHz. This work illustrates the potential advantages of using a transfer standard photodiode as a reference device and is the first report of such a comparison.

In chapter 3, a comparison was made between three different heterodyne systems at 1.5 μm. The results indicated that a continuously tunable system is necessary for accurate device metrology. Potentially serious sources of systematic error were identified in conventional DFB based systems. This is believed to be the first report of such a comparison.

A heterodyne system using a novel detection scheme has been developed. A preliminary report of this new system has been presented at an IEE colloquium [1]. The system has been used to measure photodiodes at up to

40 GHz and a dynamic range in excess of 20 dB has been demonstrated. This new system represents a significant advance in optoelectronic device metrology as it is less sensitive to optical feedback and has a wider dynamic range than conventional techniques.

A new *Vector* Heterodyne system to measure both the magnitude and the phase responses of an unknown detector has been demonstrated. The measured results have been compared with magnitude and phase responses obtained by the deconvolution of time domain measurements. This system has the potential for operation to considerably higher frequencies than is possible with other techniques. This is the first report of both the measurement system and the comparison.

A second new Vector Heterodyne system, based on *acousto-optic modulators*, has been proposed. The principle of operation of the system has been described.

In chapter 4 a system based on *Integrated Optic Modulators* was demonstrated. This new system has been reported as both journal[2] and conference[3] papers. The system, based on a nominally 8 GHz modulator, gives a continuously tunable, levelled, modulated optical signal of 4 μW at up to 22.6 GHz. The technique has the potential for operation to 40 GHz using commercially available equipment.

In chapter 5, correlation techniques were reviewed and the difficulty of extracting the photodiode response from a waveform, measured with a sampling oscilloscope, was shown. A measurement system based on r.f. autocorrelation was demonstrated. The bandwidth of the system tested was approximately 40 GHz. This technique is an advance for optoelectronic device metrology as the equipment used is inexpensive provided that a suitable source of picosecond optical pulses is available. This is believed to be the first report of electrical correlation methods being used to measure the response of an optoelectronic device.

The r.f. correlation technique can be extended to provide jitter-free cross-correlation measurements. The temporal response of the unknown device can be determined using the response of the transfer standard; a measurement of the autocorrelation response of the transfer standard; and a cross-correlation measurement of the transfer standard and unknown devices.

Techniques to improve the accuracy of frequency domain measurements have been described in chapter 6. Results, measured at up to 40 GHz, show that the smoothness of the measured response can be considerably improved by the application of this new procedure. The first report of this method was given recently at an IEE colloquium[1]. The improvement in measurement accuracy is typically fourfold, representing a significant improvement in the optoelectronic device metrology.

The first report of an informal international intercomparison of frequency response measurements has been presented in chapter 7. Three different techniques were compared and the results agree typically to within ±1 dB. This comparison conclusively demonstrated the advantages of using the error correction procedure described in chapter 6.

ACHIEVEMENTS OF PART 2

The second part of this thesis was concerned with the development of numerical techniques to improve the accuracy and interpretability of the measured results.

The different deconvolution strategies were described in chapter 2 and the significance of the filtering function was discussed. An optimal deconvolution method has been described. This new method allows devices measured using different laser systems to be compared. The technique has been extended to allow many sets of measurements to be combined to give a single result. These methods will improve optoelectronic device metrology as they can be used to de-embed the device response from the measured results. This is the first report of these deconvolution methods.

In chapter 3 the effects of noise on a sampling system were discussed and the distortion introduced by *Jitter* was described. The effects of noise and jitter on the variance of the measured signal were presented. The expected responses of a sampling system to a signal with noise, jitter, amplitude dependent noise and amplitude dependent jitter added were demonstrated using simulated data. The results show distinct patterns for the mean, the variance and the raw data. This may assist users to estimate the characteristics of the noise in their measurement systems.

A numerical algorithm to reduce or remove the effects of jitter has been developed. This new method requires the measurement of both the

mean and the variance of the signal at each temporal point. The algorithm has been tested using data containing simulated jitter. The error between the original signal and the jittered signal after processing was small. This is the first report of this new strategy to remove jitter from measured signals.

Techniques were presented to measure jittered signals using the first generation (analogue) and second generation (digital) sampling oscilloscopes. The limitations of the measurement systems were discussed. Results have been presented using both measurement methods. The quality of the fit between the measured and calculated variances was extremely high for measurements made using the analogue sampling oscilloscope system.

The techniques reported in this part of the thesis can be used to overcome the effect of jitter which is a serious measurement problem occurring on a picosecond timescale. This work therefore represents a considerable advance for optoelectronic and electrical waveform metrology.

ACHIEVEMENTS FOR PART 3

In this part of the thesis the results of a collaborative research programme, to develop a fast photodiode for use as a reference device for high speed optoelectronic measurements, have been described. The aim of the programme was to produce a photodiode with a large active area, high bandwidth and good electrical properties. Such a device could be used, with the techniques described in parts 1 and 2 of this thesis, to measure unknown device responses. The concept and application of a photodiode as a transfer standard for frequency or temporal response measurements was first published by this author[4].

A suite of modelling programs, described in chapter 3, has been developed to allow the diode design to be optimised. These modelling programs were designed to be fast and flexible, so that a number of parameters could be varied without incurring large cost penalties. The accuracy of the model was checked against the measured performance of a photodiode with a known structure. This work was reported as both a journal paper[4] and at an IEE colloquium[5].

Three iterations of the device design cycle have been described. Devices produced in the second iteration have frequency responses of

approximately 17 GHz for a 40 μm device. This is believed to be the highest bandwidth reported for a device of this size.

An informal collaborative project with British Telecom Research Laboratories, to mount a fast pin photodiode in a microstrip holder, is described in chapter 5. The resultant device had a 3 dB frequency of 20.5 GHz and was free from any high frequency resonances. This mounting strategy offers the potential for the development of photodiodes with frequency responses extending to above 40 GHz.

FURTHER WORK

The planned future work falls into four main catagories: the improvement of techniques and measurement systems described in this thesis; the comparison of different measurement techniques; the development of techniques to accurately estimate the temporal response of the transfer standard photodiodes; and the provision of future standards for the next generation of fibre optic systems. The first of these topics is adequately covered in the appropriate chapter conclusions and will not be discussed further.

An international round-robin of photodiode frequency response measurements has been planned. This will allow a compaison to be made between a variety of different measurement techniques and may identify some systematic errors in the methods used. Two GaInAs diodes will be circulated to each of the eight participating establishments in turn. The measurements are expected to take eight months to complete and should be finished by September 1990. This work will provide valuable data on the current state of the art in optoelectronic device metrology.

At present the temporal response of the transfer standard photodiode is estimated on the basis of a simple device model. The procedure to improve the accuracy of frequency response measurements ($|S_{21}|$), described in part 1, chapter 6, also provides a measurement of the photodiode return loss (S_{22}). It should be possible to use these data to improve the device model and thus more accurately estimate the phase of the optoelectronic response.

The future optical fibre communication systems may use coherent techniques. These are akin to superheterodyne reception but at optical frequencies and using an optical local oscillator to recover the

signal. Coherent communication gives an increase in the sensitivity of a system and also allows a number of channels, at different wavelengths, to be used in the same optical fibre. These new techniques will require the provision and dissemination of accurate frequency standards so that the frequencies of the different optical transmitters can be locked together. Some preliminary work has been performed to develop optoelectronic mixing devices[6] which could be used to accurately disseminate the frequency standards. A programme of work is planned to develop these optoelectronic mixing devices as a metrological tool. The work will build on the modelling and measurement techniques presented in this thesis.

REFERENCES

1. Paper 10, Appendix 2.

2. Paper 8, Appendix 2.

3. Paper 9, Appendix 2.

4. Paper 5, Appendix 2.

5. Paper 3, Appendix 2.

6. Paper 4, Appendix 2.

ACKNOWLEDGEMENTS

I wish to thank my supervisors at NPL and UCL, Drs Alan Roddie and Mike Wilson for their encouragement and many stimulating conversations. I also wish to thank my past supervisors: Dr D Ross, Prof B Culshaw and Dr J G Edwards for their support.

I am greatly endebted to Dr C A Burrus of AT&T Crawfords Corner Laboratories, NJ for supplying the GaInAs research photodiode. This device became the mainstay for the work to develop and improve measurement techniques.

Many thanks are due to my collegues at NPL for their help and encouragement: Dr D Henderson for the electro-optic sampler results and help with the comb harmonic and correlation measurements; Mr J M Williams for stimulating discussions on the measurement of jitter; Dr H Antony and Mr P Harris for the numerical optimisation and spline programs; Mr D Ives for help with the Vector Heterodyne measurements; Mr A P Gregory and Mr R N Clarke for help with the HP8510 network analyser; and Dr D Knight for many helpful discussions and the use of his HP8566B spectrum analyser.

Thanks to my collegues and friends at Plessey Research (Caswell). I am especially grateful to Drs A J Moseley and C Park for their work on the fabrication of the photodiodes and the DFB lasers.

I thank my collegues at British Telecom Research Laboratories: Dr R Wyatt for the use of his external cavity laser system and Mr D Wake for the high speed pin photodiodes.

I am grateful to Dr R Lauer and Mr J Schlafer of GTE inc, MA, USA, for the loan of the three high speed GaInAs photodiodes and for participating in the measurement intercomparison.

I thank the Director of the National Physical Laboratory for his permission to undertake this work and for financial support.

Finally I would like to thank my family and friends for their encouragement and I am especially endebted to Sharon, my wife, for her patience and support.

APPENDIX 1:ADAPTIVE TIME-DRIFT COMPENSATION

In this analysis the Adaptive time-drift compensation technique (*H Meckleburg and K Matkey*[1]) has been extended to allow an improved estimate for the drift parameter and to give the uncertainty of the parameter.

A delay in the time domain corresponds to a multiplication by a phase shift term in the frequency domain as shown in equation A1.1:

$$f(t-\tau) \rightarrow F(j\omega)\exp(-j\omega\tau) \qquad \text{(eq. A1.1)}$$

where τ is the delay parameter.

By comparing the phases of the reference and delayed signal at one harmonic an estimate can be made for the delay. However the time range within which the delay τ is uniquely calculable decreases with increasing frequency. The range of unique values of τ is given by equation A1.2:

$$-\frac{T}{n} < \tau \leq \frac{T}{n} \qquad \text{(eq. A1.2)}$$

where T is the period of the deconvolved results; and n is the harmonic number.

The delay τ is uniquely calculable over the full period for only the fundamental frequency (n=1). If the phase differences between successive harmonics are compared (equations A1.3 and A1.4), instead of the absolute phase, then the delay τ will be unique over the full period T as shown in equation A1.5.

$$\phi_i - \bar{\phi}_i = i\Delta\omega\tau \qquad \text{(eq. A1.3)}$$

$$\phi_{i+1} - \bar{\phi}_{i+1} = (i+1)\Delta\omega\tau \qquad \text{(eq. A1.4)}$$

where ϕ and $\bar{\phi}$ are the phases of the unknown signal and the reference respectively.

$$\Delta\omega\tau = \Delta\phi - \Delta\bar{\phi} \qquad \text{(eq. A1.5)}$$

If the delay is calculated from the phase shift at a single pair of frequencies then the uncertainty in the delay due to noise cannot be estimated. The analysis can be extended to use all the measured data. This will improve the accuracy of the calculated delay and give a figure for the uncertainty. The complex exponential corresponding to the delay is given by equations A1.6 and A1.7 for the signal and reference:

$$\exp(-j\Delta\omega\bar{\phi}) = \frac{B^*_{i+1}B_i}{|B_{i+1}B_i|} \qquad \text{(eq. A1.6)}$$

$$\exp(j\Delta\omega\phi) = \frac{A_{i+1}A^*_i}{|A_{i+1}A_i|} \qquad \text{(eq. A1.7)}$$

where A is the signal; and B is the reference.

The delay correction is given by equation A1.8:

$$\Theta_i = \frac{A_{i+1}A^*_iB^*_{i+1}B_i}{|A_{i+1}A_iB_{i+1}B_i|} \qquad \text{(eq. A1.8)}$$

where Θ_i is the delay correction.

If the delay correction parameters Θ_i for each of the harmonics are summed with a weight proportional to the product of the magnitudes of the components the mean phase shift will be given by equations A1.9 and A1.10. The sum of the weighting parameters K_i is greater than unity so that the magnitude of $\bar{\Theta}$ will be one.

$$\bar{\Theta} = \sum_{i=1}^{n-1} K_i\Theta_i \qquad \text{(eq. A1.9)}$$

where

$$K_i = \frac{|A_{i+1}A_iB_{i+1}B_i|}{|\sum_{j=1}^{n-1} A_{j+1}A^*_jB^*_{j+1}B_j|} \qquad \text{(eq. A1.10)}$$

The variance of the delay correction parameter gives the uncertainty of the delay correction calculations. This is given by equation A1.11:

$$\sigma_\theta^2 = \frac{2\sum_{j=1}^{n-1} |A_{j+1}A_j^*B_{j+1}^*B_j|}{|\sum_{j=1}^{n-1} A_{j+1}A_j^*B_{j+1}^*B_j|} - 2 \qquad \text{(eq. A1.11)}$$

where σ_θ^2 is the variance of the delay correction parameter.

REFERENCES FOR APPENDIX 1

1 *H Meckelburg and K Matkey*: 'A highly sensitive microwave sampling system with adaptive time-drift compensation', IEEE Trans. on Instrumen. and Meas., Vol **IM-34** (3), September 1985, pp 427 - 430

APPENDIX 2: PAPERS PUBLISHED DURING THE PERIOD OF THE THESIS

1. *D A Humphreys, R J King, D Jenkins and A J Moseley*: 'Measurement of absorption coefficients of $Ga_{0.47}In_{0.53}As$ over the wavelength range 1.0-1.7 μm', Electron. Letts., Vol. **21** (25/26), pp. 1187 - 1189.

2. *D Erasme, D A Humphreys, A G Roddie and M G F Wilson*: 'Optimisation and experimental results for a phase-reversal travelling-wave modulator', Proc. ECIO conference, Glasgow, May 1987.

3. *D A Humphreys*: 'Small signal modelling of photodiodes using a finite difference/lumped parameter approach', IEE colloquium, 'Modelling and analysis of circuits and devices', paper 18, 4 December 1987.

4a. *D A Humphreys*: 'Nonlinear mixing effect in GaInAs photodiodes', SIOE'87 conference, Cardiff, paper 25, abstract only, March 1987.

4b. *D A Humphreys and R A Lobbett*: 'Investigation of an optoelectronic nonlinear effect in a GaInAs photodiode, and its application in a coherent optical communication system', IEE Proc. Pt. J, Vol. **135** (1), pp. 45 - 51, February 1988. (*1)

5a. *D A Humphreys*: 'Development of GaInAs photodiodes for use as transfer standards', SIOE'87 conference, Cardiff, paper 26, abstract only, March 1987.

5b. *D A Humphreys and A J Moseley*: 'GaInAs photodiodes as transfer standards for picosecond measurements', IEE Proc. Pt. J, Vol. **135** (2), pp. 146 - 152, April 1988.

6. *D Erasme, D A Humphreys, A G Roddie and M G F Wilson*: 'Design and performance of Phase Reversal Traveling Wave Modulators', IEEE J. of Lightwave Tech., Vol. **6** (6), pp. 933 - 936, June 1988.

7. *A J Moseley, A C Carter, M Q Kearley, C A Park and D A Humphreys*: 'High speed InGaAs/InP photodiodes for application to 40 GHz', OE Fiber/Lase conference (Boston), SPIE Vol. **955**, pp. 61 - 67, September 1988.

(*1) This paper was awarded the IEE *Ambrose Fleming premium* for the 1987/1988 session

8. *D A Humphreys*: 'Integrated-Optic system for high-speed photodetector bandwidth measurements', Electron. Letts., Vol. 25 (23), pp. 1555 - 1556, November 1989.

9. *D A Humphreys*: 'Integrated Optic system for high speed photodetector bandwidth measurements', IEE colloquium, 'Optical detectors', January 1990.

10. *D A Humphreys and C A Park*: 'High accuracy frequency response measurements of mm-wave photodiodes using a DFB heterodyne system with a novel detection scheme', IEE colloquium, 'Optical detectors', January 1990.

APPENDIX 3: ERRATA

Page 43. The first sentance of section 3.6. should read *'A beat frequency measurement system consisting of two external cavity lasers was used to measure the performance of two GaInAs high speed photodiodes.'*.

Page 63. In figure 3.27, the optical attenuator to balance the r.f. powers is not shown. This attenuator was placed in series with the 19 GHz monitor photodiode.

Page 96. In paragraph 3, line 4, the sentance *'transformed to the frequency domain and deconvolved'* is superfluous.

Page 124. Figure 2.2 shows a photographic record of the photodiode response with a FWHM of 62 ps. The digitised and stored record for the same device was 65 ps FWHM as described in the text.

Page 124. Figure 2.3 shows the results of the forward convolution method on measurements made with an 898 nm laser diode, not the 850 nm device described in the text. The numbers in both sets of results (i.e. in the text and in the diagram) are self consistant.

Page 214. Section 3.8 (Chapter conclusion) refers to both chapters 2 and 3.